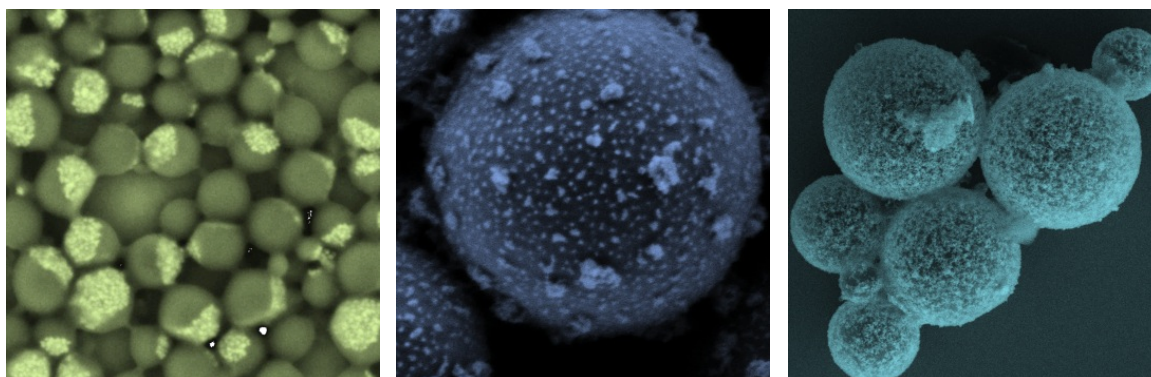




# Multifunctional Polymer/Inorganic Hybrid Nanoparticles with Controlled Structure

by

**Olaia Álvarez Bermúdez**



A thesis submitted in fulfillment of the requirements for the degree of:

**Doctor in Chemistry**

Under the supervision of

**Rafael Muñoz-Espí and Katharina Landfester**



Valencia, January 2019



**REPORT OF THE ADVISORS FOR THE SUBMISSION OF DOCTORAL THESIS  
INFORME DELS DIRECTORS PER AL DIPÒSIT DE TESI DOCTORAL**

**Rafael Muñoz-Espí**, researcher at the Institute of Materials Science of the University of Valencia, and **Katharina Landfester**, professor and director at the Max Planck Institute for Polymer Research, Mainz, Germany,

*Rafael Muñoz-Espí, investigador de l'Institut de Ciència dels Materials de la Universitat de València, i Katharina Landfester, catedràtica i directora de l'Institut Max Planck de Recerca en Polímers de Magúncia, Alemanya,*

as advisor and co-advisor, respectively, of the doctoral thesis of  
*com a director i co-directora, respectivament, de la tesi doctoral d'*



***Olaia Álvarez Bermúdez,***

student of the Doctoral Program in Chemistry of the University of València,  
*estudiant del Programa de Doctorat en Química de la Universitat de València,*

issue the present **favorable report** for the submission and defense of the doctoral thesis.

*emeten el present **informe favorable** per a la realització del dipòsit i la defensa de la tesi doctoral.*

December 20, 2018 / *20 de desembre de 2018*

  
  
Rafael Muñoz-Espí  
Advisor / Director

  
  
Katharina Landfester  
Advisor / Directora







## **Abstract**

Hybrids and composite materials offer a synergic combination of polymer and inorganic features. The integration of specific functionalities at the nanoscale leads to the improvement of the characteristics of macroscopic materials. In this context, the attractiveness of multifunctional polymer–inorganic nanoparticles is remarkable. The relative arrangement of the components forming the hybrid nanostructure determines the accessibility of the functionalities, the properties, and the applicability of the material. Colloidal methods have been traditionally used for the preparation of hybrid nanoparticles, but the precise control of their morphology remains still a challenge.

The objective of this thesis is to establish the bases for the preparation of multifunctional polymer–metal oxide hybrid nanoparticles and capsules with a morphology controlled according to the application. The miniemulsion technique was used to overcome the structural restrictions of other synthetic platforms. For this aim, inorganic species with complementary catalytic (ceria and titania) and magnetic (magnetite) properties were simultaneously incorporated within different polymer supports (polystyrene, PMMA, and polyurethane) via miniemulsion polymerization processes and their variations. The inorganic species were functionalized with different silanes. The control of the hybrid morphology was approached by tuning the differences of polarity and the interfacial chemistry involved between the inorganic functionalities and the polymer. The chemical structure of the coupling agent was related to the specific deposition of metal oxides nanoparticles on the polymer surface, within the matrix or to the formation of Janus-like structures. The control allowed by this strategy was used for the preparation of magnetoresponsive polymer-supported catalysts. The catalytic functionalities were also incorporated by functionalization of the polymer surface with chiral units of amino acids. The hybrid nanoparticles were proposed for heterogeneous and enantioselective catalysis with industrial relevance. In addition, miniemulsions were used for the preparation of a specific type of particles with a liquid core (capsules), which were exploited for the encapsulation of hydrated salts as phase change materials for energy storage applications. The efficiency and scalability of the synthetic strategy was studied and related to the performance of the product in energy-related applications. In this fashion, the work proposes the substitution of traditional surfactants by surface active monomers (surfmers) and inorganic nanoparticles as functional emulsifiers.

In summary, this thesis proves the versatility of the miniemulsion technique as a synthetic platform for the preparation of multifunctional hybrid nanomaterials with a controlled structure for catalytic and energy–related applications.



# Contents

<b>1 Motivation .....</b>	<b>1</b>
<b>2 Theoretical Background .....</b>	<b>3</b>
2.1 Synthesis of Polymer–Inorganic Hybrid Nanoparticles and Capsules in Miniemulsion .....	3
2.2 Basic Principles for the Structure of Hybrid Nanoparticles Prepared in Miniemulsion .....	4
2.3 Synthesis of Polymer–Inorganic Hybrid Nanocapsules in Miniemulsion .....	8
2.3.1 General Overview .....	8
2.3.2 Basic Principles for Structure Control of Hybrid Capsules via Phase Separation .....	8
2.4 Stability of Emulsions .....	10
2.4.1 Stabilization of Miniemulsions .....	11
2.4.2 Pickering Stabilization .....	14
2.4.3 Polymerizable Surfactants (Surfmers) .....	15
2.5 Synthesis of Inorganic Nanoparticles .....	17
2.5.1 Synthesis of Superparamagnetic Magnetite Nanoparticles .....	17
2.5.2 Synthesis of Crystalline Ceria Nanoparticles .....	18
2.5.3 Functionalization of Inorganic Nanoparticles .....	19
2.6 Specific Strategies for the Preparation of Polymer–Inorganic Hybrid Nanoparticles and Capsules in Miniemulsion .....	21
2.6.1 Synthesis of Hybrid Nanoparticles by Miniemulsion Polymerization Processes in the Presence of Preformed Inorganic Components .....	21

2.6.2	Synthesis of Nanoparticles by Pickering Miniemulsion Polymerization .....	24
2.6.3	Synthesis of Hybrid Nanoparticles in Minimemulsion Using the Surface of Preformed Polymers as Supports for the In-Situ Inorganic Crystallization.....	26
2.6.4	Synthesis of Hybrid Capsules by Phase Separation.....	28
2.6.5	Synthesis of Hybrid Capsules via Chemical Processes at the Droplet Interface of Miniemulsions.....	29
<b>3</b>	<b>Characterization Techniques .....</b>	<b>31</b>
3.1	Colloidal Characterization.....	31
3.1.1	Dynamic Light Scattering (DLS).....	31
3.1.2	Polyelectrolyte Titration (PCD).....	33
3.2	Thermal Characterization .....	34
3.2.1	Thermogravimetric Analysis (TGA).....	34
3.2.2	Differential Scanning Calorimetry (DSC) .....	35
3.3	Electron Microscopy (EM) Characterization .....	35
3.3.1	Transmission Electron Microscopy (TEM) .....	36
3.3.2	Scanning Electron Microscopy (SEM) .....	36
3.4	Characterization of Chemical Composition and Chemical Structure.....	37
3.4.1	Inductively Coupled Plasma-Mass Spectrometry (ICP-MS) .....	37
3.4.2	X-Ray Diffraction (XRD) .....	37
3.4.3	Ultraviolet-Visible Spectroscopy or Spectrophotometry (UV-Vis).....	38
3.4.4	High Performance Liquid Chromatography (HPLC).....	39

<b>Results and Discussion .....</b>	<b>43</b>
<b>4 Preparation of Hybrid Polymer–Metal Oxide Nanoparticles with Controlled Morphology .....</b>	<b>43</b>
4.1 Synthesis and Functionalization of Functional Inorganic Nanoparticles.....	43
4.2 Preparation of Polymer–Metal Oxide Hybrid Nanoparticles with Specific Morphology Controlled via Inorganic Surface Functionalization .....	46
4.3 Influence of the Initiator over the Morphology of the Polymer–Metal Oxide Hybrid Nanoparticles Prepared by Miniemulsion Polymerization .....	52
4.4 Preparation of Multifunctional Polymer–Metal Oxide Hybrid Nanoparticles.....	55
4.5 Conclusions.....	58
<b>5 Magnetically Enhanced Polymer-Supported Ceria Nanocatalysts .....</b>	<b>59</b>
5.1 State of the Art of the Preparation of Magnetoresponse Polymer-Supported Nanoparticles for Heterogeneous Catalysis .....	59
5.2 Synthesis and Functionalization of Inorganic Nanoparticles.....	61
5.3 Preparation of Polystyrene-Supported Ceria Nanoparticles .....	62
5.4 Catalysis of the Hydration of 2-Cyanopyridine to 2-Picolinamide .....	67
5.5 Conclusions.....	72
<b>6 Proline-Functionalized Polymer Nanoparticles for Enantioselective Catalysis in Aqueous Media.....</b>	<b>73</b>
6.1 State of the Art of the Preparation of Chiral Hybrid Nanoparticles for Asymmetric Catalysis .....	74
6.2 Synthesis of Proline-Based Building Blocks .....	76
6.3 Preparation of Magnetoresponse Chiral Nanoparticles .....	80
6.4 Asymmetric Catalysis of an Intermolecular Aldol Reaction in Water .....	84
6.5 Conclusions.....	89

<b>7</b>	<b>Magnetic Polyurethane Microcarriers from Nanoparticle-Stabilized Emulsions for Thermal Energy Storage .....</b>	<b>91</b>
7.1	State of the Art: Phase Change Materials for Thermal Energy Storage Applications .....	91
7.2	Preparation of Nanoparticle-Stabilized Inverse Emulsions.....	94
7.3	Preparation of Polyurethane–Metal Oxide Hybrid Capsules by Interfacial Polymerization in Inverse Pickering Emulsion .....	96
7.4	Study of the Suitability of the Hybrid Structures for Encapsulation Purposes.....	100
7.4.1	Encapsulation of Phase Change Materials for Thermal Energy Storage.....	102
7.5	Conclusions .....	106
<b>8</b>	<b>Summary and Outlook .....</b>	<b>109</b>
<b>9</b>	<b>Experimental Section .....</b>	<b>113</b>
9.1	Materials and Methods .....	113
9.2	Synthesis and Functionalization of Inorganic Nanoparticles .....	114
9.2.1	Synthesis of Magnetite Nanoparticles.....	114
9.2.2	Synthesis of Ceria Nanoparticles .....	114
9.2.3	Functionalization of Ceria and Magnetite Nanoparticles .....	115
9.2.4	Functionalization of Titania and Silica Nanoparticles .....	115
9.3	Experimental Section Specific for the Chapter 4 .....	116
9.3.1	Preparation of Polymer–Metal Oxide Hybrid Nanoparticles with Controlled Morphology by Miniemulsion Polymerization.....	116
9.3.2	Preparation of Multifunctional Nanoparticles.....	116
9.4	Experimental Section Specific for Chapter 5 .....	117

9.4.1	Preparation of Polystyrene-Supported Ceria Nanoparticles (C1 and C2) by Pickering Miniemulsion Polymerization (Route P1).....	117
9.4.2	Preparation of Polystyrene-Supported Ceria Nanoparticles (C5 and C6) by Miniemulsion Polymerization and In-situ Crystallization (Route P2) .....	117
9.4.3	Catalysis of the Hydrolysis Reaction of 2-Cyanopyridine to 2-Picolinamide.....	118
9.4.4	Recycling Study.....	119
9.5	Experimental Section Specific for Chapter 6.....	119
9.5.1	Synthesis of 10-undecenoyl- <i>trans</i> -4-hydroxy-L/D-proline (L/D-S1) <i>O</i> -methacryloyl- <i>trans</i> -4-hydroxy-L/D-proline (L/D-S2), and Decanoyl- <i>trans</i> -4-hydroxy-L-proline (L-S3) .....	119
9.5.2	Preparation of Proline-Functionalized PMMA Nanocatalysts AC1–AC10 by Miniemulsion Polymerization .....	121
9.5.3	Aldol Reaction.....	122
9.5.4	Recycling Study.....	123
9.6	Experimental Section Specific for Chapter 7.....	124
9.6.1	Synthesis of Polyurethane-Based Hybrid Capsules Incorporating Metal Oxide Nanoparticles by Interfacial Polymerization in an Inverse Pickering Miniemulsion.....	124
9.6.2	Release Study.....	124
9.7	Analytic Techniques .....	125
9.7.1	Dynamic Light Scattering (DLS).....	125
9.7.2	Polyelectrolyte Titration (PCD).....	125
9.7.3	Thermogravimetric Analysis (TGA) .....	125
9.7.4	Inductively Coupled Plasma-Mass Spectrometry (ICP-MS).....	125
9.7.5	Transmission Electron Microscopy (TEM).....	125



9.7.6	Scanning Electron Microscopy (SEM) .....	126
9.7.7	X-Ray Diffraction (XRD) .....	126
9.7.8	Brunauer–Emmett–Teller (BET) Surface Area Analysis .....	126
9.7.9	High Performance Liquid Chromatography (HPLC).....	126
9.7.10	Nuclear Magnetic Resonance Spectroscopy .....	126
9.7.11	Ultraviolet-Visible Spectroscopy or Spectrophotometry (UV-Vis).....	127
9.7.12	Differential Scanning Calorimetry (DSC) .....	127
<b>References .....</b>		<b>129</b>
<b>A. List of Figures .....</b>		<b>147</b>
<b>B. List of Tables .....</b>		<b>153</b>
<b>C. List of Schemes.....</b>		<b>155</b>
<b>D. List of Acronyms .....</b>		<b>157</b>
<b>E. Scientific Contributions .....</b>		<b>159</b>
<b>F. Acknowledgments.....</b>		<b>161</b>

# 1 Motivation

**“The science of today is the technology of tomorrow”**

– Edward Teller

The increase of the impact of technology in our current society requires the development of advanced multifunctional materials with high performance and improved properties. In addition, the unaffordable growth of the population and the consumption of resources demand the continuous optimization of the energy, the chemical, and the pharmaceutical sectors. In this context, the research on hybrids and composites is being greatly developed. The attractiveness of polymer–inorganic hybrid materials relies on the synergic combination of the features of polymers (e.g., biocompatibility, chemical stability, and easy processability) and the specific functionalities of inorganic compounds (e.g., with optical, thermal, electrical, magnetic or catalytic properties).<sup>1</sup>

The integration of elements with different nature in a hybrid material needs to deal with problematic interfacial processes and loss of continuity (e.g., of thermal or electric conductivity) related to the presence of pores or aggregates. Bottom-up strategies are highlighted in the design of materials with specific characteristics achievable only at the nanoscale, and the controlled assembly of such nanomaterials leads to enhanced macroscopic systems. The morphology of the nanostructures plays also an essential role in the properties of the final material. Therefore, the requirement of accessibility of the different functionalities will be strongly determined by the application. With the increase of complexity of the system (e.g., the incorporation of several inorganic functionalities) and the decrease of the size of the individual structures (e.g., nanometric size), the relevance of the morphology is even greater. The preparation of complex hybrid nanomaterials has been approached by different methods,<sup>2</sup> but the control of their structure remains still a challenge.<sup>3-5</sup>

Colloidal methods offer a versatile synthetic platform for the preparation of hybrid polymer–inorganic nanoparticles via wet-chemistry processes. Both inorganic and polymer particles can act as hard templates allowing precipitation and crystallization processes on their surface.<sup>6-7</sup> In addition, micelles and stable droplets can act as soft templates or nanoreactors to confine physicochemical processes. Therefore, inorganic precipitation or polymerization processes have been carried out in emulsions, allowing the encapsulation and compartmentation of the inorganic compounds within a polymer matrix.<sup>7-8</sup> The droplet confinement introduces also a high surface area where interfacial processes can be controlled.<sup>6,9,10</sup>

This thesis aims the development of a synthetic toolbox for the preparation of polymer–inorganic hybrid nanomaterials with controlled morphology by methods involving the miniemulsion technique. The prepared nanostructures are specifically designed for catalytic and energy-related applications.

Chapter 2 offers an introduction to the theoretical background and the state of the art in the use of miniemulsion for the synthesis of polymer–inorganic hybrid nanoparticles and capsules with magnetic and catalytic properties. Chapter 3 describes the main techniques that are used in this thesis for the characterization of the produced hybrid materials. Chapter 4 is dedicated to the establishment of the synthetic strategies that allow the preparation of hybrid nanostructures with controlled morphology by miniemulsion polymerization. The specific migration of the inorganic functionalities within the matrix is governed by self-assembly processes promoted by the minimization of the interfacial energy of the system. The energy balance of the hybrid is controlled by the surface functionalization of the inorganic components with specific silanes. The chapter offers an insight on the role of the chemical structure of the functionalizing agent on the achievement of different energetic equilibria and the development of the final morphology.

The following two chapters are based on the application of the magnetoresponse and/or catalytically active hybrid nanostructures in specific fields. In every case, we consider the use of straightforward processes and the reduction of the consumption of time and resources associated to the synthesis in miniemulsion. Chapter 5 is focused on the preparation of magnetoresponse polystyrene-supported metal oxide nanocatalysts, highly efficient for reactions with great industrial relevance such as the hydration reaction of nitriles. In Chapter 6, the immobilization of catalytically active inorganic species is substituted by the incorporation of chiral amino acids on the surface of polymer particles. The specific biological behavior of the chiral substances is a source of interest of the pharmaceutical companies. The chapter describes the synthesis of proline-functionalized polymer nanoparticles for the enantioselective catalysis of an intermolecular aldol reaction in aqueous media.

Finally, the development of magnetically recoverable polyurethane-based capsules is discussed in Chapter 7. Hybrid carriers are studied for the encapsulation of hydrated salts as phase change materials (PCMs) with promising features for thermal energy storage applications.

## 2 Theoretical Background

### 2.1 Synthesis of Polymer–Inorganic Hybrid Nanoparticles and Capsules in Miniemulsion

The incorporation of inorganic components within polymer particles has gained a great interest in the materials science community during the last two decades. The integration of the easy processability, the stability, or the biocompatibility of polymer materials and the functional features specifically provided by inorganic components (e.g., optical, magnetic, electrical, catalytic functions) offers the possibility of developing complex and multifunctional hybrid materials with applicability in a wide range of sectors.<sup>11</sup> Inorganic species are also used as a reinforcement of mechanical, thermal, chiral, and electric properties of specific polymer matrices. The characteristics of the resulting polymer–inorganic hybrids go beyond the simple addition of the individual properties of the forming components and allow the achievement of materials with enhanced characteristics. Nevertheless, the morphology of the hybrid structures plays an essential role in the properties of the final material, and its relevance increases with the complexity and the reduction of the size of the system. From the synthetic point of view, the preparation of hybrid nanomaterials with a precisely controlled structure remains as the “holy grail” looked for many researchers.<sup>3, 12-13</sup>

The miniemulsion technique stands out in colloidal chemistry for the preparation of polymer–inorganic hybrid nanoparticles that overcomes the structural limitations of other methods.<sup>2</sup> For instance, layer-by-layer deposition, suspension or emulsion polymerization processes are commonly restricted to the production of hybrid nanostructures with inorganic particles located on the polymer surface or of single inorganic particles covered by a polymer shell. Miniemulsions offer higher versatility and allow the incorporation of inorganic functionalities at different locations within a polymer matrix. In our recent publication,<sup>14</sup> we have dedicated a specific chapter of the book *Nanoemulsions: formulation, applications, and characterization* for the description of the theory and the state of the art in the preparation of hybrid nanoparticles in miniemulsion.

Polymer–inorganic hybrid nanoparticles (and capsules) have been prepared via different synthetic strategies. According to the presence or the absence of the counterpart species or precursors during the synthesis of the polymer and/or the inorganic components, we propose a classification of the different strategies based on the groups listed below.

- Strategies type A consist of the self-assembly of preformed polymer and inorganic components and involve typical processes of inorganic complexation on functionalized polymers or solvent evaporation techniques.
- Strategies type B are polymerization processes in the presence of preformed inorganic components. Typical miniemulsion polymerization, interfacial polymerization, semi-batch polymerization or seed emulsion polymerization processes in the presence of inorganic components synthesized ex-situ are considered in this group.
- Strategies type C use the polymer nanoparticles as supports for inorganic synthesis. In these processes, the in situ formation of the inorganic species takes place on the preformed polymer by inorganic crystallization, precipitation/mineralization, or interfacial sol-gel processes.
- Strategies type D or the so-called *all in-situ* strategies are challenging syntheses related to the formation of the inorganic nanoparticles via hydrolysis and condensation reactions of inorganic precursors occurring simultaneously to miniemulsion polymerization processes.
- Finally, multi-step strategies involve complex cases resulting from the mixture of *pure* synthetic processes, which occur either simultaneously or consecutively.

In all cases considered in this work, at least one of the steps of the process takes place in miniemulsion. Despite the great interest of the all in-situ strategies, groups A and D are beyond the scope of this thesis. The preparation of polymer–inorganic hybrid nanoparticles and capsules with controlled structure has been addressed mainly via strategies type B (i.e., miniemulsion polymerization, Pickering miniemulsion polymerization, and interfacial polyaddition) and type C (i.e., in-situ inorganic crystallization on the surface of preformed polymer nanoparticles).

## 2.2 Basic Principles for the Structure of Hybrid Nanoparticles Prepared in Miniemulsion

The specific arrangement of the different components of polymer–inorganic hybrid nanostructures synthesized in miniemulsion results from self-assembly processes driven by the minimization of the global energy of the system ( $E$ ):

$$E = \sum_{ij} A_{ij}\gamma_{ij} = A_{PW}\gamma_{PW} + A_{IW}\gamma_{IW} + A_{IP}\gamma_{IP} \quad (2.1)$$

For an aqueous dispersion of hybrid nanoparticles,  $E$  is expressed according to eq. (2.1) as the sum of the individual interfacial energies ( $E_i$ ) between the different phases ( $i, j$ ) (i.e., the polymer (P),

the inorganic species (I), and the aqueous phase (W). In the equilibrium, the development of the preferential hybrid morphology takes place by lowering the interfacial areas ( $A_{ij}$ ) and interfacial tensions ( $\gamma_{ij}$ ) related to the three phases. According to this theory, the control of the inner structure of hybrid nanoparticles synthesized in miniemulsion can be addressed by tuning the energy balance of the system. In this sense, Gonzalez-Ortiz and Asua<sup>4, 15</sup> proposed a mathematical correlation between the interfacial tensions ( $\gamma_{PW}$ ,  $\gamma_{IP}$  and  $\gamma_{IW}$ ) and the development of different hybrid structures. The authors established morphology diagrams that were used to evaluate the theoretical predictions by comparison with the empirical results reported for different polymer–inorganic combinations.<sup>4, 15</sup> The study points out the nature and the amount of the surfactant,<sup>16</sup> the type of initiation<sup>17</sup> of the polymerization, and the differences of polarity of the monomer/polymer<sup>18</sup> versus the inorganic species as the three main parameters influencing the interfacial tensions in a miniemulsion polymerization process and governing the hybrid structures reached in the equilibrium. Figure 2.1 presents schematically the synthesis of polymer–inorganic nanoparticles by miniemulsion polymerization and the different morphologies achievable. The miniemulsion formulation will strongly determine the homogeneous distribution of the inorganic species within the polymer matrix, the phase segregation of the species with formation of Janus-like or core–shell morphologies, or the complete separation of the polymer and the inorganic materials.

The concentration of the surfactant determines the interfacial tension between the polymer ( $\gamma_{PW}$ ) and the inorganic components ( $\gamma_{IW}$ ) with the aqueous phase. At low surfactant concentrations, the phase with the lower interfacial tension respect to the water (usually the polymer) will be exposed at the droplet interface. The use of high surfactant concentrations lowers both  $\gamma_{PW}$  and  $\gamma_{IW}$ , whose difference becomes negligible. Then, the development of the hybrid morphology relies on the interfacial tension between the polymer and the inorganic components ( $\gamma_{PI}$ ). According to these considerations, the inorganic encapsulation is favored at low concentrations of the surfactant, whereas high concentrations allow phase segregation and Janus-like structures.

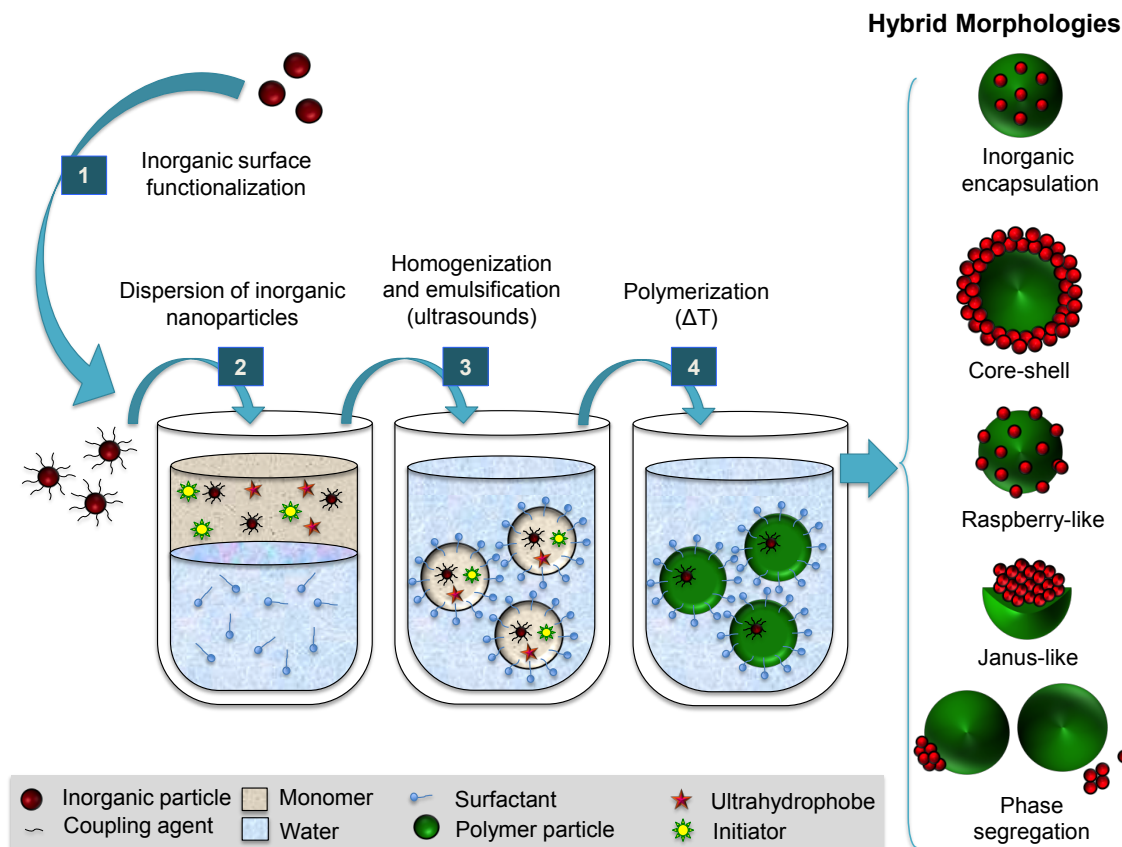


**Figure 2.1.** Scheme of the preparation of polymer–inorganic nanoparticles by miniemulsion polymerization and the possible hybrid morphologies achieved. (Based on ref. 14)

In a free-radical polymerization process in a direct miniemulsion, the initiator has a direct influence in the interfacial tension between the polymer and the aqueous phase ( $\gamma_{PW}$ ). Table 2.1 presents the solubility in water, the associated radicals, and the chemical structure of the initiators that have been used in this thesis. Water-soluble initiators, such as potassium persulfate (KPS), commonly present charged groups that make the molecular structure water-compatible. Therefore, the radicals generated in the aqueous phase enter in the hydrophobic droplets and lead to an increase of the charge at the droplet interface. Consequently, the decrease of the interfacial tension,  $\gamma_{PW}$ , favors the increase of the interfacial area between the hybrid nanoparticle and water ( $A_{WP}$ ) by keeping the hydrophobic inorganic species within the polymer matrix. When oil-soluble initiators, such as 2,2'-azobis(2-methylpropionitrile) (AIBN) or 2,2'-azobis-(2-methylbutyronitrile) (AMBN), are used, the generation of the radicals takes place within the droplet confinement making more likely the contact of the inorganic components with the water phase. Thus, the encapsulation of the inorganic species occurred using KPS, whereas for identical polymer–inorganic combinations the use of AIBN and AMBN resulted into phase segregation and the formation of Janus-like structures.



**Table 2.1.** Free-radical initiators commonly used for heterophase polymerization processes in direct miniemulsions.

Initiator	Chemical structure	Radicals generated	Solubility in water at 20 °C / g·L <sup>-1</sup>
AIBN <sup>a</sup>	$\begin{array}{c} \text{CN} \quad \text{CN} \\   \quad   \\ \text{H}_3\text{C}-\text{C}-\text{N}=\text{N}-\text{C}-\text{CH}_3 \\   \quad   \\ \text{CH}_3 \quad \text{CH}_3 \end{array}$	$\begin{array}{c} \text{CN} \\   \\ \text{H}_3\text{C}-\text{C} \cdot \\   \\ \text{CH}_3 \end{array}$	< 1
AMBN	$\begin{array}{c} \text{CN} \quad \text{CN} \\   \quad   \\ \text{H}_3\text{CH}_2\text{C}-\text{C}-\text{N}=\text{N}-\text{C}-\text{CH}_2\text{CH}_3 \\   \quad   \\ \text{CH}_3 \quad \text{CH}_3 \end{array}$	$\begin{array}{c} \text{CN} \\   \\ \text{H}_3\text{CH}_2\text{C}-\text{C} \cdot \\   \\ \text{CH}_3 \end{array}$	< 1
KPS	$\text{K}^{\oplus} \quad \ominus \quad \begin{array}{c} \text{O} \\    \\ \text{O}-\text{S}-\text{O} \\    \\ \text{O} \end{array} - \text{O} - \begin{array}{c} \text{O} \\    \\ \text{O}-\text{S}-\text{O} \\    \\ \text{O} \end{array} - \text{O} \quad \ominus \quad \text{K}^{\oplus}$	$\ominus \quad \begin{array}{c} \text{O} \\    \\ \text{O}-\text{S}-\text{O} \cdot \\    \\ \text{O} \end{array}$	27

<sup>a</sup> AIBN: 2,2'-azobis(2-methylpropionitrile).

<sup>b</sup> AMBN: 2,2'-azobis-(2-methylbutyronitrile).

<sup>c</sup> KPS: potassium peroxydisulfate.

<sup>d</sup> Based on the product/safety data sheet of AzkoNobel and Sigma-Aldrich.

The third parameter controlling the development of hybrid morphologies is related to the polarity of the different species in the hybrid and its essential role played in the interfacial energy of the whole system. The polarities of the polymer and the inorganic components determine the respective interfacial tensions with the aqueous phase ( $\gamma_{pW}$  and  $\gamma_{iW}$ ). For a certain polymer–inorganic combination, the differences of polarity can be tuned via the surface functionalization of the inorganic components. Comonomers are also used for compatibilization of the different species and the control of their self-assembly. Besides tuning the hydrophobicity, the functionalization of the inorganic surface is a versatile tool to introduce reactive groups, which can copolymerize and act as linker between polymer and inorganic materials. The copolymerization allows the control of the structure development, which cannot be simply explained with Gonzalez-Ortiz and Asua's model.<sup>4</sup>

Not only the formulation of the miniemulsion but also the selection of the organic–inorganic species and the synthetic strategy will strongly determine the hybrid structure. Sections 2.6.1, 2.6.2, and 2.6.3 present an overview of the state of the art in the preparation of polymer–inorganic hybrid nanoparticles via the strategies type B and C described in section 2.1.1.

In this thesis, the control of the morphological development of hybrid nanomaterials prepared in miniemulsion is addressed by selection of both the synthetic strategy and the surface functionalization of metal oxides via silane chemistry.

## 2.3 Synthesis of Polymer–Inorganic Hybrid Nanocapsules in Miniemulsion

### 2.3.1 General Overview

Miniemulsions can be used for the preparation of polymer–inorganic hybrid nanocapsules, a specific type of nanoparticles characterized by the presence of a solid shell occluding an inner core (e.g., a liquid). The capsule structures present a great potential for a wide range of applications (e.g., as hermetic encapsulating units, tracking carriers, or as vectors for the controlled release of substances). The combination of the polymer and inorganic features highlights the attractiveness of hybrid nanocapsules for the development of self-healing coating films,<sup>19-20</sup> energy storage materials,<sup>9</sup> or drug delivery systems applied in biomedicine.<sup>21</sup>

The synthetic methods allowing the achievement of a capsule-like morphology are divided into phase separation strategies and interfacial processes involving polymerization reactions (i.e., polymerization, polyaddition and polycondensation) and/or inorganic synthesis (i.e., crystallization and hydrolysis/ condensation of inorganic precursors).<sup>10, 14</sup>

### 2.3.2 Basic Principles for Structure Control of Hybrid Capsules via Phase Separation

The development of the capsule morphology by phase separation mechanisms is governed by similar physical principles to the ones described for hybrid nanoparticles in section 2.3.2. The minimization of the overall energy of a system consisting into three immiscible liquid phases ( $i$ ,  $j$ , and  $k$ ) is defined as the driving force for the achievement of the liquid core–shell structure.<sup>14</sup> The mathematical model proposed by Torza and Mason<sup>22</sup> is applied to explain the formation of capsules according to the spreading coefficient of each liquid phase ( $s_i$ ):

$$s_i = \gamma_{jk} - (\gamma_{ij} + \gamma_{jk}) \quad (2.2)$$

For a certain phase  $i$ ,  $s_i$  is determined with the contribution the interfacial tensions ( $\gamma_{ij}$ ) between the different phases, as expressed in eq. (2.2). If in a direct miniemulsion the oil phase to be encapsulated is named as phase 1 (e.g., the hydrophobe), the continuous polar phase as 2 (e.g., an aqueous solution of a surfactant), and the oil phase precursor of the solid shell as 3 (e.g., monomer), different possible situations (shown in Figure 2.2) can be predicted by the model.

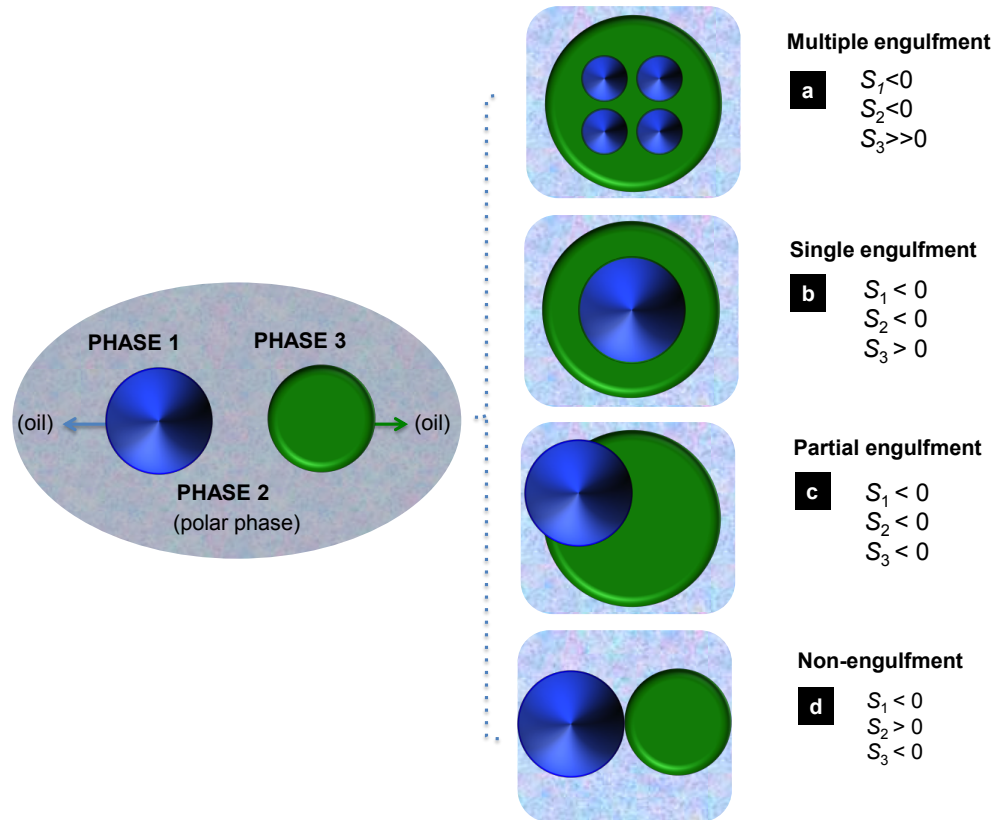


**Figure 2.2.** Phase segregation in a three-component system comprised of two oil dispersed phases (1 and 3) and a polar continuous phase (2), determined by the spreading coefficients ( $s_i$ ). (Based on refs. 14 and 22)

- If the hydrophobicity of phase 3 is much higher than phase 1 ( $\gamma_{12} \gg \gamma_{23}$ ) and the interfacial tension between the oil phases is low (Figure 2.2(a)), a multiple engulfment of oil 1 in 3 is achieved.
- A liquid core–shell morphology is reached with the single engulfment of phase 1 into 3, which occurs when the oil 3 is more hydrophobic than the oil 1 ( $\gamma_{12} \gg \gamma_{23}$ ) and the interfacial tension between the oil phases is still low (Figure 2.2(b)).
- If phases 1 and 3 present similar hydrophobicity ( $\gamma_{12} \approx \gamma_{23}$ ) and the interfacial tension between them is low, one of the oil phases (1) is partially engulfed by the other one (3) (Figure 2.2(c)).
- If the interfacial tension between two oil phases (1 and 3) with similar polarity is high, the non-engulfment and the separation of the droplets from Figure 2.2(d) occur.

Only the single engulfment of a second liquid phase within the nanodroplets of the miniemulsion (Figure 2.2(b)) leads to the capsule morphology. With regard to the morphology development of the hybrid capsules, the process is again considered a result of the minimization of the overall energy of the system ( $E$ ), expressed in terms of interfacial energies. Therefore, the energy balance

of hybrid nanocapsules prepared in a direct miniemulsion is understood as the sum of the energetic contribution of four phases (i.e., the inorganic component (I), the aqueous phase (W), the monomer/dissolved polymer system (P), and the oil phase to be encapsulated (O)):

$$E = \sum_{ij} A_{ij} \gamma_{ij} = A_{PW} \gamma_{PW} + A_{IW} \gamma_{IW} + A_{IP} \gamma_{IP} + A_{OW} \gamma_{OW} + A_{OP} \gamma_{OP} + A_{OI} \gamma_{OI} \quad (2.3)$$

The spreading coefficient drives the phase separation of the liquid phases from the initial miniemulsion, among which the inorganic components assemble depending on the relative interfacial energies with the different liquids. After polymerization or solvent evaporation processes, the formation of a solid polymer shell leads to the most favorable hybrid structure with minimal interfacial energies.<sup>23</sup>

## 2.4 Stability of Emulsions

Emulsions are dispersions of droplets of a liquid (the disperse phase) in a second immiscible liquid (the continuous phase). Depending on the relative nature of the phases, direct or oil-in-water (O/W) emulsions are defined when a non-polar liquid is dispersed within a polar continuous phase, and inverse or water-in-oil (W/O) emulsions in the opposite case. According to the size and stability of the droplets, emulsions are classified in three groups: macroemulsions, miniemulsions, and microemulsions.<sup>24</sup>

The so-called *macroemulsions* are thermodynamically unstable emulsions with large droplet sizes (1–10  $\mu\text{m}$ ), which are kinetically stabilized with the aid of surfactants. The relatively high amount of surfactant required for the colloidal stabilization results in the coexistence of droplets and empty micelles. In the absence of a suitable mixture, macroemulsions experience fast processes of droplet growth, phase separation, and destabilization.

In the other extreme, *microemulsions* are translucent and thermodynamically stable emulsions that form spontaneously without requiring further homogenization. The stabilization is achieved by using surfactant concentrations well above the critical micelle concentration (cmc) and typically short-chain alcohols as cosurfactants. The emulsifier assembles at the interface of the nanodroplets (10–100 nm) forming a complete coverage and allowing minimal interfacial tensions.<sup>25-26</sup>

*Miniemulsions* are critically stabilized emulsions (kinetically stable but thermodynamically metastable) with intermediate droplet sizes (50–500 nm). The achievement of the miniemulsion state requires the use high shear forces (e.g., ultrasonication, microfluidizers, or high pressure

homogenizers) to reach a equilibrium between droplet fission and fusion processes. The presence of surfactants at concentrations below the cmc and, typically, the addition of costabilizers or osmotic agents (long chain alkanes, alcohols or salts) confer a colloidal stability to the miniemulsions that ranges from days to months. The term of miniemulsion is also commonly used with mechanistic implications, involving polymerization processes based in a “one-to-one copy” concept.<sup>27</sup> According to this generally accepted concept, the miniemulsion polymerization process occurs in pre-existing monomer droplets without the formation of new particles. Consequently, the particle size corresponds to the size of the droplet of the initial miniemulsion. This feature of the miniemulsions is especially attractive for the controlled incorporation of inorganic functionalities within a forming polymer matrix.

This thesis addresses the preparation of polymer–inorganic hybrid nanoparticles with controlled morphology via synthetic strategies in miniemulsion. Traditionally, both direct and inverse miniemulsions have been exploited for the synthesis of polymer nanoparticles.<sup>28</sup> The strategy has been further extended towards the preparation of organic–inorganic hybrid nanostructures (particles and capsules),<sup>5,29</sup> which stand for promising scenarios for the development of the aimed materials.

#### **2.4.1 Stabilization of Miniemulsions**

Coalescence and Ostwald ripening are the two main mechanisms governing the droplet growth and destabilization of miniemulsions.<sup>3, 27</sup> Figure 2.3 presents schematically the phenomenon of coalescence, which is based on the fusion of droplets promoted by van der Waals attractive forces existing between them. The droplets being in a continuous Brownian motion and propelled by the stirring system collide and form larger droplets. As a consequence, the interfacial contact area and surface free energy of the emulsion is reduced.

The collision and coalescence of the droplets can be suppressed (or at least reduced) by electrostatic, steric or electrosteric strategies, mainly based on the use of efficient surfactants. Surfactants are surface active and amphiphilic molecules that lower both the surface tension of the medium in which they are dissolved and the interfacial tension between two immiscible liquid phases. Ionic surfactants, with either anionic (e.g., sulfate or phosphate) or cationic (e.g., ammonium) groups in the hydrophilic head of the molecule provide electrostatic stabilization of miniemulsions. The charged species tend to assemble at the droplet interface avoiding the collision of the droplets with identical charge via Coulomb repulsions. The conditions of the continuous phase (especially the pH value) play an essential role in the miniemulsion stability, as they will determine the charges of the surfactant.<sup>30</sup> Thus, the acidity or basicity of the media needs to be

carefully controlled to allow the efficient interdroplet electrostatic repulsion interactions. Similar results can be achieved with the use of large amounts of ionic initiators (e.g., initiators with persulfate groups). Steric stabilization plays a major role when non-ionic surfactants (e.g., block copolymers with ethylene oxide groups) are used. In this case, the polymer chains at the interface of two approaching droplets interact leading to a repulsion based on two phenomena. On the one hand, the droplet repulsion is promoted by the decrease of the entropy of the system due to the restriction of the movement and the possible conformations of the surfactant chains. On the other hand, the osmotic pressure between droplets increases due to the gradient of concentration created by the polymer chains, which also contributes to the steric repulsion. Electrosteric stabilization is reached by a combination of electrostatic repulsion and steric hindrance.

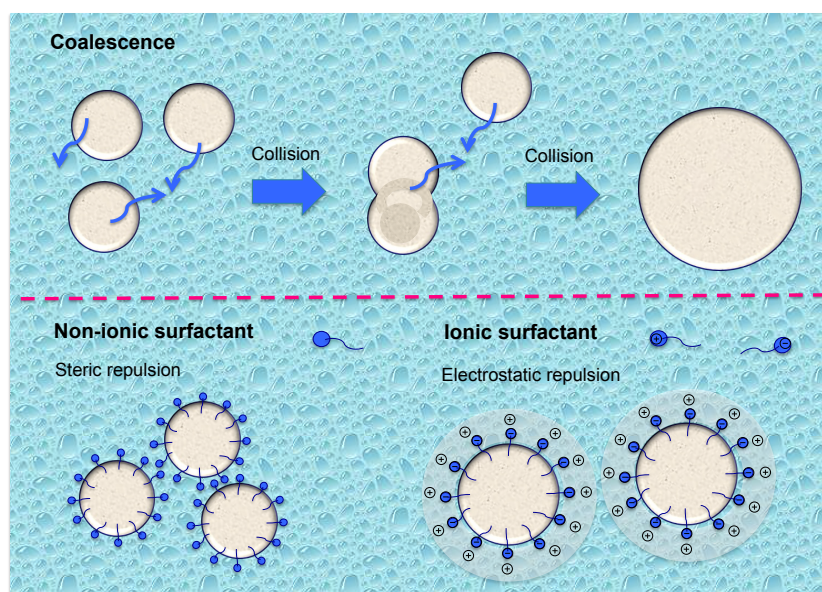


**Figure 2.3.** Schematic representation of the coalescence and the droplet growth in miniemulsions. Colloidal stabilization offered by surfactants, based on steric and electrostatic repulsion between droplets. (Based on ref. 3)

Ostwald ripening is based on the interdroplet diffusion of mass occurring from smaller to bigger droplets as a consequence of the differences of the Laplace pressure between droplets. The Laplace pressure ( $p_L$ ) describes the differences between the inner and outer pressures in a curved surface (as the droplet interface), as a function of the interfacial tension ( $\gamma$ ) and the droplet radius ( $r$ ):

$$p_L = P_{\text{inside}} - P_{\text{outside}} = \frac{2\gamma}{r} \quad (2.4)$$

The inverse proportionality defined in eq. (2.4) between  $p_L$  and  $r$  is translated into an increase of the Laplace pressure with the decrease of the droplet size. The equilibration between the pressures of the droplets with slight differences in size causes Ostwald ripening.<sup>31</sup> In miniemulsions, Ostwald

ripening is suppressed with the incorporation of osmotic agents, as represented in Figure 2.4. These “costabilizers” are soluble in the disperse phase and insoluble in the continuous phase, which avoids their diffusion out of the droplet confinement. Because of these specific solubility features, osmotic agents in direct miniemulsions are known as hydrophobes (e.g., hexadecane), whereas they are named as lipophobes in inverse systems (typically inorganic salts, such as sodium chloride). If an interdroplet diffusion occurred to compensate a gradient of Laplace pressure from smaller to bigger droplets, the increase of the concentration of the osmotic agent in the shrinking droplets would let to the increase of the osmotic pressure ( $\Pi_{osm}$ ). Then, the counterbalance between the Laplace and the osmotic pressure of the droplets hinders the Ostwald ripening. The osmotic pressure is expressed in terms of the universal constant of the gases ( $R$ ), the absolute temperature ( $T$ ), the concentration of the osmotic agent ( $c$ ), and the molecular weight of the costabilizer ( $M$ ):

$$\Pi_{osm} = \frac{RTc}{M} \quad (2.5)$$

The suppression of both coalescence and Ostwald ripening allow the colloidal stability of miniemulsions. The stable droplet confinement can be used as a nanoreactor for polymerization and inorganic synthesis reactions.<sup>7-8</sup>

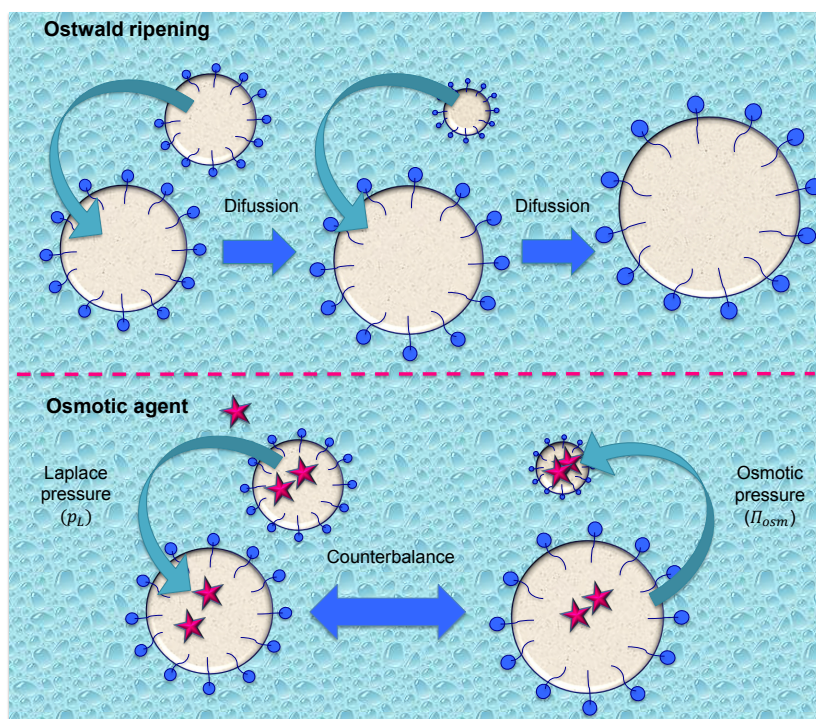


**Figure 2.4.** Schematic representation of the Ostwald ripening principle in miniemulsions. Stabilization against the interdroplet mass diffusion allowed with the incorporation of osmotic agents. (Based on ref. 3)



### 2.4.2 Pickering Stabilization

The so-called Pickering stabilization of emulsions, described for the first time by Ramsdem in 1904,<sup>32</sup> but systematically studied by Pickering,<sup>33</sup> is based on the substitution of molecular surfactants by a layer of nanoparticles irreversibly adsorbed at the droplet interface. The environmental advantages offered by these nanoparticle-stabilized emulsions are complemented with the absence of adsorption–desorption mechanisms in emulsions stabilized with conventional surfactants. Additionally, inorganic particles have no significative influence in the droplets interfacial tension. These particularities of Pickering emulsions confer robustness on the colloidal stability against external variations. The colloidal stability essentially depends on the ability of the inorganic emulsifier to form an adsorbed layer at the droplet interface. This ability is quantified with the adsorption energy ( $\Delta E$ ):

$$\Delta E = \pi r^2 \gamma (1 - \cos \theta) \quad (2.6)$$

Eq. (2.6) expresses the dependence of  $\Delta E$  on the radius of the particles ( $r$ ), the interfacial tension between the continuous and the disperse phase ( $\gamma$ ), and the contact angle of the particles at the droplet interface ( $\theta$ ). The contact angle determines the wettability of the inorganic particles in the liquid phases forming the droplet interface. Only situations close to  $\theta \approx 90^\circ$  will allow the two-side wettability of the nanoparticles and the creation of an interfacial layer. The preferential wettability of the particles by a more or less polar liquid determines the type of emulsion that is formed. In general, particles stabilize the liquid phase in which they present lower wettability. According to this statement, Figure 2.5 depicts the stabilization of direct (O/W) emulsions by hydrophilic particles with  $\theta < 90^\circ$ , whereas the hydrophobic particles with  $\theta > 90^\circ$  will form inverse emulsions. If  $\theta = 90^\circ$ , the particles will be equally wettable and partitioned between the liquid phases. This situation is related to the formation of theoretical structures of bicontinuous interfacially jammed emulsion gels (*bijes*).

The wettability of inorganic nanoparticles at the oil–water interface is affected by the surface chemistry, the concentration of the emulsifier, the pH value or the ionic strength of the media (i.e., the presence of salts).<sup>34-35</sup> In this sense, the stability and even the inversion of Pickering emulsions can be controlled by tuning the amphiphilicity of the stabilizing particles.<sup>35</sup> Among the different functionalization strategies, the use of silanes offers a wide range of possibilities.

Chapter 5 describes the use of direct Pickering miniemulsions, stabilized with unmodified ceria nanoparticles, for the preparation of polystyrene-supported ceria nanocatalysts. Chapter 7 discusses the influence of the surface functionalization of titania, ceria and magnetite nanoparticles using

silane components with different chemical structure on the stabilization of inverse Pickering emulsions for the synthesis of polyurethane-based hybrid capsules.

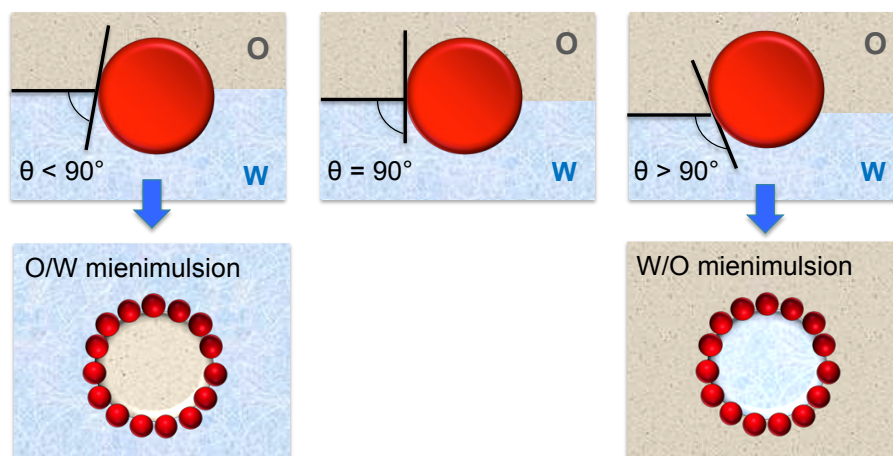


**Figure 2.5.** Schematic representation of the nature of the Pickering emulsions formed depending on the contact angle of the particles at the oil/water interface. (Based on ref. 36)

### 2.4.3 Polymerizable Surfactants (Surfmers)

Polymerizable surfactants, often named with the acronym *surfmers*, are *surface active monomers* with an amphiphilic structure that makes them suitable to act as surfactants. They offer an attractive alternative to the use of traditional surfactants, being able to provide miniemulsions with colloidal stabilization against coalescence and to incorporate building blocks with polymerizable units and specific functionalities.<sup>37</sup>

The copolymerization between surfmers and the main monomers included in the disperse phase of miniemulsions allows the preparation of surface-active polymer nanoparticles. The functionalized polymers can act as supports for interfacial processes (e.g., inorganic crystallization) or as carriers of biomolecules for specific applications (e.g., biomedicine, asymmetric organocatalysis). In addition, the covalent bond formed between the surfmer and the polymer overcomes the typical problems of traditional surfactants related with adsorption–desorption equilibria and the consequent risk of colloidal destabilization.

Since the pioneer work of Freedman et al.<sup>38</sup> about the preparation of vinyl monomers also used as surfactants, surfmers with a wide range of structures, colloidal and polymerization behaviors have been developed.<sup>39, 40-43</sup> Typically, the molecular structure of surfmers consists of a hydrophobic segment with a polymerizable head, and a second hydrophilic part incorporating a specific functionality. However, the location of the polymerizable section in the hydrophilic head or as an

intermediate conjunctive link<sup>44</sup> have also been reported, leading to other structural variations (e.g., a polymerizable group connecting two hydrophobic chains with their corresponding hydrophilic heads from the so-called *Gemini* surfactants).<sup>44</sup> Polymerizable surfactants can be classified according to different criteria including the nature of the polar head, the type of polymerizable unit and its location, the hydrophilic–hydrophobic balance (HLB) of the molecule, and the presence of functional groups.<sup>37</sup> The surface activity of surfmers is related to the group in the polar head and defines the structures as non-ionic, anionic, cationic or zwitterionic (if the head present two groups with opposite charges).

The polymerizable unit (e.g., maleic, acrylic, methacrylic, styrenic or maleimide units) determines the polymerization ability of the compound. However, the polymerization ability itself will not determine its surface incorporation, the efficient copolymerization yield with the main monomer, nor the colloidal stabilization of the miniemulsion. In this sense, the relative reactivity of the polymerizable group versus the monomer will also have an essential role. In general, a moderate reactivity between the polymerizing units is required to avoid both the entrapment within the polymer particle and the loss of the surfmer within the continuous phase.<sup>45</sup>

The nature and length of the hydrophobic blocks, as well as the origin of the hydrophilic fragment, determine the colloidal properties of the surfmer structure. In this sense, the hydrophilic–lipophilic balance is used to describe the distribution of the molecule between the disperse and the continuous phase of a miniemulsion. The HLB for non-ionic surfmers is expressed in terms of the molecular mass of the hydrophilic section and the entire molecule, whereas incremental methods are proposed for the characterization of ionic surfmers.

Surfmers can be also classified according to the presence and the type (if existing) of functional groups in the hydrophilic head of their structure. Among the functional groups, mostly sulfate,<sup>46</sup> phosphate,<sup>47-48</sup> phosphonate,<sup>47, 49</sup> carboxylate, quaternary ammonium<sup>46</sup> or even BODIPY (4,4-difluoro-4-bora-3a,4a-diaza-s-indacene)<sup>50</sup> functional groups have been linked to different hydrophobic chains. The combination of polar amino acids and non-polar alkyl chains (with different lengths, structures, and number) leads to the development of chiral and polymerizable molecules with high surface activity, and specific physicochemical and biological properties.

Amino acids and amino acid-based molecules are chiral structures that cannot be superposed with their mirror image. The asymmetry property of chirality counts with great relevance in many branches of science. In chemistry, the chirality of molecules is generally related to the presence of an asymmetric atom of carbon and to the existence of two different enantiomers or optical isomers.

The plane of polarization of a linearly polarized light that passes through a chiral molecule rotates along the axis of the source clockwise (to the left) or anticlockwise (to the right) in the presence of dextrorotatory (D) or levorotatory (L) enantiomers. Equimolecular mixtures of enantiomers with the same constitution (i.e., racemic mixtures) cancel the rotation of the linearly polarized light. The enantiomers present identical chemical and physical properties in a symmetric environment, which hinders their identification or separation by physical/chemical methods. However, their ability of rotation of the polarization plane of linearly polarized light in opposite directions establishes the bases for identification of the chirality of molecules by circular light polarization. The biological behavior of a pair of pure enantiomers is commonly different, which justifies the great interest of the pharmaceutical sector on the development synthetic processes with controlled enantioselectivity.<sup>51</sup> In this context, the use of chiral molecules has been widespread to introduce stereochemistry in inorganic chemistry, organic chemistry, physical chemistry, biochemistry, and supramolecular chemistry.<sup>52</sup>

In biology, all natural amino acids (except glycine) are homochiral (with uniform chirality) and are produced in the L-form, whereas sugars are naturally present in D-form. Such homochirality seems to be a form of storage of biological information, which reduces the entropic barriers for the formation of large organized molecules. We have used this principle for the preparation of amino acid-based nanoparticles to control the stereochemistry of asymmetric organocatalysis.

The synthesis of amino acid-based polymerizable surfactants (e.g., sodium lauroyl sarcosinate (SLSar), sodium myristoyl sarcosinate (SMSar), and sodium lauroyl glutamate (SLGlu),<sup>53</sup> or undecanoyl-L/D-glutamic acid, and methacryloyl-aminoundecanoyl-L/D-glutamic acid<sup>54</sup>) has been reported for the preparation of stable polymer particles by free-radical emulsion<sup>53</sup> and miniemulsion<sup>54</sup> polymerization. The chiral nanoparticles were used for the enantioselective crystallization of a conglomerate system (i.e., *rac*-asparagine).<sup>54</sup> A proline-based polymerizable surfactant has been conceived in Chapter 6 for the preparation of chiral and magnetoresponsive nanoparticles for the enantioselective catalysis of the intermolecular aldol reaction.

## 2.5 Synthesis of Inorganic Nanoparticles

### 2.5.1 Synthesis of Superparamagnetic Magnetite Nanoparticles

Superparamagnetic nanoparticles are commonly related to transition metal oxides with a spinel structure ( $M_3O_4$ ) and sizes in the range of Weiss domains (4–5 nm).<sup>55</sup> Due to the alignment of the

spins, the nanostructures present a paramagnetic behavior upon exposition of even small external magnetic fields, and high magnetic fields are consequently induced within the particles without any retention.<sup>3</sup> Regarding the synthesis, such particles are mainly synthesized by thermal or pH-based methods.<sup>56</sup> On the one hand, the thermal techniques consist of a controlled decomposition of precursor molecules at high temperatures followed by crystallization (i.e., nucleation and growth) processes. The strategy allows the achievement of controlled particle sizes and morphologies.<sup>57</sup> On the other hand, the change of the pH value results into the deprotonation of precursor molecules and further formation of particles<sup>58-59</sup> with a wider size distribution under basic conditions. This second technique has been used in this work for the preparation of 5–10 nm magnetite ( $\text{Fe}_3\text{O}_4$ ) nanoparticles whose surface was functionalized for the incorporation within different polymer matrices.

### 2.5.2 Synthesis of Crystalline Ceria Nanoparticles

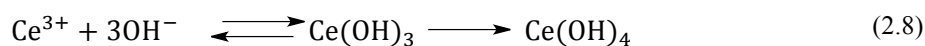
Crystalline cerium(IV) oxide ( $\text{CeO}_2$ ) nanoparticles offer excellent physical and chemical (i.e., acid–base, redox ( $\text{Ce}^{4+}/\text{Ce}^{3+}$ ), and oxygen exchange) properties, which are significantly enhanced with respect to the bulk particle properties. Nanosized ceria has been considered for applications in nanotechnology, such as catalysis,<sup>60</sup> fuel cells, oxygen or hydrogen storage,<sup>61</sup> or for the development of optical devices.<sup>62</sup> According to the requirements of these applications, in the last two decades, the synthesis of crystalline ceria nanoparticles and the control over the crystallinity, the particle size, and the morphology has been achieved by a wide variety of methods. In this context, sol–gel,<sup>63</sup> sonochemical,<sup>64</sup> spray hydrolysis,<sup>65</sup> combustion,<sup>66</sup> precipitation,<sup>67-68</sup> hydrothermal,<sup>69-71</sup> mechanochemical,<sup>72</sup> or more complex combinations of sonochemical and microwave assisted<sup>73</sup> or sol–gel and microwave methods<sup>74</sup> have been developed. Precipitation strategies (i.e., chemical precipitation, or other variations as two-emulsion,<sup>75</sup> semi-batch,<sup>76</sup> in micelles/microemulsion<sup>77</sup> precipitation) present a great attractiveness due to the low price of the salt precursors, and the simplicity, easy scalability, and the mild conditions of pressure and temperature of the method. Furthermore, the precipitation technique has been used for the straightforward preparation of surface-functionalized ceria nanocrystals in an aqueous solution containing different capping agents.<sup>78</sup>

We have prepared crystalline ceria nanoparticles by chemical precipitation at room temperature in an aqueous medium. Depending on the requirements of hydrophobicity of the particles, the inorganic surface functionalization was achieved afterwards via silane chemistry strategies, described in section 2.5.3. The synthesis is based on the oxidation of the cerium(III) ions from an aqueous solution of a metal precursor salt (i.e., cerium nitrate hexahydrate salt) to cerium(IV) with

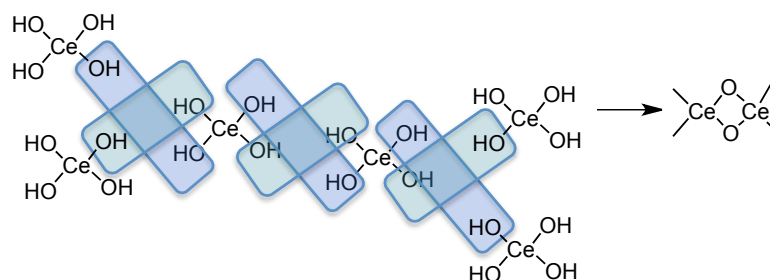
the controlled basification of the media (i.e., with sodium hydroxide). The overall process<sup>79</sup> results from a multistep synthesis, whose complexity in terms of formation of possible hydrated complexes has been simplified.



Initially, the precipitation of the unstable hydroxides of  $\text{Ce}(\text{OH})_3$  occurred and the initially transparent solution turned into light brown, characteristic from this product with low solubility constant ( $K_s = 7 \times 10^{-21}$ ) in water.<sup>77</sup> With the evolution of the reaction in basic media, the oxidation of Ce(III) to Ce(IV) leads to the formation of more stable hydroxides,  $\text{Ce}(\text{OH})_4$ , and the precipitated turned into purple.



The final white pale solution with crystalline structures of ceria ( $\text{CeO}_2$ ) was achieved by condensation of the hydroxides, as shown in Scheme 2.1. For simplicity reasons, the formation of hydrated Ce(IV) ions, and hydroxides complexes ( $\text{Ce}(\text{OH})_x(\text{H}_2\text{O})_y^{(4-x)+}$ ),<sup>80-81</sup> whose deprotonation by the molecules of water leads to the nucleation of ceria nanoparticles,<sup>77-78, 82-83</sup> has not been considered in the scheme. The yellowish nanocrystals of cerianite were recovered after centrifugation.



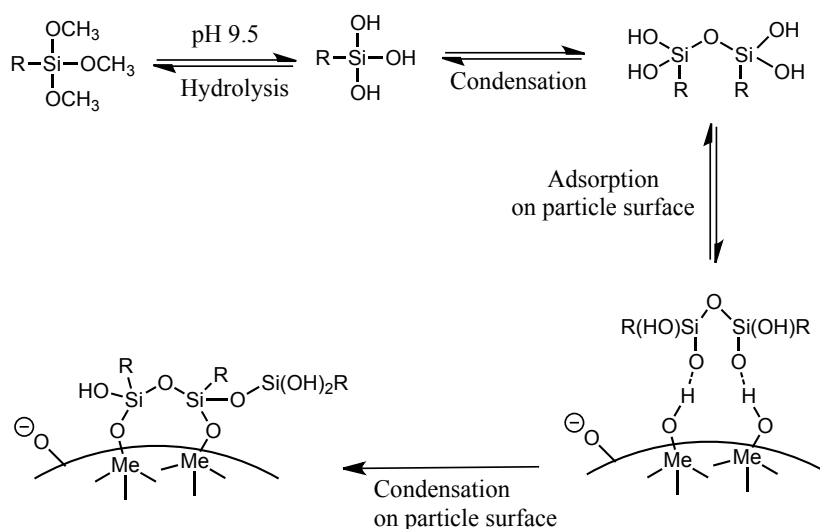
**Scheme 2.1.** Simplified representation of the condensation of hydroxides  $\text{Ce}(\text{OH})_4$  to  $\text{CeO}_2$ . The presence of hydrated complexes has been omitted for simplicity reasons.

### 2.5.3 Functionalization of Inorganic Nanoparticles

Inorganic nanoparticles commonly present a homogeneous composition in the whole structure, which is protected by hydrophilic surfaces with charged groups (e.g.,  $\text{OH}^-$  groups). For most of the applications, post-synthetic functionalization strategies are required to provide the metal/metal oxide surface with functional, reactive, or compatibilizing groups. The inorganic surface functionalization has been traditionally addressed by different strategies, using surfactants (e.g., cetyltrimethylammonium chloride, CTAB)<sup>84-85</sup> specific reactive groups (e.g., oleic acid (OA) for

magnetite,<sup>58</sup> or thiol groups for gold<sup>86</sup>) or by preparation of core-shell structures.<sup>86-88</sup> These strategies allowed either the direct application of the inorganic species or favored further surface modifications.

In this thesis, the incorporation of functional metal oxide (i.e., titania, ceria, and magnetite) nanoparticles within polymer matrices (i.e., polystyrene (PS), poly(methyl methacrylate) (PMMA) and polyurethane (PU)) has been approached via inorganic surface functionalization with silane components. Chapter 4 presents the use of three alkoxy silane components for the hydrophobization of metal oxides nanoparticles. Not only the hydrophobicity, but also the chemical structure of the functional groups would determine the inorganic incorporation within the hybrid nanostructures. Due to the variability in terms of inorganic species, particle size and morphologies, and the aimed final morphologies, the silanization strategy was used as a versatile technique that offers a wide spectrum of functional groups and chain lengths. Surface functionalization of metal oxide nanoparticles using alkoxy silane components is a sequential process with different steps as shown in Scheme 2.2.



**Scheme 2.2.** Schematic representation of the functionalization of metal oxide nanoparticles using trialkoxysilane components as coupling agents. (Based on ref. 89)



## 2.6 Specific Strategies for the Preparation of Polymer–Inorganic Hybrid Nanoparticles and Capsules in Miniemulsion

### 2.6.1 Synthesis of Hybrid Nanoparticles by Miniemulsion Polymerization Processes in the Presence of Preformed Inorganic Components

In the last decade, the preparation of superparamagnetic hybrid nanoparticles with no cytotoxicity and high biocompatibility has been intensively studied for tracking, targeting, and treatment and diagnosis applications in biomedicine. In this context, magnetite ( $\text{Fe}_3\text{O}_4$ ) nanoparticles have been encapsulated within different polymer matrices (e.g., poly(methyl methacrylate) (PMMA),<sup>37,90,91,92</sup> polystyrene (PS),<sup>93,94</sup> poly(styrene-*co*-methacrylic acid) (P(S-MA)),<sup>93,95</sup> poly(styrene-*co*-styrene sulfonate) (PS-SS),<sup>96</sup> poly(styrene-*co*-4-vinyl pyridine) (P(S-4-VP)),<sup>96</sup> or poly(acrylic acid) (PAA)<sup>97</sup> via miniemulsion polymerization processes. In this type of strategies, the incorporation of inorganic nanoparticles required the hydrophobization of their surface for the compatibilization with the monomer and the forming polymer. Different degrees of encapsulation of magnetite were reached using oleic acid (OA),<sup>90-92</sup> ammonium oleate in acid media,<sup>93-96</sup> or silane compounds such as 3-(methacryloyloxy)propyl trimethoxysilane (MPS)<sup>97-98</sup> and octadecyl trimethoxysilane (ODTMS)<sup>13,98</sup> as coupling agents. In this fashion, the surface functionalization of preformed inorganic nanoparticles (e.g., silica ( $\text{SiO}_2$ )<sup>99-100</sup> or magnetite<sup>98</sup>) via silane chemistry is highlighted as a versatile strategy to address the inorganic migration within a forming polymer matrix. The wide range of chain lengths and functional groups available among trialkoxysilane components offer more flexibility and effectiveness than the traditional carboxylic acids (e.g., OA) or ionic surfactants (e.g., CTAB). The use of silanes with polymerizable vinyl moieties, such as MPS, allowed the homogeneous encapsulation and fixation of metal oxide nanoparticles via the copolymerization with the surrounding monomer (e.g., MMA). In the case of polymer matrices based on the use of mixtures of the styrene (S) and 4-vinyl pyridine (4-VP), the MPS-functionalized silica nanoparticles formed an inorganic core chemically bonded to polystyrene, whereas raw silica nanoparticles added post-sonication stayed anchored to the polymer surface through acid–basic interactions between the silanol group of silica and the amino group of 4-VP.<sup>101</sup> At high pH values, double-decked raspberry-like morphologies were reached. The use of silane components, such as ODTMS, with longer alkyl chains and the absence of polymerizable units resulted into thermodynamically preferred structures with the inorganic component at the surface of polymer particles or Janus-like morphologies.<sup>13,98-100</sup> The combination of traditional coupling agents

(e.g., OA) and silane components (e.g., MPS) was also reported as a synergic hydrophobization strategy that lead to mono- or multi-core structures depending on the sonication time.<sup>102</sup>

Polymer-grafting strategies have also been used for inorganic (e.g., silica) surface functionalization. Alkoxyamine initiators with a functional group were used as an alternative to functionalizing agents, which allowed the controlled growth of polystyrene chains on the silica surface. After miniemulsion polymerization, the polystyrene-grafted silica nanoparticles resulted entrapped within a polystyrene matrix. In this case, hybrid core-shell structures were achieved by adjusting the molecular weight of the grafted polymer.<sup>103</sup>

Other authors have addressed the structural control of hybrid nanoparticles by tuning the size of the inorganic nanoparticles (e.g., silica),<sup>13,104,105,106</sup> the nature and the concentration of the surfactant,<sup>105</sup> or the use of auxiliary comonomers.<sup>104-107</sup> MPS-functionalized silica nanoparticles were incorporated within polystyrene<sup>102-104</sup> and PMMA<sup>106</sup> matrices, including auxiliary comonomers such as 4-VP<sup>101</sup> or butyl acrylate (BA).<sup>105-106</sup> The incorporation of soft comonomers with carboxylic groups (e.g., BA) reduces the surface energy of the nanodroplets due to structural similarity with the organomodified silica.<sup>107</sup> The encapsulation of silica forming multi-core structures was improved with the reduction of size of the inorganic nanoparticles, whereas raspberry-like or core-shell structures were achieved by modification of the surfactant concentration.<sup>104-105</sup>

From an inorganic perspective, a wide range of species has been incorporated within polymer matrices prepared by miniemulsion polymerization processes. For instance, clay platelets were used in the preparation of poly(methyl methacrylate-*co*-butyl acrylate) (P(MMA-BA) hybrid nanoparticles for the development of films. According to the application, butyl acrylate, allyl methacrylate, stearyl acrylate, and *n*-dodecyl mercaptan were used as soft comonomer, cross-linking agent, costabilizer, and as chain-transfer agent to control the crosslinking density and the adhesion properties of the material. The larger dimensions of the clay platelets respect to the miniemulsion droplets resulted into dumbbell-like structures with the clay platelets embedded between two polymer particles or located at the particle/water interface. The hybrid morphology was determined by the functionalization of the clay platelets with (2-methacryloxyethyl)hexadecyldimethylammonium bromide or methyl-bis-2-hydroxyethyl tallow ammonium.<sup>108</sup> P(MMA-BMA) nanoparticles with clay platelets engulfed within the matrix were also prepared by a semi-batch miniemulsion polymerization processes using a redox system (*t*-butyl hydroxyperoxide (TBHP) and ascorbic acid) as initiators. A fresh inlet of monomers, stearic acid and boric acid for auxiliary stabilization, and an oil-soluble initiator (AIBN) lead to a seed-emulsion polymerization governed by droplet and micellar nucleation mechanisms. The

strategy allowed the increase of the solid content of the final dispersion close to industrial requirements.<sup>109</sup> Nickel nanoparticles hydrophobized with oleylamine and triphenylphosphine were also incorporated within polystyrene and PMMA matrices. The hybrid morphology was related to the anionic (e.g., sodium dodecyl sulfate (SDS)) or non-ionic (e.g., poly(ethylene oxide) hexadecyl ether (Lutensol AT50)) nature of the surfactant and the high (e.g., KPS) or low polarity (e.g., AMBN) of the initiator. The study revealed that the compatibilization with the monomer does not ensure the encapsulation of the inorganic nanoparticles within the polymer. Increasing the level of complexity of the inorganic system,  $\beta$ -diketonate metal complexes  $\text{Me}(\text{tmhd})$  (tmhd = 2,2,6,6-tetramethyl-3,5-heptanedione) of Gd, Eu, Tb, La, Yb, Co, Cr, Al, Mn, In, Bi, Ga, Cu and Ag were integrated within a PMMA matrix using different surfactants combinations. The metal components were restricted via complex self-assembly processes in a bilayer conformation created between lamellar surfactants and the polymer matrix. The hybrid morphology was controlled with the chain length of the anionic surfactants, which determines the interlayer distance. Nano-onions or kebab-like structures were respectively formed when sodium alkylsulfates or dodecylphosphates, and sodium carboxylates were used as surfactants.<sup>110</sup> The miniemulsion polymerization strategy was also suitable for the incorporation magnetic  $(\text{Mn}_{12}\text{O}_{12}(\text{VBA})_{16}(\text{H}_2\text{O})_4)$  and  $\text{Mn}_8\text{Fe}_4\text{O}_{12}(\text{VBA})_{16}(\text{H}_2\text{O})_4$ <sup>111</sup> and zirconium  $(\text{Zr}_4\text{O}_2[\text{O}(\text{O})\text{CC}(\text{CH}_3)=\text{CH}_2]_{12} (\text{Zr4}))$ <sup>112</sup> oxoclusters within PS<sup>111</sup> and PMMA<sup>112</sup> matrices. The incorporation of the vinylbenzoate (VBA) ligand and vinyl groups in the hybrid structure of the oxoclusters enabled the copolymerization with the monomers. The hybrid morphology, the cross-linking, and the swelling degree of the final structure was related to the anionic (e.g., SDS) or non-ionic (e.g., Lutensol AT50) nature of the surfactant, the cluster content, and the reticulation of the polymer chains.<sup>112</sup>

In contrast to direct miniemulsions, only few examples have been reported on free-radical polymerization processes in inverse systems for the preparation of hybrid particles. Poly(2-hydroxyethyl methacrylate) (PHEMA) nanoparticles containing hydrophilic metal salts (combinations of metal cations ( $\text{Fe}^{2+}$ ,  $\text{Fe}^{3+}$ ,  $\text{Co}^{2+}$ ,  $\text{Ni}^{2+}$ ,  $\text{Cu}^{2+}$ , and  $\text{Zn}^{2+}$ ) and  $\text{BF}_4^-$ ,  $\text{NO}_3^-$ , and  $\text{Cl}^-$  ions) were prepared by miniemulsion polymerization in cyclohexane by using AIBN as initiator. The distribution of the salt within the polymer was mainly determined by electrostatic cation–ion interactions of the salt.<sup>113</sup>

In Chapter 4, catalytically active (ceria ( $\text{CeO}_2$ ) or titania ( $\text{TiO}_2$ )), or magnetoresponsive (magnetite) nanoparticles were incorporated within polystyrene or PMMA matrices via free-radical polymerization processes in direct miniemulsions. The selective migration of the inorganic nanoparticles within the polymer was addressed by inorganic surface functionalization using

alkoxysilane components with different chemical structures. The strategy was further extended towards the preparation of a second generation of multifunctional nanoparticles incorporating complementary inorganic functionalities with different surface chemistry.

### 2.6.2 Synthesis of Nanoparticles by Pickering Miniemulsion Polymerization

Pickering stabilization (described in section 2.4.2) has been used as a surfactant-free strategy for the synthesis of hybrid nanoparticles by miniemulsion polymerization. Schrade et al.<sup>34</sup> published a detailed revision about heterophase polymerization processes in Pickering-stabilized emulsions. Nowadays, the technique is widely spread in direct systems, in which the chemical environment determined by the pH value and the ionic strength of the aqueous phase has a great influence in the characteristics of the surface and the stabilizing ability of the particles. The electrochemical principle of the electric double layer shown in Figure 2.6 is related to the colloidal stability of miniemulsions and it establishes that a charged particle in an electrolyte solution is surrounded by a double layer of ions with opposite charge.<sup>114</sup>

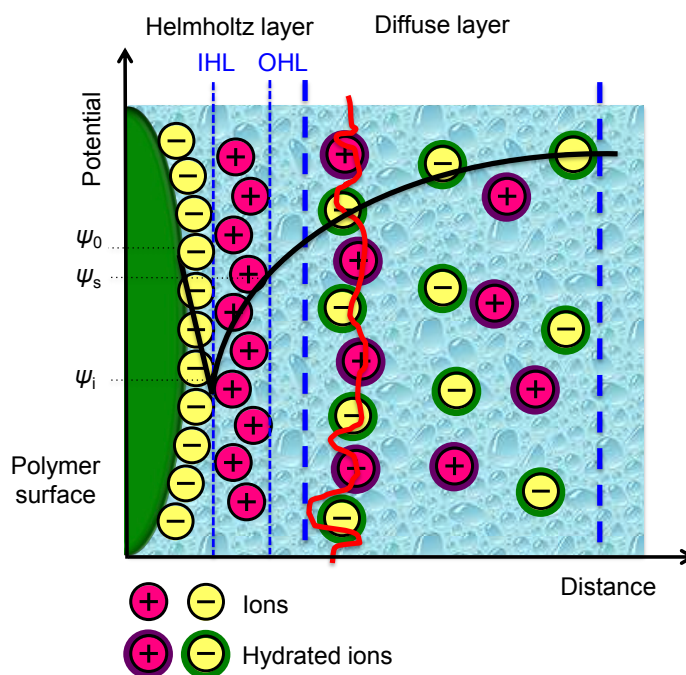


**Figure 2.6.** Schematic representation of the electrostatic principle of the double layer. (Based on ref. 115)

The ionic corona is constituted by two regions formed by the Helmholtz inner layer (with its respective inner (IHL) and outer Helmholtz (OHL) layers) and the diffuse layer. The Helmholtz layer includes the ions more strongly bonded to the particle surface, whereas the distribution of the ions in the diffuse layer is governed by electrostatic forces and a random thermal motion. The

surface potential ( $\Psi_0$ ) surrounding the particle surface drops until a minimum value in the IHL ( $\Psi_i$ ), and follows a linear tendency along the Helmholtz layer until the Stern potential at the OHL ( $\Psi_s$ ). Then, the electric potential follows an exponential tendency towards the zero value in the diffuse layer. The addition of salts (e.g., sodium chloride) to the aqueous phase of direct Pickering miniemulsions is commonly used as a costabilization factor. The salt promotes a slight colloidal instability compressing the electrostatic corona of the nanodroplets, creating partial flocculation and increasing the partitioning of the inorganic particles to the oil-water interface where they reversibly adhere during emulsification.<sup>116</sup>

Poly(vinyl acetate-*co*-vinyl neodecanoate) latexes were prepared using silica nanoparticles modified with 2-[methoxy (polyethyleneoxy)propyl] trimethoxy silane as inorganic stabilizer.<sup>117-118</sup> The authors used the polyethylene oxide chains as coupling agent, which allowed Pickering stabilization but did not guarantee the stability of the final dispersion. In this context, the nature of the initiator (i.e., hydrophobic or hydrophilic, ionic or non-ionic, and with thermal or redox activation) played a critical role on the final stability. At higher loads of emulsifier, the particle size and the molecular weight of the polymer decreased. Titania nanoparticles functionalized with acetyl acetone and parabenzene sulfonic acid,<sup>119,120</sup> and ceria nanoclusters<sup>121</sup> were used as emulsifiers in the free-radical copolymerization of BA and MMA. Titania resulted into homogeneously covered honeycomb nanostructures,<sup>119</sup> whereas the irregular shape of the clusters of ceria hindered a complete inorganic coverage.<sup>121</sup> During the early stages of the polymerization in nanoparticle-stabilized miniemulsions, the changes between the droplet/water and the forming particle/water interfaces can affect the metal oxide-polymer affinity, modify the inorganic adsorption energy, and create slight coalescence problems. Therefore, the total conversion of the monomers was restricted and some bucket morphologies appeared due to the accumulation and further evaporation of the unreacted monomer.<sup>119,121</sup> In addition, some empty polymer particles (i.e., without inorganic species) were formed due to homogeneous nucleation processes generated by radicals from the aqueous phase.<sup>117</sup> Similar drawbacks were observed when clay disks were used as stabilizers in the polymerization of MMA or MA using water-soluble initiators.<sup>122</sup> Better results were achieved using hydrophobic monomers (e.g., styrene, lauryl methacrylate, butyl methacrylate, octyl acrylate or 2-ethyl hexyl acrylate), and dimethyl-2, 2-azobis(isobutyrate) as oil-soluble and non-ionic initiator. Nevertheless, some compartmentalization and intermediate monomer conversions were still found within the smaller nanoparticles.

In this thesis, Pickering miniemulsion polymerization was used for the preparation of magnetoresponsive polystyrene-supported ceria nanoparticles for catalytic applications. Figure 2.7

offers a schematic representation of the synthetic strategy. The encapsulation of MPS-functionalized magnetite nanoparticles within a polystyrene matrix by miniemulsion polymerization described in the section 2.6.1 is combined with the Pickering stabilization achieved using catalytically active ceria nanoparticles.

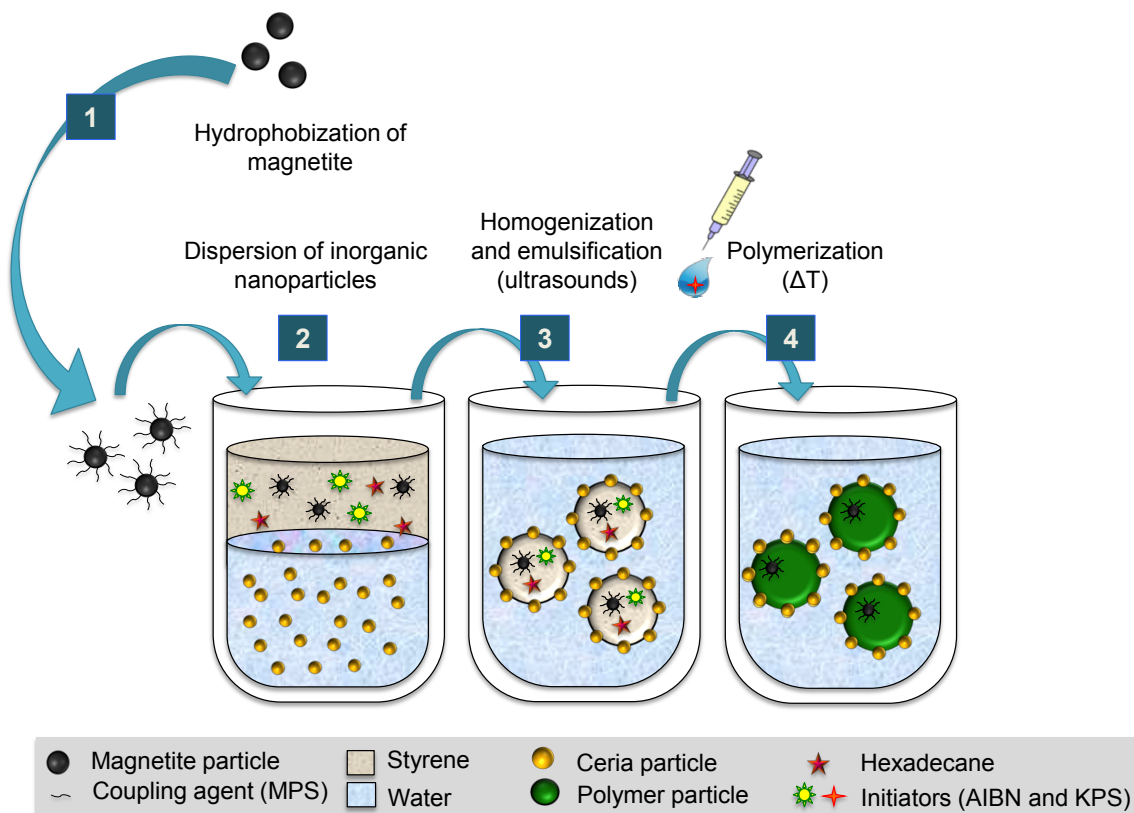


**Figure 2.7.** Scheme of the preparation of magneto-responsive polystyrene-supported ceria nanocatalysts by Pickering miniemulsion polymerization. (Based on ref. 14)

### 2.6.3 Synthesis of Hybrid Nanoparticles in Minimulsion Using the Surface of Preformed Polymers as Supports for the In-Situ Inorganic Crystallization

The use of polymer nanoparticles as supporting templates for inorganic synthesis via in-situ crystallization processes belongs to the strategies type C defined in section 2.1.1. The controlled crystallization of different metal oxides (e.g., ceria,<sup>6</sup> maghemite ( $\text{Fe}_2\text{O}_3$ ), magnetite ( $\text{Fe}_3\text{O}_4$ ) or zinc oxide ( $\text{ZnO}$ ))<sup>47</sup> has been performed using PMMA and polystyrene nanoparticles as organic templates for the preparation of hybrid nanoparticles with accessible inorganic functionalities. The polymer structures were prepared by miniemulsion polymerization processes in aqueous<sup>47</sup> or alcoholic (methanol, ethanol, and 2-propanol) media.<sup>47</sup> This type of synthesis requires the

introduction of functional groups (e.g., carboxylic, phosphate, phosphonate or sulfate groups) accessible on the polymer surface to allow the complexation of metal ions (e.g., Ce(IV) ions), as precursors of the final crystalline particles. After polymerization, the metal ions are incorporated in the system by external addition of a metal-based salt (e.g., cerium nitrate hexahydrate). The metal ions complexate on the polymer surface and the subsequent the metal oxide (e.g., ceria) nanoparticles are crystallized by controlled addition of a precipitating agent (e.g., sodium hydroxide). As a consequence, a layer of crystalline inorganic species assembles on the polymer surface. The resulting inorganic particles enter in competence with the molecular surfactant and lead to a certain Pickering stabilization of the final dispersion.

The surface functionalization of polymers has been traditionally reached by using available comonomers (e.g., acrylic acid,<sup>6, 123</sup> maleic acid,<sup>6</sup> ethylene glycol methacrylate, phosphate vinylphosphonic acid,<sup>124</sup> or vinylbenzylphosphonic acid). The functionalization strategy was effective for different monomers, functional comonomers, and surfactants.<sup>6</sup> In a similar way, the bioinspired mineralization of calcium phosphate was performed on differently surface-functionalized polystyrene nanoparticles. The mineralization process was achieved through a sequential addition of calcium (e.g., with  $\text{Ca}(\text{NO}_3)_2 \cdot 4\text{H}_2\text{O}$ ) and phosphate (e.g., with  $(\text{NH}_4)_2\text{HPO}_4$ ) ions, sufficiently spaced on time to ensure the binding of the Ca(II) ions to the polymer surface.<sup>124</sup> In this case, the inorganic coverage and the crystalline morphology depended only on the negative charges present on the polymer surface, independently of the comonomer used. Thus, the concentration and the nature of the surfactant, and the combined effect of the pH and the functional comonomer allowed to tune the crystallinity, the morphology (needle-like or platelet) of the (if formed) hydroxyapatite crystals, and the inorganic density on the polymer surface.<sup>123</sup>

The incorporation of functionalities (e.g., phosphate or phosphonate groups) on the polymer surface by combinations of comonomers and traditional surfactants was alternatively achieved using the so-called surfmers (described in section 2.4.3).<sup>47</sup> In this approach, the complexation chemistry has a critical role on morphology control. A dense and homogeneous coverage of the polystyrene nanoparticles functionalized with phosphate and phosphonate surfmers was achieved with the crystallization of ceria nanoparticles in aqueous media, whereas iron oxide (i.e., maghemite and magnetite) nanoparticles resulted into raspberry-like structures. The use of alcohol in the continuous phase allowed the development of raspberry-like morphologies also with ZnO and improved the inorganic surface density with  $\text{Fe}_2\text{O}_3$  via a sol-gel-like oxide formation. The use of sulfate-based surfmers and hydrophilic initiators (i.e., KPS) resulted into bulk inorganic crystallization.

The in-situ crystallization strategy using acrylic acid as functional comonomer is developed in Chapter 5 for the preparation of magneto-responsive polystyrene-supported ceria nanoparticles. An overview of the synthetic process is schematically presented in Figure 2.8. The great efficiency of inorganic coverage traditionally reported for this technique is compared with hybrid materials prepared via more challenging synthesis based on Pickering stabilization.

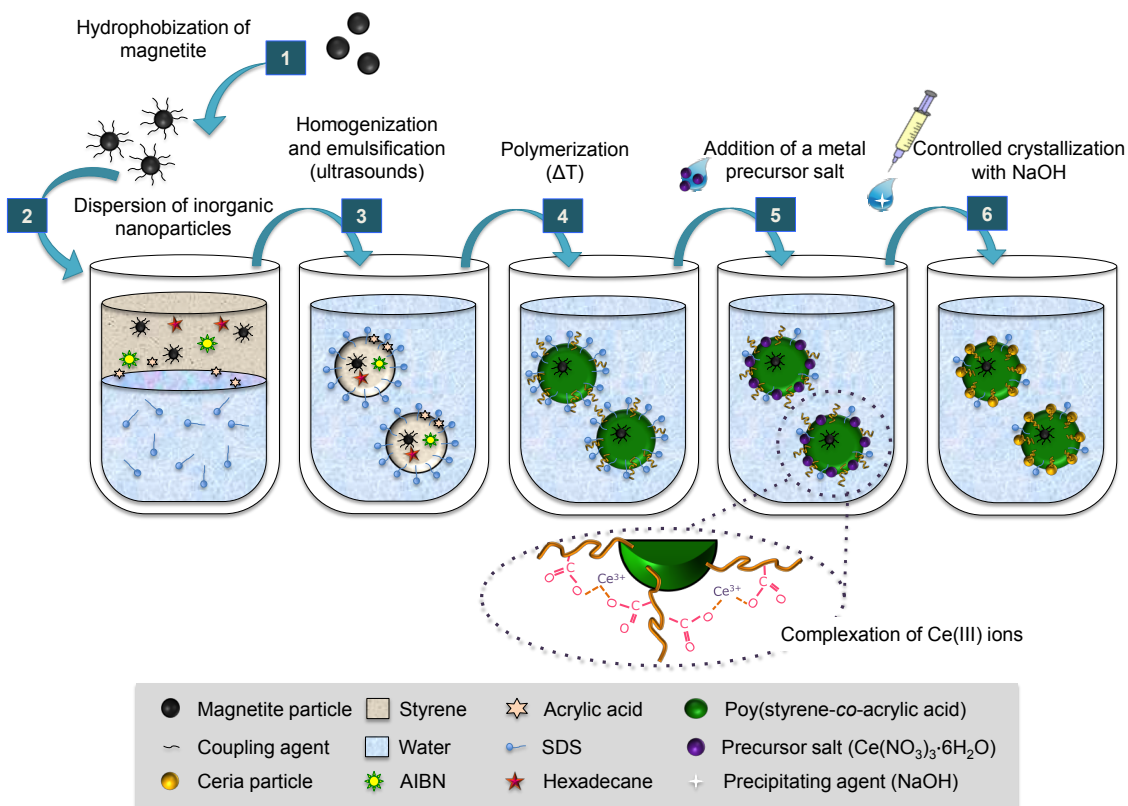


**Figure 2.8.** Schematic representation of the preparation of magneto-responsive polystyrene-supported ceria nanocatalysts via miniemulsion polymerization and in-situ inorganic crystallization on the polymer surface. (Based on ref. 6)

#### 2.6.4 Synthesis of Hybrid Capsules by Phase Separation

Polymerization processes have been commonly performed with an increased content of the hydrophobe phase for the preparation of capsules in direct miniemulsions via phase separation mechanisms. Raspberry-like nanocapsules of P(S-4-VP) with silica nanoparticles embedded within the polymer shell were prepared by Pickering miniemulsion copolymerization processes using hexadecane as soft template and divinylbenzene as cross-linking agent.<sup>1</sup> The colloidal stability relied on the interaction between a commercial silica sol and 4-VP moieties, which was highly influenced by the extension of the polymerization to the aqueous phase, the pH value, and the size of the silica particles. There exist only a few examples of the preparation of hybrid polymer-



inorganic hybrid nanocapsules in miniemulsion, in which the metal oxide nanoparticles resulted contained within the liquid core. Hydrophobized silica nanoparticles were encapsulated within PMMA nanocapsules with a hexadecane core using the solvent evaporation approach. The chemical similarity between the surface of the MPS-functionalized silica and the monomer/polymer system resulted into a low interfacial tension between phases and the assembly of the inorganic species within the PMMA shell. The higher affinity of ODTMS-functionalized silica nanoparticles for the hexadecane phase lead to the preferred retention of the inorganic system within the liquid core of the capsules. Double emulsions or solvent evaporation strategies have also been used for the encapsulation of inorganic nanoparticles (e.g., magnetite)<sup>1,125</sup> within different polymer capsules. Sundber<sup>126</sup> carried out a complex theoretical and empiric study based on the morphological development of a system consisting of three organic phases inside an emulsion droplet. However, the complexity of the control of such systems is beyond the scope of this thesis.

### **2.6.5 Synthesis of Hybrid Capsules via Chemical Processes at the Droplet Interface of Miniemulsions**

The droplet interface of miniemulsions offers a platform for the preparation of hybrid polymer–inorganic nanocapsules. Both the organic and/or the inorganic components from the hybrid structure can be synthesized via interfacial processes. This type of strategies has been mostly exploited in inverse miniemulsions.

The inorganic species of hybrid nanocapsules can be synthesized via sol–gel processes taking place at the droplet interface of miniemulsions. In this fashion, the synthesis of silica nanocapsules has been commonly reported using tetraethyl orthosilicate (TEOS), a traditional silica precursor, whose hydrolysis and condensation reactions are driven at the droplet interface under acidic or basic conditions.<sup>127,128</sup> Similar interfacial sol–gel processes have been reported for the preparation of nanocapsules with metals from group 4. In those cases, the metal precursor present in the nanodroplet was precipitated by the controlled addition of a base soluble in the continuous phase and partially soluble in the disperse phase (e.g., triethylamine).<sup>129</sup>

From a polymer perspective, the synthesis of hybrid capsules has been commonly related to polyurea, polyurethane,<sup>130</sup> or biopolymers (e.g., potato starch)<sup>131</sup> shells formed via interfacial polyaddition or polycondensation of diisocyanates using low-molecular diamines or diols in the presence of inorganic nanoparticles. Polyurea–magnetite nanocapsules were prepared via an interfacial polyaddition reaction between 1,6-diaminohexane (HMD) and toluene-2,4-diisocyanate (TDI). The amine moieties of polyisobutylene-succinimide pentamine allowed the control of the

partial reaction of TDI according to its ratio with the monomer. Magnetite nanoparticles were embedded within the polymer shell as a result of the phase segregation occurred during the polymerization.<sup>130</sup> A similar interfacial polyaddition reaction between 1,6-hexanediol and TDI in cyclohexane allowed the preparation of polyurethane–silica hybrid capsules with an aqueous core.<sup>9</sup> The surface of commercial silica nanoparticles was tuned with trimethoxy(propyl)silane (PTMS) to promote the Pickering stabilization of the miniemulsion. Figure 2.9 shows the preparation of the polyurethane–metal oxide hybrid capsules by interfacial polymerization in inverse Pickering emulsions. Furthermore, interfacial polymerization processes and inorganic synthesis have been simultaneously combined in more challenging strategies, which are beyond the scope of this thesis.<sup>2</sup>

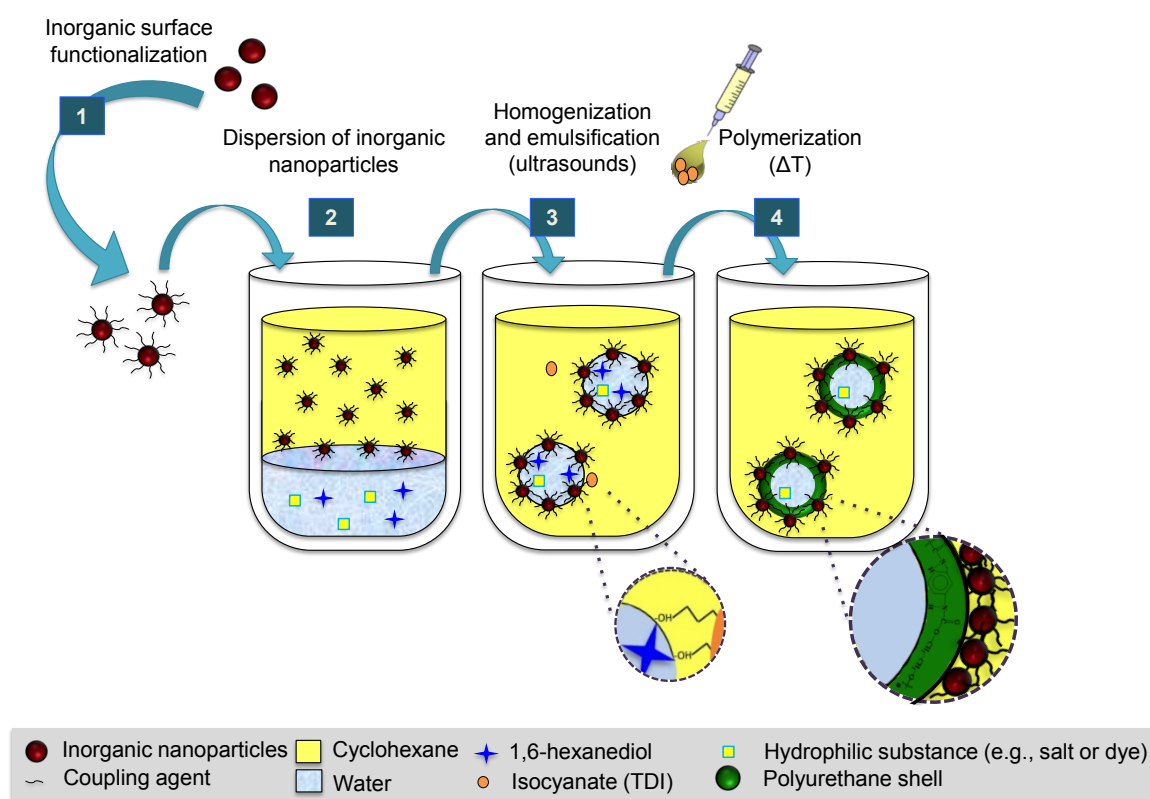


**Figure 2.9.** Scheme of the preparation of polyurethane–inorganic capsules by interfacial polymerization process in an inverse Pickering miniemulsion.

Interfacial polyaddition reaction between 1,6-hexanediol and TDI has been used in this thesis for the preparation of magneto-responsive polyurethane capsules in inverse emulsions stabilized with magnetite and/or titania or ceria nanoparticles. The development of magneto-responsive capsules is described in Chapter 7 for the encapsulation of phase change materials (PCMs) for thermal energy storage applications.

## 3 Characterization Techniques

### 3.1 Colloidal Characterization

#### 3.1.1 Dynamic Light Scattering (DLS)

The technique of dynamic light scattering (DLS), also named as quasi-elastic light scattering (QELS) or photon correlation spectroscopy (PCS), uses the Brownian motion of the macromolecules present in a dispersion of nanostructures to establish a correlation with the particle size and size distribution. The solvent molecules and the surrounding nanoparticles in a colloidal dispersion promote the continuous and random Brownian motion of individual particles.<sup>132-133</sup> The Brownian motion can be described with the translational diffusion coefficient ( $D$ ), which is directly proportional to the Boltzmann constant ( $k_B$ ) and the temperature ( $T$ ), and inversely proportional to the particle size (the hydrodynamic radius,  $R_h$ ) and the viscosity of the media ( $\eta$ ):<sup>133</sup>

$$D = \frac{k_B T}{6\pi\eta R_h} \quad (3.1)$$

A dynamic light scattering equipment produce monochromatic light beams that scatter in all directions when encountering the macromolecules/particles diffusing within a dispersion. The intensity of the scattered light is recorded in a detector. As the scattering particle is moving, a stationary observer (i.e., the detector) will appreciate differences between the frequency (and, thus, the intensity) of the scattered and the incident radiation, which is known as the Doppler effect. Therefore, the Brownian motion of the particles in the dispersion will cause a fluctuation of the intensity of the signal collected in the detector. The particle size plays an essential role in the diffusion of the particles in the media, and it also determines the rate of the fluctuation in the intensity of the scattered light. A digital autocorrelator interprets the statistical fluctuations of the intensity in time of ns to  $\mu$ s. On the one hand, the system uses correlation functions ( $G$ ) that describe the motion of the particles as an integral of the product of the intensities at a time  $t$  and a delayed time ( $t + \tau$ ) with a lapse of time  $\tau$ :

$$G(\tau) = \langle I(t)I(t + \tau) \rangle \quad (3.2)$$

On the other hand, the relative motion of the particles in solution is correlated by an electric field correlation function. Both the electric field and the intensity correlation functions can be coupled assuming that only the scattered light is detected and that the photons are counted via a random Gaussian process. For monodisperse samples the electron field correlation factor decays

exponentially depending on a decay constant or relaxation rate ( $\Gamma$ ), which is related to the diffusion coefficient:

$$\Gamma = -Dq^2 \quad (3.3)$$

According to eq. (3.3), the relation is based on the magnitude of the scattering vector ( $q$ ), which is defined as the difference between the scattered and the incident wave vectors. Thus,  $q$  is expressed in terms of the refractive index of the medium ( $n_0$ ), the wavelength of the incident radiation in air ( $\lambda_0$ ), and the scattering angle ( $\theta$ ):

$$q = \frac{4\pi n_0}{\lambda_0} \sin\left(\frac{\theta}{2}\right) \quad (3.4)$$

The adjustment of the intensity of the correlation function to a simple exponential decay using two constants (A and B) associated to the base line and the intercept of a correlation function, allows the calculation of the diffusion coefficient:

$$G(\tau) = A[1 + Be^{-2\Gamma\tau}] \quad (3.5)$$

Then, the hydrodynamic radius, defined as the radius of a hypothetical sphere that diffuses at the same rate than the particle of study is calculated using the Stokes–Einstein equation for hard spheres:

$$R_h = \frac{k_B T}{6\pi\eta D} \quad (3.6)$$

In the case of polydisperse samples, the intensity correlation function is expressed as a combination of several exponential decays. As an accepted convention, the logarithm of this function is fitted to a quadratic expression with constants  $a$ ,  $b$  and  $c$ :

$$\ln G(\tau) = a + b\tau + c\tau^2 \quad (3.7)$$

The width of the distribution defines polydispersity index (PDI):

$$\text{PDI} = \frac{2c}{b^2} \quad (3.8)$$

The resulting particle size distribution is an intensity distribution, which can be translated into volume and number distributions assuming the spherical morphology of the particles.<sup>134</sup> The intensity distribution commonly gives a more accurate characterization of homogeneous size distributions. In the presence of two (or more) size populations the volume distribution would provide a more realistic approach, whereas the number distribution would become unreliable.

### 3.1.2 Polyelectrolyte Titration (PCD)

The polyelectrolyte titration is an analytic technique used to determine the surface charge density of polymer particles with a functional surface. The method relies on the stoichiometric reaction between the surface charges and an oppositely charged polyelectrolyte (e.g., poly(diallyldimethylammonium chloride) (polyDADMAC) as shown in Figure 3.1.

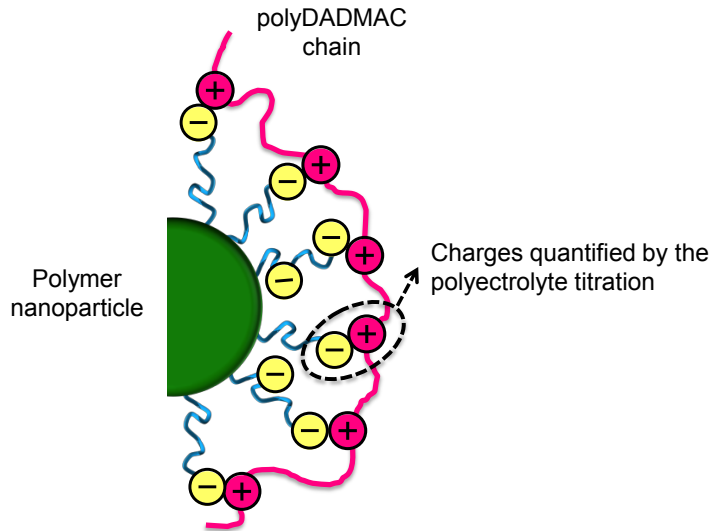


**Figure 3.1.** Schematic representation of the electrostatic interaction between the negatively charged surface of a functionalized polymer particle and the positively charged chains of polyDADMAC. (Based on ref. 115)

For the determination of the effective charge of functional nanoparticles, an aqueous dispersion of charged nanoparticles with a volume  $V_s$  and a solid content or fraction of solid  $F_s$  is titrated with an aqueous solution of an oppositely charged polyelectrolyte with a molar concentration  $c$ . The volume ( $V$ ) of polyelectrolyte required for the inflexion of the electric potential ( $PCD = 0$ ) of the sample can be translated into a number of charged groups ( $N_{ch}$ ) using the Avogadro constant ( $N_A$ ):

$$N_{ch} = VcN_A \quad (3.9)$$

The number of groups (or charges) per gram of particles is calculated as the coefficient of  $N_{ch}$  by the total mass of the particles of the sample ( $m_s$ ), which can be calculated using the density of water ( $1 \text{ g}\cdot\text{cm}^{-3}$ ) as an approximation of the density of the sample ( $\rho$ ):

$$m_s = F_s V_s \rho \quad (3.10)$$

If the particles are considered as spheres with a volume  $V_p$ , the hydrodynamic radius ( $R_h$ ), and the particle density ( $\rho_p$ ) determine the mass of the particle ( $m_p$ ):

$$m_p = V_p \rho_p = \frac{4}{3} \pi R_h^3 \rho_p \quad (3.11)$$

Then, the number of charges per particle is calculated by multiplying the number of charged groups per sample ( $N_{ch}$ ) by  $m_p$ . In addition, the assumption of spherical particles allows us to determine the area of the particles ( $A_p$ ):

$$A_p = 4\pi R_h^2 \quad (3.12)$$

According to eq. (3.9), (3.10), (3.11), and (3.12) the number of charges per unit of area ( $\sigma_N$ ) is determined:

$$\sigma_N = \frac{VcN_A R_h \rho_p}{3F_S V_S \rho} \quad (3.13)$$

This technique has been used in Chapters 5 and 6 to characterize the surface charge density of P(S-AA) and proline-functionalized PMMA nanoparticles with negative charges related to the presence of carboxylic groups. The deprotonation of the functional groups of the sample, which depends on the pH value, influences the volume of cationic polyelectrolyte (e.g., polyDADMAC) required for the titration. In our case, the complete deprotonation of carboxylic groups was guaranteed at a pH value of 9.5, and thus, the samples were basified before the determination.

## 3.2 Thermal Characterization

### 3.2.1 Thermogravimetric Analysis (TGA)

Thermogravimetric analysis (TGA) offers an evaluation of the thermal degradation experienced by materials within a certain range of temperatures. The technique allows us to detect fusion and evaporation processes and to determine the amount of organic matter present in a sample via the decomposition of C–C bonds. The measurement is performed in a protective chamber incorporating a thermobalance with the sample, a resistance in charge of the heating of the process, and a cooling system for the stabilization and the decrease of the temperature at the end of the thermal cycle.

TGA measurements were carried out in this thesis under protected atmosphere of nitrogen to avoid the changes on the mass of the system due to oxidation processes. The inorganic load of hybrid materials was determined as the fraction of mass remaining after the thermal treatment. The incorporation of the coupling agent (i.e., the silane component) to the inorganic nanoparticles was also determined as the difference between the fraction of mass remaining after the thermal treatment of the raw and the functionalized nanoparticles. In all the cases, it exists a percentage of

about 2 wt.% of the organic matter that is not calcinated under inert atmosphere. The so-called residual carbon was determined by evaluation of pure polymer particles or organic functionalizing components, and it was used to correct the estimation of the inorganic/organic balance.

### 3.2.2 Differential Scanning Calorimetry (DSC)

Differential scanning calorimetry (DSC) is used to determine the thermal behavior of materials that suffer phase transformations as a consequence of an increase or a decrease of the temperature. A known weight of sample contained in a measurement cell is placed next to a second reference cell in a calorimetric chamber fluxed with nitrogen at a constant rate. The enthalpy of the phase transitions and the possible thermal processes occurring are detected with the flow of heat between the sample and the cell of reference.<sup>3</sup> Thus, the unit provides diagrams of heat flow as a function of the temperature. Thermal transitions are observed in the form of peaks, whose integration corresponds to the enthalpy associated to the process.

DSC is used in Chapter 7 to study the cycles of melting and recrystallization of phase change materials (PCMs). The chemical and thermal stability of the hydrated salts is analyzed by submitting the materials to several cycles of thermal treatment around the melting and crystallization temperatures. The integration of the melting peaks allows the calculation of the capacity of the materials for the storage of thermal energy.

## 3.3 Electron Microscopy (EM) Characterization

The shorter wavelength ( $\lambda$ ) of the electron beams compared to visible light allows a high angular resolution ( $\delta$ ) in electron microscopes, which is used for the imaging of samples at the nanoscale.

The smaller distance between two spot points that can be resolved by the Abbe equation is what is known as the angular resolution of electron microscopes:<sup>135,136</sup>

$$\delta = \frac{\lambda}{2n\sin(\alpha)} \quad (3.14)$$

According to eq. (3.14),  $\delta$  is directly proportional to the wavelength of the beam ( $\lambda$ ) and inversely proportional to two times the numerical aperture ( $n\sin(\alpha)$ ) of the lenses system, where  $n$  is the refractive index of the medium and  $\alpha$  the angular aperture of the objective lenses.

The electron microscopy techniques (i.e., transmission electron microscopy (TEM) and scanning electron microscopy (SEM)) have been complementary used in this thesis for the characterization

of polymer–metal oxide hybrid nanoparticles and capsules both at the surface and the inner levels. The information revealed by TEM about the inner hybrid structures is especially important to verify encapsulation features. Nevertheless, the TEM observations require the corroboration allowed with the surface characterization by SEM, in which the deeply encapsulated inorganic species are not observed.

#### **3.3.1 Transmission Electron Microscopy (TEM)**

Transmission electron microscopy (TEM) is a direct imaging technique based on the detection of the electrons transmitted from the interaction between the sample and an electron beam generated by thermal emission in a thermoionic cathode at acceleration voltages of 50–200 kV.<sup>3</sup> A combination of electromagnetic lenses allows the reorientation of the beam and the interaction with the sample, which results into an electron scattering phenomena. The transmitted electrons that go through the sample are detected with a chip creating a direct image from the sample. The ratio of scattering of the beam depends on the properties and the thickness of the sample (i.e., heavier and thicker materials present stronger intensities of scattering).<sup>136</sup> This principle is exploited for the differentiation between the inorganic and polymer species with greater and lighter intensities of scattering, respectively. The transmitted electrons allow the observation of deeply encapsulated inorganic species within a polymer matrix, which will not be observed with the surface observation allowed by SEM.

#### **3.3.2 Scanning Electron Microscopy (SEM)**

Scanning electron microscopy (SEM) is based on the detection of secondary electrons emitted from the surface of a sample as a result of the interaction of the material with an electron beam.<sup>3</sup> The beam is generated by thermal emission at acceleration voltages of 0.1–30 kV, and the secondary electrons are observed via a detector sideways located above the sample. This indirect imaging technique offers an observation of the sample via a scanning process performed line by line. The intensity of the signal received by the detector and the brightness of the image formed is proportional to the number of electrons emitted and the relative position of the sample and the detector. Thus, a three-dimensional image of the surface of the sample is generated with a spatial resolution determined by the size of the different sample spot points instead of the wavelength of the applied electron beam.



## 3.4 Characterization of Chemical Composition and Chemical Structure

### 3.4.1 Inductively Coupled Plasma-Mass Spectrometry (ICP-MS)

Inductively coupled plasma mass spectrometry (ICP-MS) is a mass spectrometry analytic technique with high speed, sensitivity, and precision used for the detection of chemical elements (specially metals) at very low concentrations (i.e., in the range of ppt).

The technique uses a plasma, a partially ionizing argon gas ( $\text{Ar} \rightarrow \text{Ar}^+ + \text{e}^-$ ) generated in an electromagnetic torch at extremely high temperatures (i.e., 10,000 K) to promote the nebulization, atomization and further ionization ( $\text{M} \rightarrow \text{M}^+ + \text{e}^-$ ) of the samples. The ions from the plasma are extracted through a series of cones into a mass spectrometer. In this unit, the ions are separated according to the mass/charge ratio providing the detector with signals proportional to the specific concentration of each ion.

In this thesis, ICP-MS analysis was used for the determination of specific metals (i.e., titanium, cerium or iron), present in multifunctional hybrid nanoparticles. The metal concentration allowed us to quantify the inorganic load (i.e., titania, ceria or magnetite) of multifunctional hybrid materials in which TGA is not able to discern between the different inorganic species. Due to the presence of polymer-based matrix particles, a digestion process of the samples with strong acids was required before characterization.

### 3.4.2 X-Ray Diffraction (XRD)

X-ray diffraction (XRD) is a physicochemical technique used to investigate the structural and the crystalline characteristics of materials. It allows the description of the phase composition of the sample, and the order and perfection of crystals (i.e., crystallinity, unit cell parameters, crystal structure refinement or Rietveld,<sup>137</sup> and crystallite size).<sup>138</sup>

X-rays are electromagnetic waves with a wavelength ( $\lambda$ ) that scatter when striking with a regular array of electrons.<sup>139</sup> The elastic scattering generates secondary waves, which are mostly cancelled by a destructive interference between each other. However, when the waves scattered by different planes present a path-length equivalent to a multiple  $n$  of the wavelength of the incident wave, it takes place a constructive interaction and the addition of the secondary waves in specific directions. Thus, the physical phenomenon of XRD is based on the diffraction experimented by incident X-rays on a crystalline lattice, whose interatomic distances (1–100 Å) are comparable to the incident wavelength. In a diffractometer, a monochromatic beam of wavelength  $\lambda$  with an angle  $\theta$  falls upon the family of parallel crystalline planes separated a distance  $d$  from each other. The

peaks obtained in the diffractograms correspond to the constructive interactions and their position allows us to calculate the interplanar distances  $d$  according to Bragg's law:<sup>140</sup>

$$n\lambda = 2d \sin \theta \quad (3.15)$$

A crystalline structure is characterized by the unit cell and the crystalline planes. The unit cell consists of the smallest unit forming the crystalline lattice by three-dimensional repetition, and it is defined by the crystallographic axis (with lengths  $a$ ,  $b$ ,  $c$ , and relative angles  $\alpha$ ,  $\beta$ ,  $\gamma$ ) and the vertices, which are occupied by atoms, molecules or ions. Regarding the crystalline planes, it exist a convention to identify them using the intercepts of the crystalline planes and the axis, known as the Miller indices ( $hkl$ ). The parameters of the unit cell are related to the interplanar distance ( $d$ ) via geometrical considerations. At the same time, according to Bragg's law, the space between the crystalline planes  $d$  is a function of the diffraction angle ( $\theta$ ), which identifies the directions of the constructive interactions. The diffraction angles appear as reflections spots in the diffraction pattern, which are translated into specific positions of the peaks in the diffractograms whose diffracted intensity is also a function of  $\theta$ . Therefore, the crystalline structure of the sample can be elucidated by calculating the interplanar distance and the unit cell parameters determined from the position of the peaks of a diffractogram.

If the instrumental and the lattice strain (i.e., the presence of crystalline distortions) factors are neglected, the broadening of the diffraction lines can be used to estimate size of the coherently scattering domains, commonly called as crystallite size ( $L_{hkl}$ ):

$$L_{hkl} = \frac{K\lambda}{\beta_{1/2} \cos \theta} \quad (3.17)$$

The Scherrer formula (eq. (3.17)) introduces a form factor ( $K$ ) ranging from 0.89 to 1.39, which is often assumed as 0.94, and the full width ( $\beta_{1/2}$ ) at the half maximum of a reflection on the  $2\theta$  scale (in radians).<sup>141</sup>

### 3.4.3 Ultraviolet-Visible Spectroscopy or Spectrophotometry (UV-Vis)

Ultraviolet-visible (UV-Vis) spectroscopy is an absorption (or reflectance) spectroscopic technique, which determines the amount of light with a certain wavelength in the electromagnetic spectra from the ultraviolet to visible region that is absorbed (or reflected) by a sample. In this region, the absorption processes are related to atomic and molecular electronic transitions that occur when the requirement of energy is comparable to the energy of the photon.<sup>142</sup> According to the Lambert–Beer law, the absorbance of a sample in solution is related to the concentration of the absorbing species:

$$A = \log \frac{I_0}{I} = \epsilon cd \quad (3.18)$$

The decrease of the intensity of the incident light ( $I_0$ ) after passing through a sample in solution (i.e., with a transmitted beam ( $I$ )) is related to the molar absorptivity or the extinction coefficient ( $\epsilon$ ) of a solvent at a certain temperature and pressure conditions, the concentration of the absorbing species ( $c$ ) and the path length ( $d$ ) of the light through the sample. For a fixed path length corresponding to the width of a measurement cell, the concentration of absorbing species in solution can be calculated. With the aid of a calibration curve, which allows us to adjust the changes of the absorbance with the concentration, the technique is used to track the evolution of the concentration of absorbing species.

UV-Vis spectroscopy has been used in Chapter 7 to study the release of the dye Brilliant Blue FCF encapsulated within magneto-responsive and/or catalytic hybrid capsules.

#### 3.4.4 High Performance Liquid Chromatography (HPLC)

High performance liquid chromatography (HPLC) is a separation method whose mechanism can be related to a simple liquid–liquid extraction process. The technique is based on the partitioning of the molecules of a sample between two liquid phases, a mobile phase in constant movement relative to a second phase, stationary. The molecules in the mobile phase are eluted with the phase movement, whereas the ones partitioned in the stationary phase are retained mostly by adsorption interactions. During a chromatographic separation, the partition of the solute between the phases occurs in a range of thousands of times, which confers to the technique a high resolution for the separation of components with similar physical properties.<sup>143</sup>

A pump system injects a pressurized liquid solvent (50–350 bar) containing a certain concentration of sample at a desired flow in a column filled with an adsorbent material. The different interactions of the molecular components in the sample with the column lead to specific flow rates and their separation occurs according to the time that they remain retained by the stationary phase.

The travel of the solutes can be described as a random walk in which the molecules experiment cycles of adsorption and desorption along the column. The solute stays a time  $t_s$  adsorbed at the stationary phase, and a time  $t_m$  migrating with the mobile phase at the velocity  $u_x$ . During the retention time  $t_R = t_m + t_s$ , the solute will spend a fraction of time ( $t_m/t_R$ ) at this speed.<sup>143</sup> If the fraction of time that the solute spends in the mobile phase is correlated with the fraction of solute in the mobile phase of a fraction of the column, the velocity of a molecule of the solute is expressed in terms of the retention factor ( $k$ ):

$$u_s = u_x \frac{t_m}{t_m + t_s} = u_x \frac{1}{1 + k} \quad (3.19)$$

The retention factor is at the same time related to the retention time and the travelling time of the solvent in the mobile phase ( $t_0$ ):

$$k = \frac{t_R - t_0}{t_0} \quad (3.20)$$

The selectivity ( $\sigma$ ) between two components is defined as the ratio of the retention factors of two species (1 and 2) with neighboring peaks ( $t_{R1} < t_{R2}$ ):

$$\sigma = \frac{k_2}{k_1} \quad (3.21)$$

At the exit of the column, the solutes are collected as separated zones. The signal generated by the detector is plotted in chromatograms as a function of time in the form of peaks with an area proportional to the concentration of the eluted component. A digital microprocessor allows the analysis of the data, the deconvolution, and the integration of the peaks to obtain the related parameters (i.e., retention time, area, height, and width of the peak). In an ideal case, the peaks would present a normal Gaussian distribution, in which the retention time ( $t_R$ ) is calculated at the maximum of the peak. The width ( $W_t$ ) of the peak would be then defined at the baseline as the distance between the crossings of the base line with the tangents of the inflection points of the distribution. In practice, the ideal distribution is commonly distorted, with a tail due to the presence of different adsorption sites in a given component. An asymmetry factor ( $A_{sfx}\%$ ) is considered for the analytical treatment of the data.<sup>143</sup> The resolution ( $R_s$ ) is used to evaluate the efficiency of the chromatographic separation of two substances with adjacent solute zones with an average width ( $W_t$ ):

$$R_s = \frac{2(t_{R2} - t_{R1})}{W_{t1} + W_{t2}} \quad (3.21)$$

A chromatogram offers qualitative information of a sample with the retention time of the contained species, as well as quantitative information about the concentration of the species, which can be related to the area of the peaks. This strategy was used in Chapter 5 to follow the advance of the hydrolysis reaction of 2-cyanopyridine to 2-picolinamide and to evaluate the catalytic performance of polymer-supported ceria nanocatalysts.

In this thesis, HPLC was performed by using a reversed-phase column (RP-HPLC) with a moderately polar phase (acetonitrile and acidified water) that flows through a non-polar stationary

phase. Fused-core silica particles (2.6  $\mu\text{m}$ ) incorporating a straight chain alkyl group  $\text{C}_{18}\text{H}_{37}$  packed in a cylindrical column were used as a stationary phase. The system was equipped with a pre-column, which allowed us to decrease the working pressure and to afford the increase of the water content in the mobile phase. The retention time in this type of columns is decreased with the polarity of the molecules, whereas hydrophobic structures are retained longer. The chemical structure of the molecules determines the retention characteristics. In general, molecules with C–H, C–C and non-polar atomic bonds such as S–S are retained longer than others with a higher polarity (presenting polar groups such as  $-\text{OH}$ ,  $-\text{COO}^-$ ,  $-\text{NH}_2$ , or  $\text{NH}_3^+$ ) and greater affinity to the mobile phase. Not only the chemical composition, but also the spatial conformation of the molecules influenced by steric effects and the accessible hydrophobic surface area determine the interaction with the pores of the stationary phase. In general, the surface hindrance results in faster elutions. Thus, larger molecules or branched structures present lower retention times with respect to the corresponding linear isomers or shorter molecules.

The mobile phase also determines the retention of molecules in the column. The retention of the different species in a sample can be increased or decreased with the addition of a less or more polar solvent in the mobile phase to modify the relative surface tension. The use of gradients of elution allows an automatic modification of the polarity and the surface tension relative to the mobile phase during the course of the analysis. This strategy enables the adjustment of the separation in the chromatogram of adjacent peaks corresponding to substances with similar chemical structures. The chromatographic resolution can be increased with the incorporation of inorganic salts influencing the surface tension of the eluent solvent, or with changes of the pH value. In this sense, the addition of acids or buffering agents is used to modify the polarity of the chemical species by protonation or deprotonation mechanisms.



## Results and Discussion

### 4 Preparation of Hybrid Polymer–Metal Oxide Nanoparticles with Controlled Morphology

This chapter is dedicated to the preparation of polymer–metal oxide hybrid nanoparticles with controlled morphology by direct miniemulsion polymerization. The selective migration of inorganic functionalities within a polymer matrix is addressed via the specific surface functionalization of metal oxide nanoparticles. Three alkoxy silane components with different chemical structures were used as coupling agents for the compatibilization of the hydrophilic surface of catalytically active (ceria and titania) and magnetoresponsive (magnetite) inorganic nanoparticles, with hydrophobic polystyrene or poly(methyl methacrylate) (PMMA) matrices. Silane chemistry allowed us to establish a synthetic platform to control the encapsulation of the inorganic nanoparticles within the polymer, the phase segregation, and the deposition of the inorganic functionalities on the polymer surface, or the formation of Janus-like structures.

The strategy was extended to the preparation of a second generation of multifunctional polymer–metal oxides hybrid nanoparticles. For this aim, two types of inorganic species with complementary (catalytic and magnetoresponsive) functionalities and surface functionalization were combined. The final accessibility of the different functionalities resulted from a self-assembly process, which was controlled by tuning the surface chemistry of the inorganic nanoparticles. The miniemulsion technique was proven to be suitable for the preparation of recyclable heterogeneous catalysts consisting of polymer-supported hybrid nanoparticles with a catalytic surface and a magnetoresponsive core.

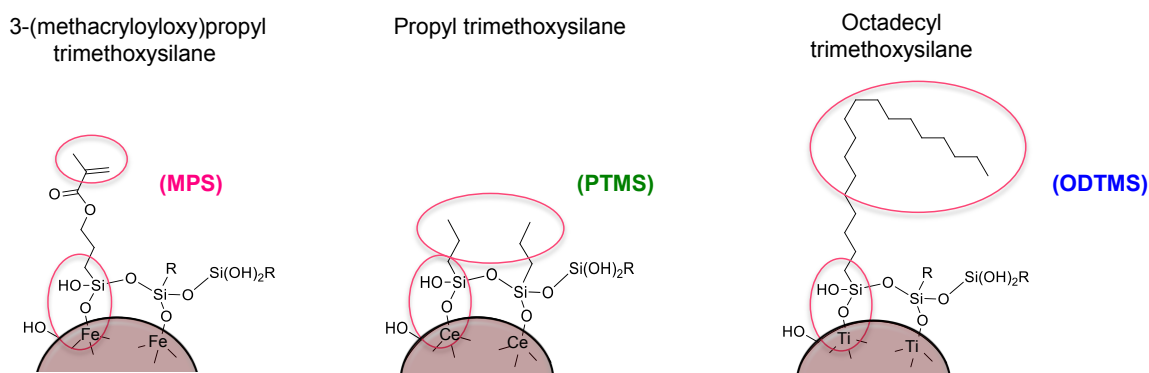
#### 4.1 Synthesis and Functionalization of Functional Inorganic Nanoparticles

Magnetite ( $\text{Fe}_3\text{O}_4$ ), ceria ( $\text{CeO}_2$ ), and titania ( $\text{TiO}_2$ ) were selected as model inorganic species with catalytic and magnetic functionalities. We used a commercial dispersion of titania nanorods with an average length of 20 nm, whereas magnetite and ceria nanoparticles with sizes about 5–10 nm were prepared by (co)precipitation methods. Working with aqueous dispersions and inorganic nanoparticles synthesized without any calcination step minimizes the formation of inorganic

aggregates. The great surface area and dispersibility in aqueous media of the nanoparticles is critical to guarantee an efficient surface functionalization of the inorganic species.

The surface of metal oxide nanoparticles is originally hydrophilic due to the presence of charged groups, such as  $\text{OH}^-$ . The incorporation of hydrophilic nanoparticles within hybrid nanostructures with polymer matrices is commonly hindered by the differences of polarity between inorganic and polymer species. Typically, hydrophobization of the surface of inorganic species is required for compatibilization with the monomer/polymer system. The versatility of alkoxy silanes in terms of structure and their chemical affinity to metal oxides makes silane chemistry an attractive option for hydrophobization of the inorganic species. As explained in section 2.5.3, under basic reaction conditions, silanes are hydrolyzed to silanol groups, which condense and form oligomers that adsorb at the inorganic particles through interactions with the charged groups on the surface. With the increase of temperature, oligomers condense and form covalent bonds on the particle surface. After equilibration and drying, silane functionalities are irreversibly and covalently attached to the inorganic species.

The functionalization strategy from previous works focused on silica<sup>75</sup> and magnetite<sup>98</sup> nanoparticles was adapted to the catalytic species. The control of the development of the hybrid morphologies was addressed using three silane components with specific length of the alkyl chain and functional end groups. Therefore, 3-(methacryloyloxy)propyl trimethoxysilane (MPS), propyl trimethoxysilane (PTMS), and octadecyl trimethoxysilane (ODTMS), whose specific chemical structures are presented in Scheme 4.1, were used to tune the hydrophobicity and reactivity of the inorganic particles.



**Scheme 4.1.** Chemical structures of the three alkoxy silane components used as coupling agents for the surface functionalization of the magnetite, ceria, and titania nanoparticles.

The effectiveness of the functionalization was analyzed by thermogravimetric analysis (TGA) of the dried nanoparticles before and after functionalization. The thermal degradation of the organic



matter and the subsequent loss of mass observed in Figures 4.1 and 4.2 can be associated with the incorporated silanes. The similar thermal degradation between the last cycles of washing of the nanoparticles observed in Figure 4.1(a) is a hint of a covalent attachment of MPS to the ceria nanoparticles, which did not desorb even under application of ultrasounds in an ethanol/water media. Analogous results were obtained for the other combinations of silanes and inorganic species. Taking into account the molar mass of each silane ( $M_{\text{ODTMS}} = 375$  g/mol,  $M_{\text{PTMS}} = 164$  g/mol, and  $M_{\text{MPS}} = 248$  g/mol) and the use of an identical amount of coupling agent proportional to the mass of inorganic nanoparticles, similar yields of functionalization were reached for the three silanes.

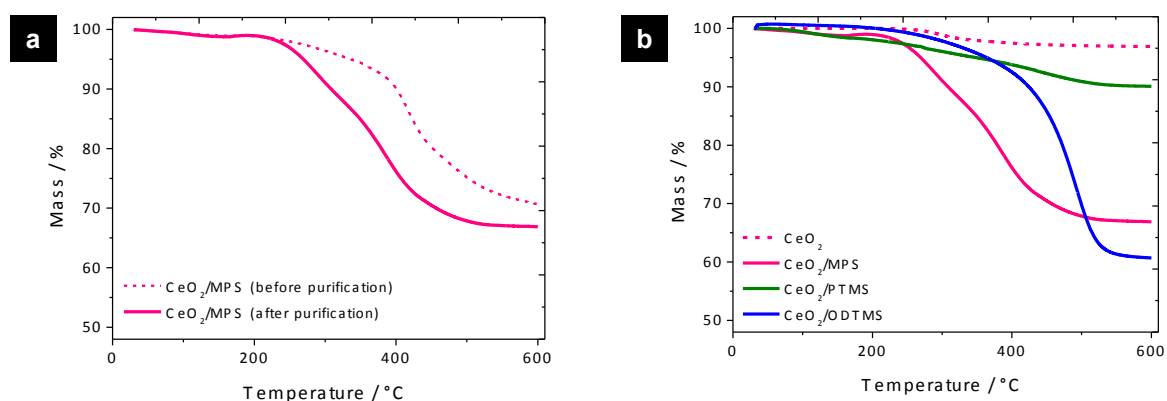


**Figure 4.1.** TGA curves of ceria nanoparticles functionalized with MPS before and after the last washing operation (a), and comparative of the curves of ceria nanoparticles with the functionalization achieved with the three different silane compounds used in the work (MPS, PTMS, and ODTMS) (b).

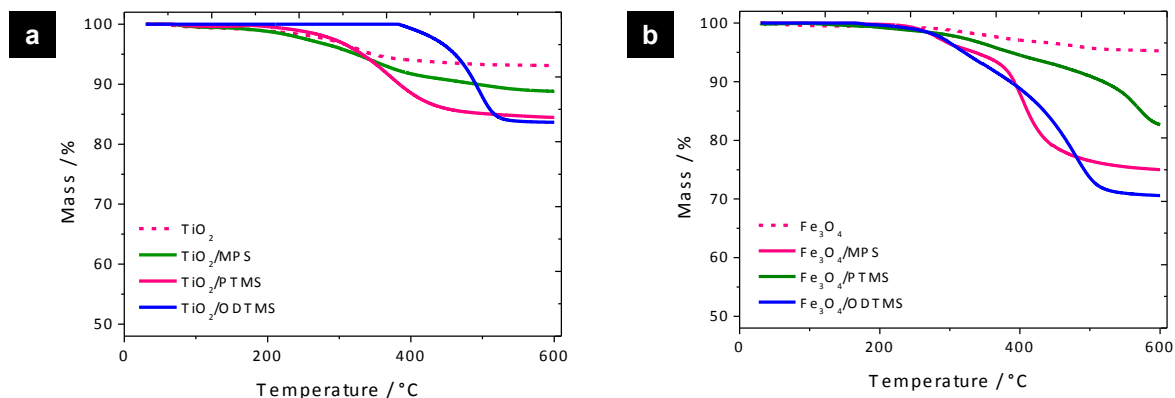


**Figure 4.2.** TGA curves of titania (a) and magnetite (b) nanoparticles functionalized with three different silane components (MPS, PTMS, and ODTMS), compared with the raw nanoparticles.

In the case of magnetite, an incorporation of 35, 30, and 20 wt.% of coupling agent was obtained for ODTMS, MPS, and PTMS, respectively. For ceria nanoparticles, of similar size and morphology as the magnetite ones, 35, 30, and 10 wt.% were respectively observed. Due to the

higher hydrophobicity of ODTMS with respect to MPS and PTMS, the oligomers formed in solution precipitate faster, leading to a reduction of the silane available for the inorganic functionalization. From a macroscopic point of view, the precipitation of the oligomers was observed through the increase of turbidity of the media as previously reported by Schoth et al.<sup>75</sup> The respective percentages of incorporation of silanes achieved with titania nanoparticles were of 15, 15, and 10 wt.%. The efficiency of hydrophobization of titania, especially lower with respect to ceria and magnetite, can be attributed to the rod-like shape and to the presence of a pre-functionalization in the commercial particles, which allows the stability of the dispersion but hinders the post-functionalization with silanes.

## **4.2 Preparation of Polymer–Metal Oxide Hybrid Nanoparticles with Specific Morphology Controlled via Inorganic Surface Functionalization**

Polymer–metal oxide hybrid nanoparticles were prepared by incorporation of preformed inorganic nanoparticles within a polymer support by free-radical polymerization in direct miniemulsion, as described in section 2.6.1. Miniemulsions were stabilized using sodium dodecyl sulfate (SDS) as a surfactant. The inorganic nanoparticles (20 wt.% with respect to the monomer), functionalized at their surface with the three previously mentioned silanes (ODTMS, PTMS or MPS), were dispersed within the disperse phase together with the monomer, 2,2'-azobis(2-methylpropionitrile) (AIBN) as an oil-soluble free-radical initiator and hexadecane as an osmotic pressure agent. The incorporation of different metal oxide (ceria or titania) nanoparticles with a specific surface functionalization was investigated by using methyl methacrylate (MMA) or styrene (S) as monomers forming the polymer matrix. The relative polarity between the inorganic and the polymer species plays a major role in the morphology development of the nanostructures. In principle, ODTMS- and PTMS-functionalized inorganic nanoparticles would be more affine to hydrophobic polymers such as polystyrene, whereas MPS-functionalized species would be better integrated within PMMA.

A certain level of dispersity in size is one of the most critical issues almost inherent to the miniemulsion technique. Whereas miniemulsion offers an optimized media for the preparation of model polymer (e.g., polystyrene) nanoparticles, the development of homogeneous hybrid nanostructures deals with greater complexity. The incorporation of inorganic species leads to a different partition within the nanodroplets. The steps of dispersion of the inorganic nanoparticles, homogenization of the miniemulsion phases, pre-emulsification and emulsification are essential to guarantee an acceptable homogeneity in size and inorganic load. Nevertheless, the formation of

empty polymer particles or a heterogeneous distribution of the inorganic load is practically unavoidable. The purification or fractioning of the particle dispersions achieved after polymerization offers the possibility to optimize the homogeneity of the sample and to collect the functional fraction of the product. As described in the following sections, the incorporation of magnetically recoverable inorganic species (magnetite) is the key of purification by simple application of an external magnetic field. In the absence of such magneto-responsive components, centrifugation was used as a separation method to collect the heavier fraction of the dispersion (i.e., the bigger particles, which also correspond to the particles with higher inorganic load). Table 4.1 lists the different types of polymer–metal oxide hybrid nanoparticles prepared by miniemulsion polymerization using different polymer, inorganic, and coupling agent combinations. The materials consisting of polystyrene–ceria nanoparticles are labeled as **SC**, followed by **1**, **2** or **3** according to the functionalization of ceria with ODTMS, PTMS or MPS, respectively. Analogously, the samples named as **MC** present PMMA as polymer support. The labels **ST** and **MT** correspond to the incorporation of titania nanoparticles within polystyrene and PMMA matrices, respectively.

**Table 4.1.** Material composition and main features of the polymer–metal oxide hybrid nanoparticles incorporating catalytic species with specific surface functionalization.

Sample	Monomer	Inorganic Component	Coupling Agent	$d^a$ / nm	Solid Content / wt. %		Inorganic Load <sup>d</sup> / wt. %
					BP <sup>b</sup>	AP <sup>c</sup>	
<b>SC1</b>	S	CeO <sub>2</sub>	ODTMS	160 ± 40	20.0	0.7	35
<b>SC2</b>	S	CeO <sub>2</sub>	PTMS	170 ± 40	18.1	0.7	15
<b>SC3</b>	S	CeO <sub>2</sub>	MPS	190 ± 60	19.2	1.3	10
<b>MC1</b>	MMA	CeO <sub>2</sub>	ODTMS	180 ± 60	8.8	5.1	5
<b>MC2</b>	MMA	CeO <sub>2</sub>	PTMS	200 ± 40	17.7	7.4	5
<b>MC3</b>	MMA	CeO <sub>2</sub>	MPS	200 ± 40	19.9	7.6	5
<b>ST1</b>	S	TiO <sub>2</sub>	ODTMS	180 ± 50	5.6	1.1	30
<b>ST2</b>	S	TiO <sub>2</sub>	PTMS	140 ± 30	16.2	4.6	25
<b>MT1</b>	MMA	TiO <sub>2</sub>	ODTMS	200 ± 70	15.7	8.3	15
<b>MT2</b>	MMA	TiO <sub>2</sub>	PTMS	280 ± 40	11.2	4.6	15
<b>MT3</b>	MMA	TiO <sub>2</sub>	MPS	170 ± 50	19.8	2.9	5

<sup>a</sup> Determined by DLS before purification.

<sup>b</sup> BP: Solid content determined before purification.

<sup>c</sup> AP: Solid content determined after purification.

<sup>d</sup> Determined by TGA after purification.

Particle sizes (hydrodynamic diameters,  $d$ ), determined by dynamic light scattering (DLS), are in the range 150 to 250 nm. In general, the PMMA nanoparticles are slightly larger than polystyrene ones with similar inorganic content. According to the one-to-one copy concept of the miniemulsion polymerization, this observation might be ascribed to differences in droplet sizes. In general, the droplet size is determined by the droplet break-up reached during the sonication step. The break-up

depends on the viscosity ratio between disperse and the continuous phases, in the case of pure liquids.<sup>144</sup> According to this statement, the lower viscosity of MMA (0.6 cP at 20 °C) with respect to styrene (0.76 cP at 20 °C) would result into smaller droplets and, consequently, smaller particles under the same synthetic conditions, which is not the case. The incorporation of inorganic nanoparticles leads to an increase of the viscosity of the droplets, the viscosity ratio between the miniemulsion phases, and the droplet size. In addition, some counter-acting stresses appear and the droplet deformation occurs in the presence of high inorganic contents, aggregates or inorganic species with large sizes and irregular shapes (as it is the case for titania nanoparticles). The larger particle sizes of the PMMA-based hybrids would be explained by the higher affinity of the monomer/polymer system to the silanized nanoparticles, which can lead to a better entrapment of the inorganic functionalities within the polymer matrix. The copolymerization between the monomer and the functionalizing species can also favor the inorganic encapsulation and the subsequent increase of the particle size. Nevertheless, no clear trend is observed in the influence of the coupling agent or the metal oxide with respect to the size of the resulting hybrid structures.

The comparison of the solid content before and after purification offers an estimation of the efficiency of the overall synthetic process. Since the purification process applied for each type of particles was the same, the value of the fraction recovered will depend not only on the quantity of sample with a minimal presence of empty polymer particles, but also on the quality of the material (inorganic load and homogeneity). The inorganic load was determined by thermogravimetric analysis (TGA) of the dried particles recovered after purification. Styrene offers an incorporation about 20–35 wt.% of inorganic nanoparticles functionalized with PTMS and ODTMS, as observed in the TGA curves shown in Figures 4.3 and 4.4. Percentages of 5–15 wt.% of inorganic load were achieved with of MPS-functionalized inorganic nanoparticles and PMMA-based hybrid structures.

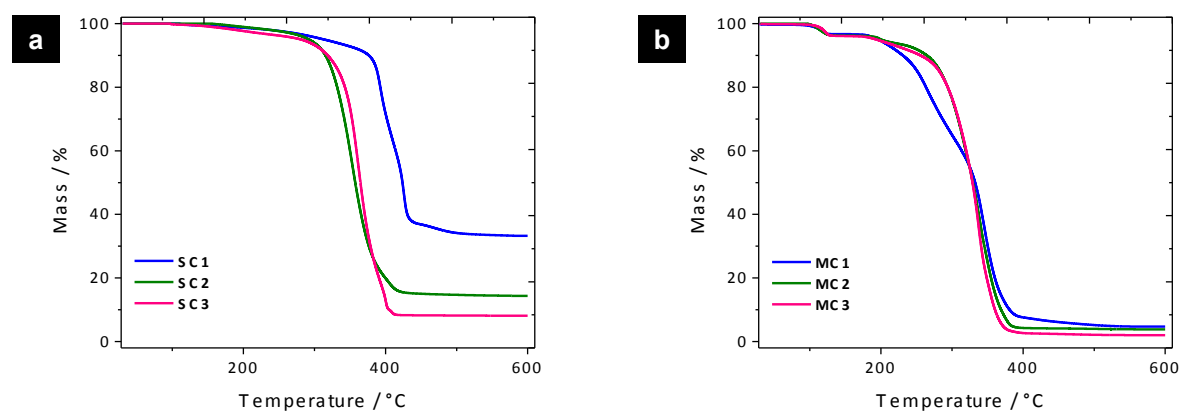


**Figure 4.3.** TGA curves of the hybrid nanoparticles incorporating ceria functionalized with ODTMS (blue line), PTMS (green line), or MPS (magenta line) within polystyrene (SC1-3) (a) and PMMA (MC1-3) (b).

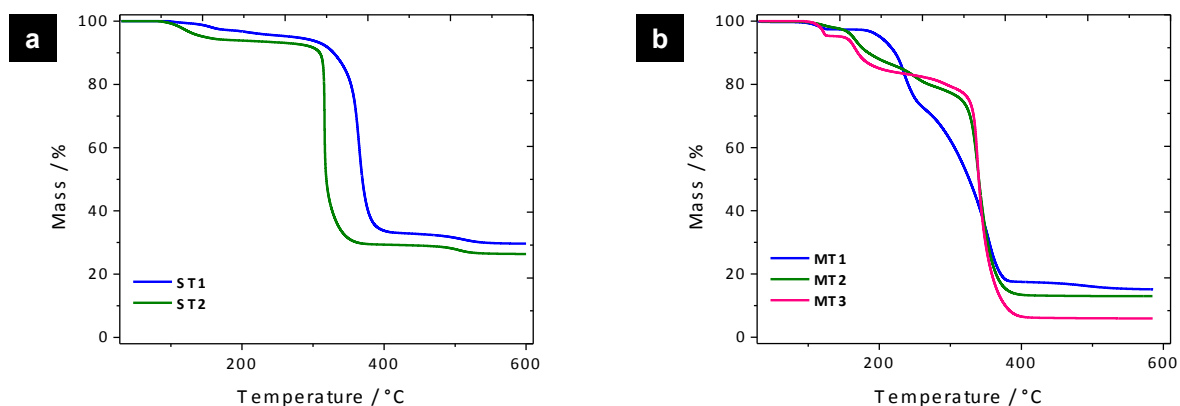


**Figure 4.4.** TGA curves of the hybrid nanoparticles incorporating titania functionalized with ODTMS (blue line), PTMS (green line), or MPS (magenta line) within polystyrene (ST1-3) (a) and PMMA (MT1-3) (b).

Electron microscopy was used to discern the migration of the inorganic functionalities within the polymer. Transmission electron microscopy (TEM) offers the possibility to identify encapsulated inorganic species that remain invisible with the surface characterization allowed by scanning electron microscopy (SEM). The combination of both techniques was used to build up a global image of the hybrid morphology, both at surface and inner levels. Figures 4.5 and 4.6 show TEM and SEM images of polystyrene and PMMA nanoparticles incorporating ceria with different surface functionalization (with ODTMS, PTMS, and MPS), whereas Figures 4.7 and 4.8 present the analogous cases with titania as an inorganic system.

In agreement with the results previously reported for silica<sup>13</sup> and magnetite<sup>98</sup> nanoparticles, the long alkyl chains of ODTMS and the absence of copolymerizable end groups results into Janus-like structures, that is, nanoparticles show a two-sides with different nature (polymer or inorganic). The low affinity between the ODTMS-functionalized catalytic nanoparticles (ceria and titania) and the polymer matrix promotes the minimization of the contact area between polymer and inorganic species. The phase segregation results into the agglomeration of the inorganic nanoparticles in one side. In the case of polystyrene-based systems **SC1** and **ST1**, the inorganic functionalities are mostly deposited on the polymer surface, as shown in Figures 4.5 and 4.7(a, d). The asymmetric morphology was maintained in the PMMA hybrids **MC1**, and **MT1**. For both ceria and titania species, inorganic agglomerates resulted partially embedded at one side of the polymer/water interface as observed in Figures 4.6 and 4.8(a, d). Nevertheless, the larger particle size and the 2D shape of titania nanorods compared with ceria nanoparticles lead to hybrid materials with greater polydispersity in terms of particle size and inorganic load per particle.

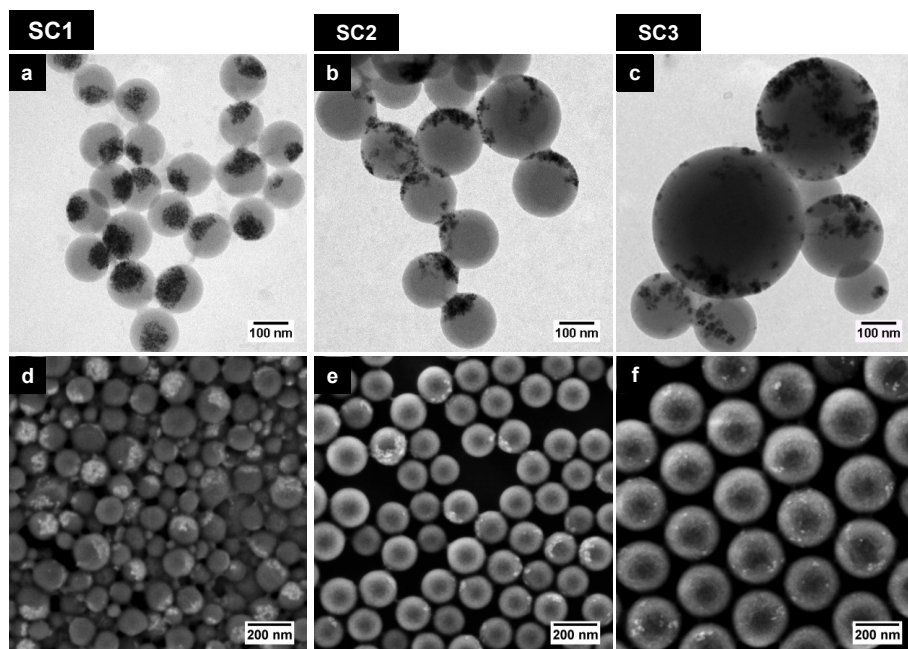


**Figure 4.5.** TEM and SEM micrographs of the polystyrene–based hybrid nanoparticles incorporating ceria nanoparticles functionalized with ODTMS (a, d), PTMS (b, e), and MPS (c, f).

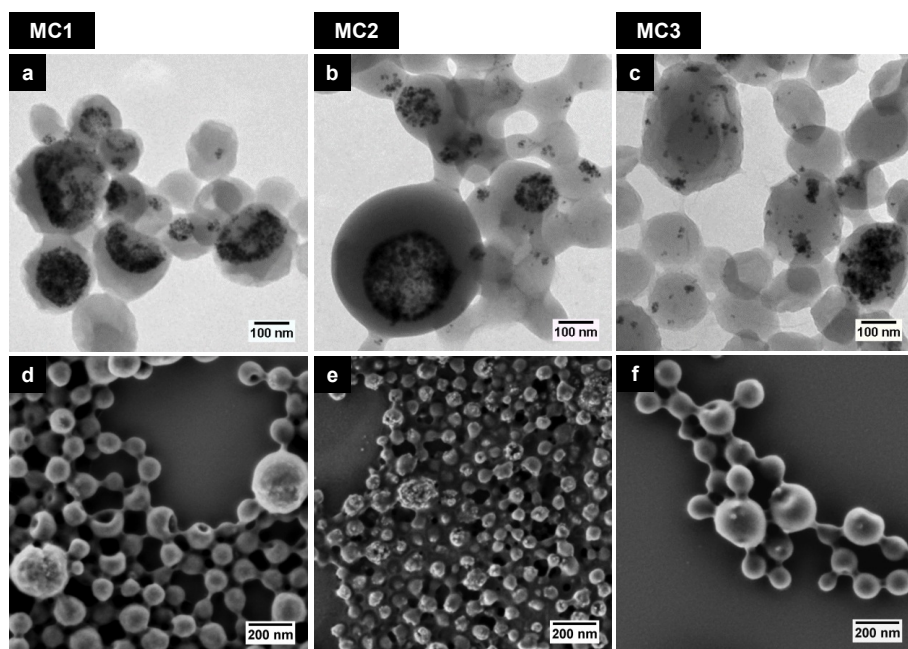


**Figure 4.6.** TEM and SEM micrographs of the PMMA–based hybrid nanoparticles incorporating ceria nanoparticles functionalized with ODTMS (a, d), PTMS (b, e), and MPS (c, f).

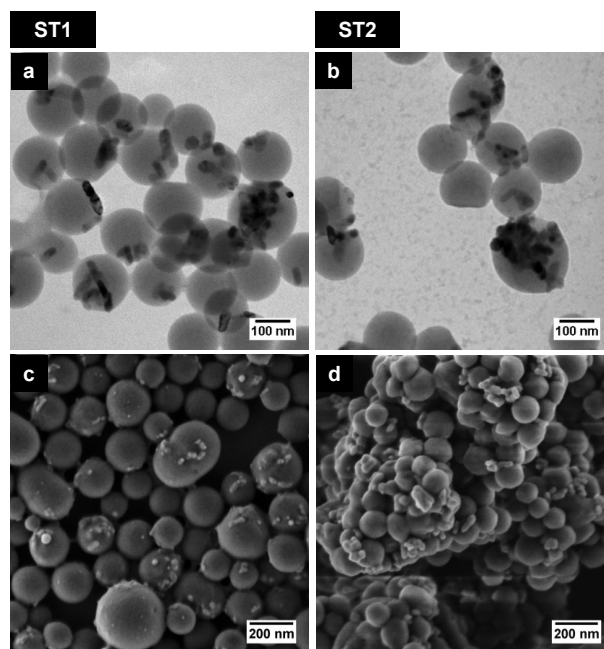


**Figure 4.7.** TEM and SEM micrographs of the polystyrene-based hybrid nanoparticles incorporating titania nanoparticles functionalized with ODTMS (a, d) and PTMS (b, e).

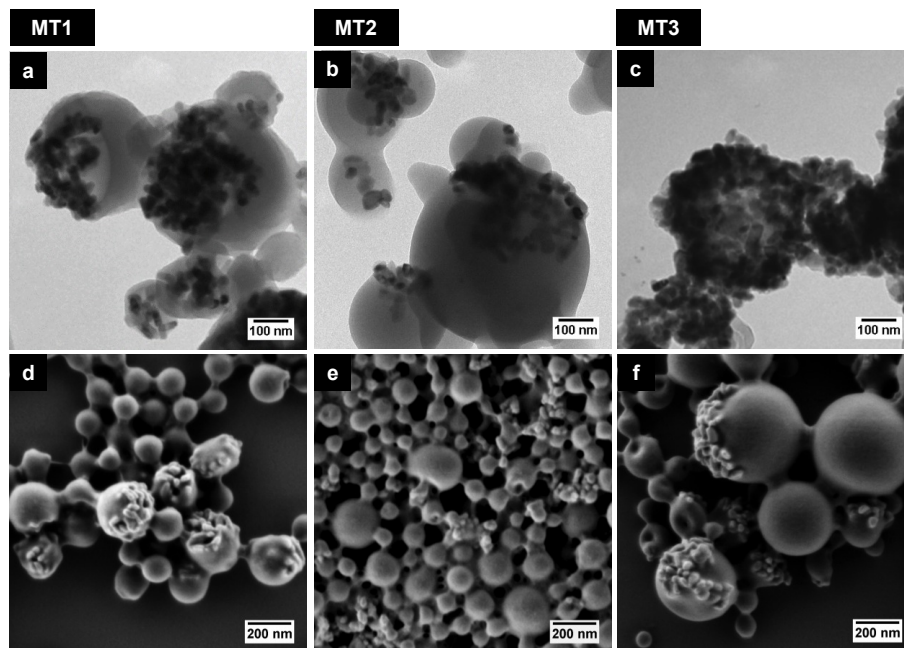


**Figure 4.8.** TEM and SEM micrographs of the PMMA-based hybrid nanoparticles incorporating titania nanoparticles functionalized with ODTMS (a, d), PTMS (b, e), and MPS (c, f).

Analogous morphologies to those obtained with ODTMS were observed when using in samples PTMS as a coupling agent with non-polymerizable alkyl chains. This result indicates that the development of the hybrid morphology is mostly governed by the (in)compatibility between the



monomer and the hydrophobized inorganic species. The shorter alkyl chains in PTMS in comparison with ODTMS increase the phase segregation process. Therefore, the inorganic nanoparticles remain aggregated in one side of the polymer surface, as shown in Figures 4.5, 4.6, 4.7, and 4.8(b, e) for **SC2**, **MC2**, **ST2**, and **MT2**, respectively.

In comparison with the previous silanes, MPS presents a methacrylic acid ester with the ability to copolymerize with surrounding monomers (e.g., MMA). The covalent bond between the inorganic species and the forming polymer matrix reduces the energetically preferred inorganic agglomeration and the phase segregation. Thus, a relatively homogeneous encapsulation of the inorganic component within the polymer matrix can be achieved,<sup>98,75</sup> as it was proven for sample **MC3** (PMMA–ceria nanoparticles), shown in Figure 4.6(c, f). The reduction of the inorganic aggregation and a more homogeneous distribution of the inorganic load were also achieved by using polystyrene, as observed in Figure 4.5(c, f) for sample **SC3**. Nevertheless, a greater exposition of the inorganic nanoparticles on the polystyrene surface is revealed. The incorporation of MPS-functionalized titania nanoparticles within the polystyrene matrix leads to the destabilization of the miniemulsion during the polymerization process. The lower efficiency of the hydrophobization of titania with MPS, together with the difficulties related to the size and morphology of the inorganic species hindered its incorporation. The balance between the entrapment and the inorganic aggregation resulted into the partial encapsulation of titania within PMMA in **MT3**, as observed in Figure 4.8(c, f).

### **4.3 Influence of the Initiator over the Morphology of the Polymer–Metal Oxide Hybrid Nanoparticles Prepared by Miniemulsion Polymerization**

Heterophase polymerization processes are mainly governed by three different mechanisms: droplet, homogeneous, and micellar nucleation. In an ideal miniemulsion polymerization process, performed below the critical micelle concentration (cmc) of the surfactant, the micellar nucleation is ideally suppressed. When highly hydrophobic monomers and initiators are used, droplet nucleation predominates. The initiator present in each single droplet initiates the generation of radicals reacting with the monomer molecules. However, homogeneous nucleation in the aqueous phase might also occur and gain relevance, depending on the concentration of the initiator and, mostly, on the solubility of both the monomer and the initiator in the aqueous phase. As explained in section 2.2, the nature and the type of initiator are parameters governing the development of hybrid morphologies. Therefore, the effect of the initiator over the hybrid morphology was studied



for the incorporation of ODTMS-functionalized ceria nanoparticles within polystyrene and titania within PMMA. In the previous section (4.2), the corresponding materials **SC1** and **MC1**, achieved using AIBN as a free-radical initiator, offered the better results in terms of inorganic load and defined morphology, at expenses of the reduction of the yield of the synthesis. For comparison, 2,2'-azobis-(2-methylbutyronitrile) (AMBN) and potassium peroxydisulfate (KPS) were used as initiators with different polarity respect to AIBN, leading to the respective hybrids named as **SC4**, **SC5**, and **MT4**, **MT5**. The synthetic conditions and the characterization of the resulting materials are described in Table 4.2. The concentration and the type of initiator and the polarity of the monomer would determine the nucleation and heterophase polymerization process. In addition, the polymerization temperature will increase or decrease the rate of formation of radicals, the polymerization reaction, and the termination step. The conditions of polymerization were established based on the temperature of formation of radicals specific for each initiator. To avoid high rates of generation of radicals, problems of colloidal stability, or low monomer conversions, the reactions using AIBN were performed at 72 °C. In the case of the processes initiated with AIBN or KPS, the polymerization was driven at 65 °C. The presence of inorganic nanoparticles and, consequently, the differences in droplet sizes could influence the polymerization rate. However, in a similar synthetic context to the one considered in this chapter, the presence of MPS- and ODTMS-functionalized silica nanoparticles did not greatly affect the polymerization kinetics of MMA.<sup>13</sup>

**Table 4.2.** Synthetic details and material features of polymer–metal oxide hybrid nanoparticles incorporating ODTMS-functionalized catalytic species, prepared with different initiators and polymerization temperatures.

Sample	Monomer	Inorganic Component	Coupling Agent	Initiator	<i>T</i> / °C	<i>d</i> <sup>a</sup> / n	Solid Content <sup>b</sup> / wt. %
<b>SC1</b>	S	CeO <sub>2</sub>	ODTMS	AIBN	65	160 ± 40	20.0
<b>SC4</b>	S	CeO <sub>2</sub>	ODTMS	AMBN	72	160 ± 50	19.0
<b>SC5</b>	S	CeO <sub>2</sub>	ODTMS	KPS	65	380 ± 70	12.3
<b>MT1</b>	MMA	TiO <sub>2</sub>	ODTMS	AIBN	65	200 ± 70	15.4
<b>MT4</b>	MMA	TiO <sub>2</sub>	ODTMS	AMBN	72	170 ± 50	19.0
<b>MT5</b>	MMA	TiO <sub>2</sub>	ODTMS	KPS	65	360 ± 60	10.0

<sup>a</sup> Determined by DLS before purification.

<sup>b</sup> Solid content determined before purification.

The oil-soluble initiators offer analogue results in terms of particle size and solid contents, close to the theoretical values around 20 wt.%. The use of KPS as a water-soluble initiator promoting the homogeneous nucleation leads to the formation of more coagulum and to an increase of the average particle size. The thermographs shown in Figure 4.9 for polystyrene–ceria nanoparticles (samples

SC1, SC4, and SC5) reveal the lower incorporation of ceria achieved with KPS (10 wt.%) in comparison with AIBN and AMBN (with a load about 30 wt.%).

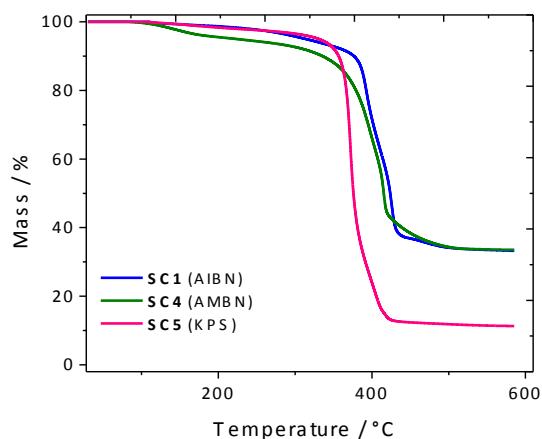


**Figure 4.9.** TGA curves obtained for the polystyrene–ceria hybrid nanoparticles SC1 (blue line), SC4 (green line), and SC5 (magenta line) prepared by miniemulsion polymerization using AIBN, AMBN, and KPS as free-radical initiators, respectively.

With regard to the morphology of the hybrids, Janus-like structures were achieved for all polymer–inorganic materials, as observed in the TEM micrographs of Figure 4.10. These results highlight the dominance of the inorganic surface functionality as controlling parameter over the role of the initiator.

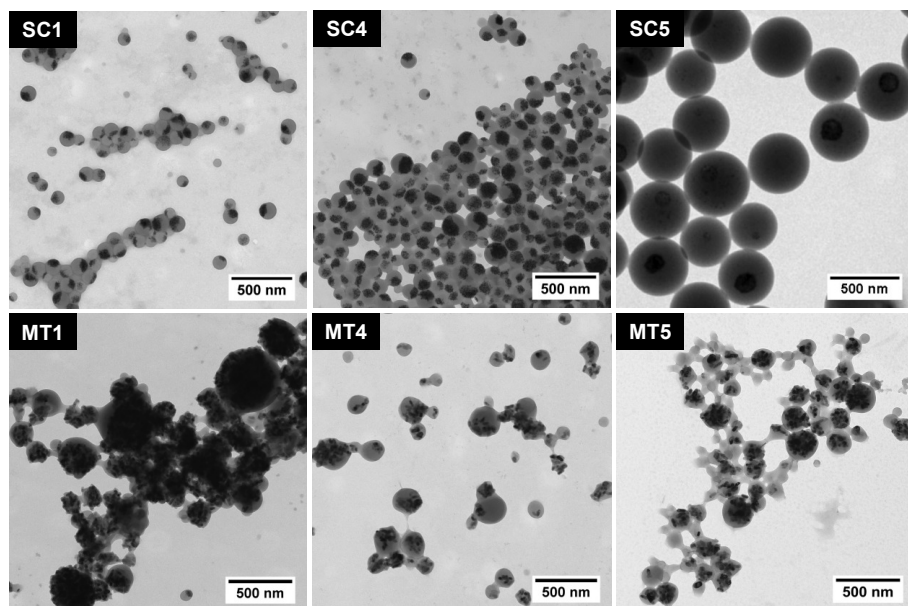


**Figure 4.10.** TEM micrographs of the polystyrene with ODTMS-functionalized ceria (SC1, SC4, and SC5) and PMMA with ODTMS-functionalized titania (MT1, MT4, and MT5) hybrid nanoparticles, prepared by miniemulsion polymerization using AIBN, AMBN, and KPS as free-radical initiators respectively.

## 4.4 Preparation of Multifunctional Polymer–Metal Oxide Hybrid Nanoparticles

The control over the morphology development of polymer–metal oxide hybrid nanoparticles was further extended to the preparation of a second generation of multifunctional materials via the combination of two inorganic species with complementary functionalities (magnetic and catalytic) and different surface functionalization. Aiming for the development of magnetically recoverable heterogeneous nanocatalysts, structures with a catalytically active surface and a magnetoreponsive inorganic component within the supporting polymer matrix were conceived. Based on the results discussed in section 4.2, ODTMS-functionalized catalytic species (ceria and titania) were incorporated within polystyrene and PMMA matrices by miniemulsion polymerization. The synthesis was combined simultaneously with the fixation of MPS-functionalized magnetite nanoparticles, which incorporated the magnetic functionality within the polymer matrix. Table 4.3 presents the polymer and inorganic composition, the surface functionalization of the catalytic and magnetic species, and the particle size of the multifunctional hybrid materials studied in this section. The systems of polystyrene–magnetite incorporating ceria and titania are named as **SF1** and **SF2**, respectively. Analogously, the samples of PMMA with ceria and titania are designed as **MF1** and **MF2**, respectively.

**Table 4.3.** Material composition and particle size of multifunctional polymer–metal oxide hybrid nanoparticles incorporating catalytic and magnetic species with specific surface functionalization.

Sample	Monomer	Inorganic Component 1	Coupling Agent 1	Inorganic Component 2	Coupling Agent 2	$d^a$ / nm
<b>SF1</b>	S	CeO <sub>2</sub>	ODTMS	Fe <sub>3</sub> O <sub>4</sub>	MPS	100 ± 50
<b>SF2</b>	MMA	CeO <sub>2</sub>	ODTMS	Fe <sub>3</sub> O <sub>4</sub>	MPS	140 ± 60
<b>MF1</b>	S	TiO <sub>2</sub>	ODTMS	Fe <sub>3</sub> O <sub>4</sub>	MPS	150 ± 60
<b>MF2</b>	MMA	TiO <sub>2</sub>	ODTMS	Fe <sub>3</sub> O <sub>4</sub>	MPS	170 ± 70

<sup>a</sup> Determined by DLS before purification.

The multifunctional polymer–metal oxide nanoparticles cannot be directly compared with the hybrid structures from section 4.2 (with only one catalytic species) because the corresponding synthetic processes are not equivalent. Nevertheless, both systems present similar trends in morphology and material properties. In this case, the inorganic components (MPS-functionalized magnetite and ODTMS-functionalized ceria or titania nanoparticles) were incorporated as 10 wt.% with respect to the organic phase. Particle size of the multifunctional hybrids ranges from 100 to 200 nm, and slightly bigger particle sizes are observed for structures containing MMA and titania. The higher ratio of the surfactant concentration and the disperse phase with respect to the

formulation used in section 4.2 leads to smaller multifunctional nanoparticles compared to the previous ones.

The incorporation of a magnetoresponse species allowed the magnetic purification (and thus fractioning) of the samples. Table 4.4 presents the main features of the multifunctional hybrid nanoparticles (**SF1**, **SF2**, **MF1**, and **MF2**) before and after purification. The solid content determined after polymerization (8–9 wt.%) is close to the theoretical value (10 wt.%), which is a good hint of the nearly complete conversion of the monomer. The solid content remaining after the magnetic purification reveals a similar efficiency of the method for the encapsulation of magnetite despite the presence of a second inorganic component.

The load of catalytic and magnetoresponse inorganic species was determined by inductively coupled plasma mass spectrometry (ICP-MS). The magnetic purification offered an increase of the content of magnetite from 2–5 wt.% to 40 wt.%. The technique revealed the different partition of the inorganic species. In this sense, there is a segregation between ceria and magnetite systems, which are mostly incorporated in different polystyrene-based nanoparticles. Both the catalytic and magnetic functionalities are simultaneously embedded within PMMA particles. PMMA allows the best encapsulation for the MPS-functionalized magnetite, which is not hindered by the presence of ceria nanoparticles. The incorporation titania nanoparticles leads to a lower load of magnetite, both for polystyrene or PMMA matrices. The magnetic content was increased in a factor of 30 with the purification process, whereas the titania content raised only in a factor of 3.

**Table 4.4.** Main features of the multifunctional polymer–metal oxide hybrid nanoparticles before and after magnetic purification.

Sample	Before purification			After purification		
	Solid Content / wt. %	Catalyst Load <sup>a</sup> / wt.%	Fe <sub>3</sub> O <sub>4</sub> Load <sup>a</sup> / wt.%	Solid Content / wt. %	Catalyst Load <sup>b</sup> / wt.%	Fe <sub>3</sub> O <sub>4</sub> Load <sup>b</sup> / wt.%
<b>SF1</b>	8.6	1.92 ± 0.05	2.02 ± 0.02	0.14	1.5 ± 0.5	45.3 ± 0.2
<b>SF2</b>	8.9	2.09 ± 0.05	1.595 ± 0.008	0.15	4.15 ± 0.09	37.5 ± 0.3
<b>MF1</b>	7.7	3.36 ± 0.06	4.87 ± 0.03	0.13	28.9 ± 0.3	39.3 ± 0.6
<b>MF2</b>	8.6	3.52 ± 0.02	1.69 ± 0.06	0.15	9.81 ± 0.02	37.5 ± 0.6

<sup>a</sup> Determined by ICP-MS before purification.

<sup>b</sup> Determined by ICP-MS after purification.

The morphology of the magnetoresponse and catalytically active hybrid nanoparticles collected after purification was elucidated by SEM and TEM. The corresponding micrographs, presented in Figure 4.11, evidence the absence of a significant competition in the migration of the different inorganic species with specific surface functionalization within the polymer matrix. The similarities on contrast, size, and morphology between ceria and magnetite species make difficult the specific

identification of the species, which seems easier in the case of the titania. MPS-functionalized species tend to be homogeneously distributed within the polymer, whereas ODTMS-hydrophobized species form aggregates close to the polymer surface. Nevertheless, the hybrid nanoparticles present an irregular shape as a consequence of the incorporation of the inorganic components.

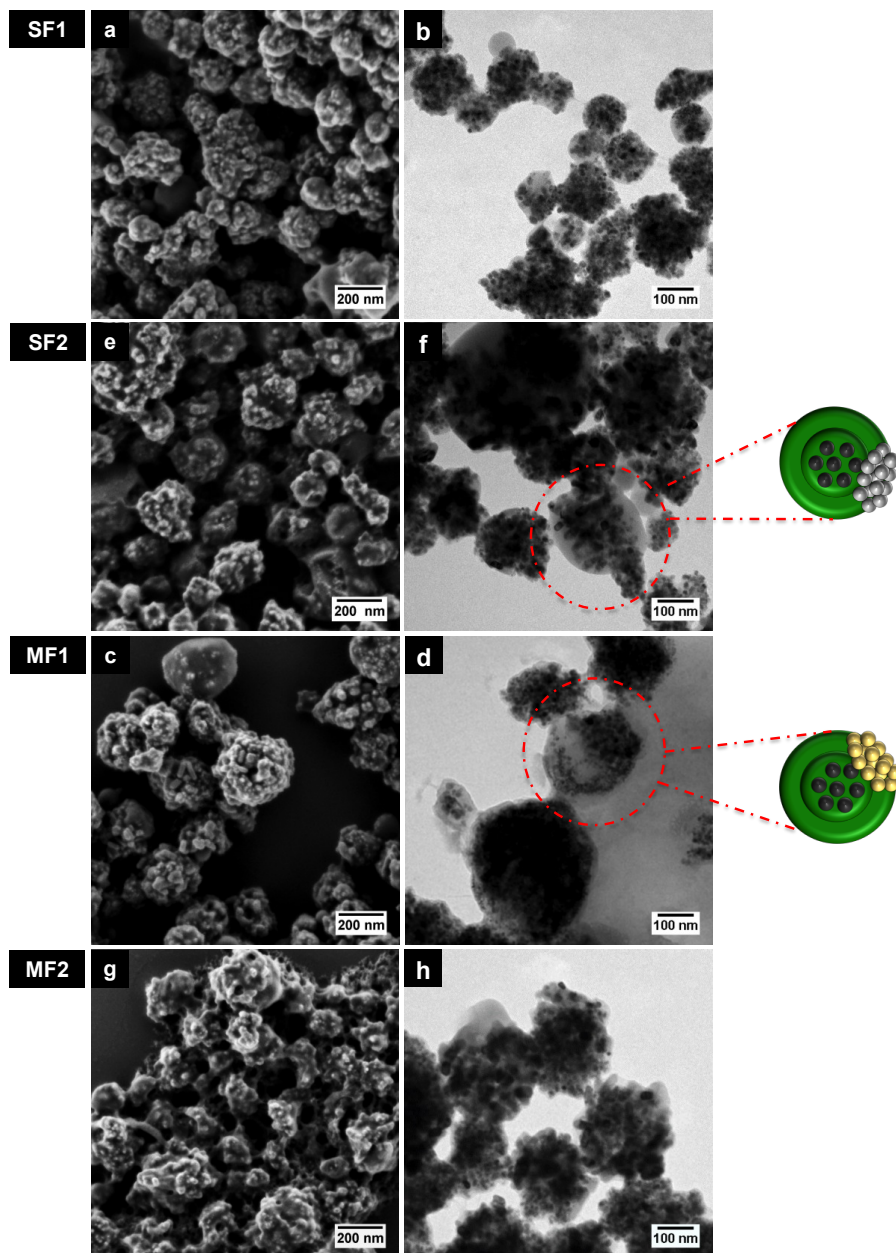


**Figure 4.11.** SEM and TEM micrographs of the multifunctional nanoparticles **SF1** (a, b), **SF2** (c, d), **MF1** (e, f), and **MF2** (g, h).

## 4.5 Conclusions

The versatility of miniemulsion polymerization for the synthesis of polymer–metal oxide hybrid nanoparticles with controlled morphology was proven for different polymer matrices, inorganic supports, and hybrid structures. The relevance of the surface chemistry between the polymer and the inorganic species was highlighted over other miniemulsion parameters (i.e., the type of initiator) governing the energy balance of the hybrid structure. Therefore, inorganic surface functionalization was identified as the driving force of morphology development. The use of silanes with inert alkyl chains (e.g., ODTMS and PTMS) leads to the agglomeration or the deposition of the inorganic components on the polymer surface, and formation of Janus-like structures. The presence of vinyl copolymerizable end groups in the functionalizing agent (e.g., MPS) compatibilizes the inorganic surface with the surrounding monomer (e.g., MMA). In the absence of shape or size hindrance, the copolymerization between the monomer and the coupling agent results into the inorganic distribution or embedment within the polymer matrix. The purification of the dispersion of nanoparticles allowed the fractioning of the sample. The fraction of the particles recovered showed an increased inorganic load homogeneously distributed within the sample, at expenses of the decrease of the solid content and production efficiency. The strategy was extended towards the preparation of multifunctional hybrid combining two metal oxides with catalytic and magnetic properties. The specific surface functionalization of inorganic species was addressed in order to control the accessibility of their functionalities. The synthesis of PMMA with a magnetic component distributed within the polymer matrix and catalytic species agglomerated on one side of the hybrid was achieved by combining the functionalization of magnetite and ceria nanoparticles with MPS and ODTMS, respectively. The synthetic strategy could be useful for the preparation of magnetically recoverable particles with applicability in catalysis and photocatalysis. The asymmetry of the particles could be interesting to achieve a self-assembly of the hybrid between two reactive media or to guarantee the accessibility to substrates of specific polarity.

# 5 Magnetically Enhanced Polymer-Supported Ceria Nanocatalysts

This chapter presents the preparation of two types of polystyrene-supported ceria nanoparticles specifically designed for heterogeneous catalysis, taking the hydration reaction of 2-cyanopyridine to 2-picolinamide in aqueous media as a model reaction.

The control achieved in the development of hybrid morphologies described in Chapter 4 is applied for the simultaneous incorporation of magnetoresponsive and catalytic species with a controlled accessibility on a polymer support. The presence of magnetite allows the recyclability of the catalyst with the application of an external magnetic field. The performances of the catalysts prepared by multi-step processes of miniemulsion polymerization and in-situ crystallization (described in section 2.6.3) is compared with the efficiencies offered by easily scalable and straightforward Pickering miniemulsion polymerization processes (from section 2.6.2).

## 5.1 State of the Art of the Preparation of Magneto-responsive Polymer-Supported Nanoparticles for Heterogeneous Catalysis

The production of amides via the hydrolysis of nitriles has a great relevance due to the high value of the product for pharmacological and other chemical industrial processes.<sup>145-146</sup> The hydrolysis of nitriles has been traditionally performed under harsh acidic and basic conditions, which often resulted into the over-hydrolysis of the amides to carboxylic acids and the requirement of purification due to the great amount of salt generated during a final neutralization step.<sup>147</sup>

The homogenous catalysis of the hydration of nitriles under neutral conditions has been reported using Pt(II),<sup>148</sup> Ru(II),<sup>147</sup> Co(III),<sup>149</sup> or Mo(IV)<sup>150</sup> complexes. The strategies commonly deal with difficulties related to the recovery of the catalyst, purity of the product, high prizes, use of organic solvents, or low conversions due to the strong coordination of heteroaromatic nitriles to the metal centers. The selective hydration of nitriles in water under mild conditions was also reached using recoverable heterogeneous catalyst such as Ru(OH)<sub>3</sub> supported in alumina,<sup>151</sup> MnO<sub>2</sub>,<sup>152-10</sup> or CeO<sub>2</sub>.<sup>10, 153</sup>

Metals and metal oxides are well-known heterogeneous catalysts. Among them, cerium(IV) oxide (also referred to as ceria) presents an interesting combination of acid–base properties and redox

activity between the couple Ce(IV)/Ce(III),<sup>154</sup> which makes it suitable for the catalysis of a wide range of organic reactions.<sup>155</sup> Substitution reactions, such as alkylation of aromatic compounds,<sup>156</sup> dehydration and dehydrogenation of alcohols,<sup>157</sup> ketonization of esters,<sup>158</sup> aldehydes,<sup>159</sup> and carboxylic acids;<sup>160</sup> reduction of carboxylic acids<sup>53</sup> or oxidation of organic components,<sup>161-162</sup> and hydrolysis reactions<sup>163</sup> are catalyzed by ceria nanoparticles. Furthermore, the application of the metal oxide is being extended to other energy-related and green chemistry applications (e.g., fuel cells, reforming of hydrocarbons or oxygenated compounds, water splitting and photocatalysis, or oxidation of volatile compounds).<sup>164</sup> The scope of the reactions catalyzed by ceria can be enlarged with the incorporation of other noble metals (e.g., Au)<sup>161</sup> or metal oxides (e.g., ZnO, MnO<sub>x</sub>, MoO<sub>4</sub>, or ZrO<sub>2</sub>),<sup>164</sup> or with the modification of the reaction media and the subsequent alteration of the acid–base and redox properties. Specifically for the case of the hydration of nitriles with a heteroatom (N or O) adjacent to the  $\alpha$ -carbon of the CN group, cerium(IV) oxide nanoparticles present an outstanding catalytic efficiency.<sup>153</sup> Nevertheless, as other metal oxides, nanocatalysts suffer from problems of dispersion and tendency to aggregation, with the subsequent reduction of the active surface, and difficult recovery and recyclability. In this context, polymer-supported metal or metal oxide hybrid catalysts emerged as a solution that provides chemical and mechanical stability to the inorganic catalytic species.

Supported catalytic structures favor the recoverability and recycling of the catalysts by physical methods (for instance by centrifugation).<sup>6,164-166</sup> In this fashion, hybrid nanocatalysts with high efficiencies in the hydration reaction of 2-cyanopyridine<sup>6,164</sup> were prepared by in-situ crystallization of ceria on the functional surface of polymer nanoparticles preformed by miniemulsion copolymerization of styrene with commercial monomers or synthetic surfmers.<sup>148</sup> Similarly, polystyrene–cadmium sulfide hybrid nanoparticles were prepared incorporating magnetite nanoparticles, which were homogeneously encapsulated within the organic matrix during the polymerization process.<sup>47</sup> Although the last case aimed no catalytic purposes, it provides a promising strategy for the preparation of magnetoresponsive catalysts. Compared to the separation of the catalyst by centrifugation, a magnetic recovery presents a great advance in terms of simplicity, energy consumption and softness of the treatment. For this reason, the development of magnetically separable catalysts has been spotlighted during the last decade.<sup>165-169</sup>

The in-situ crystallization method offers high efficiency in terms of surface functionalization and inorganic deposition,<sup>7</sup> but it requires two or three steps for the synthesis of the inorganic and the polymer nanoparticles, and in certain cases, the surfmer. Multistep processes present greater drawbacks in the scale-up of the process to industrial levels. In contrast, the so-called all in-situ



strategies<sup>2</sup> are promising and challenging alternatives for the straightforward preparation of magnetically recoverable nanocatalysts. Furthermore, colloidal polymerization processes in Pickering miniemulsions (described in section 2.6.2) allow the immobilization of catalytic species on a polymer support without the requirement of conventional surfactants. The Pickering miniemulsion polymerization strategy was used for the preparation of polymer-supported catalysts using multiple inorganic stabilizers (e.g.,  $\text{TiO}_2$ ,<sup>170</sup>  $\text{Fe}_3\text{O}_4$ ,<sup>171</sup> Pd and Pd on metal frameworks,<sup>172</sup> Au<sup>173</sup>, Ag, or Pt<sup>174</sup>). Ceria nanoparticles were proven to be efficient inorganic stabilizers for the miniemulsion polymerization of different acrylic monomers (MMA and BA co-polymerized with MA),<sup>121</sup> demonstrating the potential of the strategy for the preparation of polymer-supported ceria catalysts. The strategy allows the selective incorporation of different inorganic functionalities (i.e., magnetic components in the core and catalytic species accessible on the polymer surface), whose accessibility can be controlled by tuning the hydrophobicity and the surface chemistry of the metal oxide nanoparticles.<sup>98-95</sup> Bonnefond et al.<sup>120</sup> combined the immobilization of titania via Pickering stabilization on the surface of polystyrene nanoparticles with the simultaneous encapsulation of magnetite nanoparticles for the preparation of magnetically recoverable photocatalyst.

The following sections describe the synthesis of two types of magnetoresponsive polystyrene-supported ceria nanoparticles. The hybrids were used for the heterogeneous catalysis of the hydration reaction hydration of 2-cyanopyridine to 2-picolinamide.

## 5.2 Synthesis and Functionalization of Inorganic Nanoparticles

Both the catalytically active (ceria) and the magnetic (magnetite) nanoparticles were synthesized by (co)precipitation methods using the corresponding metal precursor salts and a base (ammonia or sodium hydroxide) as a precipitating agent. The control of the accessibility of the inorganic functionalities within the supporting polymer (i.e., the magnetic component within the polymer core and the catalytic species at the surface) was addressed via the surface functionalization of either the polymer or the inorganic nanoparticles. Ceria nanoparticles required no further post-functionalization for their effective migration to the polymer surface. As reported by Schoth et al.,<sup>98</sup> an alkoxy silane component with a short alkyl chain and a copolymerizable end group (MPS) allowed the homogeneous encapsulation of magnetite nanoparticles within the polymer matrix. Not only the hydrophobicity but also the surface chemistry of the magnetic nanoparticles has a great influence on the migration of the inorganic component within the supporting polymer. In this sense,

the copolymerization of the methacrylate group of MPS with styrene allowed the entrapment of the magnetite within the forming polymer matrix during a miniemulsion polymerization process.

### 5.3 Preparation of Polystyrene-Supported Ceria Nanoparticles

Polystyrene-supported ceria nanocatalysts incorporating a magnetic core were synthesized by two alternative routes labeled as **P1** and **P2**:

- Route **P1** is based on Pickering miniemulsion polymerization processes, described in section 2.6.2, using ceria nanoparticles as an inorganic stabilizer.
- Route **P2** is a multi-step route consisting of miniemulsion polymerization and further in-situ crystallization of ceria nanoparticles on the preformed polymer surface, as described in section 2.6.3.

From a synthetic point of view, the in-situ crystallization strategy is not trivial; it has many parameters to be controlled, it involves multiple steps (i.e., miniemulsion polymerization, dialysis, and inorganic crystallization), and it demands a high consumption of time and resources. In comparison, the Pickering miniemulsion process is straightforward, and it minimizes the use of resources and time. The main features of the different types of nanoparticles prepared by routes **P1** and **P2** are listed in Table 5.1. The table includes polystyrene-supported ceria nanoparticles (**C1** and **C5**), magnetically active polystyrene-supported ceria nanoparticles (**C2** and **C6**), non-catalytic polymer nanoparticles with (**C4**) and without (**C3**) a magnetic core, and unsupported ceria nanoparticles (**C0**), which were crystallized in bulk for comparison purposes.

**Table 5.1.** Characteristics of the nanoparticles prepared by different synthetic strategies: material composition, particle diameter ( $d$ ), and inorganic (ceria and magnetite) content.

Catalyst	Synthetic Route	Polymer Matrix <sup>a</sup>	Inorganic Components	$d^b$ / nm	Inorganic Content <sup>c</sup> / wt.%	
					CeO <sub>2</sub>	Fe <sub>3</sub> O <sub>4</sub>
<b>C0</b>	–	–	CeO <sub>2</sub>	–	100	–
<b>C1</b>	<b>P1</b>	PS	CeO <sub>2</sub>	480 ± 150	11.5 <sup>c</sup>	–
<b>C2</b>	<b>P1</b>	PS	CeO <sub>2</sub> and Fe <sub>3</sub> O <sub>4</sub>	360 ± 150	10.6 <sup>c</sup>	9.0 <sup>c</sup>
<b>C3</b>	<b>P2</b>	P(S/AA)	–	80 ± 20	–	–
<b>C4</b>	<b>P2</b>	P(S/AA)	Fe <sub>3</sub> O <sub>4</sub>	260 ± 70	–	23.5
<b>C5</b>	<b>P2</b>	P(S/AA)	CeO <sub>2</sub>	90 ± 20	18.9	–
<b>C6</b>	<b>P2</b>	P(S/AA)	CeO <sub>2</sub> and Fe <sub>3</sub> O <sub>4</sub>	260 ± 90	17.1	15.5

<sup>a</sup> S: Styrene, AA: Acrylic acid.

<sup>b</sup> Determined by statistical treatment of TEM images accounting at least 200 nanoparticles.

<sup>c</sup> Determined by TGA or ICP-MS. Refer to Chapter 9 for details.

The Pickering miniemulsion strategy (**P1**) allows the substitution of conventional organic surfactants by functional inorganic nanoparticles that remain irreversibly adsorbed at the droplet interface. The inorganic stabilization ability is determined by the relative wettability of the particles between the liquid phases of the miniemulsion. In this case, the hydrophilic ceria nanoparticles were directly used after being crystallized in bulk solution, and allowed the colloidal stabilization of a direct miniemulsion with styrene and magnetite in the disperse phase. After a free-radical miniemulsion polymerization process using a combination of an oil-soluble (AIBN) and a water-soluble (KPS) initiator, the catalytically active nanoparticles remained at the surface of polystyrene nanoparticles with (**C2**) and without (**C1**) a magnetic core.

The in-situ crystallization strategy (**P2**) has been previously employed for the preparation of polymer-supported hybrid catalysts with great inorganic coverage and catalytic performances.<sup>1,98</sup> In this case, the methodology was extended towards the encapsulation of MPS-functionalized magnetite nanoparticles for purification purposes. The efficiency of the crystallization process relies on the affinity between the surface-functionalized polystyrene nanoparticles and the cerium ions introduced by the addition of a precursor salt. For this aim, styrene (S) was copolymerized with a hydrophilic comonomer, acrylic acid (AA), which led to the incorporation of carboxylic groups accessible on the surface of the polymer nanoparticles.<sup>175</sup> The resulting poly(styrene-co-acrylic acid) (P(S-AA)) nanoparticles, with (**C4**) and without (**C3**) magnetite, were used as polymer supports for the preparation of samples **C6** and **C5**, respectively.

Particle suspensions were dialyzed to eliminate the excess of surfactant, which may affect the complexation of cerium ions, the crystallization of ceria, and the adsorption of the substrates during catalytic applications. The presence of charged groups at the surface was confirmed by polyelectrolyte titration with an oppositely charged polyelectrolyte (poly-DADMAC) reaching a value of 1.6 groups/nm<sup>2</sup> for sample **C4** after dialysis. This result is close to the value of 1.2 groups/nm<sup>2</sup> reported by Mari et al.<sup>6</sup> for nanoparticles similar to system **C3**, and it reveals the success of the copolymerization process despite the incorporation of magnetite. The presence of carboxylic groups at the surface of the polymer particles allows the complexation of the cerium cations. The controlled addition of a precipitating base (sodium hydroxide) results into the crystallization of ceria nanoparticles on the polymer surface. The presence of crystalline ceria nanoparticles on sample **C5** and the integrity of the MPS-functionalized magnetite within the multifunctional nanoparticles **C6** were proven by XRD (diffractograms shown in Figure 5.1). The diffraction patterns observed in the ceria nanoparticles prepared by bulk crystallization, as well as in the samples **C5** and **C6**, corresponds with the cerium oxide cerianite, whose reference pattern

(ICDD card no. 00-043-1002) is presented with the turquoise dashed lines in vertical. In addition, the catalyst **C6** presents the diffractions related to the experimental pattern of MPS-functionalized magnetite (blue dashed lines). The presence of the polymer (in **C5** and **C6**) and the functionalizing agent (i.e., MPS) attached to the magnetic particles justifies the amorphous halo shown in the diffractograms.

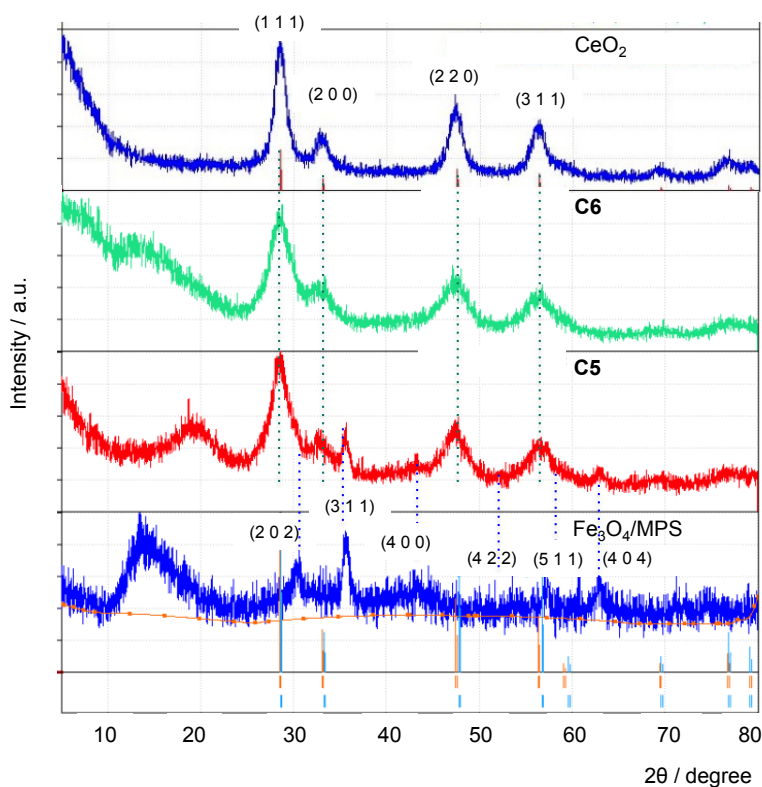


**Figure 5.1.** X-ray diffraction (XRD) patterns of ceria and MPS-functionalized magnetite nanoparticles, and catalysts **C5** and **C6**.

The specific surface area determined using Brunauer–Emmett–Teller (BET) isotherms obtained by nitrogen adsorption measurements revealed values of around 117 and 90 for **C0** and **C2**, respectively.

The TGA thermographs corresponding to samples **C3**, **C4**, **C5** and **C6**, from Figure 5.2, were used to determine the catalytic and the magnetic loads, reported in Table 5.1. In addition, the figure shows the TGA traces of MPS-functionalized magnetite nanoparticles ( $\text{Fe}_3\text{O}_4/\text{MPS}$ , green line), after several washing operations. The mass loss (25 wt.%) is related to the amount of coupling agent covalently attached to the magnetite nanoparticles. The fraction (2 wt.%) of mass from the polymer sample **C3** remaining after the thermal treatment (the residual C) was used for correction

purposes. The inorganic incorporation is compared with the corresponding results achieved in Pickering miniemulsions (i.e., route **P1**). The general trend indicates better efficiencies of encapsulation of magnetite and deposition of ceria nanoparticles allowed by the in-situ crystallization strategy (i.e., route **P2**).

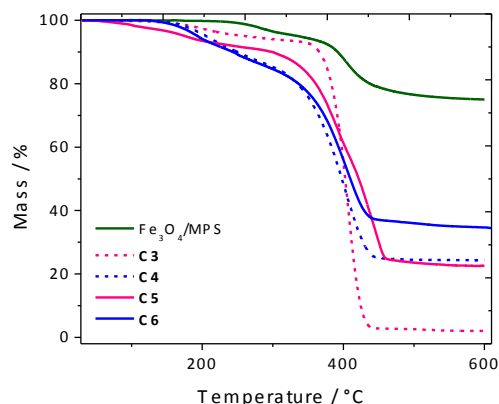


**Figure 5.2.** Thermographs of MPS-functionalized magnetite nanoparticles (green line), catalysts **C3** (magenta dashed line), **C4** (blue dashed line), **C5** (magenta line), and **C6** (blue line).

The hybrid catalysts **C1**, **C2**, **C5**, and **C6** present differences on polydispersity, particle size, and catalytic coverage. Particle size increases when magnetite is encapsulated and when ceria nanoparticles are used to promote the colloidal stabilization instead of SDS. As observed in the SEM and TEM images of Figure 5.3, the specific characteristics of the hybrids are related to the routes **P1** and **P2** used for their preparation. In general, the surface deposition of the inorganic species is observed by TEM in the form of a darker corona surrounding the polymer nanoparticles. Figure 5.3(c) proves the distribution of the ceria nanoparticles forming tinny aggregates on the polymer surface of sample **C1**. The similarity in size and morphology between the particles of magnetite and ceria makes very difficult the observation of the specific arrangement of each species in the case of the catalysts **C2** prepared by Pickering miniemulsion polymerization (Figure 5.3(f)).

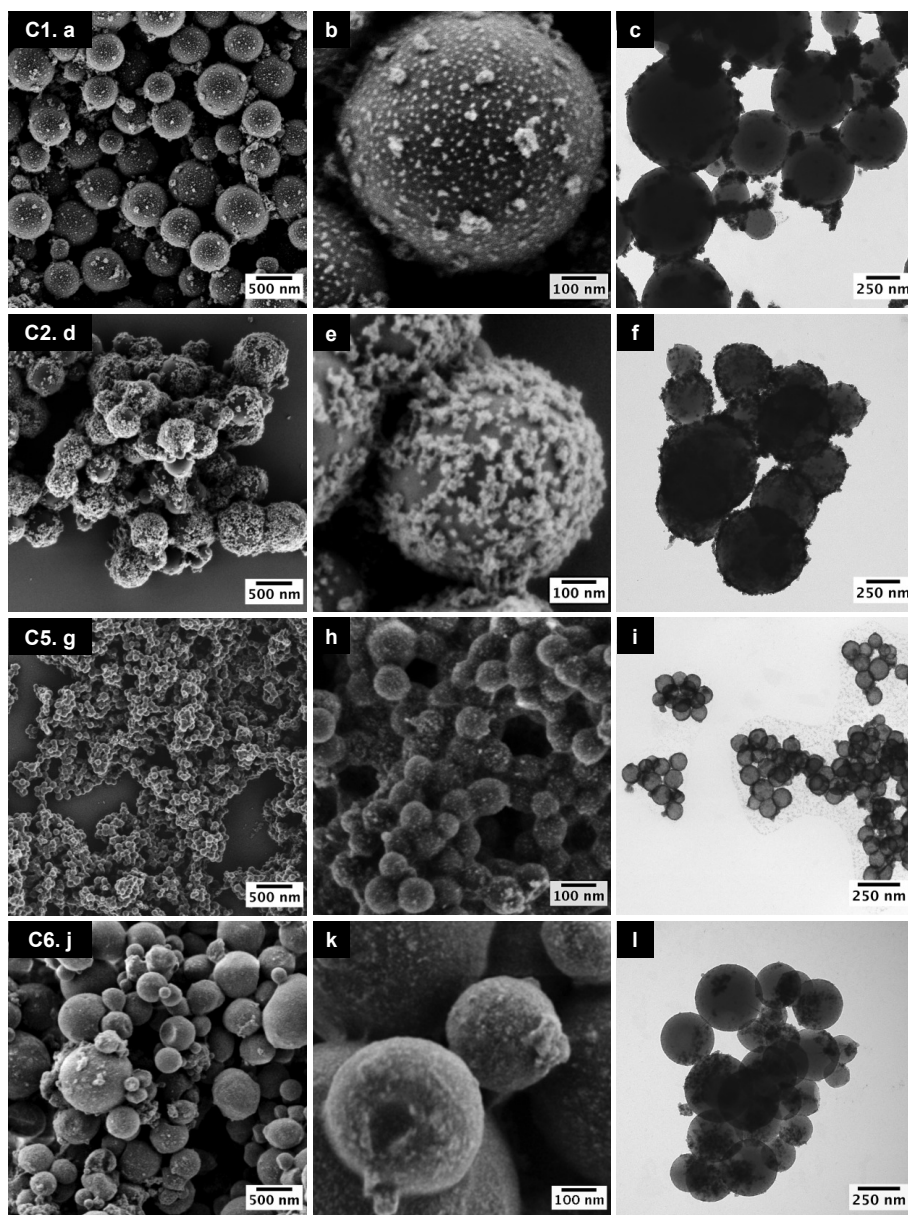


**Figure 5.3.** SEM micrographs at two different magnifications (a, d, g, j) and (b, e, h, k), and TEM (c, f, i, l) images of the polystyrene-supported ceria catalysts **C1** (a, b, c) and **C5** (g, h, i) prepared via routes **P1** and **P2**, respectively. Analogue images of the corresponding samples **C2** (d, e, f) and **C6** (g, h, i), incorporating a magnetic core.

The arrangement of the catalytic and magnetic species in the catalysts prepared by the route **P1** was identified by comparison of TEM and SEM images of samples **C4** and **C6** shown in Figure 5.4 and 5.3(j–l), respectively. Although the encapsulation of magnetite cannot be confirmed nor excluded from the SEM images of sample **C4**, the dark spots observed in the corresponding TEM micrograph (Figure 5.4(a)) reveal the presence of magnetite within the polymer matrix. Thus, a “quasi-encapsulation” of magnetite in samples **C4** and **C6** was assumed.

The characterization of samples **C5** and **C6** by electronic microscopy, shown in Figure 5.3(g–l), highlights the homogeneous coverage of the polymer surface with fine and crystalline ceria nanoparticles achieved after the crystallization step of route **P2**.

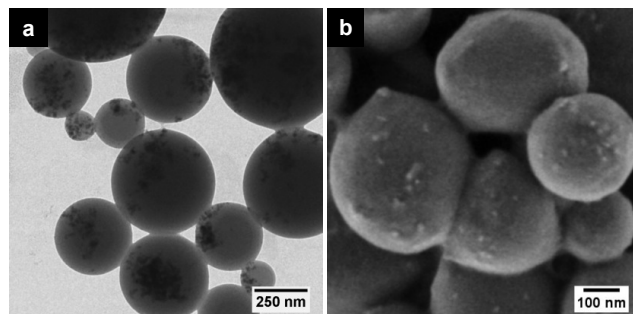
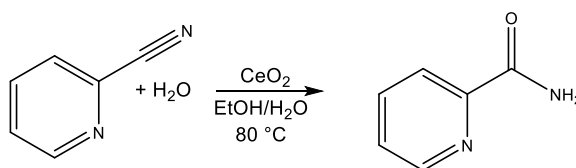


**Figure 5.4.** TEM (a) and SEM (b) micrographs of sample **C4**.

#### 5.4 Catalysis of the Hydration of 2-Cyanopyridine to 2-Picolinamide

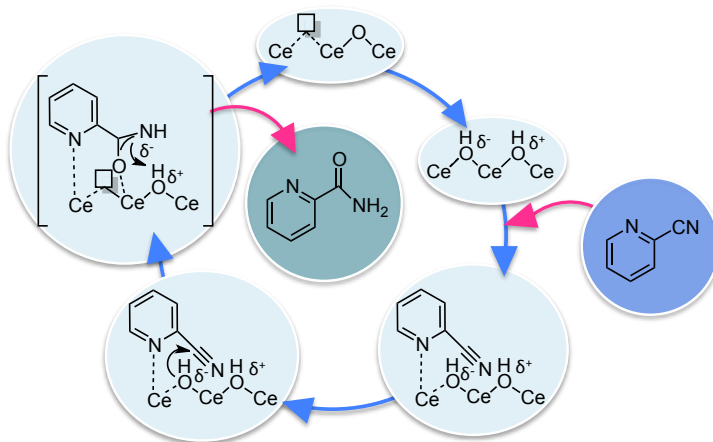
The reaction of hydrolysis of 2-cyanopyridine to 2-picolinamide, presented in Scheme 5.2, was chosen to study the catalytic performance of the magneto-responsive polystyrene-supported ceria nanoparticles. The catalysis of the reaction by ceria nanoparticles is a well-established process, in which both non-supported and supported ceria nanoparticles have shown outstanding catalytic efficiencies and recyclability via centrifugation.<sup>6, 179</sup>



**Scheme 5.2.** Hydration of 2-cyanopyridine to 2-picolinamide.

The kinetics of the reaction was independently studied by using the magneto-responsive catalytic nanoparticles prepared with the two routes (i.e., samples **C2** and **C6**). The effect of the concentration of catalyst on the reaction rate was analyzed for concentrations of ceria of 0.003, 0.006, 0.009, 0.012, and 0.024 mol·L<sup>-1</sup>. The evolution of the conversion was followed by high performance liquid chromatography (HPLC) for each concentration of the catalyst as a function (1- $\alpha(t)$ ) of time ( $t$ ), where  $\alpha$  is the remains fraction ( $C_s(t)/C_s(t_0)$ ) of the limiting substrate ( $s$ ) (2-cyanopyridine).

In agreement with the mechanism of the reaction reported by Tamura et al.<sup>153, 176-177</sup> and shown in Scheme 5.2, the evolution of the conversion depended exclusively on the concentration of 2-cyanopyridine, whereas the contribution of water, which was clearly in excess, can be neglected.



**Scheme 5.2.** Reaction mechanism of the hydrolysis of 2-cyanopyridine to 2-picolinamide catalyzed by ceria nanoparticles. (Based on refs. 153, 176, and 177)

Thus, the hydrolysis of 2-cyanopyridine catalyzed by polystyrene-supported ceria is a first order reaction ( $n = 1$ ) whose the reaction rate ( $k$ ) depends linearly of the concentration of the catalyst ( $C$ ). The linearization of the corresponding expression of the first order kinetics allows the calculation of the kinetic parameters according to:

$$\frac{C_s(t)}{C_s(t_0)} = e^{-kt} \rightarrow -\ln\left(\frac{C_s(t)}{C_s(t_0)}\right) = -\ln(\alpha(t)) = k(C_{CeO_2})t \quad (5.1)$$

Figure 5.5 presents  $-\ln(\alpha)$  as a function of time for the different concentrations of catalyst. The correlation of the experimental data to eq. (5.1) confirms the first order reaction and allowed the calculation of the kinetic constants ( $k$ ), whose values are presented in Table 5.2.

Optimum concentrations of cerium of  $0.012$  and  $0.009 \text{ mol}\cdot\text{L}^{-1}$  were defined for catalysts **C2** and **C6**, respectively. The selection of those concentrations was based on the highest achievable reaction rate and the partial aggregation with the subsequent reduction of the active surface of the catalysts, which occurred when the concentration of **C6** was increased. The catalytic system **C2** allowed us to work at higher concentrations to compensate its catalytic deficiencies. Nevertheless, the amount of sample **C2** required for a concentration of ceria of  $0.024 \text{ mol}\cdot\text{L}^{-1}$  was considered excessive. Therefore,  $0.012 \text{ mol}\cdot\text{L}^{-1}$  was chosen as a good compromise between the catalytic efficiencies and the amount of hybrid catalysts used.



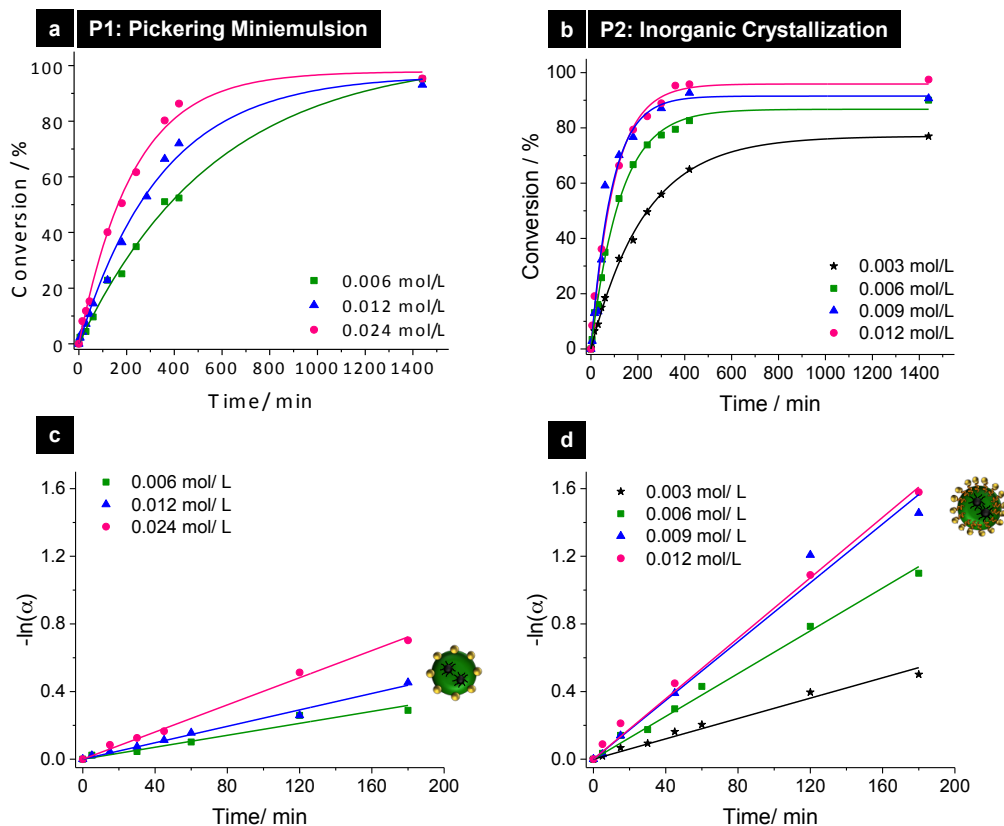


**Figure 5.5.** Influence of the concentration of  $CeO_2$  on the kinetics of the hydration of 2-cyanopyridine catalyzed by C2 (a, c) and C6 (b, d). Evolution of the conversion ( $1-\alpha$ ) (a, b) and  $-\ln(\alpha)$  (c, d) of the reaction achieved with different concentrations of each catalyst.

**Table 5.2.** Conversion after 7 h and reaction rate ( $k$ ) achieved with different catalysts and concentrations.

Synthetic Route	Catalyst	$C_{CeO_2} / \text{mol}\cdot\text{L}^{-1}$	Conversion <sup>a</sup> / %	$k^b \cdot 10^5 / \text{s}^{-1}$
–	C0	0.009	88	20.4
–	C0	0.012	100	29.2
P1	C1	0.012	56	3.2
P1	C2	0.006	52	3.0
P1	C2	0.012	72	4.1
P1	C2	0.024	86	6.7
P2	C5	0.009	86	9.3
P2	C6	0.003	65	5.0
P2	C6	0.006	83	10.6
P2	C6	0.009	93	14.5
P2	C6	0.012	96	14.9

<sup>a</sup> Determined by HPLC at 7 h of reaction time.

<sup>b</sup> Determined by linear adjustment of the experimental data.

Figure 5.6 compares the evolution of the conversion ( $1-\alpha$ ) and the reaction rate  $-\ln(\alpha)$  for for each optimum concentration of the magneto-responsive catalysts (**C2** and **C6**) with the analogous supported catalyst without the magnetic component (**C1** and **C5**, respectively) and the inorganic reference (**C0**). The performance of the magneto-responsive hybrid catalyst **C6** prepared by in-situ crystallization showed similar catalytic efficiencies to the unsupported ceria nanoparticles (**C0**). As predicted from the SEM observations, **C2** presented lower catalytic performances, which was explained by the less efficient inorganic coverage and the reduction of the active surface of the catalyst prepared by the Pickering miniemulsion strategy. Nevertheless, the final conversion of the substrate achieved after 24 h of reaction using catalyst **C2** was comparable to the performances reached with catalysts **C0** and **C6**. The conversion achieved after 7 h and the values of the kinetic constant ( $k$ ) for each catalyst are summarized in Table 5.2.

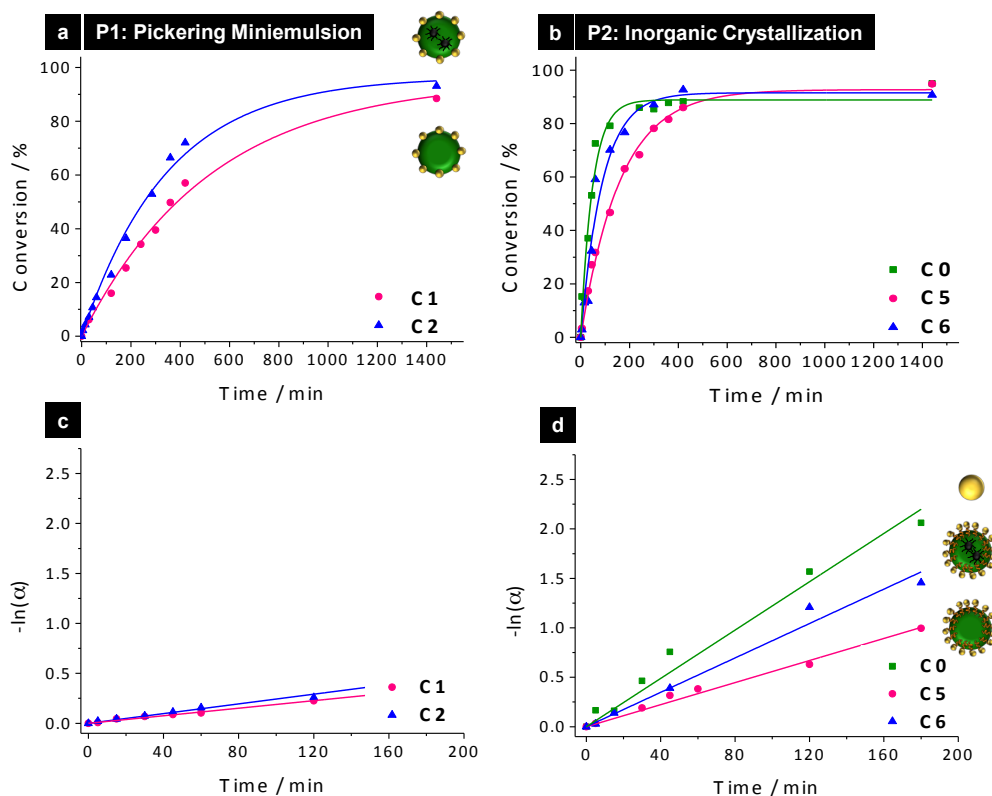


**Figure 5.6.** Comparison of the catalytic efficiency of hybrid catalysts prepared via **P1** and **P2** strategies, and the non-supported ceria nanoparticles. Kinetics of the hydration of 2-cyanopyridine catalyzed by **C1**, **C2** (a, c) and **C5**, **C6** (b, d). Evolution of the conversion ( $1-\alpha$ ) (a, b) and  $-\ln(\alpha)$  (c, d) of the reaction achieved with each catalyst.

Interestingly, regardless of the synthetic method, the catalytic performance of both hybrid systems was significantly enhanced with the incorporation of magnetite. The hydration of nitriles to amides is susceptible of being catalyzed by a wide range of metal oxides. If magnetite was only partially encapsulated, the remaining fraction accessible on the surface of the polymer support could then

contribute to the catalysis together with ceria. However, as shown in Figure 5.7, no significant conversion of 2-cyanopyridine was observed when polystyrene (C3) or polystyrene–magnetite nanoparticles (C4) were used as the sole catalyst. Therefore, the enhanced activity of the magnetoresponsive nanocatalysts C2 and C6 could not be explained by a direct contribution of the magnetite nanoparticles in the catalytic mechanism.

Magnetic particles under oscillating magnetic fields act as hot spots that heat the surrounding environment via hysteresis or relaxation mechanisms.<sup>178</sup> This behavior of magnetite has been widely exploited for hyperthermia and biomedical applications,<sup>179</sup> but up to now, it has been barely explored in chemical reactions<sup>180</sup> and catalysis. In this work, the catalytic enhancement achieved with the incorporation of a magnetoresponsive component is assumed to be likely related with the increase of the local temperature promoted by the vibration of the magnetite particles while being submitted to an intense orbital shaking.

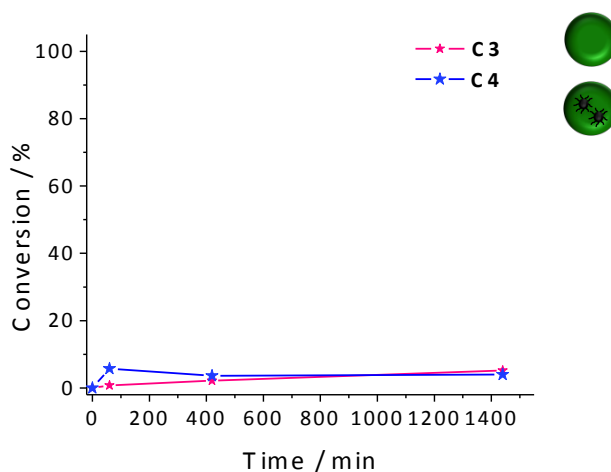


**Figure 5.7.** Kinetic study of the hydration of 2-cyanopyridine in the presence of polymer (C3) and polymer–magnetite hybrid nanoparticles (C4).

The presence of the magnetic nanoparticles allowed the recovery and recycling of the catalyst by application of an external magnetic field. The magnetoresponsive nanocatalysts (C2 and C6) were recycled, washed, and reused in four cycles of 24 h of reaction. Figure 5.8 presents the conversion achieved after each reaction cycle and proves the stability of both catalytic systems, which maintained the catalytic activity without degradation during at least four cycles.

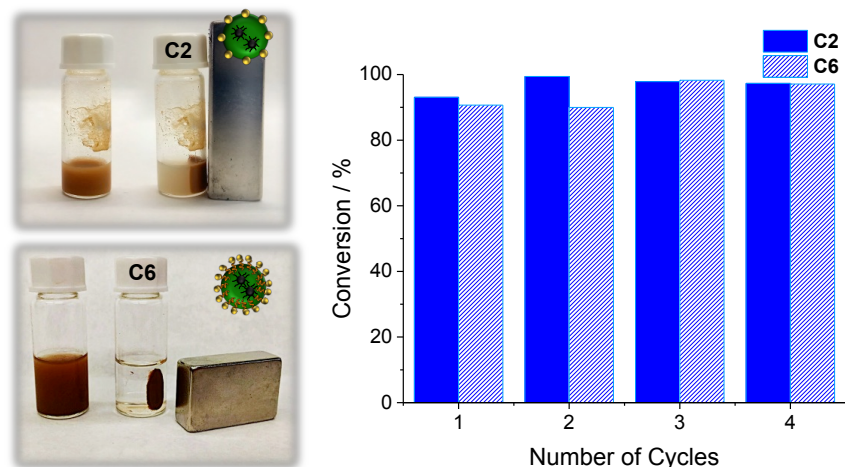


**Figure 5.8.** Recycling study of the magnetically recoverable catalysts **C2** and **C6**.

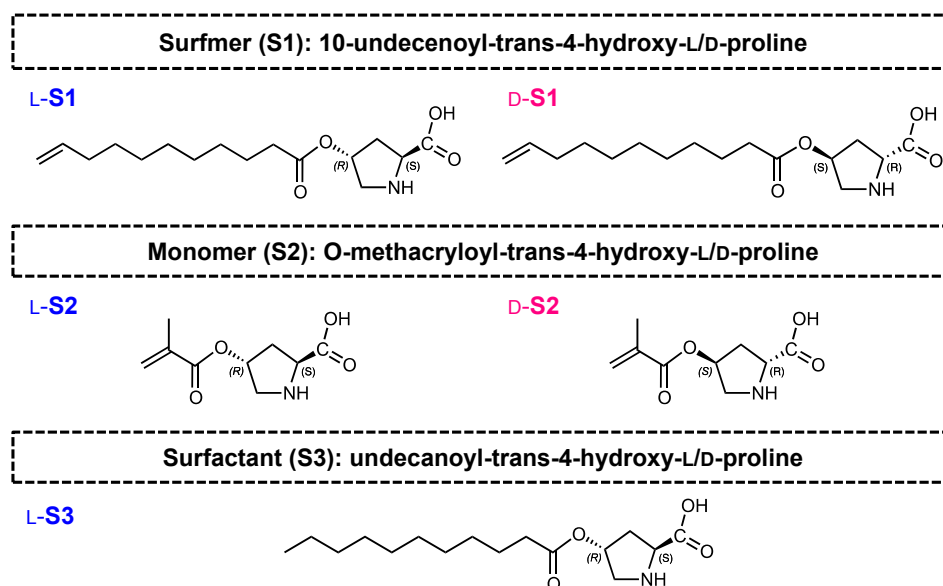
## 5.5 Conclusions

This chapter demonstrates the suitability of Pickering miniemulsions for a straightforward preparation of magneto-responsive polystyrene-supported ceria nanoparticles, avoiding the use of molecular surfactants and the requirement of multi-step processes. The material was compared with the achieved by two-step strategies based on the encapsulation of MPS-functionalized magnetite nanoparticles by miniemulsion polymerization and further in-situ crystallization of ceria on the preformed polymer surface. The advantages of the traditional multi-step crystallization strategies were confirmed in terms of inorganic incorporation and efficient deposition of the catalyst. However, the use of Pickering miniemulsions as a synthetic platform offers great synthetic advantages related to the reduction of the consumption of time, resources, and the complexity of the process.

The resulting materials showed high performances in the heterogeneous catalysis of the hydration of 2-cyanopyridine to 2-picolinamide in aqueous media. The conversion achieved using the catalysts prepared by the Pickering miniemulsion strategy was comparable with the great performance of the catalysts produced via an in-situ crystallization process. The incorporation of magnetite in the core of the nanoparticles allowed the recovery and the recycling of the catalyst with the application of an external magnetic field and guaranteed the maintenance of its activity after four cycles of reaction. In addition, magnetite offered a synergic effect in the catalysis, which was assumed to be related to the local heat produced as a consequence of the oscillating magnetic fields created by orbital shaking of the nanocatalysts.

## 6 Proline-Functionalized Polymer Nanoparticles for Enantioselective Catalysis in Aqueous Media

This chapter describes the synthesis of magnetoresponse chiral nanoparticles highly efficient for asymmetric catalysis in aqueous media. Miniemulsion polymerization is used for the immobilization of chiral units of proline on the surface of PMMA nanoparticles and other additional inorganic functionalities (e.g., magnetite) with a controlled accessibility within the catalytic system. Three different molecules, labeled as **S1**, **S2**, and **S3** were synthesized for the incorporation of chiral moieties of hydroxy-L/D-proline on the surface of polymer nanoparticles. The chemical structure of the proline-based molecules, shown in Scheme 6.1, guarantees the role of **S1**, **S2**, and **S3** as surfmer, only comonomer, and only surfactant, respectively.



**Scheme 6.1.** Chemical structure of the proline-based chiral molecules: L/D-**S1**, L/D-**S2**, and L-**S3**.

The use of the methacrylic comonomer<sup>45, 181</sup> (**S2**) requires the addition of conventional surfactants (e.g., SDS) that need to be removed for catalytic applications. The proline-based surfactant (**S3**) is subjected to adsorption–desorption equilibrium. The surfmer structure (**S1**) offers the colloidal stabilization of the miniemulsion and the covalent incorporation of proline via the copolymerization with MMA as the main monomer forming the polymer support. In addition, the presence of the long alkyl chains with proline in the hydrophilic head and the absence of additional surfactants provide a great accessibility of the chiral units for catalytic applications. The encapsulation of magnetite nanoparticles within the polymer core offers the key for the

purification, recovery, and recyclability of the catalyst under mild conditions. The magneto-responsive chiral nanoparticles were used for the asymmetric catalysis of an intermolecular aldol reaction in water.

## 6.1 State of the Art of the Preparation of Chiral Hybrid Nanoparticles for Asymmetric Catalysis

In the last decades, asymmetric organocatalysis has been exploited for the synthesis of chiral molecules and complex structures with controlled enantioselectivity.<sup>182</sup> In this context, amino acids and amino acid derivatives have been used in the homogeneous catalysis of a wide range of organic reactions and synthesis of chiral products with high additional value (e.g., for pharmaceutical applications).<sup>183</sup> Amino acid-based organocatalysts are spotlighted because of their great availability, low toxicity, and the simplicity of their application. Many organic reactions (e.g., aldol reactions,<sup>184</sup> Michael additions,<sup>185-187</sup> Mannich reactions,<sup>188-190</sup> cycloadditions,<sup>191</sup> C–C bond formations,<sup>192, 193</sup>  $\alpha$ -amination,<sup>194-195</sup> sulfenylation,<sup>196</sup> or halogenation reactions<sup>197</sup>) have been traditionally catalyzed using L-proline and its derivatives.<sup>198</sup> Aldol reactions are one of the most important reactions in chemistry and biology in which proline-based catalysts have shown a great efficiency and selectivity,<sup>184</sup> providing intramolecular,<sup>199</sup> intermolecular,<sup>200-201</sup> or cross-aldol C–C backbones.<sup>202-203</sup>

The structure of proline-based catalysts, such as oxyprolines,<sup>204</sup> prolinamides<sup>205</sup> or proline-like catalysts (i.e., pyrrolidine conjugated catalysts protonated with nitrogen heterocycles<sup>206</sup> or with organophilic chains<sup>207</sup> substituting the carboxylic acid) was designed to enhance the efficiency and enantioselectivity of homogeneous catalysis of aldol reactions in organic solvents. The solvent and the availability of protons have a crucial role for the selectivity of proline-catalyzed aldol reactions. The enhancement of the enantioselectivity was achieved under controlled conditions with the incorporation of water, or even solvent-free strategies.<sup>208</sup> In the presence of water, proline-functionalized surfactants allowed great selectivities and yields via the creation of miniemulsion-like environments, in which the organic molecules assemble via hydrophobic interactions.<sup>204</sup> However, the use of water as sole solvent dealt with problems of solubility and inefficient contact between the substrate and the catalysts.<sup>209</sup> In this context, heterogeneous catalysts were developed as an attempt to overcome the drawbacks of homogeneous catalysis related to the purification of the product, recovery, and recycling of the catalyst.

Molecules of *trans*-4-hydroxy-L-proline were for the first time immobilized in a Merrifield resin, which allowed the catalysis of aldol reactions with poor selectivity.<sup>210</sup> This derivate of L-proline is still nowadays one of the most widespread starting materials used in the preparation of supported catalysts. Both *trans*-4-hydroxy-L-proline and L-proline units have been used for the preparation of functional monomers via the attachment of lipophilic functionalities on the side chain of the 4-hydroxy group. The corresponding chiral linear polymers or co-polymers (i.e., polyethylenglycol,<sup>211</sup> methacrylic polybetaines,<sup>212</sup> linear polystyrene,<sup>213</sup> poly(styrene-*co*-proline-methacrylate),<sup>214</sup> poly(acryloyl-proline)<sup>215</sup>) were obtained via solution polymerization processes. The catalytic load of the linear support was not as high as the expected with cross-linked polymer resins and suffered from the rapid loss of activity and selectivity during the recycling. Polymer-scaffolds were also used for the immobilization of L-proline via grafting modification reactions, but the tendency of twinning of the polymer chains reduced the accessibility of the chiral units and drastically worsened the catalytic efficiency. For those reasons, the research community turned into the development of polymer-supported organocatalysts.<sup>216</sup>

One of the most critical aspects in the design of polymer-supported catalysts is related to the availability of the active sites on the surface of the polymer support. Kirstensen et al.<sup>217</sup> published a detailed revision about the immobilization of hydroxy-proline units on polystyrene beads via post-modification<sup>218-220</sup> or cross-polymerization strategies.<sup>213, 221</sup> Acrylic and methacrylic proline-based monomers have also been synthesized via the activation (e.g., *O*-acylation)<sup>222</sup> of the 4-hydroxy group to allow their copolymerization with commercial monomers.<sup>223</sup> Suspension, dispersion,<sup>223</sup> or reversible addition–fragmentation chain transfer (RAFT)<sup>224</sup> polymerization strategies were used for the preparation of polymer beads with a controlled load of supported proline. RAFT polymerization was also used for the incorporation of proline moieties in core–shell micelles of block copolymers of poly(acrylic acid) with styrenic or methacrylic backbones.<sup>225</sup> In an aqueous environment, the micellar structure promoted the concentration of the reagents in the catalytically active core. The reactive environment resulted into the increase of the reaction rate of an intermolecular aldol reaction between *p*-nitrobenzaldehyde and cyclohexanone in water. In another work, miniemulsion was used for the in-situ polymerization of chiral *N*-oleoyl-D/L-proline monomers, leading to recyclable polymer-supported proline catalysts with poor selectivity for the same reaction.<sup>226</sup>

Proline-based moieties were also supported on functional inorganic nanoparticles (e.g., gold<sup>227-228</sup>, magnetite nanoparticles,<sup>229-230</sup> core–shell magnetite–silica<sup>231</sup> nanoparticles, or platinum nanoparticles supported on Al<sub>2</sub>O<sub>3</sub><sup>232</sup>). Yacob et al.<sup>233</sup> prepared proline-functionalized polyacrylamide and PMMA nanoparticles encapsulating a magnetic core via solution

polymerization processes in dimethylformamide (DMF). The catalysts presented high yields, and cycling stabilities but limited selectivities for the aldolization of aromatic aldehydes in the presence of benzoic acid, and an excess of ketone as main solvent.

In this chapter, magneto-responsive proline-functionalized PMMA nanoparticles were prepared by the miniemulsion polymerization process presented in Figure 6.1. The chiral nanoparticles were applied for the asymmetric catalysis of the intermolecular aldol reaction of *p*-nitrobenzaldehyde and cyclohexanone in water.

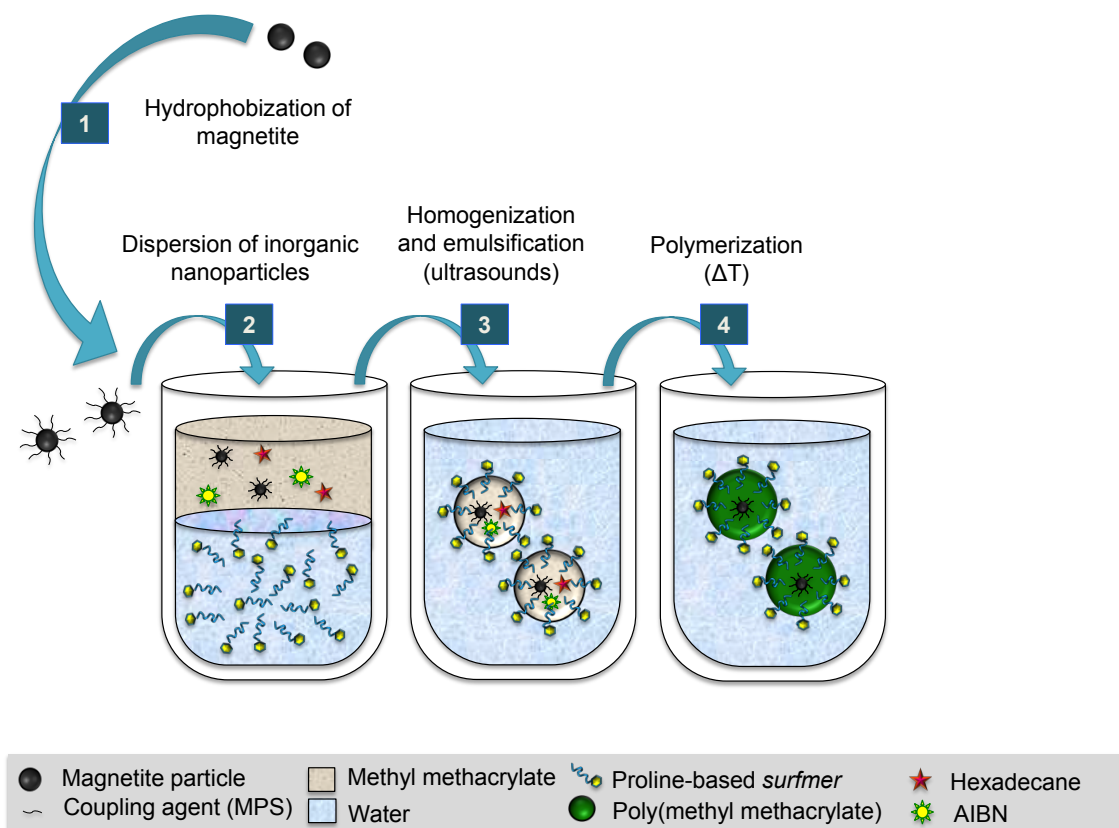


**Figure 6.1.** Schematic representation of the synthesis of magneto-responsive proline-functionalized PMMA chiral nanoparticles via miniemulsion polymerization using a proline-based surfmer.

## 6.2 Synthesis of Proline-Based Building Blocks

The three different compounds with specific chirality and functional end groups (i.e., a copolymerizable acrylic or alternatively a methacrylic group, and/or a chiral proline unit) presented in Scheme 6.1 were conceived to incorporate accessible proline units on a polymer support.



The proline-functionalized polymerizable surfactant (10-undecenoyl-*trans*-4-hydroxy-L-proline, shorten as L-S1) was synthesized by attachment of a long alkyl chain to the 4-hydroxy group of *trans*-4-hydroxy-L-proline. The resulting structure, which was confirmed by  $^1\text{H-NMR}$  and  $^{13}\text{C-NMR}$  spectroscopies (see spectra in Figure 6.2) presented a desirable amphiphilicity to act as a surfactant.

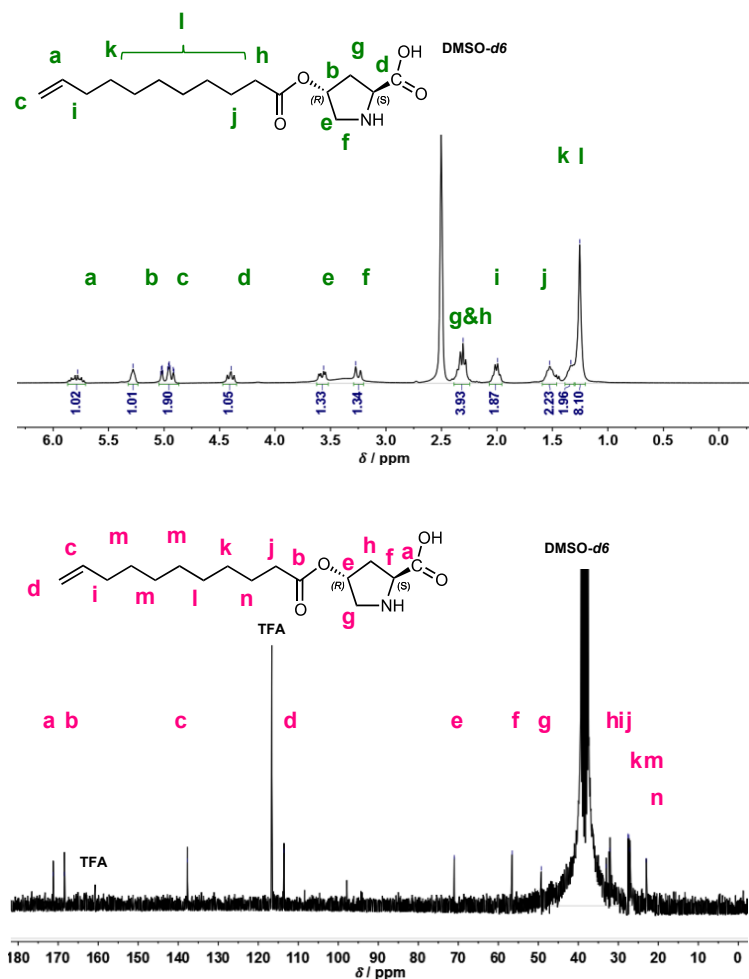


**Figure 6.2.**  $^1\text{H-NMR}$  and  $^{13}\text{C-NMR}$  spectra of the surfmer (L-S1).

A second chiral structure with the role of comonomer, *O*-methacryloyl-*trans*-4-hydroxy-L-proline, abbreviated as L-S2, was prepared by incorporation of a short alkyl chain and a methacrylic group to the starting molecule *trans*-4-hydroxy-L-proline.  $^1\text{H-NMR}$  and  $^{13}\text{C-NMR}$  spectra, shown in Figure 6.3, confirm the chemical structure. The use of L-S2 had already been reported<sup>234</sup> for the preparation of proline-supported polymer nanoparticles or gels with high efficiency in asymmetric catalysis.

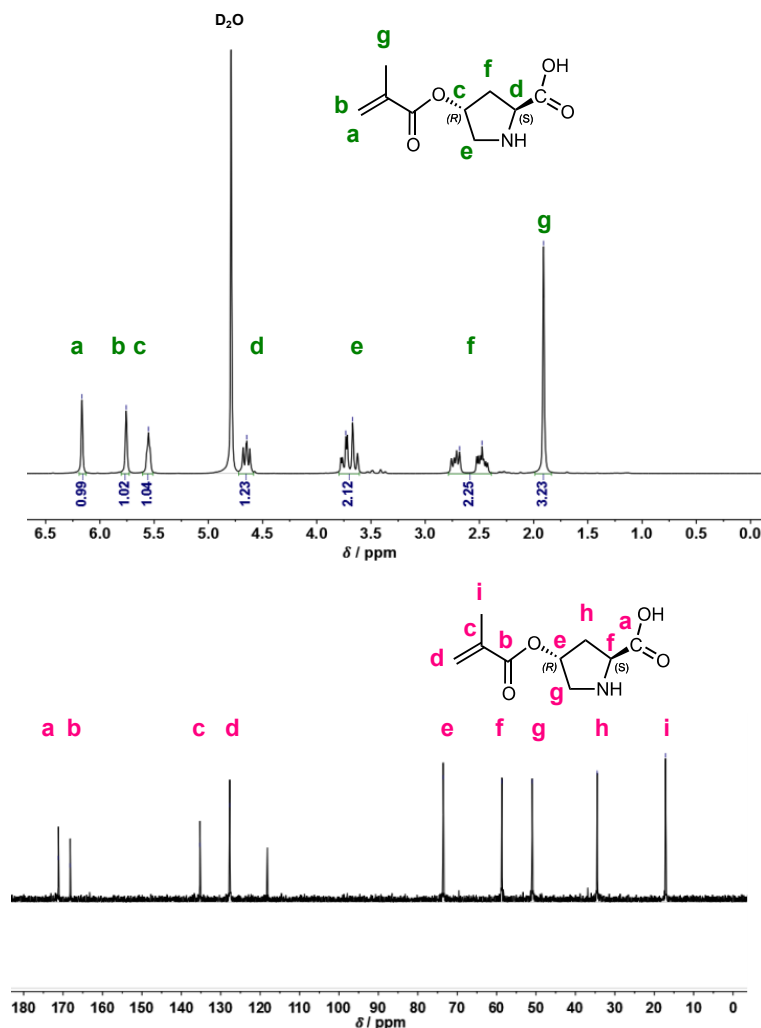


**Figure 6.3.**  $^1\text{H-NMR}$  and  $^{13}\text{C-NMR}$  spectra of the monomer (L-S2).

The enantiomers 10-undecenoyl-*trans*-4-hydroxy-D-proline (D-S1), and *O*-methacryloyl-*trans*-4-hydroxy-D-proline (D-S2) were also prepared to address the control of the enantioselectivity of the asymmetric catalysis through the specific chirality of the catalyst.

A third type of proline-based molecule with the typical structure of a surfactant, undecanoyl-*trans*-4-hydroxy-L-proline (L-S3) was also synthesized. This third compound, whose  $^1\text{H-NMR}$  and  $^{13}\text{C-NMR}$  spectra are shown in Figure 6.4, presents a long alkyl chain with analogous structure to the surfmer L-S1 but without the copolymerizable vinyl end group. As a consequence, the role of L-S3 is restricted to guarantee the colloidal stabilization of the miniemulsion while incorporating the catalytically active chiral units.

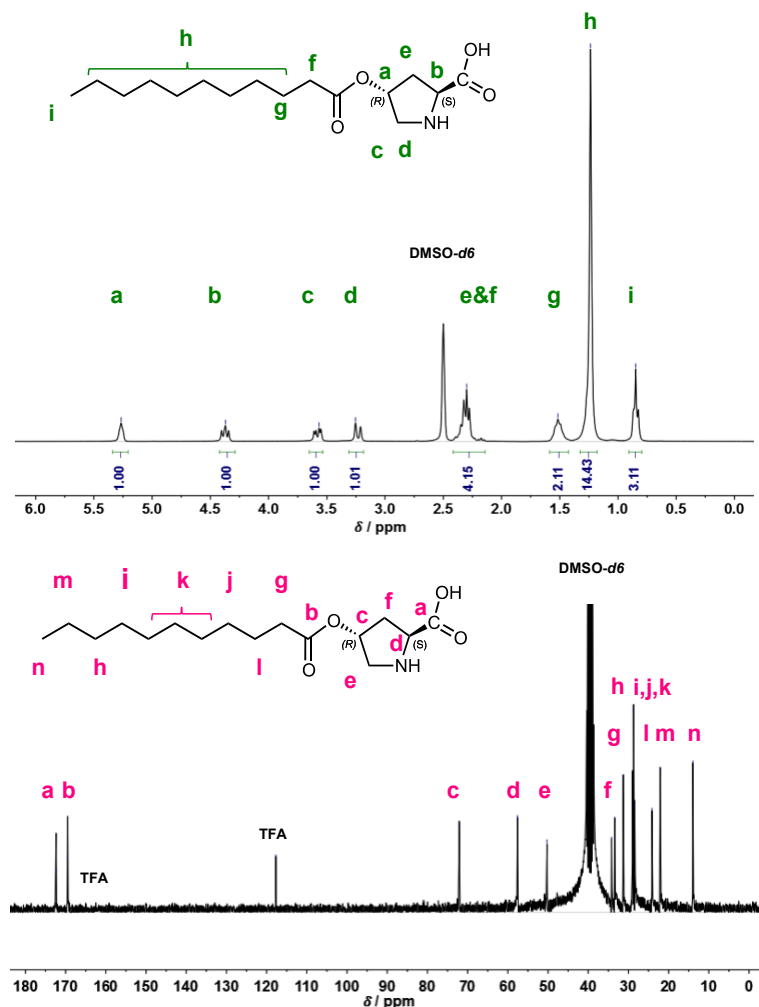


**Figure 6.4.**  $^1\text{H-NMR}$  and  $^{13}\text{C-NMR}$  spectra of the surfactant (L-S3).

The synthesis of the proline-based molecules (S1–S3) was performed by selective *O*-acylation of *trans*-4-hydroxy-*L/D*-proline in trifluoroacetic acid (TFA). The acylation capacity of the reaction media was increased with the controlled addition of trifluoromethanesulfonic acid, which offered a good compromise between the purity of the product and the reaction yield. The strategy, reported by Kirstensen et al.,<sup>222-223</sup> avoids the protection and deprotection of the reactive groups of proline required in traditional synthetic pathways. In addition, a crystalline hydrochloride product was straightforwardly crystallized with the simple addition of diethyl ether. No further purification steps are required for the catalytic purposes aimed in this chapter.

### 6.3 Preparation of Magnetoresponse Chiral Nanoparticles

The proline-based molecules L/D-**S1** and L/D-**S2** were supported on PMMA nanoparticles by miniemulsion polymerization, as shown in Figure 6.1. The acrylic or methacrylic groups of the amphiphilic chiral molecules were used for the copolymerization with a main monomer with low prize and great chemical stability. On the one hand, the acrylic group of L/D-**S1** copolymerizes with MMA at the droplet interface in the direct miniemulsion. The proline units are oriented towards the aqueous phase, and offer colloidal stabilization avoiding the use of extra surfactants. On the other hand, the high hydrophilicity and the affinity of the monomers (L/D-**S2**) to MMA let to an efficient copolymerization process occurring mostly at the droplet interface. In this case, SDS was used as a surfactant to stabilize the miniemulsion.

The proline-based surfactant (L-**S3**) does not allow a stable fixation of the active sites of proline to the polymer support due to the adsorption and desorption equilibrium typical from surfactants. In the application field (e.g, the use of the chiral nanoparticles as heterogeneous nanocatalysts), the desorption of the surfactant would lead to a homogeneous catalysis directly promoted by the free molecules in solution which would falsify the efficiency from the nanocatalyst (the nanoparticle) itself. Beyond the scope of any catalytic application, the surfactant was used to prove the viability of the stabilization of the miniemulsion as a substitute of SDS. In this fashion, L-**S3** was successfully used for the miniemulsion polymerization of MMA and the copolymerization of MMA and L-**S2**.

Regarding the formulation of the miniemulsion, L/D-**S2** was used as a comonomer (5 wt.% of the whole monomer content) and MMA as the main monomer. The surfmer (L/D-**S1**) was introduced at a concentration of 6 wt.% with respect to the continuous phase, acting as a surfactant that stabilizes the MMA droplets. For those nanoparticles synthetized using L-**S3** molecules, the concentration of the comonomer and the surfactant were both maintained. The concentration of L-**S1** and L-**S2** was optimized to maximize the incorporation of proline. The increase of the content of L-**S2** from 5 to 10 wt.% resulted into the complete destabilization of the miniemulsion. The copolymerization strategy did not stand the excess of the proline-building blocks, increasing the contribution of homogeneous polymerization in the aqueous phase. The stability of the miniemulsion decreased when the amount of surfmer was reduced from 6 to 3 wt.%, and the solid content of the final dispersion dropped from 8 to 5 wt.% (with respect to a theoretical value of 10 wt.%). The proline content (0.23–0.28 wt.% after the purification) of the particles prepared at higher concentrations of the surfmer (9 or 12 wt.%) was similar to the values (0.28 wt.%) achieved

with 6 wt.% of L-**S1**. Our study revealed that a significant fraction of the surfmer was required for stabilization purposes, but it was not covalently incorporated to the nanoparticles structure.

The solubility of both the surfmer and the surfactant in the aqueous phase was critical to provide an efficient stabilization of the direct miniemulsion, which justified the requirement of a strong basic media in the continuous phase. The basicity of the continuous phase was less restrictive in the case of the comonomer because the role of L/D-**S2** was not directly related to the colloidal stability. Nevertheless, the presence of OH<sup>-</sup> groups in the aqueous phase increased the hydrophilicity of the proline-based molecules, improving the copolymerization process at the droplet interface and the accessibility of the active moieties of the catalyst. The purification of the dispersion of nanoparticles allowed us to minimize the presence of surfactant (SDS) and the excess of the surfmer, which did not copolymerize with MMA. In addition, the rising step with TFA was essential to protonate the carboxylic group of proline, which was deprotonated during the preparation of the miniemulsion with the addition of NaOH in the aqueous phase. The protonation of the proline-supported catalysts will have a crucial effect in the enantiomeric selectivity of the reactions whose mechanism of catalysis requires a direct participation of the carboxylic group.

The magnetic functionality was achieved with the incorporation of magnetite nanoparticles in the miniemulsion (10 wt.% with respect to the disperse phase). The self-assembly of the inorganic system within the forming polymer matrix during the miniemulsion polymerization process was controlled via the surface functionalization of magnetite. According to the results presented in Chapter 4, MPS was used as a coupling agent with relative hydrophobicity, short alkyl chains, and a methacrylic copolymerizable group, which guaranteed the encapsulation of the magnetic nanoparticles.

Analogous strategies were used for the preparation of different types of chiral nanoparticles with and without magnetic core. The description and characterization of the nanostructures in terms of material composition, proline load, magnetite concentration, and particle size are presented in Table 6.1. The polymer catalysts prepared using L-**S1** and L-**S2** are named as **AC1** and **AC4**, respectively. The corresponding chiral nanoparticles incorporating magnetite are designed as **AC2** and **AC5**, or **AC3** and **AC6** if D-**S1** and D-**S2** molecules were used for the immobilization of proline. As a general trend, the comonomer (L/D-**S2**) allowed a slightly higher incorporation of catalytic and magnetic functionalities within smaller and more monodisperse nanoparticles in the case of **AC5** and **AC6**, compared to **AC2** and **AC3**. This latter feature (particle size and size polydispersity) is directly related to the stabilization ability of the surfmer (L/D-**S1**), which seems to be less effective than SDS. Similar information was revealed by the characterization of the chiral

catalysts **AC2**, **AC3**, **AC5**, and **AC6** by SEM and TEM (Figure 6.5). Nevertheless, the order of magnitude of the differences between both materials is negligible.

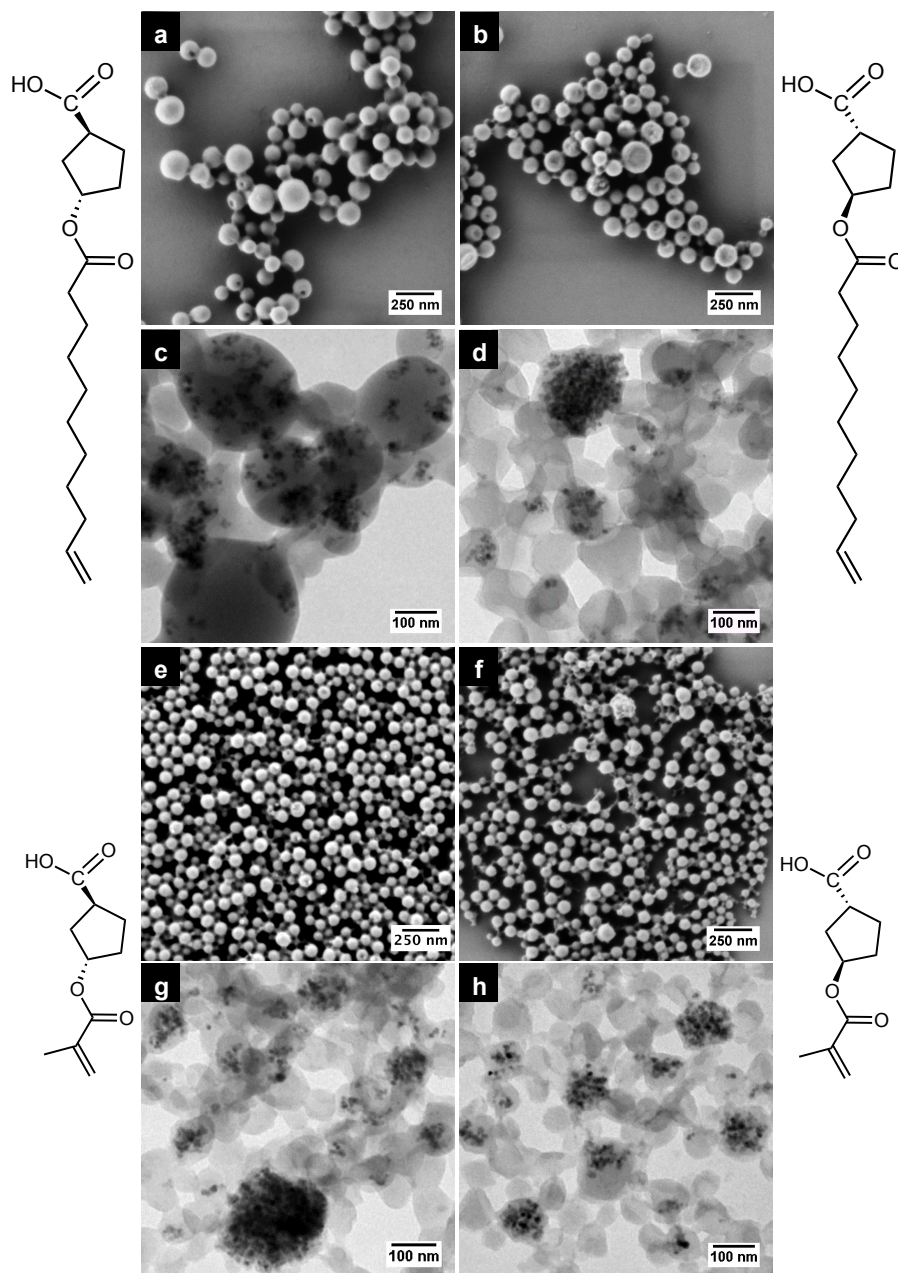


**Figure 6.5.** SEM and TEM micrographs of the magneto-responsive chiral particles **AC2** (a, e), **AC3** (b, f), **AC5** (c, g), and **AC6** (d, h).

A second group of chiral nanoparticles (**AC7–AC10**) presented in Table 6.2 was synthesized by miniemulsion polymerization using the proline-based surfactant (**L-S3**). Although only the materials presented in Table 6.1 were considered for the application as chiral nanocatalysts, the preparation

of nanoparticles **AC8** and **AC7** (with and without magnetite) proves the possibility of achieving the colloidal stabilization with amino acid-based molecular surfactants. The strategy was extended to the combining two functional chiral structures (L-S2 and L-S3) for the synthesis of **AC10** and **AC9**, respectively.

**Table 6.1.** Main features of the different polymer-supported proline nanocatalysts.

Catalyst	Monomer	Co-monomer	Surfactant	Surfmer <sup>b</sup>	Proline <sup>c</sup> / wt. %	Fe <sub>3</sub> O <sub>4</sub> <sup>d</sup> / wt%	<i>d</i> <sup>e</sup> / nm	PDI <sup>f</sup>
<b>AC1</b>	MMA	–	–	L-S1	0.5	–	190 ± 80	0.07 ± 0.04
<b>AC2</b>	MMA	–	–	L-S1	0.3	9	180 ± 80	0.13 ± 0.02
<b>AC3</b>	MMA	–	–	D-S1	0.3	8	210 ± 70	0.12 ± 0.02
<b>AC4</b>	MMA	L-S2	SDS	–	0.7	–	120 ± 60	0.14 ± 0.02
<b>AC5</b>	MMA	L-S2	SDS	–	0.5	12	200 ± 40	0.47 ± 0.13
<b>AC6</b>	MMA	D-S2	SDS	–	0.4	14	160 ± 30	0.88 ± 0.12

<sup>a</sup> **S1**: 10-undecenoyl-*trans*-4-hydroxy-L/D-proline.

<sup>b</sup> **S2**: *O*-methacryloyl-*trans*-4-hydroxy-L/D-proline.

<sup>c</sup> Determined by polyelectrolyte titration of the nanoparticles after purification.

<sup>d</sup> Determined by TGA.

<sup>e</sup> Determined by DLS.

<sup>f</sup> PDI: Polydispersity index.

**Table 6.2.** Characterization of the dispersion of polymer and hybrid nanoparticles synthesized by miniemulsion polymerization using L-S3 as a surfactant.

Catalyst	Monomer	Co-monomer <sup>a</sup>	Surfactant <sup>b</sup>	Fe <sub>3</sub> O <sub>4</sub> <sup>c</sup> / %	<i>d</i> <sup>d</sup> / nm	PDI <sup>e</sup>
<b>AC7</b>	MMA	–	L-S3	–	150 ± 40	0.04 ± 0.03
<b>AC8</b>	MMA	–	L-S3	9	150 ± 60	0.09 ± 0.03
<b>AC9</b>	MMA	L-S2	L-S3	–	170 ± 60	0.08 ± 0.03
<b>AC10</b>	MMA	L-S2	L-S3	14	240 ± 120	0.19 ± 0.02

<sup>a</sup> **S2**: *O*-methacryloyl-*trans*-4-hydroxy-L-proline.

<sup>b</sup> **S3**: Undecanoyl-*trans*-4-hydroxy-L-proline.

<sup>c</sup> Determined by TGA.

<sup>d</sup> Determined by DLS.

<sup>e</sup> PDI: Polydispersity index.

In comparison with the samples prepared using proline-based surfactant L-S3 (**AC7** and **AC9**), bigger polymer particles with a narrow size distribution were achieved using the surfmer, as shown in the SEM micrographs of Figure 6.6(a, b, and c). Similar particle size and polydispersity was achieved in the encapsulation of magnetite using L-S3 alone (**AC8**) or combined with L-S2 incorporating polymerizable units of proline (**AC10**). The stability of the final latexes validates the application of L-S3 as a surfactant for the stabilization of direct miniemulsions. The use of SDS results in a decrease of both the size and the polydispersity of the sample **AC4** incorporating a magnetic core, as observed in Figure 6.6(d, e, and f).

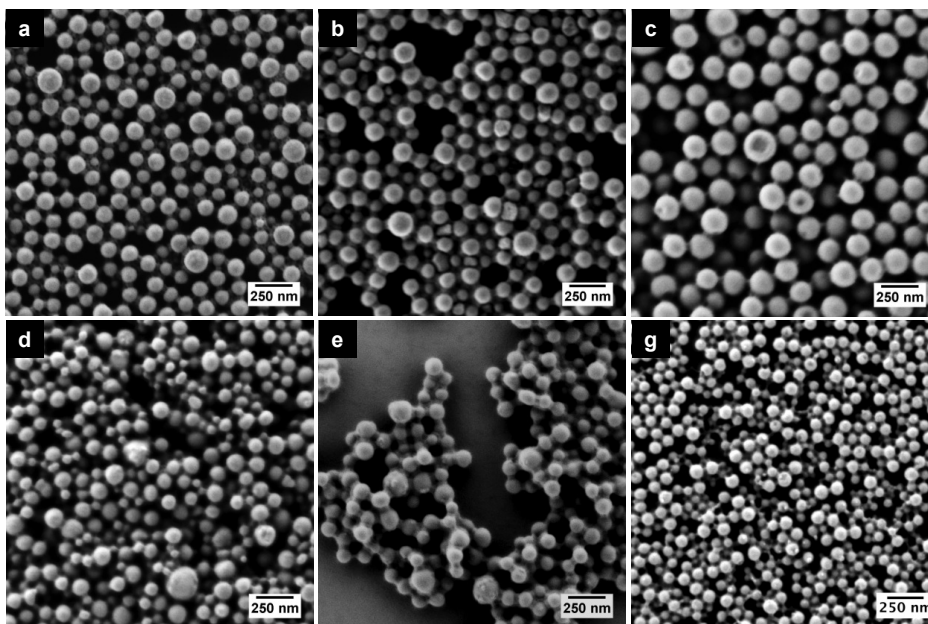
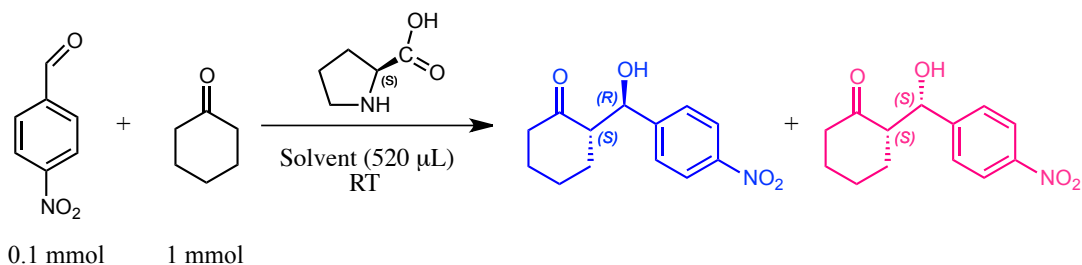


**Figure 6.6.** SEM micrographs of the polymer nanoparticles AC7 (a) and AC9 (b) synthesized using L-S3, compared with the corresponding particles AC1 (c) prepared with L-S1. Analogue comparison established between the hybrid (with a magnetic core) nanoparticles AC8 (d) and AC10 (e) with the use of SDS in AC4 (g).

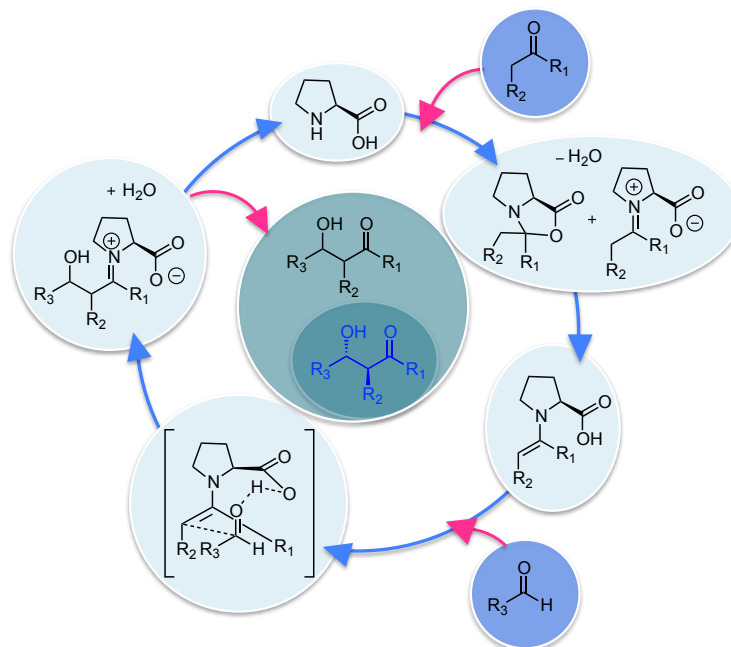
#### 6.4 Asymmetric Catalysis of an Intermolecular Aldol Reaction in Water

The catalytic efficiency of the nanoparticles was studied for the asymmetric catalysis of the intermolecular aldol reaction between *p*-nitrobenzaldehyde and cyclohexanone in water shown in Scheme 6.2. The mechanism of the reaction presented in Scheme 6.3 reveals the crucial role of the carboxylic acid of the proline in the enantioselectivity of the reaction. Therefore, the purification of the chiral nanoparticles with TFA will influence the chirality of the product of the reaction.



**Scheme 6.2.** Aldol reaction between *p*-nitrobenzaldehyde and cyclohexanone catalyzed by proline.





**Scheme 6.3.** Mechanism proposed for the aldol reaction between *p*-nitrobenzaldehyde and cyclohexanone in water catalyzed by proline units. (Based on ref. 212)

The conversion and the enantiomeric selectivity after 6 h for reactions in the presence of different proline-supported catalysts, evaluated by NMR spectroscopy, are listed in Table 6.3. The magneto-responsive surfmer-based nanoparticles (**AC2**) showed conversions over 97% and great enantiomeric selectivities (*anti/syn* ratio 92:8), comparable with the values achieved with the monomer-based particles (**AC5**). The evolution of the conversion and the selectivity achieved with the magneto-responsive chiral catalysts **AC2** and **AC5** was achieved by comparison of the intensities of specific signals of the  $^1\text{H-NMR}$  spectra, as shown in Figures 6.7 and 6.8. The conversion of the aldehyde with the advance of the respective reactions is followed with the disappearance of the signal at 10.09 ppm and the chemical shift at 8.00 and 8.32 ppm characteristic from the structure of *p*-nitrobenzaldehyde resulting into new signals at 7.45, and 8.13 ppm respectively. The appearance of signals at 4.82 and 5.41 ppm reveals the formation of 2-hydroxy-(4-nitrophenyl)methyl-cyclohexanone and the *anti* or *syn* conformation of the chiral bond created between *p*-nitrobenzaldehyde and cyclohexanone. The ratio of the intensities of the latest signals determined the enantioselectivity of the reaction.

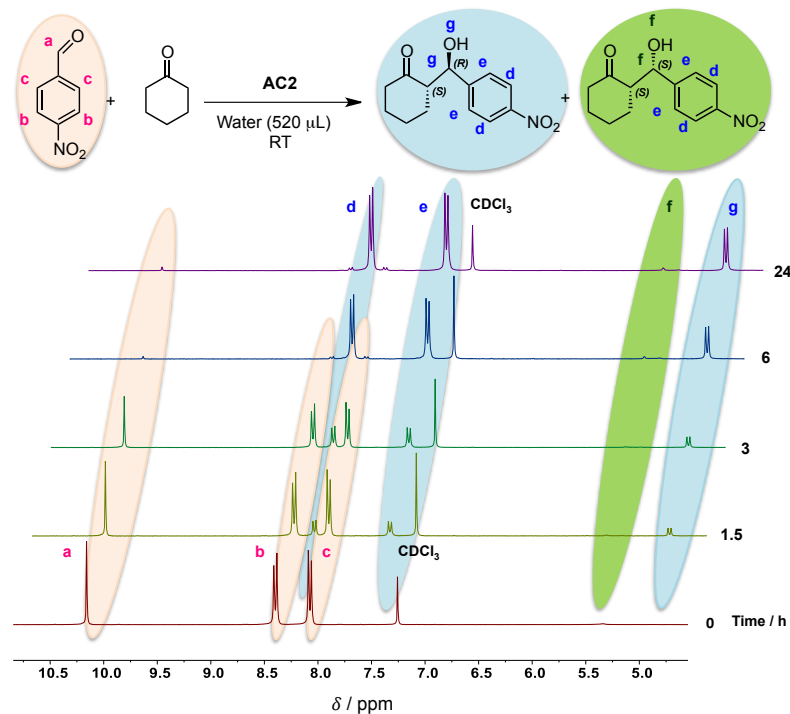


**Figure 6.7.** Evolution of the conversion and enantioselectivity of aldol reaction between *p*-nitrobenzaldehyde (0.1 mmol) and cyclohexanone (1 mmol) in water, catalyzed with the magneto-responsive chiral nanoparticles AC2 (10 mol.% with respect to the aldehyde).

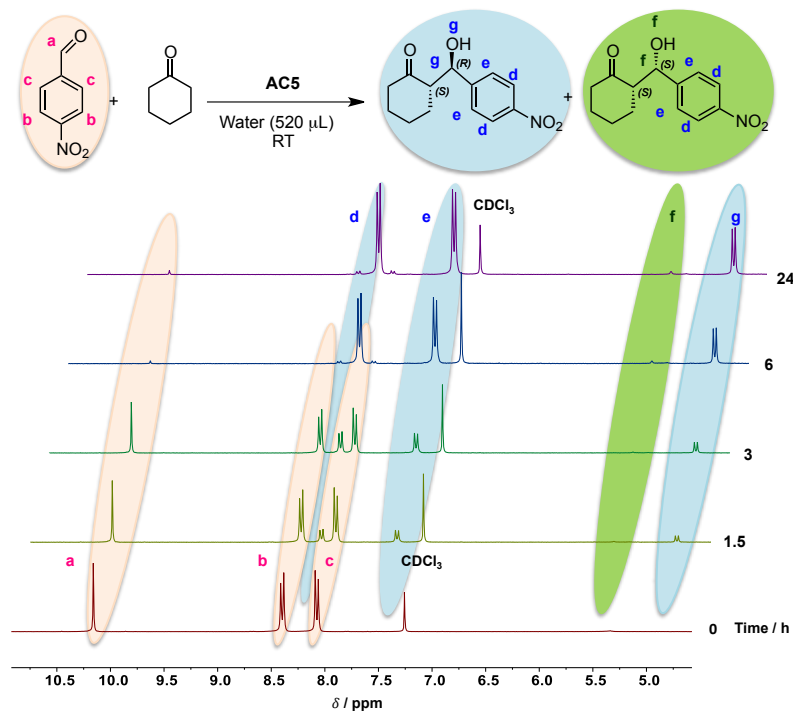


**Figure 6.8.** Evolution of the conversion and enantioselectivity of aldol reaction between *p*-nitrobenzaldehyde (0.1 mmol) and cyclohexanone (1 mmol) in water, catalyzed with the magneto-responsive chiral nanoparticles AC5 (10 mol.% with respect to the aldehyde).

**Table 6.3.** Conversion and enantioselectivity of the aldol reaction using different proline-based chiral catalysts.

Catalyst	Solvent <sup>a</sup>	Conversion <sup>b</sup> / %	<i>anti</i> <sup>b</sup> / %	<i>syn</i> <sup>b</sup> / %
Heterogeneous catalysis				
<b>AC1</b>	Water	99	91	9
<b>AC2</b>	Water	97	92	8
<b>AC2</b>	DMSO/Water (2:1)	97	84	16
<b>AC2</b>	NaOH (1M)	99	36	64
<b>AC2</b>	TFA (1M)	83	47	56
<b>AC3</b>	Water	87	92	8
<b>AC4</b>	Water	94	94	6
<b>AC5</b>	Water	96	93	7
<b>AC5</b>	DMSO/Water (2:1)	100	37	63
<b>AC5</b>	NaOH (1M)	98	41	59
<b>AC5</b>	TFA (1M)	95	40	60
<b>AC6</b>	Water	70	91	9
Homogeneous catalysis				
<b>L-S1</b>	Water	99	94	6
<b>L-S1</b>	DMSO/Water (2:1)	80	76	24
<b>L-S1</b>	NaOH (1M)	93	36	64
<b>L-S1</b>	TFA (1M)	28	45	55
<b>D-S1</b>	Water	98	96	4
<b>L-S2</b>	Water	11	74	26
<b>D-S2</b>	Water	8	75	25

<sup>a</sup> The reaction was performed using 520  $\mu$ L of solvent. Refer to section 9.5.3 for specific details.

<sup>b</sup> Determined by NMR as explained below for Figures 6.7 and 6.8.

To elucidate the effect of the solvent in the reaction, the water was substituted with aqueous solutions of NaOH (1 M), TFA (1 M), or DMSO (2:1 vol.) while keeping constant the rest of the reaction conditions. The high conversion achieved with the different solvents was accompanied with a reduction of the selectivity, the inversion of the *anti/syn* ratio, and the achievement of racemic mixtures. The acidity or basicity of the aqueous media has a direct influence on the reaction mechanism via the protonation or deprotonation of the carboxylic group of the proline and the availability of protons. The aldol reaction catalyzed with proline has been traditionally carried out in organic solvents, and the presence of a small amount of water has been demonstrated to increase the selectivity of the reaction. This work highlights the great efficiency and enantiomeric selectivity reached using water as a sole solvent, whose concentration needs to be carefully

controlled. On the one hand, an excess of water would let to low conversions due to the high polarity of the substrates. On the other hand, the water content needs to be optimized for the efficient dispersion of the catalyst, which otherwise would remain agglomerated and deprived of the support of protons from the solvent.

Similar efficiencies were achieved when the surfmer L-S1 was used for the homogeneous catalysts of the reaction under the same experimental conditions. The amphiphilic molecule located at the water/cyclohexanone interface offered an excellent contact between the substrates, the catalyst, and the solvent. However, the short alkyl chain and the high hydrophilicity of the monomer L-S2 hindered the efficient contact between the small molecules in the aqueous phase and the reactants. Thus, no significant conversion was observed even after 24 h of reaction.

The control of the selectivity of the reaction was also addressed with the modification of the chirality of the catalyst. According to theoretical predictions, the use of polymer-supported or unsupported molecules based in hydroxy-D-proline should promote the D-configuration of the product<sup>235-237</sup>. The enantiomeric selectivity achieved with non-supported D-proline-based molecules (D-S1 and D-S2) or with the polymer-supported nanocatalysts AC3 and AC6 was similar to homologues L-catalysts (L-S1, L-S2, AC2, and AC5).

The magneto-responsive catalysts AC2 and AC5 were magnetically separated from the product, extracted with diethyl ether, washed, and reused during four cycles of reaction. The conversion and the enantioselectivity of the reaction were maintained after each cycle of reaction, as shown in Figure 6.9, which reveals the consistency of the activity of the catalyst.

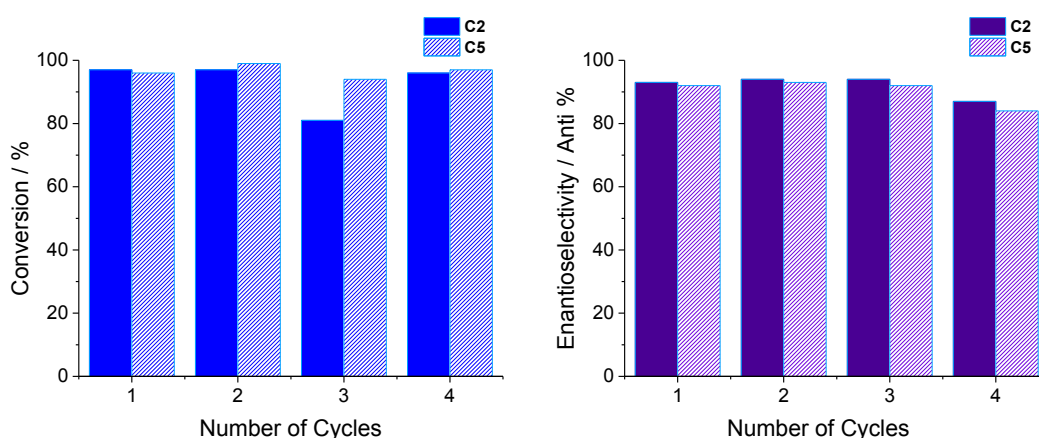


**Figure 6.9.** Recycling study: conversion (left) and enantioselectivity (right) of the aldol reaction catalyzed by the magneto-responsive chiral catalysts AC2 and AC5 during four cycles of reaction.

## 6.5 Conclusions

This work highlights the use of chiral surfmers in miniemulsion polymerization processes for the incorporation of units of hydroxy-*L/D*-proline accessible on the surface of PMMA nanoparticles with additional magnetic functionalities. The magneto-responsive chiral nanoparticles showed high performances for the asymmetric catalysis of the intermolecular aldol reaction between *p*-nitrobenzaldehyde and cyclohexanone in water. The high conversion, enantioselectivity, stability, and recyclability of the surfmer-based nanocatalyst were comparable to the results obtained using a traditional proline-based comonomer. The surfmer structure avoids the use of conventional surfactants, which need to be typically removed before the application. In addition, this work highlights the high enantioselectivity achieved for the organocatalysis of an intermolecular aldol reaction using water as a sole solvent.



# 7 Magnetic Polyurethane Microcarriers from Nanoparticle-Stabilized Emulsions for Thermal Energy Storage

This chapter is focused on the development of multifunctional polyurethane–metal oxide hybrid microcapsules via interfacial polymerization processes in nanoparticle-stabilized emulsions. Different metal oxide nanoparticles with magnetic (i.e., magnetite) and catalytic (i.e., titania or ceria) properties were used as inorganic stabilizers for the encapsulation of sodium sulfate decahydrate salt, taken as a model of an inorganic hydrated salt. The aqueous core and the capsule microstructure offered a hermetic confinement for the protection of hydrated salts to be potentially used as phase change materials (PCM) in thermal energy storage applications. The thermal and chemical stability of the salt was guaranteed by its encapsulation. The magnetic polyurethane microcarriers were optimized for thermal energy storage applications at mild temperatures with reduced supercooling. In addition, the high thermal conductivity of the magnetite nanoparticles contributed to an efficient heat transfer through the polyurethane shell.

## 7.1 State of the Art: Phase Change Materials for Thermal Energy Storage Applications

The rapid advance of industrialization in our society has driven to the uncontrolled increase of the energy consumption, the acceleration of the depletion of fossil fuels, and an important environmental pollution. In this context, competitive clean renewable energies, which still nowadays face low efficiency and intermittence problems, are highly demanded for the sustainability of our economies and our planet. For these reasons, the optimization of the production, the use, the management, the recovery, and the recycling of energy via storage technologies (i.e., thermal, mechanical, electromagnetic, hydrogen and electrochemical energy storage)<sup>238-239</sup> is highly required. In the last decades, the development of energy storage materials has been on the scope of diverse research communities and industrial sectors. In particular, thermal energy offers a simple way of energy storage, either as the sensible heat (SH) related to the thermal capacity of a fluid, as the latent heat (LH) associated to phase transitions, as thermochemical reactions (TCE), or as a combination of those.<sup>239</sup> Latent heat storage systems provide the highest

density of energy storage via isothermal processes of change of phase (i.e., solid–solid, liquid–solid or liquid–gas). The energy involved in such phase transitions is related to the number of bonds broken; thus, the liquid–gas transformations would theoretically provide the best energetic contribution. However, the great changes in volume occurring during liquid–gas transformations make the strategy unpractical. Solid–solid transitions are long processes related to changes in the crystalline structure, which often require high temperatures. Therefore, the most promising candidates for energy storage are the so-called phase change materials (PCMs), which store the latent heat of solid–liquid transitions (i.e., the energy is stored during a melting process and further recovered during the recrystallization of the system occurred with a decrease of the temperature).<sup>240-241</sup> Nowadays, PCMs are being commercially applied in a wide range of sectors (e.g., off-peak electricity storage, solar technologies, thermo-regulated textiles and buildings, refrigeration and cold storage,<sup>242</sup> or industrial waste heat recovery).<sup>239, 243-246</sup> The most recent lines of research are moving towards the development of other cutting-edge systems (e.g., heat-transfer fluids, energy harvesting, vectors for biomedicine with controlled diffusivity and drug delivery, sensing, or storage of optical information). Such applications require the optimization of the storage efficiencies and stability of the materials.<sup>240-241</sup>

According to their nature, PCMs are classified into organic (paraffin waxes, fatty acids, alcohols, and glycols), inorganic (i.e., hydrated salts, and metallic compounds) or eutectic mixtures (i.e., inorganic–organic, organic–organic, and inorganic–inorganic). Inorganic phase change materials, and more precisely hydrated salts, present attractive high energy storage capacities per mass and per volume and small changes of volume, which are clear advantages with respect to the low densities of traditional organic PCMs. Hydrated salts are inorganic salts with the typical formula  $AB \cdot nH_2O$ , containing water of crystallization. During the phase change, the dehydration of the salt occurs, leading to the formation of either the anhydrous form of the salt (AB) or another stable phase with fewer molecules of water ( $AB \cdot mH_2O$ , with  $m < n$ ). These crystallohydrates are commercially available at low prices for a wide range of operational temperatures.<sup>246-247</sup> However, this type of PCMs often suffers from problems of chemical and thermal instability (i.e., incongruent melting, and phase segregation with a progressive loss of their hydration level and storage capacity during the recycling), or corrosion of the surrounding media.<sup>243-244, 248</sup> In addition, the low nucleating ability of hydrated salts commonly results in the supercooling of the system (i.e., the material recrystallizes at a temperature much lower than the melting point), which hinders their application.<sup>249</sup> The enhancement of their energy storage capacity and stability has been addressed by incorporation of elements with high thermal conductivity or via encapsulation techniques.



The so-called core-shell encapsulation (micro-<sup>246</sup> and nano-encapsulation<sup>241</sup>) strategies have been commonly used to overcome the instability problems of the crystallohydrates. Capsules offer a confined space with higher heat transfer area, reduced reactivity with the outer environment and controlled changes of volume during the phase transition.<sup>250</sup> Diverse chemical (e.g., emulsion/miniemulsion polymerization,<sup>251-252</sup> phase separation, solvent evaporation,<sup>253-255</sup> in-situ polymerization and solvent evaporation,<sup>256-257</sup> interfacial polymerization,<sup>9</sup> or surface-thiol Michael addition polymerization<sup>258</sup>), physicochemical (e.g., sol-gel and inorganic precipitation processes),<sup>259-260</sup> and mechanical (e.g., mechanical packaging with or without electroplating methods)<sup>261</sup> techniques have been successfully used for the encapsulation of salts and hydrated salts.<sup>250</sup> Sodium phosphate dodecahydrate, sodium sulfate decahydrate, magnesium nitrate hexahydrate, and mixtures of two different salts were commonly encapsulated within different polymer (e.g., PMMA<sup>256-257</sup> or poly(ethyl-2-cyanoacrylate)<sup>251-252</sup>), inorganic (e.g., silica),<sup>255, 260</sup> or polymer-inorganic (e.g., polyurethane-silica)<sup>9</sup> hybrid capsules. The high encapsulation rates achieved (up to 94.65 wt.%)<sup>254</sup> in most of the cases did not guarantee the stability of the crystallohydrate and problems related with the lack of thermal cycling stability, phase segregation, or supercooling were still present. Figure 7.1 presents the cycles of thermal energy storage and release achieved via the melting/recrystallization process of microencapsulated PCMs.

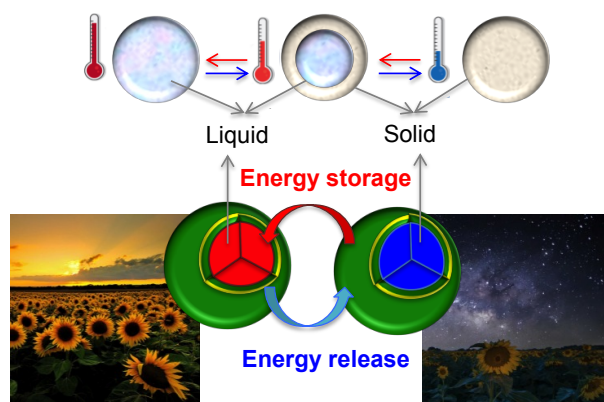


**Figure 7.1.** Schematic representation of the energy storage and release in microencapsulated PCMs. (Based on refs. 251 and 250. Image credit: Black Thumb Gardener and Sunflowers at night by Jason Squyres)

Regarding the functionalization of capsules, the techniques of layer-by-layer deposition<sup>262-264</sup> or electroless plating<sup>265</sup> have been widely used for the embedment of magnetic nanoparticles in a polymer shell. Also, superparamagnetic polyamide microcapsules with a controllable release via thermo-responsive gates of poly(*N*-isopropylacrylamide) were prepared by interfacial polymerization and further plasma-induced grafting polymerization.<sup>266</sup> The combination of

catalytic and magnetic functionalities in the protecting shell of inorganic capsules (magnetite–silica<sup>267</sup> and magnetite–titania<sup>268</sup>) was reported for the encapsulation of organic phase change materials (*n*-docosane<sup>267</sup> and eicosane<sup>268</sup>) via interfacial polycondensation processes in direct Pickering emulsions. The multifunctional capsules were used in bioapplications as thermoregulatory enzyme carriers<sup>268</sup> or biocatalytic enzyme enhancers.<sup>267</sup>

This chapter describes the encapsulation of sodium sulfate decahydrate salt ( $\text{Na}_2\text{SO}_4 \cdot 10\text{H}_2\text{O}$ ) as a PCM with a sharp melting process at 32.4 °C and high melting enthalpy ( $254 \text{ kJ} \cdot \text{kg}^{-1}$ ),<sup>243, 269-271</sup> within the aqueous core of polyurethane–metal oxide hybrid capsules. Hybrid carriers combine the stability and thermal efficiency of hydrated salts for thermal energy storage, with the synergic combination of a polymer confinement (i.e., polyurethane shell) tuned with specific inorganic functionalities (i.e., magnetic and catalytic). The special interest on the preparation of magnetic microcapsules, besides the advantages in terms of purification, is related to the controllable application (both for storage and release) in specific target locations/moments using an external magnetic field.

## 7.2 Preparation of Nanoparticle-Stabilized Inverse Emulsions

The preparation of inverse Pickering emulsions was addressed by using magnetic (i.e., magnetite), and catalytic (i.e., titania and ceria) nanoparticles as inorganic stabilizers. In addition, silica nanoparticles were also used as a model for comparison with the other functional systems. As explained in section 2.4.2, the relative wettability and the contact angle of the inorganic nanoparticles between two immiscible liquid phases (e.g., water and cyclohexane) needs to be suited to promote the formation of an adsorbed layer of inorganic nanoparticles at the droplet interface. In general, hydrophilic nanoparticles stabilize direct emulsions, whereas hydrophobic nanoparticles promote the formation of inverse emulsions. Metal oxide nanoparticles, either commercial or synthesized by precipitation methods, commonly present charged groups (e.g.,  $\text{OH}^-$  groups) on their surface creating a hydrophilic environment. The required hydrophobization was reached by surface functionalization of the metal oxides nanoparticles using three alkoxy silane components (i.e., MPS, PTMS, and ODTMS) with different polarity and chemical structure. The successful performance of the functionalization strategy was proven by thermogravimetric analysis (TGA) of the inorganic nanoparticles before and after silanization, as already shown in Chapter 4. The mass loss determined with the TGA curves (shown in Figure 7.2) for the ODTMS-functionalized and the pristine nanoparticles without functionalization allows us to determine the

amount of ODTMS that remained covalently attached to the inorganic species after several washing operations.

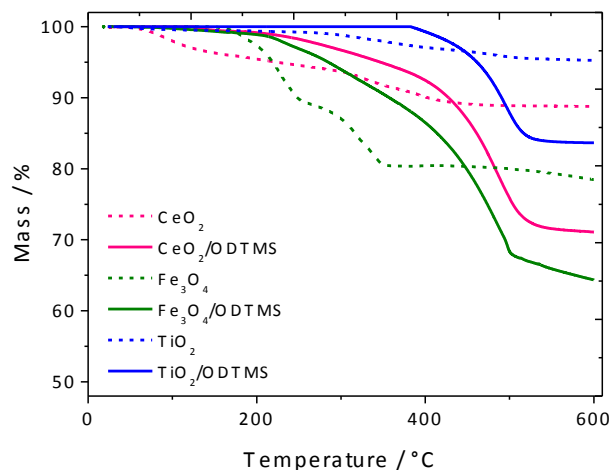


**Figure 7.2.** TGA curves of ODTMS-functionalized ceria (magenta line), magnetite (green line), and titania (blue line) nanoparticles and the corresponding pristine particles without functionalization (dashed lines).

Ceria and magnetite present an equivalent incorporation of the functionalizing agent (20 wt.%), whereas the amount of ODTMS attached to the titania nanoparticles is lower. This difference is explained by the pre-functionalization and the rod-like shape of the commercial titania nanoparticles, which hinders the attachment of silane to the inorganic surface.

Differently from the results reported in a previous work dedicated to the incorporation of silica,<sup>9</sup> the long alkyl chains and the absence of polymerizable units in the structure of ODTMS offered the best ability to promote the Pickering stabilization in the pure magnetic, catalytic, or multifunctional system, as shown in Figure 7.3.

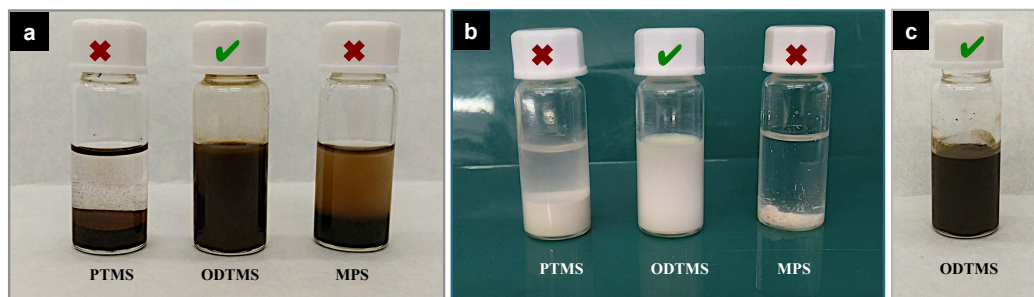


**Figure 7.3.** Colloidal stability of the dispersion polyurethane-metal oxides hybrid capsules prepared in inverse Pickering emulsion using (a) magnetite (b) titania, and (c) magnetite–titania nanoparticles with different surface functionalization (with MPS, PTMS or ODTMS) as inorganic stabilizers.

### 7.3 Preparation of Polyurethane–Metal Oxide Hybrid Capsules by Interfacial Polymerization in Inverse Pickering Emulsion

Hermetic polyurethane capsules<sup>9, 272-273</sup> have been traditionally prepared via interfacial polymerization processes, as described in section 2.6.5. In this chapter, the synthesis was carried out in Pickering-stabilized inverse emulsions aiming the development of multifunctional materials for encapsulation purposes. Inverse emulsions were prepared with an aqueous solution of a water-soluble monomer (1,6-hexanediol) and the substances to be encapsulated, dispersed in a continuous phase of cyclohexane and the ODTMS-functionalized metal oxide nanoparticles. Both phases were mixed, homogenized and the Pickering emulsion was finally achieved by ultrasonication. The diffusion of second monomer soluble in cyclohexane (i.e., toluene-2,4-diisocyanate, TDI), which was externally added resulted into an interfacial polyaddition process driven by the contact with the diol from the droplets. Therefore, a polyurethane shell protecting an aqueous core with the hydrophilic species was formed. The metal oxide nanoparticles remained incorporated on the outer surface or partially embedded within the polymer shell, providing the capsule with the aimed functionality.

The performance of the preparation method was proven by observation of the samples by electron microscopy. As proof-of-concept, the TEM micrograph in Figure 7.4 shows the integrity of the polyurethane capsules prepared using ODTMS-functionalized silica nanoparticles as a model inorganic system.

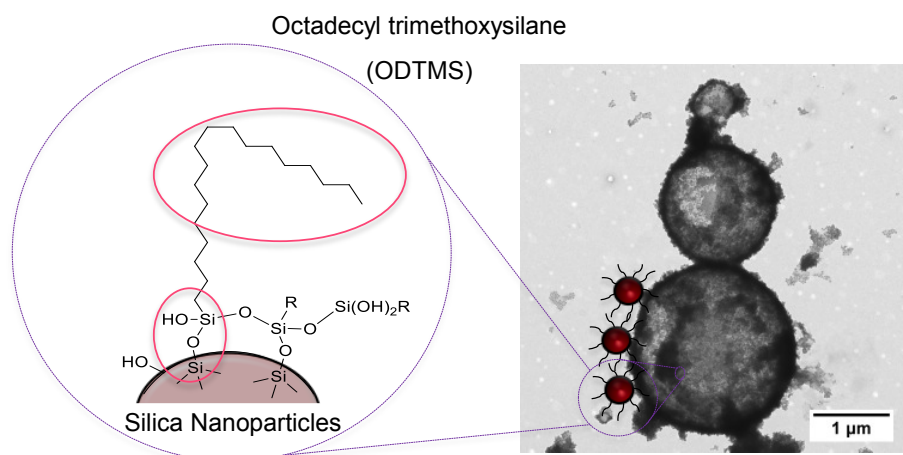


**Figure 7.4.** TEM micrographs of polyurethane capsules prepared using ODTMS-functionalized silica nanoparticles.

The size, shape, and hydrophobicity of the inorganic species explain the different stabilization ability of each inorganic system, and consequently, the size of the droplets and the capsules achieved. The capsules prepared using magnetite, titania, and ceria nanoparticles as inorganic stabilizers presented significant differences in the size. The size distribution diagrams obtained from statistical treatment of TEM images in Figure 7.5 reveal average values of  $(2.1 \pm 1.4)$ ,  $(2.0 \pm 1.3)$ , and  $(1.7 \pm 0.8)$   $\mu\text{m}$  for the systems containing titania, magnetite, and ceria nanoparticles, respectively. The difference on hydrophobicity of the nanoparticles is highlighted as the governing parameter determining the inorganic migration within the polymer shell. SEM images from Figure 7.6(a) show the partial engulfment of magnetite nanoparticles within the polymer shell, whereas titania and ceria remain mostly accessible on the surface of the capsule, as observed in Figure 7.6(b–c).

The incorporation of two different inorganic species with complementary (i.e., magnetic and catalytic) functionalities allowed the preparation of a second generation of multifunctional polyurethane–magnetite–titania and polyurethane–magnetite–ceria hybrid microcapsules. The integrity of the capsules and the reduction of size and polydispersity from  $(1.8 \pm 0.8)$  to  $(1.0 \pm 0.6)$   $\mu\text{m}$  were achieved when ceria was used as catalytic species instead of titania, as proven by the TEM images in Figure 7.7. SEM images in Figure 7.8 reveal the absence of any apparent competition in the migration and self-assembly of the catalytic and the magneto-responsive nanoparticles within the polymer shell. Accordingly, the multifunctional materials are similar with regard to the surface level.

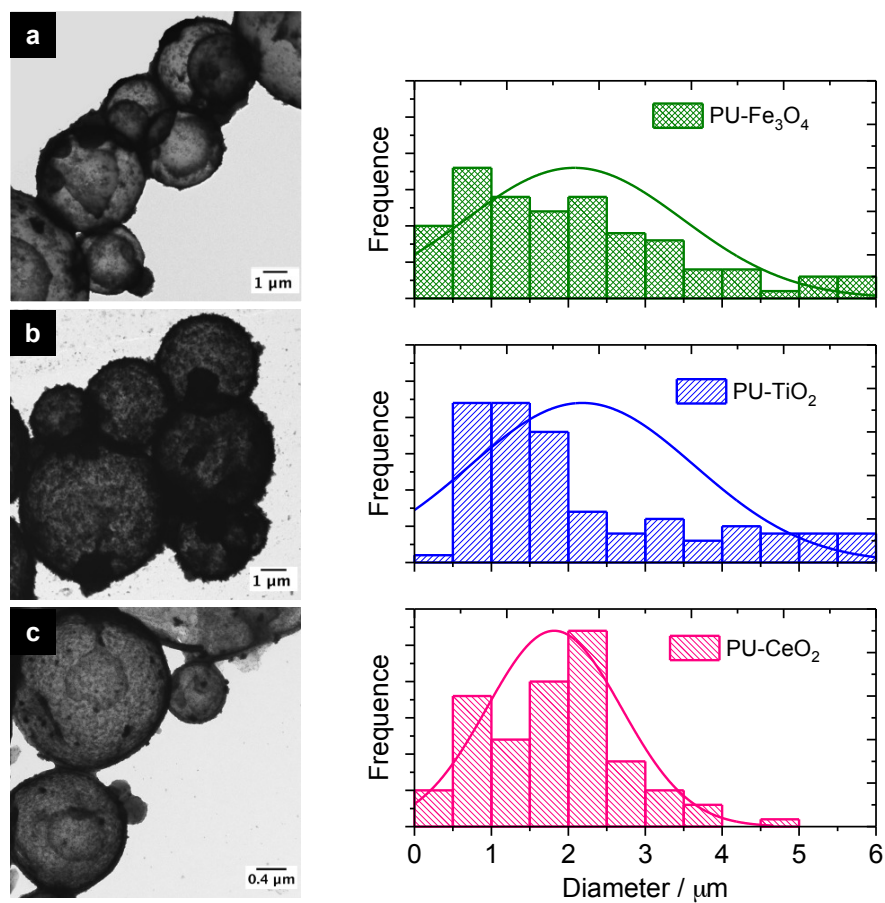


**Figure 7.5.** TEM micrographs and size distribution diagrams of polyurethane capsules incorporating magnetite (a), titania (b), and ceria (c) nanoparticles.

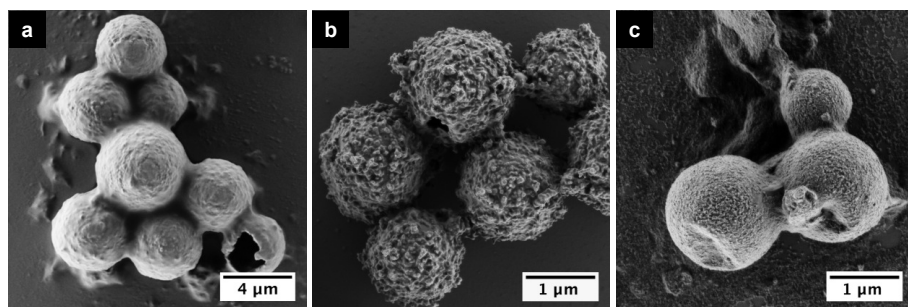


**Figure 7.6.** SEM micrographs of polyurethane capsules incorporating magnetite (a), titania (b), and ceria (c) nanoparticles.



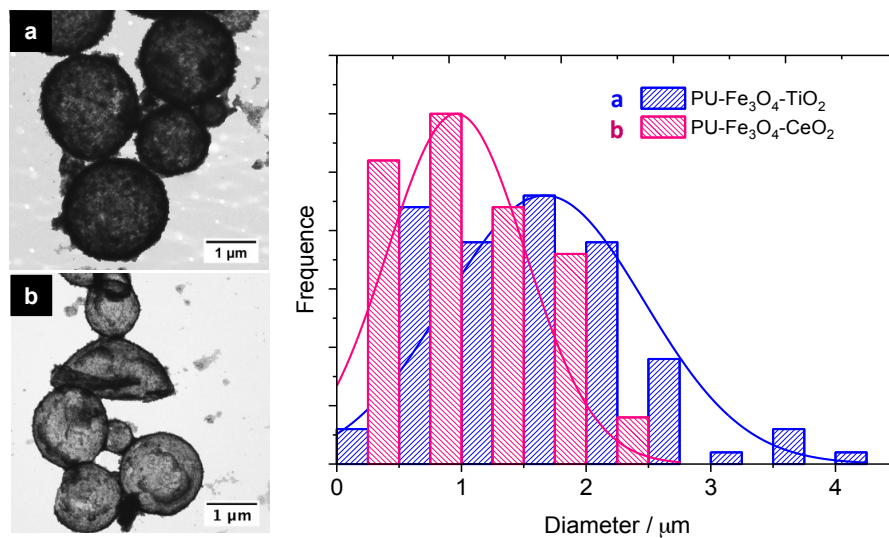


**Figure 7.7.** TEM micrographs and size distribution of multifunctional polyurethane capsules incorporating two inorganic species: magnetite–titania (a) and magnetite–ceria (b).

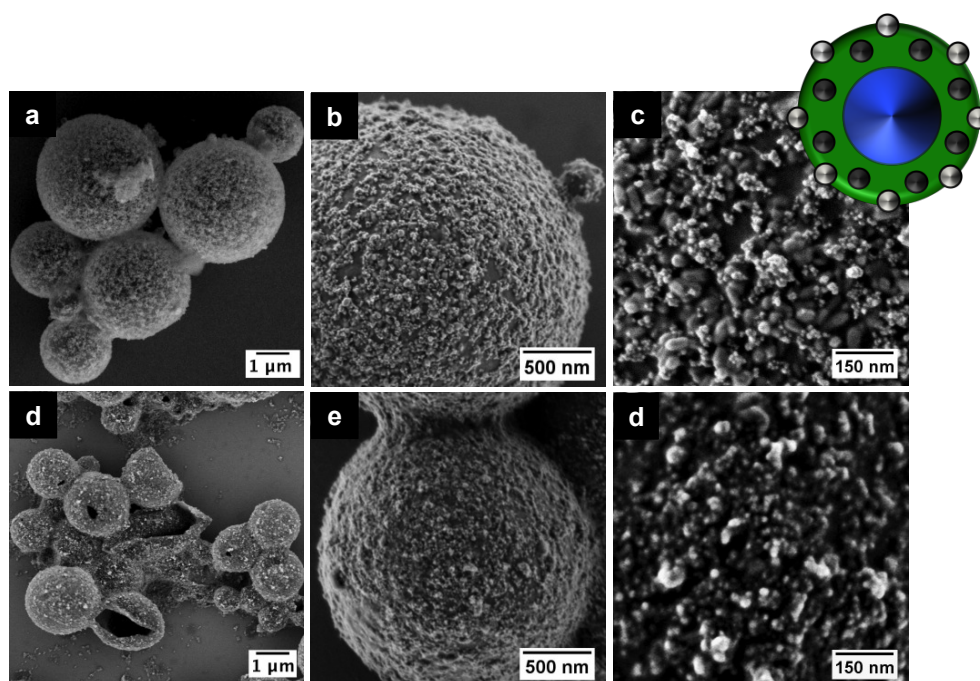


**Figure 7.8.** SEM micrographs of multifunctional microcapsules of polyurethane–magnetite–titania (a–c) and polyurethane–magnetite–ceria (d–f) at different magnifications.

## 7.4 Study of the Suitability of the Hybrid Structures for Encapsulation Purposes

The encapsulation of phase change materials for thermal energy storage applications requires highly hermetic systems (without leakages) that provide an efficient interface for heat exchange with ability to support pressure–volume changes. The suitability of the capsules as encapsulating systems was studied by an indirect method of dialysis that allowed us to track the release of a hydrophilic dye occurred when the capsules were placed in an aqueous environment.<sup>274</sup> Brilliant Blue FCF, whose chemical structure and absorption spectra are shown in Figure 7.9 was chosen as a commercial dye to be encapsulated.

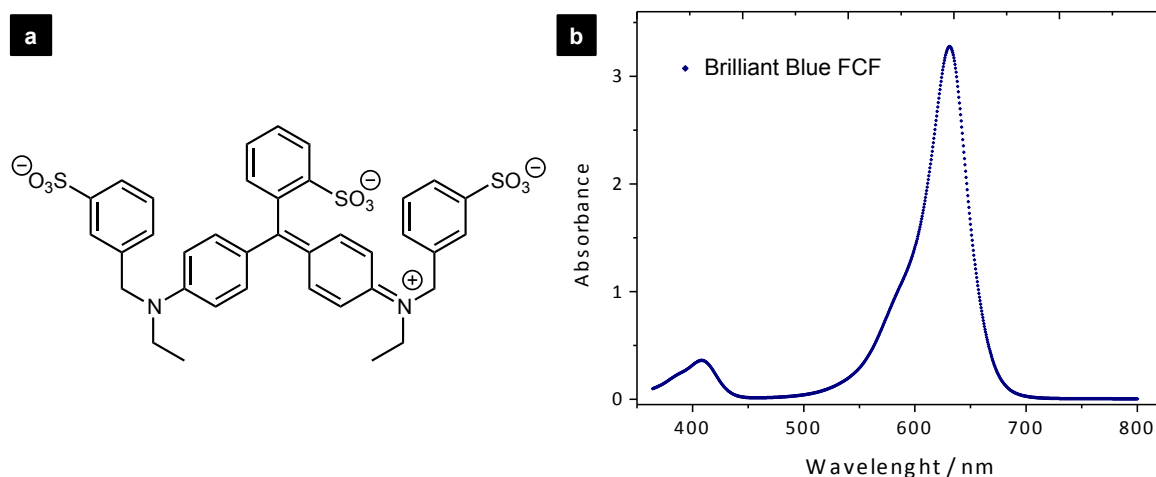


**Figure 7.9.** Chemical structure (a) and absorption spectra (b) of the dye Brilliant Blue FCF.

The triarylmethane structure of the dye guarantees the chemical stability in the presence of the starting monomers (i.e., the diol and the isocyanate). The concentration of the dye released from the capsules placed in an aqueous environment was followed by an indirect method of dialysis. For this aim, aqueous dispersions of the capsules with the dye were introduced in dialysis membranes immersed within aqueous solutions. The concentration of the dye released and diffused through the dialysis membrane was followed via determination of the absorbance of the outer solution by UV-Vis spectroscopy (Figure 7.10).



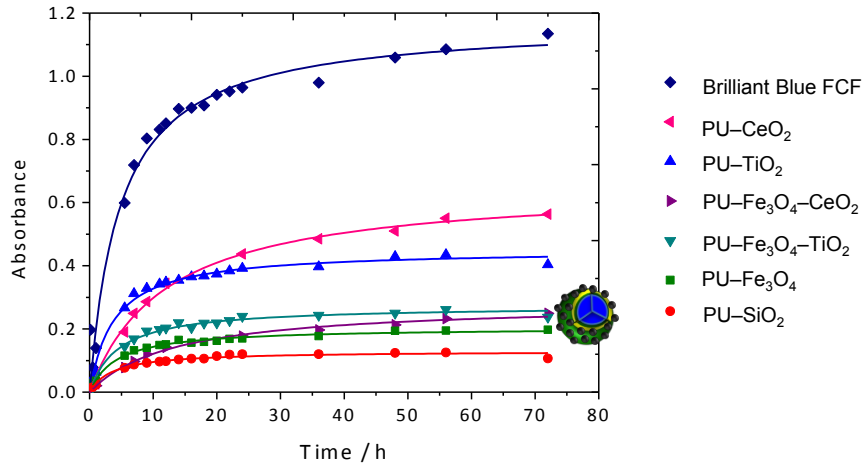


**Figure 7.10.** Study of the release of the dye Brilliant Blue FCF encapsulated (5 wt.%) within the hybrid polyurethane-based microcapsules incorporating different inorganic nanoparticles or mixtures of them.

The experimental values of absorbance ( $A$ ) were fitted to the following empiric expression, as a function of time ( $t$ ):

$$A = A_{\max} \frac{t}{k + t} \quad (7.1)$$

The empiric values of the absorbance at time infinite ( $A_{\max}$ ) and a constant ( $k$ ) associated to the diffusion rate of the dye of each type of sample are listed in Table 7.1.

**Table 7.1.** Empiric values of the parameters  $A_{\max}$  and  $k$  calculated for each experiment of release.

Sample	$A_{\max}$	$k$ ( $\text{h}^{-1}$ )
Brilliant Blue FCF	1.17	4.80
PU-SiO <sub>2</sub>	0.13	3.63
PU-Fe <sub>3</sub> O <sub>4</sub>	0.20	4.23
PU-CeO <sub>2</sub>	0.65	11.97
PU-TiO <sub>2</sub>	0.46	3.76
PU-Fe <sub>3</sub> O <sub>4</sub> -CeO <sub>2</sub>	0.28	13.38
PU-Fe <sub>3</sub> O <sub>4</sub> -TiO <sub>2</sub>	0.27	4.49

The percentage of dye released was estimated by comparison between the absorbance measured at the equilibrium of the corresponding sample and the reference experiment associated to a complete release (dark blue line). The relevance of the average release of the dye observed (with minimum values of 10–20 wt.%) was played down based on the evidences of breakage of the polyurethane shell during the last sonication step (for the redispersion of the capsules). Thus, we assume that a

significant fraction of the dye that diffuses through the dialysis membrane came from the broken capsules. The polyurethane capsules incorporating magnetite (green, turquoise, and violet lines in Figure 7.10) offer the most hermetic functional confinement, so that they are considered as suitable systems for encapsulating purposes.

#### 7.4.1 Encapsulation of Phase Change Materials for Thermal Energy Storage

Sodium sulfate decahydrate salt ( $\text{Na}_2\text{SO}_4 \cdot 10\text{H}_2\text{O}$ ), also known as Glauber salt, was chosen as a phase change material (PCM) with promising features for thermal energy storage applications close to room temperature.<sup>243, 269-270</sup> Different microencapsulation techniques have been used to minimize/avoid the inherent problems of thermal and chemical instability of the hydrated salt. Biswas et al.<sup>275</sup> established that the use of extra water prevents the formation and precipitation of heavy anhydrous forms of the salt at expenses of reducing the storage density and broadening the range of the temperature transition. Thus, an aqueous solution of  $\text{Na}_2\text{SO}_4 \cdot 10\text{H}_2\text{O}$  (20 wt.%) was encapsulated within the magneto-responsive microcapsules (i.e., polyurethane capsules with magnetite, magnetite and titania, or magnetite and ceria, designed as **PC1**, **PC2**, and **PC3** respectively). Higher concentrations of incorporation of the salt were not allowed by the technique, as a consequence of the problems of solubility reported by Schoth et al.<sup>9</sup> Table 7.2 presents the composition of the capsules containing the phase change material (i.e., the incorporation of the inorganic species and the encapsulation of the salt) determined by ICP-MS. The PCM was successfully encapsulated and homogeneously distributed within the population of magnetic carriers as observed in the TEM (dark areas within the capsules) images of Figure 7.11.

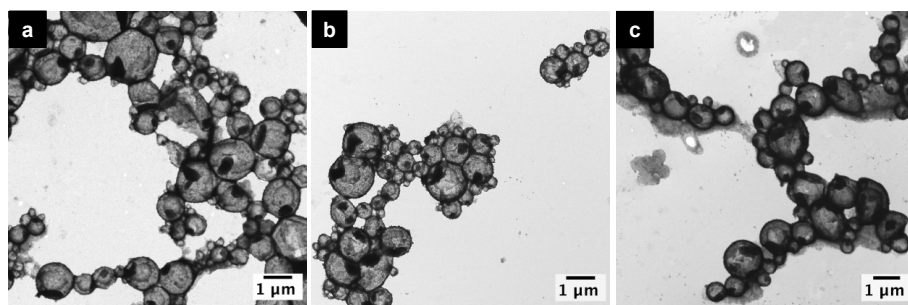


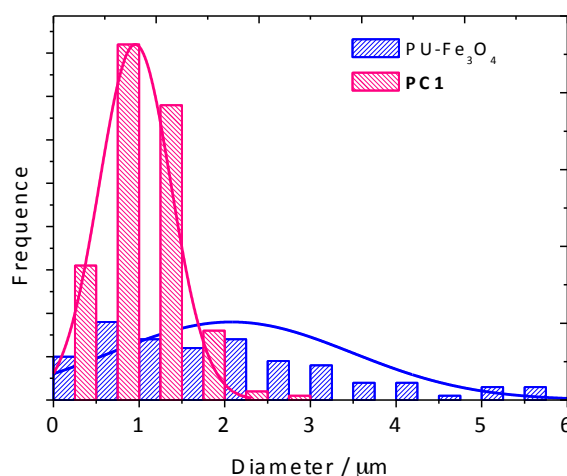
**Figure 7.11.** TEM micrographs of polyurethane capsules with magnetite (a), magnetite–titania (b), and magnetite–ceria (c) nanoparticles, encapsulating  $\text{Na}_2\text{SO}_4 \cdot 10\text{H}_2\text{O}$  salt.

**Table 7.2.** Main features of the magneto-responsive polyurethane capsules for thermal energy storage.

Material	Fe <sub>3</sub> O <sub>4</sub> <sup>a</sup> /wt. %	TiO <sub>2</sub> <sup>a</sup> / wt. %	CeO <sub>2</sub> <sup>a</sup> / wt. %	PCM <sup>a</sup> / wt.%	d <sup>b</sup> (μm)
<b>PC1</b>	25.81 ± 0.15			24.9 ± 0.2	1.0 ± 0.4
<b>PC2</b>	15.40 ± 0.12	25.5 ± 0.5		13.89 ± 0.12	0.6 ± 0.3
<b>PC3</b>	20.64 ± 0.16		10.07 ± 0.37	20.46 ± 0.12	0.7 ± 0.4
<b>PC4</b>	31.03 ± 0.17			32.2 ± 0.3	0.8 ± 0.4

<sup>a</sup> Determined by ICP-MS.<sup>b</sup> Determined by statistical treatment of TEM images accounting at least 200 capsules.

The comparison of the size distribution between the polyurethane–magnetite capsules with and without salt in Figure 7.12 confirms the role of the salt as an osmotic pressure agent. The salt minimizes the Ostwald ripening phenomena and increases the stability of the Pickering emulsion, which results in a reduction from (2.0 ± 1.3) to (0.9 ± 0.4) μm of the capsule size and polydispersity. A similar trend was observed for the magneto-responsive and catalytically active hybrid microcapsules.

**Figure 7.12.** Size distribution of the polyurethane–magnetite hybrid capsules with (magenta) and without (blue) 20 wt. % of Na<sub>2</sub>SO<sub>4</sub>·10H<sub>2</sub>O salt.

The thermal behavior of the thermosensitive and magneto-responsive carriers was studied by differential scanning calorimetry (DSC). The study of the salt in bulk shown Figure 7.13(a) confirmed a high melting enthalpy (210 J·g<sup>-1</sup>) and a low melting temperature (36 °C), close to the theoretical values (250 J·g<sup>-1</sup> and 36 °C, respectively). Problems of cycling instability, incongruent melting with a loss of thermal storage capacity to 130 J·g<sup>-1</sup> after the second thermal cycle, phase segregation, and supercooling were patent and justified the encapsulation of the salt. The magneto-responsive capsules (**PC1**, **PC2** and **PC3**) were subjected to four cycles of heating and

cooling around the melting and crystallization temperatures ( $-50$  to  $60/90$  °C) determined for the salt in bulk. The corresponding DSC diagrams are shown in Figure 7.13(b–d).

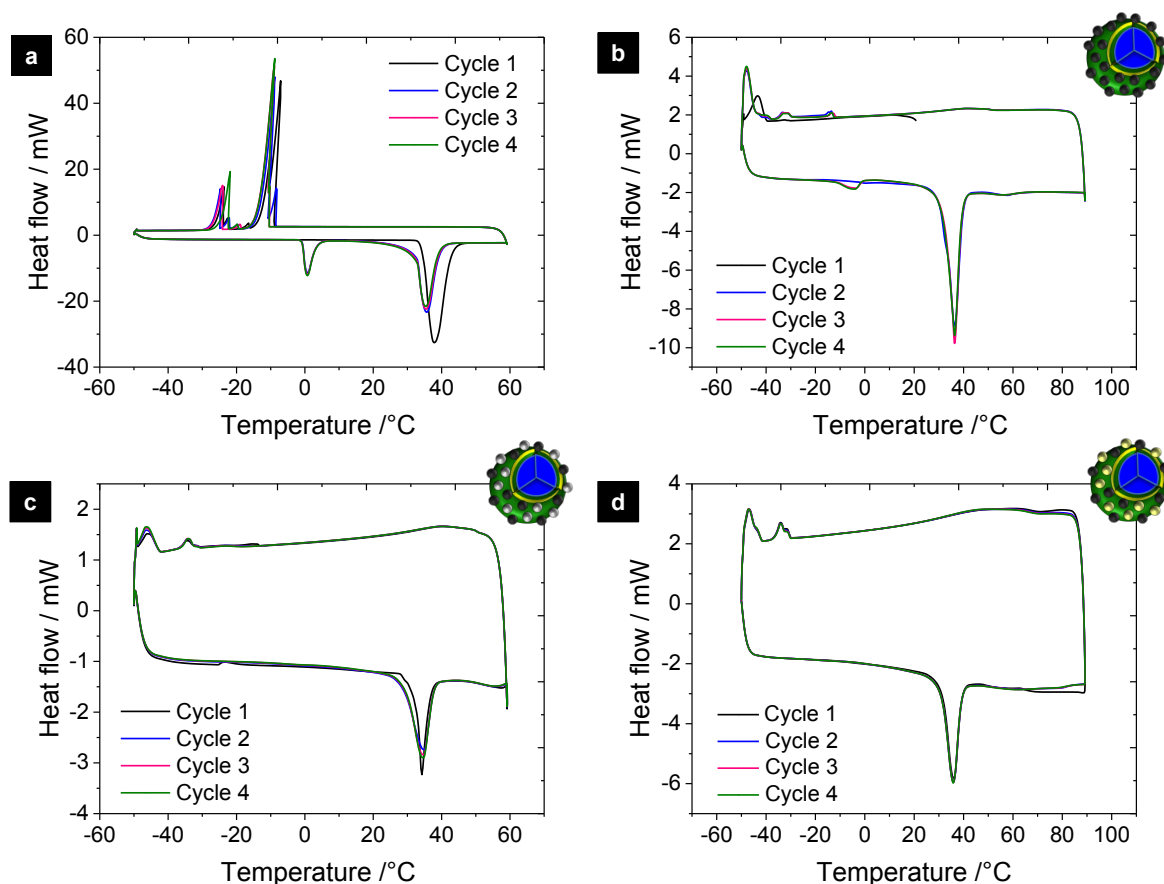


**Figure 7.13.** Thermal analysis by differential scanning calorimetry of Na<sub>2</sub>SO<sub>4</sub>·10H<sub>2</sub>O salt in bulk (a), and encapsulated (20 wt. %) within the magnetoresponsive polyurethane hybrid microcapsules **PC1** (b), **PC2** (c), and **PC3** (d).

Similarly to the results from a previous work based on polyurethane–silica capsules,<sup>9</sup> when solely magnetite was used as an inorganic component, the system **PC1** presented a melting enthalpy of  $(50.0 \pm 1.0)$  J·g<sup>-1</sup> at 36 °C. However, a noticeable reduction of the enthalpy values of  $(10.0 \pm 0.2)$  and  $(15.0 \pm 0.3)$  J·g<sup>-1</sup> were obtained for **PC2** and **PC3**, respectively. These values are in agreement with the encapsulation efficiency of each system shown in Table 7.2. Despite the efficient storage capacity of the salt during the melting process offered by the magnetite-based capsules, neither the formation of the metastable phase (i.e., sodium sulfate heptahydrate) during the recrystallization nor the supercooling of the system below  $-20$  °C were corrected.

The combination of thickening (e.g., bentonite clay) and nucleating agents (e.g., borax, or sodium dihydrogen phosphate dihydrate) has been used to overcome the phase segregation and

supercooling problems of sodium sulfate decahydrate salt, respectively.<sup>276</sup> However, the thermal conductivity of the resulting mixtures was reduced and the crystallization rate and heat transfer consequently decreased. A small amount of sodium dihydrogen phosphate dihydrate (2 wt.%  $\text{Na}_2\text{HPO}_4 \cdot 2\text{H}_2\text{O}$  with respect to  $\text{Na}_2\text{SO}_4 \cdot 10\text{H}_2\text{O}$ ) was incorporated as a nucleating agent within the aqueous core of the polyurethane–magnetite microcapsules **PC4**. The integrity of the magneto-responsive capsules was altered neither by the slightly higher concentration of salt in the aqueous core nor by the presence of different hydrated systems, as observed in the TEM and SEM images from Figure 7.14.

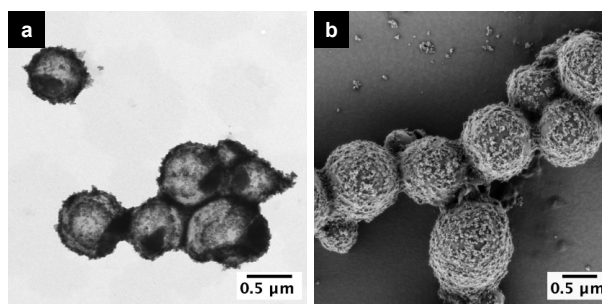


**Figure 7.14.** TEM (a) and SEM (b) micrographs of the capsules **PC4**.

The incorporation of the second salt results in an average capsule diameter of  $(0.8 \pm 0.4) \mu\text{m}$  for the magneto-responsive capsules **PC4**, which is close to the value previously determined for sample **PC1** (without nucleating agent), as shown in Figure 7.15.

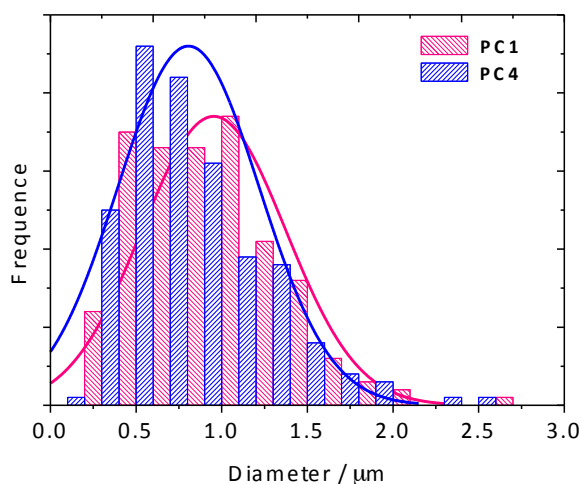


**Figure 7.15.** Size-distribution diagrams of the capsules **PC4**.

The DSC thermogram for the  $\text{Na}_2\text{HPO}_4 \cdot 2\text{H}_2\text{O}$  salt in bulk depicted in Figure 7.16(a) allows us to discard the existence of any possible thermal process related to this salt within the range of

temperatures of the thermal study. The contribution of the phosphate salt is only attributed to the increase of the nucleating ability of the sodium sulfate decahydrate, which experiments a heterogeneous nucleation process, and overcomes both phase segregation, and supercooling problems. The results obtained by DSC for **PC4** (Figure 7.16(b)) reveal a sharp recrystallization at 10 °C leading to the most stable, the decahydrated state of the salt within the operational temperatures. During four thermal cycles, the  $\text{Na}_2\text{HPO}_4 \cdot 2\text{H}_2\text{O}$  salt maintained a melting enthalpy of  $(60 \pm 1.2) \text{ J} \cdot \text{g}^{-1}$  associated to the melting process occurring at 35 °C.

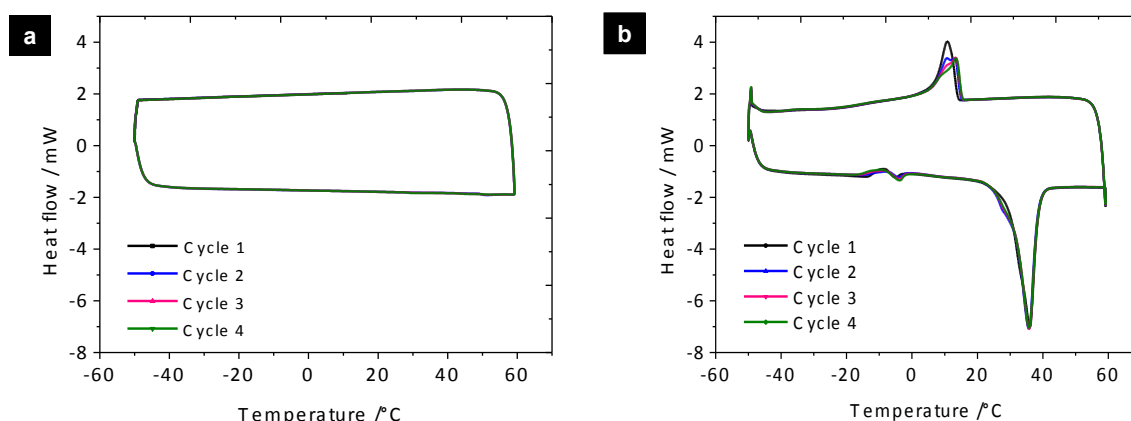


**Figure 7.16.** Thermal analysis by differential scanning calorimetry of  $\text{Na}_2\text{HPO}_4 \cdot 2\text{H}_2\text{O}$  salt in bulk (a) and the **PC4** capsules (b).

## 7.5 Conclusions

Versatile interfacial polymerization processes have been developed in inverse Pickering emulsions for the preparation of polyurethane–metal oxide hybrid submicron capsules with an aqueous core. Pickering emulsions offer synthetic advantages and allow the incorporation of specific functionalities while avoiding the use molecular surfactants. The synthetic platform has been applied for the encapsulation of hydrated salts, as phase change materials with promising properties for energy storage applications that in bulk suffer from severe problems of instability. The confinement and the thermal conductivity offered by the polyurethane shell with the magnetite nanoparticles embedded in it offered a protective environment to promote the chemical and thermal stability of sodium sulfate decahydrate salt, a PCM with high energy storage capacity. The incorporation of a second salt (i.e., disodium hydrogen phosphate dihydrate) as a nucleating agent allowed us to solve the phase segregation and supercooling problems intrinsic from the sulfate salt

in bulk. The resulting magneto-responsive polyurethane-based microcarriers showed high performance and stability for thermal energy storage applications close to room temperature.

The use of a magneto-responsive component as inorganic emulsifier for the synthesis of the hybrid microcapsules provided an added value to the final product, apart from the synthetic advantages in terms of purification. The controlled application of an external magnetic field could potentially allow the storage of thermal energy in specific locations and the control over the charge and discharge operations by redirection of the magnetic microcarriers between two points at different temperatures. This ability would be especially attractive for the preparation of semicontinuous cycles of energy storage and release, in which the heating of some units of a chemical process occurred at expenses of the cooling of others. In addition, the compatibility of the capsules with aqueous media makes them suitable for the formulation of dispersions of thermo- and magneto-responsive carriers for thermal energy storage.





## 8 Summary and Outlook

This thesis offers a toolbox for the preparation of multifunctional polymer–metal oxide hybrid nanoparticles and capsules with controlled structure via synthetic methods in miniemulsion. The morphologic development of the nanohybrids is controlled by modification of the hydrophobicity and surface chemistry of the inorganic species. Different materials with a specific arrangement and accessibility of the inorganic/organic functionalities are developed according to the requirements of the aimed application.

The control of the migration of individual inorganic species within a polymer matrix was first addressed in Chapter 4 by tuning the polarity of the inorganic surface via silane chemistry. Magneto-responsive (magnetite) or catalytically active (ceria and titania) metal oxides functionalized with silane components were incorporated within nanoparticles of polystyrene or poly(methyl methacrylate) (PMMA) by miniemulsion polymerization processes. The chemical structure of the coupling agent (a silane derivative) was proven to be the major parameter governing the hybrid morphology, overtaking the effect of the type initiator, the polymer, or the inorganic species. In this fashion, the long alkyl chain of octadecyl trimethoxysilane (ODTMS) and the absence of a polymerizable group as in the case of propyl trimethoxysilane (PTMS) lead to phase segregation and deposition of the inorganic nanoparticles at the polymer/water interface or to the formation of Janus-like structures. The presence of a copolymerizable vinyl group in the case of 3-(methacryloyloxy)propyl trimethoxysilane (MPS) resulted into its copolymerization with the surrounding monomer. Therefore, the encapsulation of inorganic species (magnetite and ceria) within PMMA-based nanoparticles was achieved via controlled mechanisms. The shape and the size of the inorganic components also influenced the hybrid morphology. The strategy was further extended to the incorporation of two complementary functionalities for the preparation of magneto-responsive and catalytically active nanomaterials. The desired accessibility of the inorganic functionalities (e.g., the formation of a magnetic core and a catalytic surface) was again guaranteed by specific surface functionalization of each inorganic species.

Once the bases of morphology control were established in Chapter 4, the following chapters (5–7) have been highlighted the use of Pickering stabilization and surfmers as synthetic alternatives that avoid the use of traditional surfactants and introduce a surface functionality on the polymer support via copolymerization of the colloidal stabilizer.

In Chapter 5, the preparation of magneto-responsive polystyrene-supported ceria catalysts was approached through two synthetic strategies. On the one hand, a heterogeneous nanocatalyst with

great inorganic coverage was prepared via in-situ crystallization of ceria on the surface of polystyrene–magnetite nanoparticles previously synthesized by miniemulsion polymerization. On the other hand, the catalyst was prepared by straightforward processes using catalytic (ceria) nanoparticles to allow the so-called Pickering stabilization of miniemulsions. This second strategy offers synthetic advantages related to the minimization of the consumption of resources (e.g., the use of a comonomer and surfactants is avoided), production steps, and time. The magnetically recoverable nanoparticles were used for the heterogeneous catalysis of the hydration of 2-cyanopyridine to 2-picolinamide. The in-situ crystallization route was related to high catalytic efficiencies, whereas Pickering stabilization offered comparable conversion of the reaction by increasing the concentration of catalyst. The incorporation of a magneto-responsive component allowed the recovery and recycling of the catalyst. Furthermore, it offered a synergic effect on the performance of the catalytic reaction probably due to the local heat produced by the vibration of magnetite nanoparticles.

Chapter 6 reported the preparation of magneto-responsive proline-functionalized PMMA nanoparticles for asymmetric catalysis. Two types amino acid-based molecules with the role of surfmer and comonomer were used for the immobilization of chiral units of proline on the surface of PMMA nanoparticles with a magnetic core. Both chiral structures provided the polymer support with similar immobilization rate and accessibility of the catalytically active amino acid moieties. The chiral nanocatalysts showed great conversion, enantioselectivity, and recyclability for the asymmetric catalysis of an intermolecular aldol reaction in water.

Finally, Chapter 7 presented the preparation of polyurethane-based hybrid capsules via interfacial polyaddition processes in inverse Pickering emulsions stabilized with different metal oxide nanoparticles. Systems using magnetite nanoparticles and their combination with catalytic species (ceria or titania) were proposed for the encapsulation of a hydrated salt as a phase change material (PCM) with attractive properties for thermal energy storage applications. The problems of chemical and thermal instability inherent to the salt in bulk were corrected with the encapsulation. The incorporation of a second salt as a nucleating agent allowed us to overcome the supercooling of the PCM. The prepared magnetically recoverable carriers (i.e., polyurethane capsules with magnetite embedded within the polymer shell and an aqueous core with the pair of salts) showed a great performance for thermal energy storage applications.

The results achieved in this thesis set up a promising scenario for the potential use of the miniemulsion technique for the incorporation of other functionalities (e.g., optical properties) or species (e.g., noble metals), allowing thereby the enhancement and the diversification of the

applications. In addition, the complete understanding of the synthesis and the control of the morphology of basic systems will allow the development of complex structures.

Regarding the synthetic strategy, future research could move further towards multistep and all-in-situ synthesis. The reduction of time and the number of steps in the processes is valuable, especially at industrial scale. The control of challenging colloidal methods, which involve both the synthesis of the inorganic functionalities and the polymer species in-situ, would lead to great advances of scalability and economy of chemical processes.

In terms of application, the development of recyclable nanoparticles with high efficiency in heterogeneous catalysis could be enlarged to other complex chemical reactions, photocatalysis, or for the generation of H<sub>2</sub> via water splitting. The enantiomer resolution of chemical synthesis based on the use chiral nanocatalysts could be applied for the preparation of different amino acid-based catalysts with applicability in asymmetric synthesis. A deep study of the mechanistic formation of the chiral bonds, supported by the characterization of the pure products by techniques like chiral high performance liquid chromatography (HPLC), would allow us to identify the patterns of the control of chirality. We propose the preparation of mixtures of PCMs with different temperatures of phase transitions for the development of thermal energy storage materials. These complex systems could store and release the thermal energy in a wider range of temperatures, which would enlarge the spectrum of application of the material.

This work has demonstrated the suitability of miniemulsions as a synthetic platform that allows the control of the morphology of multifunctional polymer–inorganic hybrid nanoparticles according to the expected application in catalysis or energy sectors.



## 9 Experimental Section

### 9.1 Materials and Methods

Chemical	Abbreviation	CAS	Purity	Supplier
Styrene <sup>c</sup>	S	100-42-5	≥99%	Sigma-Aldrich
Methyl methacrylate <sup>c</sup>	MMA	80-62-6	99%	Sigma-Aldrich
Acrylic acid	AA	79-10-7	99%	Sigma-Aldrich
1,6-Hexanediol	Hdol	629-11-8	99%	Sigma-Aldrich
Toluene-2,4-diisocyanate	TDI	584-84-9	95%	Sigma-Aldrich
Hexadecane		544-76-3	99%	Sigma-Aldrich
2,2'-Azobis(2-methylpropionitrile)	AIBN	78-67-1	≥98%	Sigma-Aldrich
2,2'-Azobis(2-methyl butyro nitrile)	AMBN, V59	13472-08-7	≥98%	Sigma-Aldrich
Potassium peroxydisulfate	KPS	7727-21-1	≥99%	Sigma-Aldrich
Sodium dodecyl sulfate	SDS	151-21-3	99%	Sigma-Aldrich
Sodium hydroxide		1310-73-2	99%	Probus
Sodium chloride		7647-14-5	98%	Fluka
Potassium chloride		7447-40-7		Merck
Aluminum oxide		1344-28-1		Sigma-Aldrich
Sodium sulfate decahydrate		7727-73-3	98%	Sigma-Aldrich
Di-sodium hydrogenphosphate dihydrate		10028-24-7	98%	Sigma-Aldrich
Iron(III) chloride hexahydrate		10025-77-1	98%	Sigma-Aldrich
Iron(II) chloride tetrahydrate		13478-10-9	≥99%	Sigma-Aldrich
Ludox TMA (22 nm) <sup>a</sup>		7631-86-9	34 wt%	Sigma-Aldrich
Titanium dioxide, rutile (15 nm) <sup>a</sup>		13463-67-7	20 wt%	GNM
Cerium nitrate hexahydrate		10294-41-4	99%	Sigma-Aldrich
3-(Methacryloyloxy)propyl trimethoxysilane	MPS	2530-85-0	98%	Sigma-Aldrich
Octadecyl trimethoxysilane	ODTMS	3069-42-9	90%	Sigma-Aldrich
Propyl trimethoxysilane	PTMS	1067-25-0	97%	Sigma-Aldrich
4-Hydroxy-L-proline		51-35-4	99%	Acros Organics
4-Hydroxy-D-proline		3398-22-9	97%	Sigma-Aldrich
Methacryloyl chloride		920-46-7	97%	Sigma-Aldrich
Undecanoyl chloride		17746-05-3	99%	Sigma-Aldrich
10-Undecenoyl chloride		38460-95-6	98%	Fischer Scientific
2-Cyanopyridine		100-70-9	99	Sigma-Aldrich
2-Picolinamide		1452-77-3	98%	Fischer Scientific
4-Nitrobenzaldehyde		555-16-8	≥98%	Fischer Scientific

Chemical	Abbreviation	CAS	Purity	Supplier
Cyclohexanone		108-94-1	≥99.5%	Sigma-Aldrich
Brilliant Blue FCF	BB	3844-45-9		Acros Organics
Trifluoroacetic acid	TFA	76-05-1	≥99%	Carl Roth
Trifluoromethane sulfonic acid		1493-13-6	99%	Acros Organics
Hydrochloric acid		76-47-01-0	37-38% <sup>b</sup>	J. T. Baker
Ethanol	EtOH	64-17-5	≥99.	Acros Organics
Diethyl ether	Et <sub>2</sub> O	60-29-7		Fischer Scientific
Ammonia		7664-41-7	25% <sup>b</sup>	Scharlau
Acetonitrile		75-05-8	≥99.8%	J. T. Baker
Cyclohexane		100-42-5	99%	Acros Organics
Dimethyl sulfoxide	DMSO	67-68-5	extra dry	Acros Organics
Dimethyl sulfoxide-d <sub>6</sub>	DMSO-d <sub>6</sub>	926-09-0	99.5 at% D	Sigma-Aldrich
Deuterium oxide-d <sub>2</sub>		7789-20-0	99.8 at% D	Carl Roth
Chloroform-d		865-49-6	99.8 at% D	Sigma-Aldrich

<sup>a</sup> Aqueous dispersion.

<sup>b</sup> Aqueous solution.

<sup>c</sup> Purified chromatographically with an alumina plug before use.

## 9.2 Synthesis and Functionalization of Inorganic Nanoparticles

### 9.2.1 Synthesis of Magnetite Nanoparticles

Magnetite nanoparticles were synthesized and functionalized by a coprecipitation and silanization method previously reported.<sup>98</sup> A pair of iron-based precursor salts (iron(II) chloride hexahydrate (FeCl<sub>2</sub>·4H<sub>2</sub>O, 3 g, 15 mmol) and iron(III) chloride hexahydrate (FeCl<sub>3</sub>·6H<sub>2</sub>O, 6 g, 22.5 mmol)) were dissolved in water (20 mL). An aqueous solution of concentrated ammonia (10 mL) diluted with water (5 mL) was added dropwise (5 min) under vigorous mechanical stirring. The reaction proceeded under reflux at 70 °C (1 h) and 130 °C (2 h). The nanoparticles were magnetically recovered, rinsed twice with a mixture of ethanol/water (50 mL, 1:1 vol.), and dried overnight in an oven (under vacuum, 35 °C).

### 9.2.2 Synthesis of Ceria Nanoparticles

The synthesis of ceria nanoparticles in bulk was inspired in a previous process reported for in the in-situ crystallization of CeO<sub>2</sub> on the surface of preformed polymer particles.<sup>6</sup> Cerium nitrate hexahydrate salt (8 g, 18.4 mmol) was dissolved in water (50 mL). An aqueous solution of NaOH (1 M) was dosed with an addition pump (1h, 20 mL·h<sup>-1</sup>) under magnetic stirring (750 rpm). The system was left under vigorous stirring (room temperature (RT), 20 h). A change of color of the reaction volume from white, to purple, brown, and pale white was observed when the

crystallization of ceria was completed. The product was recovered by centrifugation with a Heraeus Megafuge 16 Centrifuge (20 min, 7000 rpm), it was rinsed with water, and dried overnight in an oven (under vacuum, 35 °C).

### 9.2.3 Functionalization of Ceria and Magnetite Nanoparticles

The hydrophobization of ceria nanoparticles was adapted from a functionalization strategy previously reported for magnetite nanoparticles.<sup>98</sup> The pristine inorganic particles (ceria or magnetite) were redispersed in a mixture water/ethanol (15 mL·g<sup>-1</sup> of nanoparticles, 2:1 vol.) with sodium dodecyl sulfate (SDS, 3 mg·g<sup>-1</sup> of ceria and 10 mg·g<sup>-1</sup> of magnetite) using an ultrasonic bath (15 min). The pH value of the sample was fixed at 9.5 with a concentrated solution of ammonia. The functionalizing agent (ODTMS, PTMS, or MPS; 2 mmol·g<sup>-1</sup> of nanoparticles) was added dropwise (RT, 30 min) under vigorous stirring. The reaction mixture was stirred mechanically (for magnetite) or magnetically (for ceria) at room temperature (RT, 1 h) and under reflux (105 °C, 1.5 h). Functionalized magnetite and ceria nanoparticles were recovered from the solution with a magnet or by centrifugation (20 min, 7000 rpm), respectively. The products were rinsed (once with a mixture of ethanol/water (50 mL, 1:1 vol.) and twice with ethanol) and dried overnight in an oven (under vacuum, 35 °C).

### 9.2.4 Functionalization of Titania and Silica Nanoparticles

The silanization of silica and titania nanoparticles was performed using a method<sup>9, 13</sup> adapted from of Bourgéat-Lami et al.<sup>277</sup> The pH value of a mixture of the commercial aqueous suspensions of GNM TiO<sub>2</sub> nanoparticles or Ludox TMA (50 mL) with ethanol (50 mL) and SDS (50 mg) was set at 9.5 with concentrated ammonia. The functionalizing agent (ODTMS, PTMS, or MPS, 20 mmol) was added dropwise under intense magnetic stirring. The silanization reaction was left to proceed at room temperature (RT, 24 h) and under reflux (105 °C, 2 h) for equilibration purposes. The hydrophobized nanoparticles were collected by centrifugation (30 min, 10000 rpm), rinsed (once with a mixture of ethanol/water (1:1 vol.) and twice with ethanol) and dried overnight in an oven (under vacuum, 35 °C).

### 9.3 Experimental Section Specific for the Chapter 4

#### 9.3.1 Preparation of Polymer–Metal Oxide Hybrid Nanoparticles with Controlled Morphology by Miniemulsion Polymerization

Ceria and titania nanoparticles specifically functionalized with ODTMS, PTMS, or MPS were incorporated within polystyrene or PMMA matrices using an adaptation of a miniemulsion polymerization process reported for silica.<sup>75</sup> Hydrophobic metal oxide nanoparticles (300 mg) were dispersed within the monomer (S or MMA, 3 g) and hexadecane (120 mg) with the aid of an ultrasonic bath (15 min). Then, the free-radical initiator (AIBN, AMBN, or KPS, 0.36 mmol) was added and the dispersion was homogenized in an orbital thermoshaker (Kühl-Heiz-Thermomixer MKR23) (RT, 15 min, 700 rpm). The continuous phase consisted on an aqueous solution (12 mL) of SDS (12 mg) prepared under mild magnetic stirring (250 rpm). The organic and the aqueous phase were mixed, homogenized, and pre-emulsified in the orbital thermoshaker (RT, 45 min, 700 rpm). The pre-emulsion was ultrasonified in a Branson Digital Sonifier W-450D ( $\frac{1}{2}$ " tip, 360 s, 70% amplitude, and (1.0:0.1) s pulse–pause sequence) using an ice bath. The miniemulsion was polymerized in the orbital thermoshaker (65 °C for AIBN and KPS, and 72 °C for AMBN, 16 h, 500 rpm). The resulting dispersion of nanoparticles was filtered using Kimberly-Clark professional Kimtech Science precision wipes, and it was lyophilized in a Christ Alpha 24 LD plus lyophilizer for determination of the solid content and the inorganic load before purification.

The fraction of the dispersion charged with higher load of inorganic nanoparticles was recovered by centrifugation (20 min, 8500 rpm). The particles were redispersed first in an aqueous solution of SDS (0.1 wt.%) and then in water. The mass of the aqueous dispersion between the purification steps was maintained constant. Therefore, the efficiency of the global synthesis can be evaluated in terms of the solid content achieved after polymerization and after purification. The dispersion was lyophilized for characterization of the final material.

#### 9.3.2 Preparation of Multifunctional Nanoparticles

Magnetoresponse and catalytically active nanoparticles were prepared using an adaptation of the miniemulsion polymerization developed for the incorporation of magnetite in different polymer supports.<sup>98</sup> ODTMS-functionalized ceria or titania nanoparticles, and MPS-functionalized magnetite nanoparticles (100 mg) were redispersed within MMA or S (1.65 g) and hexadecane (78 mg) in an ultrasonic bath (15 min). The initiator AIBN (30 mmol, 50 mg) was added, and the dispersion was homogenized in the thermoshaker (RT, 15 min, 700 rpm). The organic phase was



mixed with an aqueous solution (18 mL) of SDS (36 mg) and pre-emulsified by orbital shaking (RT, 45 min, 700 rpm). The miniemulsion was prepared by ultrasonication ( $\frac{1}{2}$ " tip, 360 s, 70% amplitude, and (1.0:0.1) s pulse–pause sequence) and the system was polymerized in the thermoshaker (60 °C, 16 h, 500 rpm). The dispersion of nanoparticles was filtered and submitted to three cycles of magnetic purification. The fraction of the nanoparticles with higher magnetic load was recovered with a magnet (30 min). The supernatant was discarded and the recovered particles were redispersed in an aqueous solution of SDS (0.1 wt.%). The operation was repeated twice using water for the redispersion of the particles. The mass of the product was kept constant to get representative solid contents, which were determined after lyophilization.

## 9.4 Experimental Section Specific for Chapter 5

### 9.4.1 Preparation of Polystyrene-Supported Ceria Nanoparticles (C1 and C2) by Pickering Miniemulsion Polymerization (Route P1)

Polystyrene–ceria and polystyrene–magnetite–ceria nanoparticles, named as **C1** and **C2**, were synthesized via Pickering miniemulsion polymerization. The oil phase was prepared by mixing S (1.8 g) with hexadecane (89 mg) and AIBN (60 mg) by orbital shaking (RT, 15 min, 700 rpm) in the thermoshaker. In the case of the magnetic catalyst **C2**, MPS-functionalized magnetite nanoparticles (100 mg) were redispersed within the monomer in the ultrasonic bath (15 min). The aqueous phase consisting into a stable dispersion of ceria nanoparticles (450 mg) in water (16 mL) was prepared by ultrasonication (360 s,  $\frac{1}{2}$ " tip, 90% amplitude, and (1.0:0.1) s pulse–pause sequence). The two phases were mixed, pre-emulsified by orbital shaking (RT, 45 min, 700 rpm), and ultrasonified ( $\frac{1}{2}$ " tip, 360 s, 90% amplitude, and (1.0:0.1) s pulse–pause sequence) in an ice bath. The Pickering miniemulsion placed in 40 mL vial was polymerized in the orbital thermoshaker (60 °C, 16 h, 450 rpm). After 30 min of the initiation of the polymerization, a second initiator KPS (35 mg) dissolved in water (1 mL) was added. The resulting dispersion was filtered and lyophilized.

### 9.4.2 Preparation of Polystyrene-Supported Ceria Nanoparticles (C5 and C6) by Miniemulsion Polymerization and In-situ Crystallization (Route P2)

Poly(styrene-*co*-acrylic acid) (P(S-AA)) and P(S-AA)–magnetite nanoparticles, labeled as samples **C3** and **C4** respectively, were synthesized by a miniemulsion copolymerization process adapted from Mari et al.<sup>6</sup> In the case of **C4**, the dispersion of magnetite nanoparticles within the monomers

was achieved in an ultrasonic bath (15 min). The organic phase was prepared by orbital shaking (RT, 15 min, 700 rpm) of a mixture of S (5.76 g), AA (240 mg), hexadecane (250 mg), AMBN (100 mg); and MPS-functionalized magnetite (400 mg) for **C4**. The aqueous phase, a surfactant solution of SDS (100 mg) in water (24 g) was prepared by magnetic stirring (15 min, 250 rpm). The phases were mixed and pre-emulsified under orbital shaking (45 min). The miniemulsion was prepared by ultrasonication (180 s, ½” tip, 90% amplitude, and a (1.0: 0.1) s pulse:pause sequence). The polymerization proceeded (72 °C, 16 h, 500 rpm) in a 100 mL round-bottom flask equipped with a reflux column and mechanical stirring for the magnetic nanoparticles. The final latex dispersions were filtered and dialyzed using Microsep Advance centrifuge tubes (100kDa MWCO, Pall Corporation) filled with 3 mL of sample and 8 mL of water. The samples were centrifuged (30 min, at 10000 rpm for **C3** and 3000 rpm for **C4**), the water was replaced and the process was repeated up to three times. The polymer and inorganic content of sample **C4** was determined by TGA of the sample after lyophilization.

P(S-AA)-ceria and P(S-AA)-magnetite-ceria catalysts, named as **C5** and **C6**, were prepared by the controlled crystallization of ceria on the surface of preformed **C3** and **C4** nanoparticles.<sup>6</sup> The corresponding amount of samples **C3** and **C4** to 30 mg of polymer content was redispersed in an aqueous solution (25 mL) of cerium nitrate hexahydrate (0.065 g, 0.15 mmol) under orbital shaking (1 h). Then, the precipitation of ceria was driven by controlled addition with a syringe pump (1 h, 5 mL·h<sup>-1</sup>) of a solution of sodium hydroxide (5 mL, 30 mM). Once the whole crystallization was completed (after 20 h), the hybrid nanoparticles were recovered by centrifugation (30 min, 10000 rpm). The final product was dried overnight in an oven (under vacuum, 35 °C).

#### **9.4.3 Catalysis of the Hydrolysis Reaction of 2-Cyanopyridine to 2-Picolinamide**

The equivalent amounts of the hybrid catalyst to contents of CeO<sub>2</sub> of 5, 10, 15, 20, or 40 mg were dispersed in water (5 mL) in the ultrasonic bath (15 min). The dispersion was mixed in a Vortex with a stock solution of 2-cyanopyridine in ethanol (5 mL, 0.02 M). The reaction volume was divided into 12 vials (500 µL) corresponding to the different reaction/sampling times. The vials were placed in the orbital thermoshaker and the reaction was performed (80 °C, 24 h, 600 rpm).

At each reaction time (0, 5, 15, 30, and 45 min; once per hour until 7 h; and once after 24 h of reaction), aliquots (100 µL) were taken from the corresponding vial, diluted with acetonitrile (900 µL), and kept in the freezer (-20 °C) to quench the reaction. A filter (0.02 µm) was used to remove the catalyst from the sample, which was then injected into a high performance liquid chromatography (JASCO HPLC) unit to determine the reactant/product concentrations.

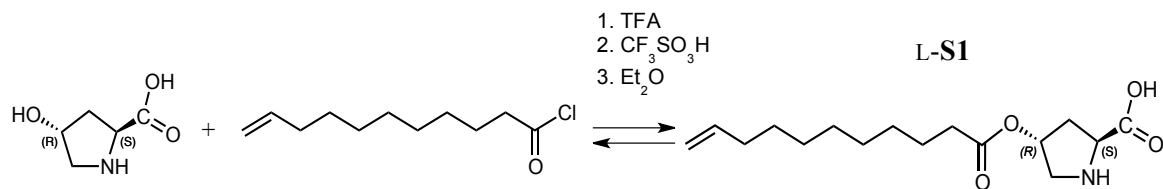
#### 9.4.4 Recycling Study

The recyclability of the magnetoresponse catalysts **C2** and **C6** was studied during 4 cycles of 24 h of reaction. After each cycle, the particles were magnetically collected, washed three times with ethanol/water (1:1 vol.), and dried overnight in an oven (under vacuum, 35 °C).

### 9.5 Experimental Section Specific for Chapter 6

#### 9.5.1 Synthesis of 10-undecenoyl-*trans*-4-hydroxy-L/D-proline (L/D-S1) *O*-methacryloyl-*trans*-4-hydroxy-L/D-proline (L/D-S2), and Decanoyl-*trans*-4-hydroxy-L-proline (L-S3)

The synthesis of the surfmer L/D-**S1**, the monomer L/D-**S2**, and the surfactant L-**S3** was performed according with an adaptation of a procedure for the preparation of *O*-methacryloyl-*trans*-4-hydroxy-L-proline (L-**S2**),<sup>215, 234</sup> as shown in Schemes 9.1, 9.2, and 9.3. The starting compound, *trans*-4-hydroxy-L-proline (3.4 g), was dissolved in TFA (12 mL) in a flask immersed in an ice bath. The proline-based precursor was added in small portions under vigorous magnetic stirring (5 min, 900 rpm). The system was fluxed with nitrogen, the ice bath was removed and trifluoromethanesulfonic acid (500 µL) was added dropwise at room temperature, leading *trans*-4-hydroxy-L-proline completely dissolved. After 5 min, 10-undecenoyl chloride (12 mL) for **S1**, methacryloyl chloride (5.5 mL) for **S2**, or undecanoyl chloride (12 mL) for **S3** was added and the acylation proceeded at room temperature (4 h, 500 rpm). The reaction was quenched in an ice bath, diethyl ether (Et<sub>2</sub>O, 36 mL for **S1** and **S3**, or 18 mL for **S2**) was added (5 min, 500 rpm) and the system was left for precipitation under mild stirring conditions (15 min, 250 rpm). The product was precipitated as a white solid, recovered by filtration, washed several times with Et<sub>2</sub>O, and dried overnight in an oven (under vacuum, 35 °C). A scale down of the procedure in a factor of ten was used for the synthesis of complementary enantiomers of the surfmer (D-**S1**) 10-undecenoyl-*trans*-4-hydroxy-D-proline and the monomer (D-**S2**) *O*-methacryloyl-*trans*-4-hydroxy-L-proline, respectively. The yield and the structure of the chiral molecules (determined by NMR) is presented below the scheme of the corresponding synthesis.



**Scheme 9.1.** Acylation reaction used for the synthesis of the surfmer 10-undecenyl-*trans*-4-hydroxy-L-proline (L-S1). D-S1 was synthesized analogously using *trans*-4-hydroxy-D-proline.

- L-S1: Yield: 39 %

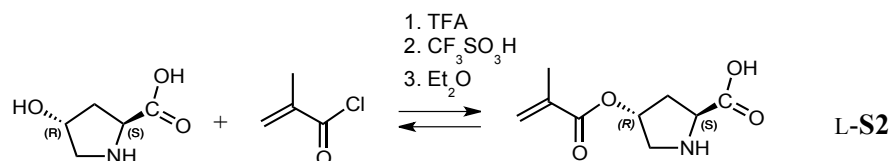
$^1\text{H-NMR}$  (300 MHz, DMSO- $d_6$ ) [ $\delta$ / ppm] = 5.78 (m, 1H), 5.28 (s, 1H), 4.95(m, 2H), 4.40(t, 1H), 3.56 (d, 1H), 3.27 (d, 1H), 2.31 (t, 4H), 1.99 (m, 2H), 1.52 (s, 2H), 1.33 (s, 2H), 1.25 (s, 8H).

$^{13}\text{C NMR}$  (75 MHz, DMSO- $d_6$ ) [ $\delta$ / ppm] = 172.32, 169.50, 138.78, 114.62, 72.06, 57.58, 50.31, 34.12, 33.13, 28.65, 28.42, 28.20, 24.07.

- D-S1: Yield: 38 %

$^1\text{H-NMR}$  (300 MHz, DMSO- $d_6$ ) [ $\delta$ / ppm] = 5.78 (s, 1H), 5.28 (s, 1H), 4.95(m, 2H), 4.40(t, 1H), 3.56 (d, 1H), 3.27 (d, 1H), 2.31 (t, 4H), 1.99 (m, 2H), 1.52 (s, 2H), 1.30 (s, 2H), 1.24 (s, 8H).

$^{13}\text{C-NMR}$  (75 MHz, DMSO- $d_6$ ) [ $\delta$ / ppm] = 172.32, 169.50, 138.78, 114.62, 72.06, 57.58, 50.31, 34.12, 33.13, 28.65, 28.42, 28.20, 24.07.



**Scheme 9.2.** Acylation reaction used for the synthesis of the monomer *O*-methacryloyl-*trans*-4-hydroxy-L-proline (L-S2). D-S2 was synthesized analogously using *trans*-4-hydroxy-D-proline. (Based on refs. 215 and 234)

- L-S2: Yield: 58 %

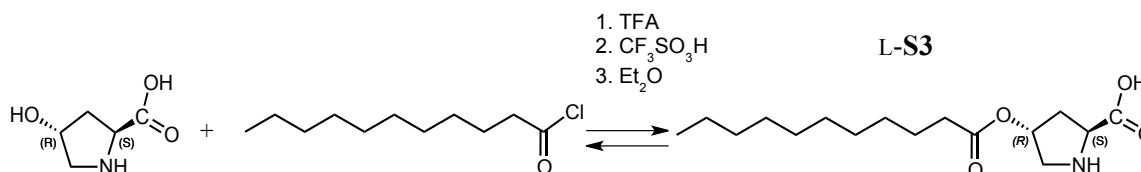
$^1\text{H-NMR}$  (300 MHz, D $_2$ O) [ $\delta$ / ppm] = 6.17 (s, 1H), 5.76 (s, 1H), 5.55 (s, 1H), 4.65 (t, 1H), 3.70 (m, 2H), 2.58 (m, 2H), 1.91 (s, 3H).

$^{13}\text{C-NMR}$  (75 MHz, D $_2$ O) [ $\delta$ / ppm] = 171.20, 168.19, 135.26, 127.72, 73.56, 58.66, 50.97, 34.47, 17.13.

- D-S2: Yield: 52 %

$^1\text{H-NMR}$  (300 MHz,  $\text{D}_2\text{O}$ ) [ $\delta$ / ppm] = 6.17(s, 1H), 5.76(s, 1H), 5.56(s, 1H), 4.61(t, 1H), 3.72(m, 1H), 3.67(m, 1H), 2.71(m, 1H), 2.46(m, 1H), 1.92(s, 3H).

$^{13}\text{C-NMR}$  (75 MHz,  $\text{D}_2\text{O}$ ) [ $\delta$ / ppm] = 171.57, 168.22, 135.28, 127.68, 73.65, 58.88, 50.92, 34.54, 17.12.



**Scheme 9.3.** Acylation reaction used for the synthesis of decanoyl-*trans*-4-hydroxy-L-proline (L-S3).

- L-S3: Yield: 88 %

$^1\text{H NMR}$  (300 MHz,  $\text{DMSO-}d_6$ ) [ $\delta$ / ppm] = 5.27 (s, 1H), 4.37 (t, 1H), 3.61 (m, 1H), 3.25 (m, 1H), 2.30 (t, 4H), 1.52 (s, 2H), 1.24 (s, 14H), 0.85 (t, 3H).

$^{13}\text{C NMR}$  (75 MHz,  $\text{DMSO-}d_6$ ) [ $\delta$ / ppm] = 172.39, 169.49, 117.71, 72.11, 57.61, 50.26, 34.19, 33.41, 31.31, 28.71, 28.45, 24.13, 22.11, 13.97.

### 9.5.2 Preparation of Proline-Functionalized PMMA Nanocatalysts AC1–AC10 by Miniemulsion Polymerization

Proline-functionalized PMMA nanoparticles corresponding to samples AC1–AC2 and AC7–AC8 were prepared using L-S1 as a surfmer or L-S3 as a surfactant, respectively, and MMA (1.35 g) as the sole monomer. The monomer content used for samples containing the proline-based comonomer (AC4, AC5, AC9, and AC10) was constituted by 1.28 g of MMA and 68 mg of L-S2. The organic phase was always prepared by mixing hexadecane (78  $\mu\text{L}$ ) and AIBN (30 mg) with the monomer/s, and magnetite in the case of the magnetoresponsive nanocatalysts. The MPS-functionalized magnetite nanoparticles (150 mg) were dispersed within the corresponding amount of MMA using an ultrasonic bath (15 min). The incorporation of L-S2 required also a previous step of ultrasonication for being properly mixed with MMA. The continuous phase consisted into an aqueous solution (12 mL) of the emulsifier (72 mg), which corresponded to L-S1 for samples AC1–AC2, SDS for AC4–AC5, or L-S3 for AC7–AC10. The aqueous phase was basified to dissolve the

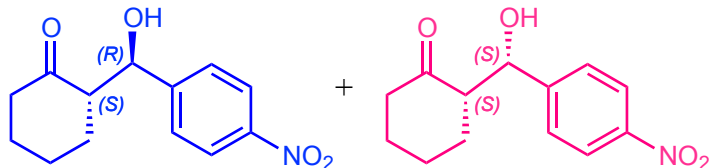
proline-based molecules by adding a solution of sodium hydroxide (1 M, 500  $\mu$ L for systems using L-S1 and L-S3, or 2 drops for L-S2). Both phases were homogenized separately by orbital shaking (15 min), then mixed, pre-emulsified in the thermoshaker (RT, 45 min, 700 rpm), and emulsified by ultrasonication ( $\frac{1}{2}$ " tip, 360 s, 70% amplitude, and (1.0:0.1) s pulse–pause sequence) in an ice bath. The polymerization was driven by thermal activation in the orbital thermoshaker (60  $^{\circ}$ C, 16 h, 500 rpm). The chiral nanoparticles were magnetically or kinetically (i.e., by centrifugation) purified, washed once with a solution of TFA to reprotonate the carboxylic acid of the proline, rinsed with water until the recovery of the neutral pH, and lyophilized.

Analogous procedures were applied for the preparation of the catalysts AC3 (with the surfmer D-S1), or AC3 (with the monomer D-S2) using a scale-down of the miniemulsion formulation in a factor of three, and a  $\frac{1}{4}$ " tip for the emulsification process.

### 9.5.3 Aldol Reaction

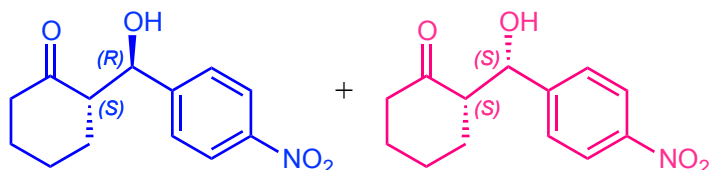
The intermolecular aldol reaction between *p*-nitrobenzaldehyde (0.1 mmol) and cyclohexanone (1 mmol) was performed using a concentration of the catalyst corresponding to 10 mol.% of proline with respect to the aldehyde. The chiral catalysts were either dissolved or dispersed by ultrasonication in water (520  $\mu$ L), which was used as sole solvent. The substrates were added, and the reaction was performed in the thermoshaker (25  $^{\circ}$ C, 6–24 h, 600 rpm). To study the effect of the solvent, water was replaced by a mixture of DMSO/water (2:1 vol, 520  $\mu$ L), or aqueous solutions of TFA (1 M) or sodium hydroxide (NaOH, 1 M), while the rest of conditions were maintained. The reaction was quenched with Et<sub>2</sub>O (2 mL) and the catalyst was magnetically or chemically isolated while the product was filtered using a silica plug. The catalyst was rinsed with Et<sub>2</sub>O and the extraction of the product was repeated three times. The organic phase was dried and the solvent was removed by solvent evaporation. The product was dried overnight in an oven (under vacuum, 35  $^{\circ}$ C) and analyzed by <sup>1</sup>H-NMR without further purification. The formation of 2-hydroxy-(4-nitrophenyl)methyl-cyclohexanone was revealed, as shown below:

- Product extracted after 6 h of the reaction catalyzed by sample **AC2**.



$^1\text{H-NMR}$  (300 MHz, Chloroform-*d*) [ $\delta$ / ppm] = 8.22 – 8.10 (m, 4H), 7.45 (d,  $J$  = 1.8 Hz, 2H), 7.20 (s, 1H), 4.83 (d,  $J$  = 8.3 Hz, 2H), 3.97 (s, 1H), 3.68 (d,  $J$  = 7.6 Hz, 1H), 3.56 (d,  $J$  = 17.3 Hz, 1H), 2.60 – 2.37 (m, 4H), 2.30 (td,  $J$  = 13.2, 6.1 Hz, 2H), 2.05 (ddt,  $J$  = 11.8, 5.6, 2.8 Hz, 2H), 1.83 – 1.71 (m, 2H), 1.64 (tt,  $J$  = 8.9, 4.7 Hz, 1H), 1.61 – 1.48 (m, 3H), 1.53 – 1.40 (m, 2H), 1.40 – 1.16 (m, 3H), 1.25 (s, 1H), 1.15 (s, 2H), 0.79 (q,  $J$  = 7.7, 6.8 Hz, 1H).

- Product extracted after 6 h of the reaction catalyzed by sample **AC5**.



$^1\text{H-NMR}$  (300 MHz, Chloroform-*d*) [ $\delta$ / ppm] = 8.14 (d,  $J$  = 8.7 Hz, 2H), 7.44 (d,  $J$  = 8.7 Hz, 2H), 4.83 (d,  $J$  = 8.3 Hz, 1H), 2.60 – 2.30 (m, 2H), 2.27 (ddd,  $J$  = 9.7, 6.4, 2.4 Hz, 1H), 2.05 (ddt,  $J$  = 11.9, 5.6, 2.8 Hz, 1H), 1.77 (dq,  $J$  = 12.5, 4.5, 3.6 Hz, 1H), 1.71 – 1.56 (m, 1H), 1.55 (s, 1H), 1.56 – 1.41 (m, 2H), 1.45 – 1.27 (m, 1H), 1.25 (s, 2H), 1.21 (d,  $J$  = 14.8 Hz, 3H), 1.15 (s, 1H), 0.79 (q,  $J$  = 8.5, 7.3 Hz, 0H).

The conversion of the aldehyde is observed with the disappearance of the characteristic signals at 10.09 ppm and the chemical shift at 8.00 and 8.32 ppm. The relative intensity of the latter and the new signals (at 7.45, and 8.13 ppm) are used to calculate the reaction conversion. In addition, the intensity of signals at 4.82 and 5.41 ppm allowed us to determine the *anti/syn* ratio.

#### 9.5.4 Recycling Study

The magneto-responsive catalysts were magnetically recovered from the product of the aldol reaction, washed twice with water (2 mL) and Et<sub>2</sub>O (2 mL) with the aid of the ultrasonic bath (15 min). The chiral nanoparticles were dried overnight in an oven (under vacuum, 35 °C) and reused for the next cycle of the aldol reaction. The strategy was repeated up to four cycles.

## 9.6 Experimental Section Specific for Chapter 7

### 9.6.1 Synthesis of Polyurethane-Based Hybrid Capsules Incorporating Metal Oxide Nanoparticles by Interfacial Polymerization in an Inverse Pickering Miniemulsion

The preparation of polyurethane capsules incorporating different metal oxides (titania, ceria, magnetite and silica) was adapted from a previous process developed for silica nanoparticles.<sup>9</sup> ODTMS-functionalized metal oxide nanoparticles (225 mg) were dispersed in cyclohexane (9 mL) with the aid of the ultrasonic bath (15 min). The disperse phase was prepared by dissolving 1, 6-hexanediol (45 mg) in either water (850  $\mu$ L) or an aqueous solution with hydrophilic substances (i.e., Brilliant Blue FCF dye (5 wt. %) or  $\text{Na}_2\text{SO}_4 \cdot 10\text{H}_2\text{O}$  (20 wt%) with or without  $\text{Na}_2\text{HPO}_4 \cdot 2\text{H}_2\text{O}$  (0.4wt. %)). The phases were mixed, pre-emulsified with a Vortex (2 min), and emulsified by ultrasonication in a Sonics Vibra-Cell V130 Sonifier from Sonics & Materials Inc. (1/4" tip, 6 min, 70% amplitude, and (1.0:0.1) s pulse–pause sequence). A solution of TDI (90 mg) in cyclohexane (2 mL) was added dropwise and the interfacial polymerization was driven in the orbital thermoshaker (25 °C, 24 h, 450 rpm). The capsules containing the  $\text{Na}_2\text{SO}_4 \cdot 10\text{H}_2\text{O}$  were dried by evaporation of cyclohexane overnight (RT, atmospheric pressure) for thermal characterization by DSC.

### 9.6.2 Release Study

An aqueous solution of the dye Brilliant Blue FCF (5 wt.%) was encapsulated within the polyurethane–metal oxide microcapsules. The cyclohexane of the final dispersion was evaporated overnight (RT, atmospheric pressure). The dried capsules were redispersed in an aqueous solution of SDS (30 mL, 1 wt.%) in the ultrasonic bath (15 min). An aliquot of the aqueous dispersion (10 mL) was placed in a dialysis membrane (14 kDa) from Carl Roth, and immersed in water (500 mL) under mild magnetic stirring (120 rpm). An indirect method was used to study the concentration of the dye that was released from the capsules and diffused through the membrane. For this aim, aliquots (1 mL) were taken during 72 h from the outer solution and the absorbance of the samples was measured by UV-Vis. A patron experiment was also performed using an aqueous solution of the dye at the concentration equivalent of a total release.



## 9.7 Analytic Techniques

### 9.7.1 Dynamic Light Scattering (DLS)

The average particle size ( $d$ ) was determined by dynamic light scattering (DLS at  $107^\circ$ ) with a Zetasizer Malvern Zen 1960 equipment in Mainz and a Zetasizer Nano ZS in Valencia. The aqueous dispersions were diluted (0.1 vol.%) previous determination.

### 9.7.2 Polyelectrolyte Titration (PCD)

The surface charge density was quantified by polyelectrolyte titration using a particle charge detector (Mütek PCD-04, BTG Mütek GmbH). The pH value of the aqueous dispersion of particles with a solid content of 0.1 wt.% was fixed at 9.0 with a solution of sodium hydroxide (0.05 M). Poly(dimethyl diallyl ammonium chloride) (polyDADMAC, 1 N) was used as polyelectrolyte for the determination.

### 9.7.3 Thermogravimetric Analysis (TGA)

The inorganic load of the hybrid samples containing individual inorganic species was determined by thermogravimetric analysis using a Mettler Toledo ThermoSTAR TGA/SDTA 851 thermobalance (Mettler-Toledo, Switzerland) in Mainz, and a thermobalance SETARAM Setsys in Valencia. The same technique with analogue operating conditions was used to quantify the amount of coupling agent (silane) attached to the inorganic nanoparticles. The samples were previously dried in an oven (under vacuum) or by lyophilization. About 20 mg of sample were heated under controlled atmosphere with nitrogen at  $10\text{ }^\circ\text{C}\cdot\text{min}^{-1}$  from 30 to 600  $^\circ\text{C}$ .

### 9.7.4 Inductively Coupled Plasma-Mass Spectrometry (ICP-MS)

The inorganic load of the multifunctional samples incorporating simultaneously at least two inorganic species was determined by inductively coupled plasma mass spectrometry (ICP-MS) using a mass detector Agilent 7900. The samples were digested with acid previous determination.

### 9.7.5 Transmission Electron Microscopy (TEM)

A JEOL 1400 Electron Microscope (JEOL Ltd., Japan) with a LAB<sub>6</sub> cathode at 120 kV and a GATAN Ultrascan 1000 CCD camera (Gatan Inc., USA) and a JEOL JEM 1010 with 100kV and a AMT RX80 digital camera were used for transmission electron microscopy (TEM) analysis in Mainz and Valencia, respectively. The samples (10  $\mu\text{L}$ , with a dilution of 0.1 vol.%) were dropped onto a 300 mesh carbon coated copper grid which further was coated with a second carbon layer

(5 nm) using a Leica EM Med020 Vacuum Coating System (Leica Micro Systems, Germany) to avoid the degradation of PMMA. Particle (and capsule) size was determined by statistical treatment of TEM images accounting at least 200 particles.

### **9.7.6 Scanning Electron Microscopy (SEM)**

A Leo Gemini Zeiss 1530 field emission Microscope (Carl Zeiss, Germany) and a Hitachi SU-8000 scanning electron microscope were used for SEM analysis at different voltages. The samples (10  $\mu$ L, with a dilution of 0.1 vol.%) were dropcasted on a silicon wafer and dried before observation.

### **9.7.7 X-Ray Diffraction (XRD)**

The X-Ray diffraction patterns were determined using an X-Ray diffractometer D8 Advance A25 (Bruker).

### **9.7.8 Brunauer–Emmett–Teller (BET) Surface Area Analysis**

The specific surface area of the catalysts was determined by nitrogen adsorption measurements performed at 120 °C in a Qantachrome Autosorbe-1 equipment, according to the Brunauer–Emmett–Teller (BET) model.

### **9.7.9 High Performance Liquid Chromatography (HPLC)**

High performance liquid chromatography was performed in a JASCO HPLC equipped with an analogic-digital conversion unit (Jasco LC-Net II), a refraction index detector (RI-2031), a quaternary gradient pump (PU-2089), and a column chamber (Jasco co-2065 Plus) with a manual injector (Reodhyne 720i). A reverse phase column C-18 (Kinetex of 2.6  $\mu$ m fused-core silica particles with 100  $\times$  4.6 mm C18 and 100 Å) was used for the determination. A mixture of acetonitrile/water acidified with HCl (0.1 wt.%) (30:70) was used as mobile phase.

### **9.7.10 Nuclear Magnetic Resonance Spectroscopy**

$^1\text{H}$ -NMR and  $^{13}\text{C}$ -NMR spectra of the samples containing (10–20 mg) of the organic product dissolved in a deuterated solvent (chloroform-*d*,  $\text{D}_2\text{O}$  or DMSO-*d*6) were obtained with a Bruker DRX spectrometer (300 MHz).

**9.7.11 Ultraviolet-Visible Spectroscopy or Spectrophotometry (UV-Vis)**

The absorbance of the samples was measured by UV-Visible Spectroscopy using a UV-2501 PC Shimadzu spectrophotometer. No dilution nor pretreatment of the samples was required before the determination.

**9.7.12 Differential Scanning Calorimetry (DSC)**

The thermal behavior of polyurethane-based capsules (after evaporation of cyclohexane) was characterized by differential scanning calorimetry using a DSC Q20 TA instrument. The samples were submitted to a thermal treatment of four cycles of heating and cooling (from  $-50^{\circ}\text{C}$  up to  $60^{\circ}\text{C}$  or  $90^{\circ}\text{C}$ , at  $10\text{ K}\cdot\text{min}^{-1}$ ).



## References

1. Fischer, V.; Lieberwirth, I.; Jakob, G.; Landfester, K.; Muñoz-Espí, R., Metal Oxide/Polymer Hybrid Nanoparticles with Versatile Functionality Prepared by Controlled Surface Crystallization. *Adv. Funct. Mater.* **2013**, *23*, 451-466.
2. Hood, M. A.; Mari, M.; Munoz-Espi, R., Synthetic Strategies in the Preparation of Polymer/Inorganic Hybrid Nanoparticles. *Materials* **2014**, *7*, 4057-4087.
3. Schoth, A., Structure Control in Polymer/Inorganic Hybrid Materials. Ph.D. Dissertation, Johannes Gutenberg-Universität, Mainz, **2015**.
4. Asua, J. M., Mapping the Morphology of Polymer–Inorganic Nanocomposites Synthesized by Miniemulsion Polymerization. *Macromol. Chem. Phys.* **2014**, *215*, 458-464.
5. Landfester, K., Miniemulsion Polymerization and the Structure of Polymer and Hybrid Nanoparticles. *Angew. Chem. Int. Ed.* **2009**, *48*, 4488-4507.
6. Mari, M.; Müller, B.; Landfester, K.; Muñoz-Espí, R., Ceria/Polymer Hybrid Nanoparticles as Efficient Catalysts for the Hydration of Nitriles to Amides. *ACS Appl. Mater. Interfaces* **2015**, *7*, 10727-10733.
7. Muñoz-Espí, R.; Mastai, Y.; Gross, S.; Landfester, K., Colloidal systems for crystallization processes from liquid phase. *CrystEngComm* **2013**, *15*, 2175-2191.
8. Muñoz-Espí, R.; Weiss, C. K.; Landfester, K., Inorganic nanoparticles prepared in miniemulsion. *Curr. Opin. Colloid Interface Sci.* **2012**, *17*, 212-224.
9. Schoth, A.; Landfester, K.; Munoz-Espi, R., Surfactant-free polyurethane nanocapsules via inverse Pickering miniemulsion. *Langmuir* **2015**, *31*, 3784-3788.
10. Hood, M. A.; Paiphansiri, U.; Schaeffel, D.; Koynov, K.; Kappl, M.; Landfester, K.; Muñoz-Espí, R., Hybrid Poly(urethane–urea)/Silica Nanocapsules with pH-Sensitive Gateways. *Chem. Mater.* **2015**, *27*, 4311-4318.
11. Mir, S. H.; Nagahara, L. A.; Thundat, T.; Mokarian-Tabari, P.; Furukawa, H.; Khosla, A., Review: Organic-Inorganic Hybrid Functional Materials: An Integrated Platform for Applied Technologies. *J. Electrochem. Soc.* **2018**, *165*, 3137-3156.
12. Schoth, A.; Keith, A. D.; Landfester, K.; Munoz-Espi, R., Silanization as a versatile functionalization method for the synthesis of polymer/magnetite hybrid nanoparticles with controlled structure. *RSC Adv.* **2016**, *6*, 53903-53911.
13. Schoth, A.; Wagner, C.; Hecht, L. L.; Winzen, S.; Muñoz-Espí, R.; Schuchmann, H. P.; Landfester, K., Structure control in PMMA/silica hybrid nanoparticles by surface functionalization. *Colloid Polym. Sci.* **2014**, *292*, 2427-2437.
14. Muñoz-Espí, R.; Álvarez-Bermúdez, O., Chapter 15 - Application of Nanoemulsions in the Synthesis of Nanoparticles. In *Nanoemulsions*, Jafari, S. M.; McClements, D. J., Eds. Academic Press: London, 2018; pp 477-515.
15. Gonzalez-Ortiz, L. J.; Asua, J. M., Development of Particle Morphology in Emulsion Polymerization. 1. Cluster Dynamics. *Macromolecules* **1995**, *28*, 3135-3145.
16. Gong, T.; Yang, D.; Hu, J.; Yang, W.; Wang, C.; Lu, J. Q., Preparation of monodispersed hybrid nanospheres with high magnetite content from uniform Fe<sub>3</sub>O<sub>4</sub> clusters. *Colloids Surf. A* **2009**, *339*, 232-239.

17. Mori, Y.; Kawaguchi, H., Impact of initiators in preparing magnetic polymer particles by miniemulsion polymerization. *Colloids Surf. B* **2007**, *56*, 246-254.
18. Staudt, T.; Machado, T. O.; Vogel, N.; Weiss, C. K.; Araujo, P. H.; Sayer, C.; Landfester, K., Magnetic Polymer/Nickel Hybrid Nanoparticles Via Miniemulsion Polymerization. *Macromol. Chem. Phys.* **2013**, *214*, 2213-2222.
19. Fickert, J.; Rupper, P.; Graf, R.; Landfester, K.; Crespy, D., Design and characterization of functionalized silica nanocontainers for self-healing materials. *J. Mater. Chem.* **2012**, *22*, 2286-2291.
20. Fickert, J. Nanocapsules for self-healing materials. Johannes Gutenberg-Universität, Mainz, 2013.
21. Mora-Huertas, C. E.; Fessi, H.; Elaissari, A., Polymer-based nanocapsules for drug delivery. *Int. J. Pharm.* **2010**, *385*, 113-142.
22. Torza, S.; Mason, S. G., Three-phase interactions in shear and electrical fields. *J. Colloid Interface Sci.* **1970**, *33*, 67-83.
23. Shirin-Abadi, A. R.; Khoee, S.; Rahim-Abadi, M. M.; Mahdavian, A. R., Kinetic and thermodynamic correlation for prediction of morphology of nanocapsules with hydrophobic core via miniemulsion polymerization. *Colloids Surf. A* **2014**, *462*, 18-26.
24. Sudol, E. D.; El-Aasser, M. S., Miniemulsion Polymerization. In *Emulsion Polymerization and emulsion polymers*. Lovell, P. A.; El-Aasser, M. S., Ed. John Wiley: 1997; pp 699-722.
25. Strey, R., Microemulsion microstructure and interfacial curvature. *Curr. Opin. Colloid Interface Sci.* **1994**, *272*, 1005-1019.
26. Cosgrove, T., *Colloid Science: Principles, Methods and Applications*. 2nd ed.; John Wiley & Sons: Bristol, 2010.
27. Landfester, K., Polyreactions in Miniemulsions. *Macromol. Rapid. Commun.* **2001**, *22*, 896-936.
28. Landfester, K.; Willert, M.; Antonietti, M., Preparation of Polymer Particles in Nonaqueous Direct and Inverse Miniemulsions. *Macromolecules* **2000**, *33*, 2370-2376.
29. Landfester, K., Miniemulsions for Nanoparticle Synthesis. In *Colloid Chemistry II*, Antonietti, M., Ed. Springer: Berlin, Heidelberg, 2003; pp 75-123.
30. Rosen, M. J., *Surfactants and Interfacial Phenomena*. 3rd ed.; John Wiley & Sons: Hoboken, 2004.
31. El-Aasser, M. S., Miniemulsion: Overview of Research and Applications. *J. Coat. Technol. Res.* **2004**, *1*, 20-31.
32. Ramsden, W., Separation of solids in the surface-layers of solutions and 'suspensions' (observations on surface-membranes, bubbles, emulsions, and mechanical coagulation). *Proc. R. Soc. Lon.* **1904**, *72*, 156-164.
33. Pickering, S. U., Emulsions. *J. Chem. Soc.* **1907**, *91*, 2001-2021.
34. Schrade, A.; Landfester, K.; Ziener, U., Pickering-type stabilized nanoparticles by heterophase polymerization. *Chem. Soc. Rev.* **2013**, *42*, 6823-6839.
35. Wang, Z.; Wang, Y., Tuning Amphiphilicity of Particles for Controllable Pickering Emulsion. *Materials* **2016**, *9*, 903-928.

36. Binks, B. P., Particles as surfactants: similarities and differences. *Curr. Opin. Colloid Interface Sci.* **2002**, *7*, 21-41.
37. Borzenkov, M.; Hevus, O., Synthesis of Surface Active Monomers. In *Surface Active Monomers: Synthesis, Properties, and Application*. Borzenkov, M.; Hevus, O., Eds. Springer International: Berlin, Heidelberg, 2014; pp 1-22.
38. Freedman H.H., M. J. P., Medalia A.I., Polysoaps-II: the preparation of vinyl soaps. *J. Am. Chem. Soc.* **1958**, *23*, 76-82.
39. Borzenkov, M.; Hevus, O., Colloidal Properties of Surface Active Monomers. In *Surface Active Monomers: Synthesis, Properties, and Application*. Borzenkov, M.; Hevus, O., Eds. Springer International: Berlin, Heidelberg, 2014; pp 23-37.
40. Borzenkov, M.; Hevus, O., Polymerization Behavior of Surface-Active Monomers. In *Surface Active Monomers: Synthesis, Properties, and Application*, Borzenkov, M.; Hevus, O., Eds. Springer International: Berlin, Heidelberg, 2014; pp 39-55.
41. Laschewsky, A., Molecular concepts, self-organisation and properties of polysoaps. In *Polysoaps/Stabilizers/Nitrogen-15 NMR*, Springer: Berlin, Heidelberg, 1995; pp 1-86.
42. Asua, J. M.; Schoonbrood, H. A. S., Reactive surfactants in heterophase polymerization. *Acta Polym.* **1999**, *49*, 671-686.
43. Greene, B. W.; Sheetz, D. P.; Filer, T. D., In situ polymerization of surface-active agents on latex particles I. Preparation and characterization of styrene/butadiene latexes. *J. Colloid Interface Sci.* **1970**, *32*, 90-95.
44. Caillier, L.; Taffin de Givenchy, E.; Levy, R.; Vandenberghe, Y.; Geribaldi, S.; Guittard, F., Polymerizable semi-fluorinated gemini surfactants designed for antimicrobial materials. *J. Colloid Interface Sci.* **2009**, *332*, 201-207.
45. Guyot, A., Polymerizable surfactants. *Curr. Opin. Colloid Interface Sci.* **1996**, *1*, 580-586.
46. Matahwa, H.; McLeary, J. B.; Sanderson, R. D., Comparative study of classical surfactants and polymerizable surfactants (surfmers) in the reversible addition-fragmentation chain transfer mediated miniemulsion polymerization of styrene and methyl methacrylate. *J. Polym. Sci. A* **2006**, *44*, 427-442.
47. Fischer, V.; Bannwarth, M. B.; Jakob, G.; Landfester, K.; Muñoz-Espí, R., Luminescent and Magnetoresponse Multifunctional Chalcogenide/Polymer Hybrid Nanoparticles. *J. Phys. Chem. C* **2013**, *117*, 5999-6005.
48. Crespy, D.; Musyanovych, A.; Landfester, K., Synthesis of polymer particles and nanocapsules stabilized with PEO/PPO containing polymerizable surfactants in miniemulsion. *Colloid Polym. Sci.* **2006**, *284*, 780-787.
49. Sauer, R.; Froimowicz, P.; Scholler, K.; Cramer, J. M.; Ritz, S.; Mailander, V.; Landfester, K., Design, synthesis, and miniemulsion polymerization of new phosphonate surfmers and application studies of the resulting nanoparticles as model systems for biomimetic mineralization and cellular uptake. *Chemistry* **2012**, *18*, 5201-5212.
50. Sauer, R.; Turshatov, A.; Baluschev, S.; Landfester, K., One-Pot Production of Fluorescent Surface-Labeled Polymeric Nanoparticles via Miniemulsion Polymerization with Bodipy Surfmers. *Macromolecules* **2012**, *45*, 3787-3796.
51. Williams, K.; Lee, E., Importance of Drug Enantiomers in Clinical Pharmacology. *Drugs* **1985**, *30*, 333-354.

52. Krische, M. J., Asymmetric Organocatalysis. From Biomimetic Concepts to Applications in Asymmetric Synthesis. By Albrecht Berkessel and Harald Gröger. *Angew. Chem. Int. Ed.* **2005**, *44*, 4285-4286.
53. Rosenbauer, E. M.; Triftaridou, A. I.; Karpati, S.; Tournilhac, F.; Leibler, L.; Auguste, S.; Pernot, J.-M., Synthesis of (meth)acrylate water-borne latexes using amino-acid based surfactants: effect of surfactant on film properties. *Polym. Chem.* **2012**, *3*, 2178-2185.
54. Preiss, L. C.; Wagner, M.; Mastai, Y.; Landfester, K.; Munoz-Espi, R., Amino-Acid-Based Polymerizable Surfactants for the Synthesis of Chiral Nanoparticles. *Macromol. Rapid. Commun.* **2016**, *37*, 1421-1426.
55. Xu, C.; Sun, S., New forms of superparamagnetic nanoparticles for biomedical applications. *Adv. Drug. Deliv. Rev.* **2013**, *65*, 732-743.
56. Verma, J.; Lal, S.; Van Noorden, C. J., Nanoparticles for hyperthermic therapy: synthesis strategies and applications in glioblastoma. *Int. J. Nanomedicine* **2014**, *9*, 2863-2877.
57. Park, J.; An, K.; Hwang, Y.; Park, J. G.; Noh, H. J.; Kim, J. Y.; Park, J. H.; Hwang, N. M.; Hyeon, T., Ultra-large-scale syntheses of monodisperse nanocrystals. *Nat. Mater.* **2004**, *3*, 891-895.
58. Ramírez, L. P.; Landfester, K., Magnetic Polystyrene Nanoparticles with a High Magnetite Content Obtained by Miniemulsion Processes. *Macromol. Chem. Phys.* **2003**, *204*, 22-31.
59. Bannwarth, M. B.; Kazer, S. W.; Ulrich, S.; Glasser, G.; Crespy, D.; Landfester, K., Well-defined nanofibers with tunable morphology from spherical colloidal building blocks. *Angew. Chem. Int. Ed.* **2013**, *52*, 10107-10111.
60. Bera, P.; Gayen, A.; Hegde, M. S.; Lalla, N. P.; Spadaro, L.; Frusteri, F.; Arena, F., Promoting Effect of CeO<sub>2</sub> in Combustion Synthesized Pt/CeO<sub>2</sub> Catalyst for CO Oxidation. *J. Phys. Chem., B* **2003**, *107*, 6122-6130.
61. Sohlberg, K.; Pantelides, S. T.; Pennycook, S. J., Interactions of Hydrogen with CeO<sub>2</sub>. *J. Am. Chem. Soc.* **2001**, *123*, 6609-6611.
62. Goubin, F.; Rocquefelte, X.; Whangbo, M. H.; Montardi, Y.; Brec, R.; Jovic, S., Experimental and Theoretical Characterization of the Optical Properties of CeO<sub>2</sub>, SrCeO<sub>3</sub>, and Sr<sub>2</sub>CeO<sub>4</sub> Containing Ce<sup>4+</sup> Ions. *Chem. Mater.* **2004**, *16*, 662-669.
63. Kumar, S.; Srivastava, M.; Singh, J.; Layek, S.; Yashpal, M.; Materny, A.; Ojha, A. K., Controlled synthesis and magnetic properties of monodispersed ceria nanoparticles. *AIP Adv.* **2015**, *5*, 27109-2113.
64. Vatanparast, M.; Saedi, L., Sonochemical-assisted synthesis and characterization of CeO<sub>2</sub> nanoparticles and its photocatalytic properties. *J. Mater. Sci. Mater. Electron.* **2018**, *29*, 7107-7113.
65. Xu, H.; Gao, L.; Gu, H.; Guo, J.; Yan, D., Synthesis of solid, spherical CeO<sub>2</sub> particles prepared by the spray hydrolysis reaction method. *J. Am. Ceram. Soc.* **2002**, *85*, 139-144.
66. Chen, W.; Li, F.; Yu, J., Combustion synthesis and characterization of nanocrystalline CeO<sub>2</sub>-based powders via ethylene glycol-nitrate process. *Mater. Lett.* **2006**, *60*, 57-62.
67. Zhang, F.; Chan, S. W.; Spanier, J. E.; Apak, E.; Jin, Q.; Robinson, R. D.; Herman, I. P., Cerium oxide nanoparticles: Size-selective formation and structure analysis. *Appl. Phys. Lett.* **2002**, *80*, 127-129.
68. Zhang, F.; Jin, Q.; Chan, S.W., Ceria nanoparticles: Size, size distribution, and shape. *J. Appl. Phys.* **2004**, *95*, 4319-4326.



69. Panahi-Kalamuei, M.; Alizadeh, S.; Mousavi-Kamazani, M.; Salavati-Niasari, M., Synthesis and characterization of CeO<sub>2</sub> nanoparticles via hydrothermal route. *J. Ind. Eng. Chem.* **2015**, *21*, 1301-1305.
70. Zhou, Y. C.; Rahaman, M. N., Hydrothermal synthesis and sintering of ultrafine CeO<sub>2</sub> powders. *J. Mater. Res.* **2011**, *8*, 1680-1686.
71. Wu, N. C.; Shi, E. W.; Zheng, Y. Q.; Li, W. J., Effect of pH of Medium on Hydrothermal Synthesis of Nanocrystalline Cerium(IV) Oxide Powders. *J. Am. Ceram. Soc.* **2005**, *85*, 2462-2468.
72. Li, Y. X.; Chen, W. F.; Zhou, X. Z.; Gu, Z. Y.; Chen, C. M., Synthesis of CeO<sub>2</sub> nanoparticles by mechanochemical processing and the inhibiting action of NaCl on particle agglomeration. *Mater. Lett.* **2005**, *59*, 48-52.
73. Wang, H.; Zhu, J. J.; Zhu, J. M.; Liao, X. H.; Xu, S.; Ding, T.; Chen, H. Y., Preparation of nanocrystalline ceria particles by sonochemical and microwave assisted heating methods. *Phys. Chem. Chem. Phys.* **2002**, *4*, 3794-3799.
74. Tamizhdurai, P.; Sakthinathan, S.; Chen, S. M.; Shanthi, K.; Sivasanker, S.; Sangeetha, P., Environmentally friendly synthesis of CeO<sub>2</sub> nanoparticles for the catalytic oxidation of benzyl alcohol to benzaldehyde and selective detection of nitrite. *Sci. Rep.* **2017**, *7*, 46372-46385.
75. Lee, J. S.; Lee, J. S.; Choi, S. C., Synthesis of nano-sized ceria powders by two-emulsion method using sodium hydroxide. *Mater. Lett.* **2005**, *59*, 395-398.
76. Zhou, X. D.; Huebner, W.; Anderson, H. U., Room-temperature homogeneous nucleation synthesis and thermal stability of nanometer single crystal CeO<sub>2</sub>. *Appl. Phys. Lett.* **2002**, *80*, 3814-3816.
77. Masui, T.; Fujiwara, K.; Machida, K.; Adachi, G.; Sakata, T.; Mori, H., Characterization of Cerium(IV) Oxide Ultrafine Particles Prepared Using Reversed Micelles. *Chem. Mater.* **1997**, *9*, 2197-2204.
78. Tunusoğlu, Ö.; Muñoz-Espí, R.; Akbey, Ü.; Demir, M. M., Surfactant-assisted formation of organophilic CeO<sub>2</sub> nanoparticles. *Colloids Surf., A* **2012**, *395*, 10-17.
79. Benmouhoub, C.; Kadri, A.; Benbrahim, N.; Hadji, S., Synthesis and Characterization of Cerium Oxide (CeO<sub>2</sub>) Nanoparticles. *Mater. Sci. Forum* **2009**, *609*, 189-194.
80. Chen, P. L.; Chen, I. W., Reactive Cerium(IV) Oxide Powders by the Homogeneous Precipitation Method. *J. Am. Ceram. Soc.* **1993**, *76*, 1577-1583.
81. Hirano, M.; Kato, E., Hydrothermal synthesis of nanocrystalline cerium(IV) oxide powders. *J. Am. Ceram. Soc.* **1999**, *82*, 786-788.
82. Djuričić, B.; Pickering, S., Nanostructured cerium oxide: Preparation and properties of weakly-agglomerated powders. *J. Eur. Ceram. Soc.* **1999**, *19*, 1925-1934.
83. Chen, H. I.; Chang, H. Y., Synthesis of nanocrystalline cerium oxide particles by the precipitation method. *Ceram. Int.* **2005**, *31*, 795-802.
84. Garabagiu, S.; Bratu, I., Thiol containing carboxylic acids remove the CTAB surfactant onto the surface of gold nanorods: An FTIR spectroscopic study. *Appl. Surf. Sci.* **2013**, *284*, 780-783.
85. Tiarks, F.; Landfester, K.; Antonietti, M., Silica Nanoparticles as Surfactants and Fillers for Latexes Made by Miniemulsion Polymerization. *Langmuir* **2001**, *17*, 5775-5780.

86. Berkel, K. Y.; Hawker, C. J., Tailored Composite Polymer-Metal Nanoparticles by Miniemulsion Polymerization and Thiol-ene Functionalization. *J. Polym. Sci. A* **2010**, *48*, 1594-1606.
87. Fuchs, I.; Avnir, D., Induction of amphiphilicity in polymer-silica particles: ceramic surfactants. *Langmuir* **2013**, *29*, 2835-42.
88. Groschel, A. H.; Walther, A.; Lobling, T. I.; Schacher, F. H.; Schmalz, H.; Muller, A. H., Guided hierarchical co-assembly of soft patchy nanoparticles. *Nature* **2013**, *503*, 247-51.
89. Philipse, A. P.; Vrij, A., Preparation and properties of nonaqueous model dispersions of chemically modified, charged silica spheres. *J. Colloid Interface Sci.* **1989**, *128*, 121-136.
90. Feuser, P. E.; Bubniak, L. S.; Silva, M. C. S.; Viegas, A. C.; Castilho Fernandes, A.; Ricci-Junior, E.; Nele, M.; Tedesco, A. C.; Sayer, C.; de Araújo, P. H. H., Encapsulation of magnetic nanoparticles in poly(methyl methacrylate) by miniemulsion and evaluation of hyperthermia in U87MG cells. *Eur. Polym. J.* **2015**, *68*, 355-365.
91. Feuser, P. E.; Jacques, A. V.; Arévalo, J. M. C.; Rocha, M. E. M.; Silva, M. C. S.; Sayer, C.; de Araújo, P. H. H., Superparamagnetic poly(methyl methacrylate) nanoparticles surface modified with folic acid presenting cell uptake mediated by endocytosis. *Journal of Nanoparticle Research* **2016**, *18*, 104-118.
92. Lan, F.; Liu, K. X.; Jiang, W.; Zeng, X. B.; Wu, Y.; Gu, Z. W., Facile synthesis of monodisperse superparamagnetic Fe<sub>3</sub>O<sub>4</sub>/PMMA composite nanospheres with high magnetization. *Nanotechnology* **2011**, *22*, 225604-225611.
93. Lu, S.; Forcada, J., Preparation and characterization of magnetic polymeric composite particles by miniemulsion polymerization. *J. Polym. Sci. A* **2006**, *44*, 4187-4203.
94. Ramos, J.; Forcada, J., Surfactant-free miniemulsion polymerization as a simple synthetic route to a successful encapsulation of magnetite nanoparticles. *Langmuir* **2011**, *27*, 7222-7230.
95. Lu, S.; Qu, R.; Forcada, J., Preparation of carboxylic magnetic polymeric composite particles by miniemulsion polymerization in the absence of hydrophobe. *Mater. Lett.* **2009**, *63*, 2539-2541.
96. Lu, S.; Ramos, J.; Forcada, J., Self-stabilized magnetic polymeric composite nanoparticles by emulsifier-free miniemulsion polymerization. *Langmuir* **2007**, *23*, 12893-12900.
97. Zhang, J.; Lu, Z.; Wu, M.; Wu, Q.; Yang, J., Large-scale synthesis and characterization of magnetic poly(acrylic acid) nanogels via miniemulsion polymerization. *RSC Adv.* **2015**, *5*, 58889-58894.
98. Schoth, A.; Keith, A. D.; Landfester, K.; Muñoz-Espí, R., Silanization as a versatile functionalization method for the synthesis of polymer/magnetite hybrid nanoparticles with controlled structure. *RSC Adv.* **2016**, *6*, 53903-53911.
99. Merkel, T.; Hecht, L. L.; Schoth, A.; Wagner, C.; Muñoz-Espí, R.; Landfester, K.; Schuchmann, H. P., Continuous Preparation of Polymer/Inorganic Composite Nanoparticles via Miniemulsion Polymerization. **2015**, 345-370.
100. Schoth, A.; Adurahim, E. S.; Bahattab, M. A.; Landfester, K.; Muñoz-Espí, R., Waterborne Polymer/Silica Hybrid Nanoparticles and Their Structure in Coatings. *Macromol. React. Eng.* **2016**, *10*, 47-54.
101. Qiao, X.; Chen, M.; Zhou, J.; Wu, L., Synthesis of raspberry-like silica/polystyrene/silica multilayer hybrid particles via miniemulsion polymerization. *J. Polym. Sci. A* **2007**, *45*, 1028-1037.

102. Costoyas, Á.; Ramos, J.; Forcada, J., Encapsulation of silica nanoparticles by miniemulsion polymerization. *J. Polym. Sci. A* **2009**, *47*, 935-948.
103. Bailly, B.; Donnenwirth, A. C.; Bartholome, C.; Beyou, E.; Bourgeat-Lami, E., Silica-Polystyrene Nanocomposite Particles Synthesized by Nitroxide-Mediated Polymerization and Their Encapsulation through Miniemulsion Polymerization. *J. Nanomater.* **2006**, *2006*, 1-10.
104. Zhang, S. W.; Zhou, S. X.; Weng, Y. M.; Wu, L. M., Synthesis of SiO<sub>2</sub>/Polystyrene Nanocomposite Particles via Miniemulsion Polymerization. *Langmuir* **2005**, *21*, 2124-2128.
105. Zhou, J.; Zhang, S.; Qiao, X.; Li, X.; Wu, L., Synthesis of SiO<sub>2</sub>/poly(styrene-co-butyl acrylate) nanocomposite microspheres via miniemulsion polymerization. *J. Polym. Sci. A* **2006**, *44*, 3202-3209.
106. Bourgeat-Lami, E.; Farzi, G. A.; David, L.; Putaux, J. L.; McKenna, T. F., Silica encapsulation by miniemulsion polymerization: distribution and localization of the silica particles in droplets and latex particles. *Langmuir* **2012**, *28*, 6021-6031.
107. Ramos-Fernández, J. M.; Guillem, C.; Lopez-Buendía, A.; Paulis, M.; Asua, J. M., Synthesis of poly-(BA-co-MMA) latexes filled with SiO<sub>2</sub> for coating in construction applications. *Prog. Org. Coat.* **2011**, *72*, 438-442.
108. Bonnefond, A.; Mičušik, M.; Paulis, M.; Leiza, J. R.; Teixeira, R. F. A.; Bon, S. A. F., Morphology and properties of waterborne adhesives made from hybrid polyacrylic/montmorillonite clay colloidal dispersions showing improved tack and shear resistance. *Colloid Polym. Sci.* **2013**, *291*, 167-180.
109. Diaconu, G.; Asua, J. M.; Paulis, M.; Leiza, J. R., High-Solids Content Waterborne Polymer-Clay Nanocomposites. *Macromol. Symp.* **2007**, *259*, 305-317.
110. Hauser, C. P.; Jagielski, N.; Heller, J.; Hinderberger, D.; Spiess, H. W.; Lieberwirth, I.; Weiss, C. K.; Landfester, K., Structure formation in metal complex/polymer hybrid nanomaterials prepared by miniemulsion. *Langmuir* **2011**, *27*, 12859-12868.
111. Pablico, M. H.; Mertzman, J. E.; Japp, E. A.; Boncher, W. L.; Nishida, M.; Van Keuren, E.; Lofland, S. E.; Dollahon, N.; Rubinson, J. F.; Holman, K. T.; Stoll, S. L., Miniemulsion synthesis of metal-oxo cluster containing copolymer nanobeads. *Langmuir* **2011**, *27*, 12575-12584.
112. Benedetti, C.; Cazzolaro, A.; Carraro, M.; Graf, R.; Landfester, K.; Gross, S.; Munoz-Espi, R., Dual Role of Zirconium Oxoclusters in Hybrid Nanoparticles: Cross-Linkers and Catalytic Sites. *ACS Appl. Mater. Interfaces* **2016**, *8*, 26275-26284.
113. Cao, Z.; Wang, Z.; Herrmann, C.; Landfester, K.; Ziener, U., Synthesis of narrowly size-distributed metal salt/poly(HEMA) hybrid particles in inverse miniemulsion: versatility and mechanism. *Langmuir* **2010**, *26*, 18008-18015.
114. Hunter, R. J., *Introduction to Modern Colloid Science*. 1st ed. ed.; Oxford University Press, New York, Melbourne, 1993.
115. Muñoz-Espí, R. Surface-functionalized latex particles as additives in the mineralization of zinc oxide: influence on crystal growth and properties. Ph.D. Dissertation, Johannes Gutenberg-Universität, Mainz, **2006**.
116. Bon, S. A. F.; Colver, P. J., Pickering Miniemulsion Polymerization Using Laponite Clay as a Stabilizer. *Langmuir* **2007**, *23*, 8316-8322.

117. González-Matheus, K.; Leal, G. P.; Tollan, C.; Asua, J. M., High solids Pickering miniemulsion polymerization. *Polymer* **2013**, *54*, 6314-6320.
118. González-Matheus, K.; Leal, G. P.; Asua, J. M., Pickering-Stabilized Latexes with High Silica Incorporation and Improved Salt Stability. *Part. Part. Syst. Char.* **2014**, *31*, 94-100.
119. González, E.; Bonnefond, A.; Barrado, M.; Casado Barrasa, A. M.; Asua, J. M.; Leiza, J. R., Photoactive self-cleaning polymer coatings by TiO<sub>2</sub> nanoparticle Pickering miniemulsion polymerization. *Chem. Eng. J.* **2015**, *281*, 209-217.
120. Bonnefond, A.; Ibarra, M.; Gonzalez, E.; Barrado, M.; Chuvilin, A.; Maria Asua, J.; Leiza, J. R., Photocatalytic and magnetic titanium dioxide/polystyrene/magnetite composite hybrid polymer particles. *J. Polym. Sci. A* **2016**, *54*, 3350-3356.
121. Zgheib, N.; Putaux, J. L.; Thill, A.; D'Agosto, F.; Lansalot, M.; Bourgeat-Lami, E., Stabilization of Miniemulsion Droplets by Cerium Oxide Nanoparticles: A Step toward the Elaboration of Armored Composite Latexes. *Langmuir* **2012**, *28*, 6163-6174.
122. Cauvin, S.; Colver, P. J.; Bon, S. A. F., Pickering Stabilized Miniemulsion Polymerization: Preparation of Clay Armored Latexes. *Macromolecules* **2005**, *38*, 7887-7889.
123. Ethirajan, A.; Ziener, U.; Landfester, K., Surface-functionalized polymeric nanoparticles as templates for biomimetic mineralization of hydroxyapatite. *Chem. Mater.* **2009**, *21*, 2218-2225.
124. Schöller, K.; Ethirajan, A.; Zeller, A.; Landfester, K., Biomimetic Route to Calcium Phosphate Coated Polymeric Nanoparticles: Influence of Different Functional Groups and pH. *Macromol. Chem. Phys.* **2011**, *212*, 1165-1175.
125. Cao, Z.; Schrade, A.; Landfester, K.; Ziener, U., Synthesis of raspberry-like organic-inorganic hybrid nanocapsules via pickering miniemulsion polymerization: Colloidal stability and morphology. *J. Polym. Sci. A* **2011**, *49*, 2382-2394.
126. Sundberg, E. J.; Sundberg, D. C., Morphology development for three-component emulsion polymers: Theory and experiments. *J. Appl. Polym. Sci.* **1993**, *47*, 1277-1294.
127. Chen, Z. J.; Yang, L.; Yan, Y. J.; Qi, D. M.; Cao, Z. H., Preparation of silica capsules via an acid-catalyzed sol-gel process in inverse miniemulsions. *Colloid Polym. Sci.* **2014**, *292*, 1585-1597.
128. Cao, Z.; Dong, L.; Li, L.; Shang, Y.; Qi, D.; Lv, Q.; Shan, G.; Ziener, U.; Landfester, K., Preparation of mesoporous submicrometer silica capsules via an interfacial sol-gel process in inverse miniemulsion. *Langmuir* **2012**, *28*, 7023-7032.
129. Hajir, M.; Dolcet, P.; Fischer, V.; Holzinger, J.; Landfester, K.; Muñoz-Espí, R., Sol-gel processes at the droplet interface: hydrous zirconia and hafnia nanocapsules by interfacial inorganic polycondensation. *J. Mater. Chem.* **2012**, *22*, 5622-5628.
130. Rosenbauer, E. M.; Landfester, K.; Musyanovych, A., Surface-active monomer as a stabilizer for polyurea nanocapsules synthesized via interfacial polyaddition in inverse miniemulsion. *Langmuir* **2009**, *25*, 12084-12091.
131. Taheri, S.; Baier, G.; Majewski, P.; Barton, M.; Förch, R.; Landfester, K.; Vasilev, K., Synthesis and antibacterial properties of a hybrid of silver-potato starch nanocapsules by miniemulsion/polyaddition polymerization. *J. Mater. Chem. B* **2014**, *2*, 1838-1845.

132. Sakho, E. H. M.; Allahyari, E.; Oluwafemi, O. S.; Thomas, S.; Kalarikkal, N., Chapter 2 - Dynamic Light Scattering (DLS). In *Thermal and Rheological Measurement Techniques for Nanomaterials Characterization*, Thomas, S.; Thomas, R.; Zachariah, A. K.; Mishra, R. K., Eds. Elsevier: 2017; pp 37-49.
133. Schärfl, W., *Light Scattering from Polymer Solutions and Nanoparticle Dispersions*, Springer: Berlin, Heidelberg, 2007.
134. Horvath, H., Gustav Mie and the scattering and absorption of light by particles: Historic developments and basics. *J. Quant. Spectrosc. Radiat. Transf.* **2009**, *110*, 787-799.
135. Goldstein, J.; Newbury, D. E.; Michael, J. R.; Ritchie, N. W. M.; Scott, J. H. J.; Joy, D. C., *Scanning electron microscopy and x-ray microanalysis*. Springer: New York, 2018.
136. Flegler, S. L.; Heckan, J. W.; Klomparens, K. L., *Scanning and Transmission Electron Microscopy: An Introduction*. Freeman, W. H.: New York, 1993.
137. Rietveld, H. M., A profile refinement method for nuclear and magnetic structures. *J. Appl. Crystallogr.* **1969**, *2*, 65-71.
138. Lamas, D. G.; Oliveira Neto, M.; Kellermann, G.; Craievich, A. F., X-Ray Diffraction and Scattering by Nanomaterials. In *Nanocharacterization Techniques*, Da Róz, A. L.; Ferreira, M.; de Lima Leite, F.; Oliveira, O. N., Eds. William Andrew: 2017; pp 111-182.
139. Antonello, A., Crystallization of Complex Inorganic Systems within the Confinement of Miniemulsion Droplets. Ph.D. Dissertation, Johannes Gutenberg-Universität, Mainz, **2017**.
140. Bragg, W. H.; Bragg, W. L., The reflection of X-rays by crystals. *Proc. R. Soc. A* **1913**, *88*, 428-438.
141. Scardi, P.; Leoni, M.; Delhez, R., Line broadening analysis using integral breadth methods: a critical review. *J. Appl. Crystallogr.* **2004**, *37*, 381-390.
142. Perkampus, H. H., Principles. In *UV-VIS Spectroscopy and Its Applications*, Springer: Berlin, Heidelberg, 1992; pp 3-9.
143. T. Fornstedt, P. F., and D. Westerlund, Basic HPLC Theory and Definitions: Retention, Thermodynamics, Selectivity, Zone Spreading, Kinetics, and Resolution. In *Analytical Separation Science*, Anderson, J. L.; Berthod, A.; Pino, V., Ed. Wiley-VCH: Weinheim, 2015; pp 1-24.
144. Grace, H., Dispersion Phenomena in High Viscosity Immiscible Fluid Systems and Application of Static Mixers as Dispersion Devices in Such Systems. *Chem. Eng. Commun.* **1982**, *14*, 225-277.
145. Laaksonen, T.; Heikkinen, S.; Wahala, K., Synthesis and applications of secondary amine derivatives of (+)-dehydroabietylamine in chiral molecular recognition. *Org. Biomol. Chem.* **2015**, *13*, 10548-10555.
146. Pradip, D., Recent Advances in the Synthesis of Amides via Oxime Rearrangements and its Applications. *Curr. Org. Synth.* **2018**, *15*, 666-706.
147. Cadierno, V.; Francos, J.; Gimeno, J., Selective ruthenium-catalyzed hydration of nitriles to amides in pure aqueous medium under neutral conditions. *Chemistry* **2008**, *14*, 6601-6605.
148. Ghaffar, T.; Parkins, A. W., The catalytic hydration of nitriles to amides using a homogeneous platinum phosphinito catalyst. *J. Mol. Catal. A* **2000**, *160*, 249-261.
149. Kim, J. H.; Britten, J.; Chin, J., Kinetics and mechanism of a cobalt(III) complex catalyzed hydration of nitriles. *J. Am. Chem. Soc.* **1993**, *115*, 3618-3622.

150. Breno, K. L.; Pluth, M. D.; Tyler, D. R., Organometallic Chemistry in Aqueous Solution. Hydration of Nitriles to Amides Catalyzed by a Water-Soluble Molybdocene,  $(\text{MeCp})_2\text{Mo}(\text{OH})(\text{H}_2\text{O})^+$ . *Organometallics* **2003**, *22*, 1203-1211.
151. Yamaguchi, K.; Matsushita, M.; Mizuno, N., Efficient Hydration of Nitriles to Amides in Water, Catalyzed by Ruthenium Hydroxide Supported on Alumina. *Angew. Chem.* **2004**, *116*, 1602-1606.
152. Haefele, L. R.; Young, H. J., Catalyzed Hydration of Nitriles to Amides. *Product R&D* **1972**, *11*, 364-365.
153. Tamura, M.; Wakasugi, H.; Shimizu, K.; Satsuma, A., Efficient and substrate-specific hydration of nitriles to amides in water by using a  $\text{CeO}_2$  catalyst. *Chemistry* **2011**, *17*, 11428-11431.
154. Swartz, S. L., Catalysis by Ceria and Related Materials. *J. Am. Chem. Soc.* **2002**, *124*, 12923-12924.
155. Vivier, L.; Duprez, D., Ceria-based solid catalysts for organic chemistry. *ChemSusChem* **2010**, *3*, 654-678.
156. Sato, S.; T, Ryoji.; Sodesawa, T.; Matsumoto, K.; Kamimura, Y., Ortho-Selective Alkylation of Phenol with 1-Propanol Catalyzed by  $\text{CeO}_2$ -MgO. *J. Catal.* **1999**, *178*, 264-274.
157. Beste, A.; Overbury, S. H., Pathways for Ethanol Dehydrogenation and Dehydration Catalyzed by Ceria (111) and (100) Surfaces. *J. Phys. Chem., C* **2015**, *119*, 2447-2455.
158. Gliński, M.; Szymański, W.; Łomot, D., Catalytic ketonization over oxide catalysts. *Appl. Catal., A* **2005**, *281*, 107-113.
159. Orozco, L. M.; Renz, M.; Corma, A., Cerium oxide as a catalyst for the ketonization of aldehydes: mechanistic insights and a convenient way to alkanes without the consumption of external hydrogen. *Green Chem.* **2017**, *19*, 1555-1569.
160. Kumar, R.; Enjamuri, N.; Shah, S.; Al-Fatesh, A. S.; Bravo-Suárez, J. J.; Chowdhury, B., Ketonization of oxygenated hydrocarbons on metal oxide based catalysts. *Catal. Today* **2018**, *302*, 16-49.
161. Abad, A.; Concepcion, P.; Corma, A.; Garcia, H., A collaborative effect between gold and a support induces the selective oxidation of alcohols. *Angew. Chem. Int. Ed.* **2005**, *44*, 4066-4069.
162. Artiglia, L.; Agnoli, S., Cerium Oxide Nanostructures on Titania: Effect of the Structure and Stoichiometry on the Reactivity Toward Ethanol Oxidation. *J. Phys. Chem., C* **2018**, 20809-20816.
163. Wang, Y.; Wang, F.; Song, Q.; Xin, Q.; Xu, S.; Xu, J., Heterogeneous ceria catalyst with water-tolerant Lewis acidic sites for one-pot synthesis of 1,3-diols via Prins condensation and hydrolysis reactions. *J. Am. Chem. Soc.* **2013**, *135*, 1506-1515.
164. Montini, T.; Melchionna, M.; Monai, M.; Fornasiero, P., Fundamentals and Catalytic Applications of  $\text{CeO}_2$ -Based Materials. *Chem. Rev.* **2016**, *116*, 5987-6041.
165. Baig, R. B.; Varma, R. S., Magnetically retrievable catalysts for organic synthesis. *Chem. Commun.* **2013**, *49*, 752-70.
166. Rossi, L. M.; Costa, N. J. S.; Silva, F. P.; Wojcieszak, R., Magnetic nanomaterials in catalysis: advanced catalysts for magnetic separation and beyond. *Green Chem.* **2014**, *16*, 2906.

167. Shylesh, S.; Schunemann, V.; Thiel, W. R., Magnetically separable nanocatalysts: bridges between homogeneous and heterogeneous catalysis. *Angew. Chem. Int. Ed.* **2010**, *49*, 3428-59.
168. Varma, R. S., Nano-catalysts with magnetic core: sustainable options for greener synthesis. *Sustain. Chem. Process.* **2014**, *2*, 1-8.
169. Vono, L. L. R.; Damasceno, C. C.; Matos, J. R.; Jardim, R. F.; Landers, R.; Masunaga, S. H.; Rossi, L. M., Separation technology meets green chemistry: development of magnetically recoverable catalyst supports containing silica, ceria, and titania. *Pure Appl. Chem.* **2018**, *90*, 133-141.
170. González, E.; Bonfond, A.; Barrado, M.; Casado Barrasa, A. M.; Asua, J. M.; Leiza, J. R., Photoactive self-cleaning polymer coatings by TiO<sub>2</sub> nanoparticle Pickering miniemulsion polymerization. *Chem. Eng. J.* **2015**, *281*, 209-217.
171. Kim, Y. J.; Liu, Y. D.; Seo, Y.; Choi, H. J., Pickering-emulsion-polymerized polystyrene/Fe<sub>2</sub>O<sub>3</sub> composite particles and their magnetoresponsive characteristics. *Langmuir* **2013**, *29*, 4959-4965.
172. Jiang, W. L.; Fu, Q. J.; Yao, B. J.; Ding, L. G.; Liu, C. X.; Dong, Y. B., Smart pH-Responsive Polymer-Tethered and Pd NP-Loaded NMOF as the Pickering Interfacial Catalyst for One-Pot Cascade Biphase Reaction. *ACS Appl. Mater. Interfaces* **2017**, *9*, 36438-36446.
173. Zhang, M.; Ngo, T. H.; Rabiah, N. I.; Otanicar, T. P.; Phelan, P. E.; Swaminathan, R.; Dai, L. L., Core-shell and asymmetric polystyrene-gold composite particles via one-step Pickering emulsion polymerization. *Langmuir* **2014**, *30*, 75-82.
174. Li, Y.; Sha, S.; Wu, Z.; Yang, C.; Ngai, T., Facile synthesis of gold nanoparticle-coated polystyrene composite particles templated from Pickering emulsion. *Colloids Surf., A* **2016**, *494*, 116-124.
175. Muñoz-Espí, R.; Qi, Y.; Lieberwirth, I.; Gomez, C. M.; Wegner, G., Surface-functionalized latex particles as controlling agents for the mineralization of zinc oxide in aqueous medium. *Chemistry* **2005**, *12*, 118-129.
176. Tamura, M.; Satsuma, A.; Shimizu, K., CeO<sub>2</sub>-catalyzed nitrile hydration to amide: reaction mechanism and active sites. *Catal. Sci. Technol.* **2013**, *3*, 1386-1393.
177. Tamura, M.; Sawabe, K.; Tomishige, K.; Satsuma, A.; Shimizu, K., Substrate-Specific Heterogeneous Catalysis of CeO<sub>2</sub> by Entropic Effects via Multiple Interactions. *ACS Catal.* **2014**, *5*, 20-26.
178. Hergt, R.; Dutz, S.; Müller, R.; Zeisberger, M., Magnetic particle hyperthermia: nanoparticle magnetism and materials development for cancer therapy. *J. Phys. Condens. Matter* **2006**, *18*, 2919-2934.
179. Satarkar, N. S.; Hilt, J. Z., Magnetic hydrogel nanocomposites for remote controlled pulsatile drug release. *J. Control. Release* **2008**, *130*, 246-251.
180. Alphandéry, E.; Faure, S.; Raison, L.; Duguet, E.; Howse, P. A.; Bazylinski, D. A., Heat Production by Bacterial Magnetosomes Exposed to an Oscillating Magnetic Field. *J. Phys. Chem., C* **2011**, *115*, 18-22.
181. Summers, M.; Eastoe, J., Applications of polymerizable surfactants. *Adv. Colloid Interface Sci.* **2003**, *100-102*, 137-152.
182. Gaunt, M. J.; Johansson, C. C.; McNally, A.; Vo, N. T., Enantioselective organocatalysis. *Drug Discov. Today* **2007**, *12*, 8-27.

183. List, B., Asymmetric Aminocatalysis. *Synlett* **2001**, *11*, 1675-1686.
184. Kotsuki, H.; Okuyama, A., Organocatalytic Asymmetric Synthesis Using Proline and Related Molecules. Part 1. *Heterocycles* **2008**, *75*, 493-529.
185. Hanessian, S.; Pham, V., Catalytic Asymmetric Conjugate Addition of Nitroalkanes to Cycloalkenones. *Org. Lett.* **2000**, *2*, 2975-2978.
186. Yamaguchi, M.; Shiraishi, T.; Hiramata, M., Asymmetric Michael Addition of Malonate Anions to Prochiral Acceptors Catalyzed by l-Proline Rubidium Salt. *J. Org. Chem.* **1996**, *61*, 3520-3530.
187. Hanessian, S.; Govindan, S.; Warrier, J. S., Probing the "additive effect" in the proline and proline hydroxamic acid catalyzed asymmetric addition of nitroalkanes to cyclic enones. *Chirality* **2005**, *17*, 540-543.
188. Notz, W.; List, B., Catalytic Asymmetric Synthesis of anti-1,2-Diols. *J. Am. Chem. Soc.* **2000**, *122*, 7386-7387.
189. Cordova, A., The Direct catalytic asymmetric cross-Mannich reaction: a highly enantioselective route to 3-amino alcohols and alpha-amino acid derivatives. *Chemistry* **2004**, *10*, 1987-1997.
190. Hayashi, Y.; Urushima, T.; Shin, M.; Shoji, M., The stereoselective synthesis of  $\alpha$ -substituted  $\beta$ -amino secondary alcohols based on the proline-mediated, asymmetric, three-component Mannich reaction and its application to the formal total synthesis of nikkomyces B and Bx. *Tetrahedron* **2005**, *61*, 11393-11404.
191. Ahrendt, K. A.; Borths, C. J.; MacMillan, D. W. C., New Strategies for Organic Catalysis: The First Highly Enantioselective Organocatalytic Diels–Alder Reaction. *J. Am. Chem. Soc.* **2000**, *122*, 4243-4244.
192. Paras, N. A.; MacMillan, D. W. C., New Strategies in Organic Catalysis: The First Enantioselective Organocatalytic Friedel–Crafts Alkylation. *J. Am. Chem. Soc.* **2001**, *123*, 4370-4371.
193. Ouellet, S. G.; Tuttle, J. B.; MacMillan, D. W. C., Enantioselective Organocatalytic Hydride Reduction. *J. Am. Chem. Soc.* **2005**, *127*, 32-33.
194. Bøgevig, A.; Juhl, K.; Kumaragurubaran, N.; Zhuang, W.; Jørgensen, K. A., Direct Organocatalytic Asymmetric  $\alpha$ -Amination of Aldehydes—A Simple Approach to Optically Active  $\alpha$ -Amino Aldehydes,  $\alpha$ -Amino Alcohols, and  $\alpha$ -Amino Acids. *Angew. Chem. Int. Ed.* **2002**, *41*, 1790-1793.
195. List, B., Direct Catalytic Asymmetric  $\alpha$ -Amination of Aldehydes. *J. Am. Chem. Soc.* **2002**, *124*, 5656-5657.
196. Marigo, M.; Wabnitz, T. C.; Fielenbach, D.; Jørgensen, K. A., Enantioselective organocatalyzed alpha sulfenylation of aldehydes. *Angew. Chem. Int. Ed.* **2005**, *44*, 794-797.
197. Enders, D.; Hüttl, M., Direct Organocatalytic  $\alpha$ -Fluorination of Aldehydes and Ketones. *Synlett* **2005**, *2005*, 0991-0993.
198. Kotsuki, H.; Okuyama, A., Organocatalytic Asymmetric Synthesis Using Proline and Related Molecules. Part 2. *Heterocycles* **2008**, *75*, 757-797.
199. Pidathala, C.; Hoang, L.; Vignola, N.; List, B., Direct catalytic asymmetric enolxo aldolizations. *Angew. Chem. Int. Ed.* **2003**, *42*, 2785-2788.



200. Sakthivel, K.; Notz, W.; Bui, T.; Barbas, C. F., Amino Acid Catalyzed Direct Asymmetric Aldol Reactions: A Bioorganic Approach to Catalytic Asymmetric Carbon–Carbon Bond-Forming Reactions. *J. Am. Chem. Soc.* **2001**, *123*, 5260-5267.
201. List, B.; Lerner, R. A.; Barbas, C. F., Proline-Catalyzed Direct Asymmetric Aldol Reactions. *J. Am. Chem. Soc.* **2000**, *122*, 2395-2396.
202. Córdova, A., Direct catalytic asymmetric cross-aldol reactions in ionic liquid media. *Tetrahedron Lett.* **2004**, *45*, 3949-3952.
203. Ian Storer, R.; MacMillan, D. W. C., Enantioselective organocatalytic aldehyde–aldehyde cross-aldol couplings. The broad utility of  $\alpha$ -thioacetal aldehydes. *Tetrahedron* **2004**, *60*, 7705-7714.
204. Hayashi, Y.; Aratake, S.; Okano, T.; Takahashi, J.; Sumiya, T.; Shoji, M., Combined Proline–Surfactant Organocatalyst for the Highly Diastereo- and Enantioselective Aqueous Direct Cross-Aldol Reaction of Aldehydes. *Angew. Chem.* **2006**, *118*, 5653-5655.
205. Chimni, S. S.; Mahajan, D., Small organic molecule catalyzed enantioselective direct aldol reaction in water. *Tetrahedron: Asymmetry* **2006**, *17*, 2108-2119.
206. Nakadai, M.; Saito, S.; Yamamoto, H., Diversity-based strategy for discovery of environmentally benign organocatalyst: diamine–protonic acid catalysts for asymmetric direct aldol reaction. *Tetrahedron* **2002**, *58*, 8167-8177.
207. Mase, N.; Nakai, Y.; Ohara, N.; Yoda, H.; Takabe, K.; Tanaka, F.; Barbas, C. F., Organocatalytic Direct Asymmetric Aldol Reactions in Water. *J. Am. Chem. Soc.* **2006**, *128*, 734-735.
208. Hernandez, J. G.; Juaristi, E., Asymmetric aldol reaction organocatalyzed by (L)-proline-containing dipeptides: improved stereoselection under solvent-free conditions. *J. Org. Chem.* **2011**, *76*, 1464-1467.
209. Gruttadauria, M.; Giacalone, F.; Noto, R., Water in Stereoselective Organocatalytic Reactions. *Adv. Synth. Catal.* **2009**, *351*, 33-57.
210. Kondo, K.; Yamano, T.; Takemoto, K., Functional monomers and polymers, 129. Asymmetric robinson cyclization reaction catalyzed by polymer-bound L-proline. *Die Makromol. Chem.* **1985**, *186*, 1781-1785.
211. Benaglia, M.; Cinquini, M.; Cozzi, F.; Puglisi, A.; Celentano, G., Poly(Ethylene Glycol)-Supported Proline: A Versatile Catalyst for the Enantioselective Aldol and Iminoaldol Reactions. *Adv. Synth. Catal.* **2002**, *344*, 533-542.
212. Doyagüez, E. G.; Parra, F.; Corrales, G.; Fernández-Mayoralas, A.; Gallardo, A., New hydroxyproline based methacrylic polybetaines: Synthesis, pH sensitivity and catalytic activity. *Polymer* **2009**, *50*, 4438-4446.
213. Guo, G.; Wu, Y.; Zhao, X.; Wang, J.; Zhang, L.; Cui, Y., Polymerization of L-proline functionalized styrene and its catalytic performance as a supported organocatalyst for direct enantioselective aldol reaction. *Tetrahedron: Asymmetry* **2016**, *27*, 740-746.
214. Doyagüez, E. G.; Corrales, G.; Garrido, L.; Rodríguez-Hernández, J.; Gallardo, A.; Fernández-Mayoralas, A., Linear Copolymers of Proline Methacrylate and Styrene as Catalysts for Aldol Reactions in Water: Effect of the Copolymer Aggregation on the Enantioselectivity. *Macromolecules* **2011**, *44*, 6268-6276.
215. Kristensen, T. E.; Hansen, F. K.; Hansen, T., The Selective O-Acylation of Hydroxyproline as a Convenient Method for the Large-Scale Preparation of Novel Proline Polymers and Amphiphiles. *Eur. J. Org. Chem.* **2009**, *2009*, 387-395.

216. Benaglia, M.; Puglisi, A.; Cozzi, F., Polymer-Supported Organic Catalysts. *Chem. Rev.* **2003**, *103*, 3401-3430.
217. Kristensen, T. E.; Hansen, T., Polymer-Supported Chiral Organocatalysts: Synthetic Strategies for the Road Towards Affordable Polymeric Immobilization. *Eur. J. Org. Chem.* **2010**, *2010*, 3179-3204.
218. Gruttadauria, M.; Giacalone, F.; Mossuto Marculescu, A.; Lo Meo, P.; Riela, S.; Noto, R., Hydrophobically Directed Aldol Reactions: Polystyrene-Supported L-Proline as a Recyclable Catalyst for Direct Asymmetric Aldol Reactions in the Presence of Water. *Eur. J. Org. Chem.* **2007**, *2007*, 4688-4698.
219. Font, D.; Jimeno, C.; Pericàs, M. A., Polystyrene-Supported Hydroxyproline: An Insoluble, Recyclable Organocatalyst for the Asymmetric Aldol Reaction in Water. *Org. Lett.* **2006**, *8*, 4653-4655.
220. Giacalone, F.; Gruttadauria, M.; Marculescu, A. M.; Noto, R., Polystyrene-supported proline and prolinamide. Versatile heterogeneous organocatalysts both for asymmetric aldol reaction in water and  $\alpha$ -selenenylation of aldehydes. *Tetrahedron Lett.* **2007**, *48*, 255-259.
221. Llanes, P.; Sayalero, S.; Rodríguez-Esrich, C.; Pericàs, M. A., Asymmetric cross- and self-aldol reactions of aldehydes in water with a polystyrene-supported triazolylproline organocatalyst. *Green Chem.* **2016**, *18*, 3507-3512.
222. Kristensen, T. E., Chemoselective O-acylation of hydroxyamino acids and amino alcohols under acidic reaction conditions: History, scope and applications. *J. Org. Chem.* **2015**, *11*, 446-468.
223. Kristensen, T. E.; Vestli, K.; Fredriksen, K. A.; Hansen, F. K.; Hansen, T., Synthesis of Acrylic Polymer Beads for Solid-Supported Proline-Derived Organocatalysts. *Org. Lett.* **2009**, *11*, 2968-2971.
224. Lu, A.; Smart, T. P.; Epps, T. H.; Longbottom, D. A.; O'Reilly, R. K., L-Proline Functionalized Polymers Prepared by RAFT Polymerization and Their Assemblies as Supported Organocatalysts. *Macromolecules* **2011**, *44*, 7233-7241.
225. Lu, A.; Cotanda, P.; Patterson, J. P.; Longbottom, D. A.; O'Reilly, R. K., Aldol reactions catalyzed by L-proline functionalized polymeric nanoreactors in water. *Chem. Commun.* **2012**, *48*, 9699-9701.
226. Adler, S. R.; Mastai, Y., Chiral polymeric nanoparticles for aldol reaction. *React. Funct. Polym.* **2015**, *96*, 1-4.
227. Khair, N.; Navas, R.; Elhalem, E.; Valdivia, V.; Fernández, I., Proline-coated gold nanoparticles as a highly efficient nanocatalyst for the enantioselective direct aldol reaction in water. *RSC Adv.* **2013**, *3*, 3861-3864.
228. Sóti, P. L.; Yamashita, H.; Sato, K.; Narumi, T.; Toda, M.; Watanabe, N.; Marosi, G.; Mase, N., Synthesis of a self-assembling gold nanoparticle-supported organocatalyst for enamine-based asymmetric aldol reactions. *Tetrahedron* **2016**, *72*, 1984-1990.
229. Kong, Y.; Tan, R.; Zhao, L.; Yin, D., L-Proline supported on ionic liquid-modified magnetic nanoparticles as a highly efficient and reusable organocatalyst for direct asymmetric aldol reaction in water. *Green Chem.* **2013**, *15*, 2422-2433.
230. Nehlig, E.; Motte, L.; Guénin, E., Magnetic nano-organocatalysts: impact of surface functionalization on catalytic activity. *RSC Adv.* **2015**, *5*, 104688-104694.

231. Safaei-Ghomi, J.; Masoomi, R.; Hamadian, M.; Naseh, S., Magnetic nanoscale core-shell structured Fe<sub>3</sub>O<sub>4</sub>-L-proline: an efficient, reusable and eco-friendly nanocatalyst for diastereoselective synthesis of fulleropyrrolidines. *New J. Chem.* **2016**, *40*, 3289-3299.
232. Schrader, I.; Warneke, J.; Backenkohler, J.; Kunz, S., Functionalization of platinum nanoparticles with L-proline: simultaneous enhancements of catalytic activity and selectivity. *J. Am. Chem. Soc.* **2015**, *137*, 905-912.
233. Yacob, Z.; Nan, A.; Liebscher, J., Proline-Functionalized Magnetic Core-Shell Nanoparticles as Efficient and Recyclable Organocatalysts for Aldol Reactions. *Adv. Synth. Catal.* **2012**, *354*, 3259-3264.
234. Ning, Y.; Fielding, L. A.; Doncom, K. E.; Penfold, N. J.; Kulak, A. N.; Matsuoka, H.; Armes, S. P., Incorporating Diblock Copolymer Nanoparticles into Calcite Crystals: Do Anionic Carboxylate Groups Alone Ensure Efficient Occlusion? *ACS Macro. Lett.* **2016**, *5*, 311-315.
235. Calderón, F.; Doyagüez, E. G.; Cheong, P. H. Y.; Fernández-Mayoralas, A.; Houk, K. N., Origins of the Double Asymmetric Induction on Proline-Catalyzed Aldol Reactions. *J. Org. Chem.* **2008**, *73*, 7916-7920.
236. Chen, Y. H.; Sung, P. H.; Sung, K., Synthesis of proline-derived dipeptides and their catalytic enantioselective direct aldol reactions: catalyst, solvent, additive and temperature effects. *Amino Acids* **2010**, *38*, 839-845.
237. Cobb, A. J.; Shaw, D. M.; Longbottom, D. A.; Gold, J. B.; Ley, S. V., Organocatalysis with proline derivatives: improved catalysts for the asymmetric Mannich, nitro-Michael and aldol reactions. *Org. Biomol. Chem.* **2005**, *3*, 84-96.
238. Liu, C.; Li, F.; Ma, L. P.; Cheng, H. M., Advanced materials for energy storage. *Adv. Mater.* **2010**, *22*, 28-62.
239. Sharma, A.; Tyagi, V. V.; Chen, C. R.; Buddhi, D., Review on thermal energy storage with phase change materials and applications. *Renew. Sust. Energ. Rev.* **2009**, *13*, 318-345.
240. Hyun, D. C.; Levinson, N. S.; Jeong, U.; Xia, Y., Emerging applications of phase-change materials (PCMs): teaching an old dog new tricks. *Angew. Chem. Int. Ed.* **2014**, *53*, 3780-3795.
241. Shchukina, E. M.; Graham, M.; Zheng, Z.; Shchukin, D. G., Nanoencapsulation of phase change materials for advanced thermal energy storage systems. *Chem. Soc. Rev.* **2018**, *47*, 4156-4175.
242. Oró, E.; de Gracia, A.; Castell, A.; Farid, M. M.; Cabeza, L. F., Review on phase change materials (PCMs) for cold thermal energy storage applications. *Appl. Energ.* **2012**, *99*, 513-533.
243. Farid, M. M.; Khudhair, A. M.; Razack, S. A. K.; Al-Hallaj, S., A review on phase change energy storage: materials and applications. *Energy Convers. Manag.* **2004**, *45*, 1597-1615.
244. Xie, N.; Huang, Z.; Luo, Z.; Gao, X.; Fang, Y.; Zhang, Z., Inorganic Salt Hydrate for Thermal Energy Storage. *Appl. Sci.* **2017**, *7*, 1317-1335.
245. Lin, Y.; Jia, Y.; Alva, G.; Fang, G., Review on thermal conductivity enhancement, thermal properties and applications of phase change materials in thermal energy storage. *Renew. Sust. Energ. Rev.* **2018**, *82*, 2730-2742.
246. Pielichowska, K.; Pielichowski, K., Phase change materials for thermal energy storage. *Prog. Mater. Sci.* **2014**, *65*, 67-123.

247. Su, W.; Darkwa, J.; Kokogiannakis, G., Review of solid–liquid phase change materials and their encapsulation technologies. *Renew. Sust. Energ. Rev.* **2015**, *48*, 373-391.
248. Farrell, A. J.; Norton, B.; Kennedy, D. M., Corrosive effects of salt hydrate phase change materials used with aluminium and copper. *J. Mater. Process. Technol.* **2006**, *175*, 198-205.
249. Safari, A.; Saidur, R.; Sulaiman, F. A.; Xu, Y.; Dong, J., A review on supercooling of Phase Change Materials in thermal energy storage systems. *Renew. Sust. Energ. Rev.* **2017**, *70*, 905-919.
250. Milián, Y. E.; Gutiérrez, A.; Grágeda, M.; Ushak, S., A review on encapsulation techniques for inorganic phase change materials and the influence on their thermophysical properties. *Renew. Sust. Energ. Rev.* **2017**, *73*, 983-999.
251. Graham, M.; Shchukina, E.; De Castro, P. F.; Shchukin, D., Nanocapsules containing salt hydrate phase change materials for thermal energy storage. *J. Mater. Chem. A* **2016**, *4*, 16906-16912.
252. Graham, M.; Coca-Clemente, J. A.; Shchukina, E.; Shchukin, D., Nanoencapsulated crystalhydrate mixtures for advanced thermal energy storage. *J. Mater. Chem. A* **2017**, *5*, 13683-13691.
253. Salaün, F.; Devaux, E.; Bourbigot, S.; Rumeau, P., Development of a precipitation method intended for the entrapment of hydrated salt. *Carbohydr. Polym.* **2008**, *73*, 231-240.
254. Salaün, F.; Devaux, E.; Bourbigot, S.; Rumeau, P., Influence of the solvent on the microencapsulation of an hydrated salt. *Carbohydr. Polym.* **2010**, *79*, 964-974.
255. Hassabo, A.; Wang, C.; Popescu, M.; Moller, M., Metal salts rented in silicamicrocapsules as inorganic phase change materials for textile usage. *Inorg. Chem. Ind. J.* **2015**, *10*, 59-65.
256. Huang, J.; Wang, T.; Zhu, P.; Xiao, J., Preparation, characterization, and thermal properties of the microencapsulation of a hydrated salt as phase change energy storage materials. *Thermochim. Acta* **2013**, *557*, 1-6.
257. Wang, T.; Huang, J.; Zhu, P.; Xiao, J., Fabrication and characterization of micro-encapsulated sodium phosphate dodecahydrate with different crosslinked polymer shells. *Colloid Polym. Sci.* **2013**, *291*, 2463-2468.
258. Platte, D.; Helbig, U.; Houbertz, R.; Sextl, G., Microencapsulation of Alkaline Salt Hydrate Melts for Phase Change Applications by Surface Thiol-Michael Addition Polymerization. *Macromol. Mater. Eng.* **2013**, *298*, 67-77.
259. Liu, C.; Wang, C.; Li, Y.; Rao, Z., Preparation and characterization of sodium thiosulfate pentahydrate/silica microencapsulated phase change material for thermal energy storage. *RSC Adv.* **2017**, *7*, 7238-7249.
260. Zhang, J.; Wang, S.; Zhang, S.; Tao, Q.; Pan, L.; Wang, Z.; Zhang, Z.; Lei, Y.; Yang, S.; Zhao, H., In Situ Synthesis and Phase Change Properties of  $\text{Na}_2\text{SO}_4 \cdot 10\text{H}_2\text{O}$ - $\text{SiO}_2$  Solid Nanobowls toward Smart Heat Storage. *J. Phys. Chem., C* **2011**, *115*, 20061-20066.
261. Alam, T.; Dhau, J.; Goswami, D.; Stefanakos, E., Macroencapsulation and characterization of phase change materials for latent heat thermal energy storage systems. *Appl. Energ.* **2015**, *154*, 92-101.
262. Peyratout, C.; Dahne, L., Tailor-made polyelectrolyte microcapsules: from multilayers to smart containers. *Angew. Chem. Int. Ed.* **2004**, *43*, 3762-83.

263. Andreeva, D.; Gorin, D.; Shchukin, D.; Sukhorukov, G., Magnetic Microcapsules with Low Permeable Polypyrrole Skin Layer. *Macromol. Rapid. Commun.* **2006**, *27*, 931-936.
264. Lu, Z.; Prouty, M.; Guo, Z.; Golub, V.; Kumar, C.; Lvov, Y., Magnetic Switch of Permeability for Polyelectrolyte Microcapsules Embedded with Co–Au Nanoparticles. *Langmuir* **2005**, *21*, 2042-2050.
265. Tsuneyoshi, T.; Ono, T., Metal-coated microcapsules with tunable magnetic properties synthesized via electroless plating. *Mater. Sci. Eng. B* **2017**, *222*, 49-54.
266. Yang, W. C.; Xie, R.; Pang, X. Q.; Ju, X. J.; Chu, L. Y., Preparation and characterization of dual stimuli-responsive microcapsules with a superparamagnetic porous membrane and thermo-responsive gates. *J. Membr. Sci.* **2008**, *321*, 324-330.
267. Li, J.; Liu, H.; Wang, X.; Wu, D., Development of Thermoregulatory Enzyme Carriers Based on Microencapsulated n-Docosane Phase Change Material for Biocatalytic Enhancement of Amylases. *ACS. Sustain. Chem. Eng.* **2017**, *5*, 8396-8406.
268. Jiang, B.; Wang, X.; Wu, D., Fabrication of microencapsulated phase change materials with TiO<sub>2</sub>/Fe<sub>3</sub>O<sub>4</sub> hybrid shell as thermoregulatory enzyme carriers: A novel design of applied energy microsystem for bioapplications. *Appl. Energ.* **2017**, *201*, 20-33.
269. Donkers, P.; Linnow, K.; Pel, L.; Steiger, M.; Adan, O., Na<sub>2</sub>SO<sub>4</sub>·10H<sub>2</sub>O dehydration in view of thermal storage. *Chem. Eng. Sci.* **2015**, *134*, 360-366.
270. Telkes, M., Thermal Energy Storage in Salt Hydrates. *Sol. Energy* **1980**, *2*, 381-393.
271. Liu, Z.; Chung, D., Calorimetric evaluation of phase change materials for use as thermal interface materials. *Thermochim. Acta* **2001**, *366*, 135-147.
272. Crespy, D.; Stark, M.; Hoffmann-Richter, C.; Ziener, U.; Landfester, K., Polymeric Nanoreactors for Hydrophilic Reagents Synthesized by Interfacial Polycondensation on Miniemulsion Droplets. *Macromolecules* **2007**, *40*, 3122-3135.
273. Jagielski, N.; Sharma, S.; Hombach, V.; Mailänder, V.; Rasche, V.; Landfester, K., Nanocapsules Synthesized by Miniemulsion Technique for Application as New Contrast Agent Materials. *Macromol. Chem. Phys.* **2007**, *208*, 2229-2241.
274. Schlegel, I.; Muñoz-Espí, R.; Renz, P.; Lieberwirth, I.; Floudas, G.; Suzuki, Y.; Crespy, D.; Landfester, K., Crystallinity Tunes Permeability of Polymer Nanocapsules. *Macromolecules* **2017**, *50*, 4725-4732.
275. Biswas, D. R., Thermal energy storage using sodium sulfate decahydrate and water. *Sol. Energy* **1977**, *19*, 99-100.
276. García-Romero, A.; Diarce, G.; Ibarretxe, J.; Urresti, A.; Sala, J. M., Influence of the experimental conditions on the subcooling of Glauber's salt when used as PCM. *Sol. Energy Mater. Sol. Cells* **2012**, *102*, 189-195.
277. Bourgeat-Lami, E.; Herrera, N. N.; Putaux, J. L.; Reculosa, S.; Perro, A.; Ravaine, S.; Mingotaud, C.; Duguet, E., Surface Assisted Nucleation and Growth of Polymer Latexes on Organically-Modified Inorganic Particles. *Macromol. Symp.* **2005**, *229*, 32-46.



## A. List of Figures

<b>Figure 2.1.</b> Scheme of the preparation of polymer–inorganic nanoparticles by miniemulsion polymerization and the possible hybrid morphologies achieved. (Based on ref. 14).....	6
<b>Figure 2.2.</b> Phase segregation in a three-component system comprised of two oil dispersed phases (1 and 3) and a polar continuous phase (2), determined by the spreading coefficients ( $s_i$ ). (Based on refs. 14 and 22) .....	9
<b>Figure 2.3.</b> Schematic representation of the coalescence and the droplet growth in miniemulsions. Colloidal stabilization offered by surfactants, based on steric and electrostatic repulsion between droplets. (Based on ref. 3).....	12
<b>Figure 2.4.</b> Schematic representation of the Ostwald ripening principle in miniemulsions. Stabilization against the interdroplet mass diffusion allowed with the incorporation of osmotic agents. (Based on ref. 3) .....	13
<b>Figure 2.5.</b> Schematic representation of the nature of the Pickering emulsions formed depending on the contact angle of the particles at the oil/water interface. (Based on ref. 36).....	15
<b>Figure 2.6.</b> Schematic representation of the electrostatic principle of the double layer. (Based on ref. 115).....	24
<b>Figure 2.7.</b> Scheme of the preparation of magnetoresponsive polystyrene-supported ceria nanocatalysts by Pickering miniemulsion polymerization. (Based on ref. 14).....	26
<b>Figure 2.8.</b> Schematic representation of the preparation of magnetoresponsive polystyrene-supported ceria nanocatalysts via miniemulsion polymerization and in-situ inorganic crystallization on the polymer surface. (Based on ref. 6).....	28
<b>Figure 2.9.</b> Scheme of the preparation of polyurethane–inorganic capsules by interfacial polymerization process in an inverse Pickering miniemulsion.....	30
<b>Figure 3.1.</b> Schematic representation of the electrostatic interaction between the negatively charged surface of a functionalized polymer particle and the positively charged chains of polyDADMAC. (Based on ref. 115).....	33
<b>Figure 4.1.</b> TGA curves of ceria nanoparticles functionalized with MPS before and after the last washing operation (a), and comparative of the curves of ceria nanoparticles with the functionalization achieved with the three different silane compounds used in the work (MPS, PTMS, and ODTMS) (b). .....	45

---

<b>Figure 4.2.</b> TGA curves of titania (a) and magnetite (b) nanoparticles functionalized with three different silane components (MPS, PTMS, and ODTMS), compared with the raw nanoparticles.....	45
<b>Figure 4.3.</b> TGA curves of the hybrid nanoparticles incorporating ceria functionalized with ODTMS (blue line), PTMS (green line), or MPS (magenta line) within polystyrene ( <b>SC1-3</b> ) (a) and PMMA ( <b>MC1-3</b> ) (b). .....	48
<b>Figure 4.4.</b> TGA curves of the hybrid nanoparticles incorporating titania functionalized with ODTMS (blue line), PTMS (green line), or MPS (magenta line) within polystyrene ( <b>ST1-3</b> ) (a) and PMMA ( <b>MT1-3</b> ) (b).....	49
<b>Figure 4.5.</b> TEM and SEM micrographs of the polystyrene-based hybrid nanoparticles incorporating ceria nanoparticles functionalized with ODTMS (a, d), PTMS (b, e), and MPS (c, f). .....	50
<b>Figure 4.6.</b> TEM and SEM micrographs of the PMMA-based hybrid nanoparticles incorporating ceria nanoparticles functionalized with ODTMS (a, d), PTMS (b, e), and MPS (c, f).....	50
<b>Figure 4.7.</b> TEM and SEM micrographs of the polystyrene-based hybrid nanoparticles incorporating titania nanoparticles functionalized with ODTMS (a, d) and PTMS (b, e).....	51
<b>Figure 4.8.</b> TEM and SEM micrographs of the PMMA-based hybrid nanoparticles incorporating titania nanoparticles functionalized with ODTMS (a, d), PTMS (b, e), and MPS (c, f).....	51
<b>Figure 4.9.</b> TGA curves obtained for the polystyrene-ceria hybrid nanoparticles <b>SC1</b> (blue line), <b>SC4</b> (green line), and <b>SC5</b> (magenta line) prepared by miniemulsion polymerization using AIBN, AMBN, and KPS as free-radical initiators, respectively. ....	54
<b>Figure 4.10.</b> TEM micrographs of the polystyrene with ODTMS-functionalized ceria ( <b>SC1</b> , <b>SC4</b> , and <b>SC5</b> ) and PMMA with ODTMS-functionalized titania ( <b>MT1</b> , <b>MT4</b> , and <b>MT5</b> ) hybrid nanoparticles, prepared by miniemulsion polymerization using AIBN, AMBN, and KPS as free-radical initiators respectively. ....	54
<b>Figure 4.11.</b> SEM and TEM micrographs of the multifunctional nanoparticles <b>SF1</b> (a, b), <b>SF2</b> (c, d), <b>MF1</b> (e, f), and <b>MF2</b> (g, h).....	57
<b>Figure 5.1.</b> X-ray diffraction (XRD) patterns of ceria and MPS-functionalized magnetite nanoparticles, and catalysts <b>C5</b> and <b>C6</b> . ....	64
<b>Figure 5.2.</b> Thermographs of MPS-functionalized magnetite nanoparticles (green line), catalysts <b>C3</b> (magenta dashed line), <b>C4</b> (blue dashed line), <b>C5</b> (magenta line), and <b>C6</b> (blue line).....	65



---

<b>Figure 5.3.</b> SEM micrographs at two different magnifications (a, d, g, j) and (b, e, h, k), and TEM (c, f, i, l) images of the polystyrene-supported ceria catalysts <b>C1</b> (a, b, c) and <b>C5</b> (g, h, i) prepared via routes <b>P1</b> and <b>P2</b> , respectively. Analogue images of the corresponding samples <b>C2</b> (d, e, f) and <b>C5</b> (g, h, i), incorporating a magnetic core. ....	66
<b>Figure 5.4.</b> TEM (a) and SEM (b) micrographs of sample <b>C4</b> . ....	67
<b>Figure 5.5.</b> Influence of the concentration of CeO <sub>2</sub> on the kinetics of the hydration of 2-cyanopyridine catalyzed by <b>C2</b> (a, c) and <b>C6</b> (b, d). Evolution of the conversion (1- $\alpha$ ) (a, b) and -ln( $\alpha$ ) (c, d) of the reaction achieved with different concentrations of each catalyst. ....	69
<b>Figure 5.6.</b> Comparison of the catalytic efficiency of hybrid catalysts prepared via <b>P1</b> and <b>P2</b> strategies, and the non-supported ceria nanoparticles. Kinetics of the hydration of 2-cyanopyridine catalyzed by <b>C1</b> , <b>C2</b> (a, c) and <b>C5</b> , <b>C6</b> (b, d). Evolution of the conversion (1- $\alpha$ ) (a, b) and -ln( $\alpha$ ) (c, d) of the reaction achieved with each catalyst. ....	70
<b>Figure 5.7.</b> Kinetic study of the hydration of 2-cyanopyridine in the presence of polymer ( <b>C3</b> ) and polymer-magnetite hybrid nanoparticles ( <b>C4</b> ). ....	71
<b>Figure 5.8.</b> Recycling study of the magnetically recoverable catalysts <b>C2</b> and <b>C6</b> . ....	72
<b>Figure 6.1.</b> Schematic representation of the synthesis of magneto-responsive proline-functionalized PMMA chiral nanoparticles via miniemulsion polymerization using a proline-based surfmer. ....	76
<b>Figure 6.2.</b> <sup>1</sup> H-NMR and <sup>13</sup> C-NMR spectra of the surfmer (L-S1). ....	77
<b>Figure 6.3.</b> <sup>1</sup> H-NMR and <sup>13</sup> C-NMR spectra of the monomer (L-S2). ....	78
<b>Figure 6.4.</b> <sup>1</sup> H-NMR and <sup>13</sup> C-NMR spectra of the surfactant (L-S3). ....	79
<b>Figure 6.5.</b> SEM and TEM micrographs of the magneto-responsive chiral particles <b>AC2</b> (a, e), <b>AC3</b> (b, f), <b>AC5</b> (c, g), and <b>AC6</b> (d, h). ....	82
<b>Figure 6.6.</b> SEM micrographs of the polymer nanoparticles <b>AC7</b> (a) and <b>AC9</b> (b) synthesized using L-S3, compared with the corresponding particles <b>AC1</b> (c) prepared with L-S1. Analogue comparison established between the hybrid (with a magnetic core) nanoparticles <b>AC8</b> (d) and <b>AC10</b> (e) with the use of SDS in <b>AC4</b> (g). ....	84
<b>Figure 6.7.</b> Evolution of the conversion and enantioselectivity of aldol reaction between <i>p</i> -nitrobenzaldehyde (0.1 mmol) and cyclohexanone (1 mmol) in water, catalyzed with the magneto-responsive chiral nanoparticles <b>AC2</b> (10 mol.% with respect to the aldehyde). ....	86

<b>Figure 6.8.</b> Evolution of the conversion and enantioselectivity of aldol reaction between <i>p</i> -nitrobenzaldehyde (0.1 mmol) and cyclohexanone (1 mmol) in water, catalyzed with the magneto-responsive chiral nanoparticles <b>AC5</b> (10 mol.% with respect to the aldehyde).....	86
<b>Figure 6.9.</b> Recycling study: conversion (left) and enantioselectivity (right) of the aldol reaction catalyzed by the magneto-responsive chiral catalysts <b>AC2</b> and <b>AC5</b> during four cycles of reaction.....	88
<b>Figure 7.1.</b> Schematic representation of the energy storage and release in microencapsulated PCMs. (Based on refs. 251 and 250. Image credit: Black Thumb Gardener and Sunflowes at night by Jason Squyres).....	93
<b>Figure 7.2.</b> TGA curves of ODTMS-functionalized ceria (magenta line), magnetite (green line), and titania (blue) nanoparticles and the corresponding pristine particles without functionalization (dashed lines).....	95
<b>Figure 7.3.</b> Colloidal stability of the dispersion polyurethane-metal oxides hybrid capsules prepared in inverse Pickering emulsion using (a) magnetite (b) titania, and (c) magnetite–titania nanoparticles with different surface functionalization (with MPS, PTMS or ODTMS) as inorganic stabilizers.....	95
<b>Figure 7.4.</b> TEM micrographs of polyurethane capsules prepared using ODTMS-functionalized silica nanoparticles.....	96
<b>Figure 7.5.</b> TEM micrographs and size distribution diagrams of polyurethane capsules incorporating magnetite (a), titania (b), and ceria (c) nanoparticles.....	98
<b>Figure 7.6.</b> SEM micrographs of polyurethane capsules incorporating magnetite (a), titania (b), and ceria (c) nanoparticles.....	98
<b>Figure 7.7.</b> TEM micrographs and size distribution of multifunctional polyurethane capsules incorporating two inorganic species: magnetite–titania (a) and magnetite–ceria (b).....	99
<b>Figure 7.8.</b> SEM micrographs of multifunctional microcapsules of polyurethane–magnetite–titania (a–c) and polyurethane–magnetite–ceria (d–f) at different magnifications.....	99
<b>Figure 7.9.</b> Chemical structure (a) and absorption spectra (b) of the dye Brilliant Blue FCF.....	100
<b>Figure 7.10.</b> Study of the release of the dye Brilliant Blue FCF encapsulated (5 wt.%) within the hybrid polyurethane-based microcapsules incorporating different inorganic nanoparticles or mixtures of them.....	101

---

<b>Figure 7.11.</b> TEM micrographs of polyurethane capsules with magnetite (a), magnetite–titania (b), and magnetite–ceria (c) nanoparticles, encapsulating $\text{Na}_2\text{SO}_4 \cdot 10\text{H}_2\text{O}$ salt. ....	102
<b>Figure 7.12.</b> Size distribution of the polyurethane–magnetite hybrid capsules with (magenta) and without (blue) 20 wt. % of $\text{Na}_2\text{SO}_4 \cdot 10\text{H}_2\text{O}$ salt. ....	103
<b>Figure 7.13.</b> Thermal analysis by differential scanning calorimetry of $\text{Na}_2\text{SO}_4 \cdot 10\text{H}_2\text{O}$ salt in bulk (a), and encapsulated (20 wt. %) within the magnetoresponse polyurethane hybrid microcapsules <b>PC1</b> (b), <b>PC2</b> (c), and <b>PC3</b> (d). ....	104
<b>Figure 7.14.</b> TEM (a) and SEM (b) micrographs of the capsules <b>PC4</b> . ....	105
<b>Figure 7.15.</b> Size-distribution diagrams of the capsules <b>PC4</b> . ....	105
<b>Figure 7.16.</b> Thermal analysis by differential scanning calorimetry of $\text{Na}_2\text{HPO}_4 \cdot 2\text{H}_2\text{O}$ salt in bulk (a) and the <b>PC4</b> capsules (b). ....	106



## B. List of Tables

<b>Table 2.1.</b> Free-radical initiators commonly used for heterophase polymerization processes in direct miniemulsions. ....	7
<b>Table 4.1.</b> Material composition and main features of the polymer–metal oxide hybrid nanoparticles incorporating catalytic species with specific surface functionalization. ....	47
<b>Table 4.2.</b> Synthetic details and material features of polymer–metal oxide hybrid nanoparticles incorporating ODTMS-functionalized catalytic species, prepared with different initiators and polymerization temperatures. ....	53
<b>Table 4.3.</b> Material composition and particle size of multifunctional polymer–metal oxide hybrid nanoparticles incorporating catalytic and magnetic species with specific surface functionalization. ....	55
<b>Table 4.4.</b> Main features of the multifunctional polymer–metal oxide hybrid nanoparticles before and after magnetic purification. ....	56
<b>Table 5.1.</b> Characteristics of the nanoparticles prepared by different synthetic strategies: material composition, particle diameter ( $d$ ), and inorganic (ceria and magnetite) content. ....	62
<b>Table 5.2.</b> Conversion after 24 h and reaction rate ( $k$ ) achieved with different catalysts and concentrations. ....	69
<b>Table 6.1.</b> Main features of the different polymer-supported proline nanocatalysts. ....	83
<b>Table 6.2.</b> Characterization of the dispersion of polymer and hybrid nanoparticles synthesized by miniemulsion polymerization using L-S3 as a surfactant. ....	83
<b>Table 6.3.</b> Conversion and enantioselectivity of the aldol reaction using different proline-based chiral catalysts. ....	87
<b>Table 7.1.</b> Empiric values of the parameters $A_{\max}$ and $k$ calculated for each experiment of release. ....	101
<b>Table 7.2.</b> Main features of the magneto-responsive polyurethane capsules for thermal energy storage. ....	103



## C. List of Schemes

<b>Scheme 2.1.</b> Simplified representation of the condensation of hydroxides $\text{Ce}(\text{OH})_4$ to $\text{CeO}_2$ . The presence of hydrated complexes has been omitted for simplicity reasons. ....	19
<b>Scheme 2.2.</b> Schematic representation of the functionalization of metal oxide nanoparticles using trialkoxysilane components as coupling agents. (Based on ref. 89) .....	20
<b>Scheme 4.1.</b> Chemical structures of the three alkoxy silane components used as coupling agents for the surface functionalization of the magnetite, ceria, and titania nanoparticles. ....	44
<b>Scheme 5.2.</b> Hydration of 2-cyanopyridine to 2-picolinamide. ....	67
<b>Scheme 5.2.</b> Reaction mechanism of the hydrolysis of 2-cyanopyridine to 2-picolinamide catalyzed by ceria nanoparticles. (Based on refs. 153, 176, and 177) .....	68
<b>Scheme 6.1.</b> Chemical structure of the proline-based chiral molecules: L/D-S1, L/D-S2, and L-S3. ....	73
<b>Scheme 6.2.</b> Aldol reaction between between <i>p</i> -nitrobenzaldehyde and cyclohexanone catalyzed by proline. ....	84
<b>Scheme 6.3.</b> Mechanism proposed for the aldol reaction between <i>p</i> -nitrobenzaldehyde and cyclohexanone in water catalyzed by proline units. (Based on ref. 212) .....	85
<b>Scheme 9.1.</b> Acylation reaction used for the synthesis of the surfmer 10-undecenoyl- <i>trans</i> -4-hydroxy-L-proline (L-S1). D-S1 was synthesized analogously using <i>trans</i> -4-hydroxy-D-proline.....	120
<b>Scheme 9.2.</b> Acylation reaction used for the synthesis of the monomer <i>O</i> -methacryloyl- <i>trans</i> -4-hydroxy-L-proline (L-S2). D-S2 was synthesized analogously using <i>trans</i> -4-hydroxy-D-proline. (Based on refs. 215 and 234) .....	120
<b>Scheme 9.3.</b> Acylation reaction used for the synthesis of decanoyl- <i>trans</i> -4-hydroxy-L-proline (L-S3). ....	121





## D. List of Acronymes

AIBN	2,2'-Azobis(2-methylpropionitrile)
AM	Allyl methacrylate
AMBN	2,2'-Azobis-(2-methylbutyronitrile)
BA	Butyl acrylate
BB	Brilliant Blue FCF
BIJES	Bicontinuous interfacially jammed emulsion gels
BODIPY	4,4-Difluoro-4-bora-3a,4a-diaza-s-indacene
cmc	Critical micelle concentration
CTAB	Cetyltrimethylammonium chloride
D	Dextrogyre
DLS	Dynamic light scattering
DMF	Dimethylformamide
DSC	Differential scanning calorimetry
EM	Electron microscopy
HLB	Hydrophilic-Lipophilic Balance
HMD	1,6-Diaminohexane
HPLC	High performance liquid chromatography
ICP-MS	Inductively coupled plasma mass spectrometry
IHL	Inner Helmholtz layer
KPS	Potassium peroxydisulfate
L	Levogyre
LHS	Latent heat storage
Lutensol AT50	Poly(ethylene oxide) hexadecyl ether
MPS	3-(Methacryloyloxy)propyl trimethoxysilane
OA	Oleic acid
ODTMS	Octadecyl trimethoxysilane
OHL	Outer Helmholtz layer
O/W	Oil in water or direct emulsion
P(MMA-BA)	Poly(methyl methacrylate-co-butyl acrylate)
P(S-4-VP)	Poly(styrene-co-4-vinyl pyridine)
P(S-MA)	Poly(styrene-co-methacrylic acid)
P(S-SS)	Poly(styrene-co-styrene sulfonate)
PAA	Poly(acrylic acid)
PCD	Particle charge detector
PCM	Phase change material
PCS	Photon correlation spectroscopy
PDI	Polydispersity index

PHEMA	Poly(2-hydroxyethyl methacrylate)
PMMA	Poly(methyl methacrylate)
polyDADMAC	Poly(diallyldimethylammonium chloride)
PS	Polystyrene
PTMS	Trimethoxy(propyl)silane
PU	Polyurethane
QELS	Quasi-elastic light scattering
rac	Racemic mixture
RAFT	Reversible addition–fragmentation chain transfer
RP-HPLC	Reversed-phase column
SA	Stearyl acrylate
SDS	Sodium dodecyl sulfate
SEM	Scanning electron microscopy
SHS	Sensible heat storage
SLGlu	Sodium lauroyl glutamate
SLSar	Sodium lauroyl sarcosinate
SMSar	Sodium myristoyl sarcosinate
Surfmer	Surface active monomer
TBHP	t-Butyl hydroxyperoxide
TCES	Thermochemical energy storage
TDI	Toluene-2,4-diisocyanate
TEM	Transmission electron microscopy
TEOS	Tetraethyl orthosilicate
TFA	Trifluoroacetic acid
TGA	Thermogravimetric analysis
tmhd	2,2,6,6-Tetramethyl-3,5-heptanedione
UV-Vis	Ultraviolet-visible spectroscopy or spectrophotometry
VBA	Vinylbenzoate
4-VP	4-Vinyl pyridine
W/O	Water in oil or inverse emulsion
XRD	X-Ray diffraction

## E. Scientific Contributions

### E.1 Publications

- (Book Chapter) Application of Nanoemulsions in the Synthesis of Nanoparticles  
Muñoz-Espí, R.; Álvarez-Bermúdez, O.  
In: D. J. McClements and S. M. Jafari (eds.). Nanoemulsions: Formulation, Applications, and Characterization, pp: 477-515, Academic Press-Elsevier, 2018.
- Crystallization at Nanodroplet Interfaces in Emulsion Systems: A Soft-Template Strategy for Preparing Porous and Hollow Nanoparticles  
Varol, H.S.; Álvarez-Bermúdez, O.; Dolcet, P.; Kuerbanjiang, B.; Gross, S.; Landfester, K.; Muñoz-Espí, R. *Langmuir* **2016**, 32, 13116-13123

### E.2 Conferences

#### E.2.1 Oral Communications

- Youth Interdisciplinary Scientific Forum "New Materials" – Invited Speaker  
“Multifunctional Hybrid Colloidal Materials”  
June 2016, Sochi, Russia
- III Meeting of Young Researchers of the Group Specialized in Colloids and Interfaces of the Spanish Royal Chemistry and Royal Physics Societies (III-JICI)  
“Catalytic and Magnetic Bifunctional Polymer–Metal Oxide Hybrid Nanoparticles by Miniemulsion Polymerization”  
October 2016, Madrid, Spain
- VII Iberian Meeting on Colloids and Interfaces (RICI2017)  
“Miniemulsion Polymerization as a Synthetic Platform for Structure Control of Multifunctional Polymer/Metal Oxide Hybrid Nanoparticles”  
July 2017, Madrid, Spain
- XXXI Conference of European Colloid and Interface Society (ECIS2017)  
“Magnetically Separable Polymer/Metal Oxide Nanocarriers Prepared in Miniemulsion with High Performance in Heterogeneous Catalysis”  
September 2017, Madrid, Spain
- IV Meeting of Young Researchers of the Group Specialized in Colloids and Interfaces of the Spanish Royal Chemistry and Royal Physics Societies (IV-JICI2018)  
“Magnetoresponsive Hybrid Nanocarriers with Catalytically Active Surface for Energy Applications”  
February 2018, Córdoba, Spain

- German-Spanish Symposium in Functional Hybrid Materials - Invited Speaker  
“Polyurethane–Metal Oxide Hybrid Microcapsules: Highly Efficient Carriers for Thermal Energy Storage”  
April 2018, Valencia, Spain
- XV Biannual Meeting of the Polymer Group of the Spanish Royal Chemistry and Royal Physic Societies (GEP)  
“Morphology control of polymer–metal oxide hybrid nanoparticles towards the preparation of magnetically recoverable heterogeneous catalysts”  
September 2018, Punta Umbria, Spain

### **E.2.1 Poster Communications**

- Young Scientist Day of the Institute of Materials Science of the University of Valencia (JJI-ICMUV)  
“Functional Hybrid Nanoparticles and Capsules Prepared in Miniemulsion”  
June 2016, Valencia, Spain
- NANOTEC2016 International Conference  
“Magnetically Separable Hybrid Nanostructures for Catalytic Applications”  
September 2016, Valencia, Spain
- Young Scientist Day of the Institute of Materials Science of the University of Valencia (JJI-ICMUV)  
“Multifunctional Polymer–Metal Oxide Hybrid Nanoparticles by Miniemulsion Polymerization”  
June 2017, Valencia, Spain
- XIV Biannual Meeting of the Polymer Group of the Spanish Royal Chemistry and Royal Physic Societies (GEP) – Best Poster Award  
“Controlling the Structure of Polymer–Metal Oxide Hybrid Nanoparticles via Colloidal Methods”  
September 2016, Burgos, Spain

## F. Acknowledgments

There are many people whom I would like to thank for their contribution (in one or another way) to this thesis. First of all I would like to thank the Max Planck Society for the scholarship, which has economically supported my work during the last three years, to Katarina Landfester for allowing me to be part of her group in the Max Planck for Polymer Research of Mainz and for being an exemplary leader. Thanks to my thesis director Rafael Muñoz-Espí for introducing me into a completely unknown branch of science where I have discovered some new passions. Thanks for his support and his trust in me.

I am very grateful to all the group of Photocatalysis of Kai Zhang, to Niklas Hubert, Calum Ferguson, Jeehye Byum, Run Li, Wei Huang, Cyrine Ayed, and Wenxin Wei for their advice and their company during the development of the Chapter 6 of this thesis. Thanks to all the group of AK-Landfester for their warm reception during my stays at the MPIP, especially thanks to Eloise Barros, Chiara Pelosi, Mark Mueller, Tobias Haider, Claudia Weber, Maria Kokkinopoulou, Alice Antonello, Cesare Benedetti, Oksana Suraeva, and Héloïse Thérien-Aubin. Thanks to Elke Muth and Petra Raeder for the measurements of surface charge density and TGA, respectively; and to Gunnar Glasser for his teaching, help and contribution with the SEM imaging. Thanks to Ana Cross who has embraced me in the Institute of Materials Science of the University of Valencia, to all the colleagues I have met there and specially to Adrián Aguado, Inés Adam, Ana Torres and Andrea Jiménez for their contribution with their bachelor thesis to the work presented Chapters 5 and 7. Thanks to Prof. Francisco Pérez for his contribution in the kinetic study in Chapter 5, to David Vie for his help and advice related to the characterization by DLS, TGA and DSC, to Clara Gómez, Antonio Lázaro, María Ángeles and Julián Heredero.

More in the personal side, I would like to thank Femke Conradie, Marina Romaní and Mamen Cenit for being my family in Valencia together with Ankie Titulaer, Paula Serna, and the entire group from “Día del Parque”. Thanks to the friends from the ICMol and IATA, to the physics from the ICMUV. Even from the distance I will never forget the meaningful motivation transmitted by David Aguilà, Noelia Vilar, Jon Maiz, Sergio Gómez, María Ameneiro, Miguel Comesaña, Cintia Mateo, Laura and Alberto Álvarez, Laura Romasanta, Beatriz Lupión, Rubén Ahijado, and Tristan Bereau who have been my example to follow as persons, friends, and scientists. Merci à Iwan Caouren qui m’a encouragé à rejoindre ce projet de thèse. And overall, thanks to my parents and my brother for their care and for keeping me laughing under any situation.